



National Library
of Canada

Bibliothèque nationale
du Canada

Canadian Theses Service

Service des thèses canadiennes

Ottawa, Canada
K1A 0N4

NOTICE

The quality of this microform is heavily dependent upon the quality of the original thesis submitted for microfilming. Every effort has been made to ensure the highest quality of reproduction possible.

If pages are missing, contact the university which granted the degree.

Some pages may have indistinct print especially if the original pages were typed with a poor typewriter ribbon or if the university sent us an inferior photocopy.

Previously copyrighted materials (journal articles, published tests, etc.) are not filmed.

Reproduction in full or in part of this microform is governed by the Canadian Copyright Act, R.S.C. 1970, c. C-30.

AVIS

La qualité de cette microforme dépend grandement de la qualité de la thèse soumise au microfilmage. Nous avons tout fait pour assurer une qualité supérieure de reproduction.

S'il manque des pages, veuillez communiquer avec l'université qui a conféré le grade.

La qualité d'impression de certaines pages peut laisser à désirer, surtout si les pages originales ont été dactylographiées à l'aide d'un ruban usé ou si l'université nous a fait parvenir une photocopie de qualité inférieure.

Les documents qui font déjà l'objet d'un droit d'auteur (articles de revue, tests publiés, etc.) ne sont pas microfilmés.

La reproduction, même partielle, de cette microforme est soumise à la Loi canadienne sur le droit d'auteur, SRC 1970, c. C-30.

THE UNIVERSITY OF ALBERTA

Sources of the Cross-Tail Magnetic Field in the Earth's
Magnetotail

by

Wanda A. R. Kamocki

A THESIS

SUBMITTED TO THE FACULTY OF GRADUATE STUDIES AND RESEARCH
IN PARTIAL FULFILMENT OF THE REQUIREMENTS FOR THE DEGREE
OF Master of Science

Department of Physics

EDMONTON, ALBERTA

Fall, 1988

Permission has been granted to the National Library of Canada to microfilm this thesis and to lend or sell copies of the film.

The author (copyright owner) has reserved other publication rights, and neither the thesis nor extensive extracts from it may be printed or otherwise reproduced without his/her written permission.

L'autorisation a été accordée à la Bibliothèque nationale du Canada de microfilmer cette thèse et de prêter ou de vendre des exemplaires du film.

L'auteur (titulaire du droit d'auteur) se réserve les autres droits de publication; ni la thèse ni de longs extraits de celle-ci ne doivent être imprimés ou autrement reproduits sans son autorisation écrite.

ISBN 0-315-45659-0

THE UNIVERSITY OF ALBERTA

RELEASE FORM

NAME OF AUTHOR Wanda A. R. Kamocki
TITLE OF THESIS Sources of the Cross-Tail Magnetic
Field in the Earth's Magnetotail
DEGREE FOR WHICH THESIS WAS PRESENTED Master of Science
YEAR THIS DEGREE GRANTED Fall, 1988

Permission is hereby granted to THE UNIVERSITY OF ALBERTA LIBRARY to reproduce single copies of this thesis and to lend or sell such copies for private, scholarly or scientific research purposes only.

The author reserves other publication rights, and neither the thesis nor extensive extracts from it may be printed or otherwise reproduced without the author's written permission.

(SIGNED) Wanda A. R. Kamocki

PERMANENT ADDRESS:

..... R. R. #3 Newmarket
..... Ontario
..... L3Y 4W1

DATED August 19 1988

THE UNIVERSITY OF ALBERTA
FACULTY OF GRADUATE STUDIES AND RESEARCH

The undersigned certify that they have read, and recommend to the Faculty of Graduate Studies and Research, for acceptance, a thesis entitled Sources of the Cross-tail Magnetic Field in the Earth's Magnetotail submitted by Wanda A. R. Kamocki in partial fulfilment of the requirements for the degree of Master of Science in Physics.

..... *André Potz*

Supervisor

..... *P. P. Coyne*

..... *J. E. Samson*

..... *J. H. Kerrallan*

Date..... August 19, 1988

Dedication

To my father, in memory, whose star-gazing
in the early years inspired my desire
to pursue knowledge of things beyond
this earth.

To my mother, whose life and wisdom inspire
my determination to strive towards all
in which I believe.

To Nicholas-Alexander, who inspires dreams
and with whom all dreams are realized.

Abstract

The configuration of the earth's magnetic field is strongly influenced by the effects of electric currents generated through the solar-terrestrial interaction. In this thesis, sources of the cross-tail magnetic field component, B_y , which is aligned in a direction normal to the noon-midnight meridian plane are investigated. Of primary importance is the identification of sources responsible for observed magnetic signatures which are inconsistent with those expected from statistically derived models of the magnetotail. *In situ* magnetic field and energetic particle measurements collected by the ISEE satellites in the CPS, PSBL and tail lobe plasma regimes were analysed.

It was first demonstrated that both magnetic and energetic particle data are required for the unambiguous identification of the plasma regime being sampled. Then, three distinct categories of anomalous tail B_y signatures corresponding to encounters of the neutral sheet were outlined. Some, but not all, of these anomalous signatures could be partially attributed to choice of coordinate system in which to order the data. The dependence of tail B_y on magnetospheric activity level and on relevant interplanetary parameters was also investigated, as was the possible influence of the IMF B_y component on the tail B_y field. Only minimal justification for the postulate of IMF B_y "penetration" into the magnetotail as a potential source for tail B_y enhancement was obtained.

Finally, it was shown that large-scale field-aligned currents (FAC) threading the magnetotail in the region of the PSBL can produce magnetic perturbations capable of skewing the magnetotail field such that the earthward/anti-earthward component of the tail magnetic field in the vicinity of the PSBL is cancelled, giving the appearance of a neutral sheet encounter. It may, therefore, be inferred that FAC in the magnetotail can be a significant source of the cross-tail magnetic field.

Acknowledgments

I would like foremost to extend my sincerest appreciation to my husband, Nicholas-Alexander, whose unflinching encouragement, understanding and confidence in me made the completion of this work not only possible, but as well, worthwhile. In addition, I would like to thank Dr. G. Rostoker for his supervision and entertaining commentary throughout the course of this research. Advice from Dr. J. Samson on various theoretical aspects is also appreciated. I gratefully acknowledge Dr. L.A. Frank for allowing the use of the energetic particle (LEPEDEA) data collected by the University of Iowa, and Dr. C.T. Russell and the National Space Science Data Center through the World Data Center A for Rockets and Satellites for permitting the use of the ISEE 1 and 2 magnetometer data. I am indebted to Dr. C.Y. Huang for her invaluable assistance with the interpretation of the LEPEDEA data, and as well, for her hospitality and inspiration during a visit to the University of Iowa. Finally, I would like to thank Dr. X.S. Wang for providing the subroutines which enabled me to conduct the Principal Component Analyses of chapter 4.

Table of Contents

Chapter	Page
1. Introduction	1
1.1 Historical Notes on the Study of Geomagnetism	2
1.2 The Magnetosphere	4
1.3 Major Current Systems in the Magnetosphere	23
1.4 Thesis Objectives	41
2. Sources of the Cross-Tail Magnetic Field Component ..	44
2.1 Coordinate System Definitions	44
2.2 Hydrodynamic Tail Flare	48
2.3 Ring Current Contributions to the Magnetotail B_y Component	52
2.4 Magnetic Perturbations Due to Field-Aligned Currents	54
2.5 IMF B_y Penetration	55
2.6 Summary of the Contributions to B_y in the CPS, PSBL and Lobe	64
3. Instrumentation and Data Presentation	68
3.1 Orbit Specifications for ISEE's 1 and 2	70
3.2 Measurement and Display of the Tail Magnetic Field	73
3.3 Magnetic Signatures of the CPS, PSBL and Lobe ...	76
3.4 Energetic Particle Detection and Presentation ...	81
3.5 Energetic Particle Signatures in the CPS, PSBL and Lobe	92
3.6 Sample Event Analyses	95
3.7 Measurement of the IMF and Solar Wind Plasma Parameters	105
3.8 The Auroral Electrojet Indices	106
4. Statistical Studies Involving B_y	112

4.1	Use of Energetic Particle Spectrograms for Identification of the Plasma Regime Being Sampled	115
4.2	The Inadequacy of Employing Magnetic Field Data Alone for Magnetotail Plasma Regime Identification	117
4.2.1	Data Selection Criteria	118
4.2.2	$ B_x $ as a Function of Downtail Distance ..	119
4.2.3	$ B_x $ and $ B_y $ as Functions of AE	130
4.2.4	$ B_y $ as a Function of Downtail Distance ..	137
4.2.5	$ B_y $ as a Function of $ B_x $	145
4.2.6	Summary	156
4.3	Non-zero B_y at the Neutral Sheet	160
4.4	The Relationship Between Sun-Earth Geometry and B_y Biases	179
4.5	Investigation of Solar Wind Influence on Atypical B_y Signatures at the Neutral Sheet	196
4.5.1	IMF B_y Penetration	210
5.	Distortion of the Magnetotail Magnetic Field by Large-Scale Field-Aligned Currents	236
5.1	Case Study: Day 75, 1979	236
5.2	A Second Observation of $ B_x \approx 0$ nT in the Vicinity of the PSBL	247
5.3	The Effects of Large-Scale Field-Aligned Currents on the Magnitude of the Cross-Tail Magnetic Field Component	253
6.	Conclusions	262
	Bibliography	267
	Appendix A	278
	Appendix B	282
	Appendix C	287

List of Tables

Table		Page
4.1	Events representing each of the 4 categories of B_y behaviour at the apparent neutral sheet,	164
4.2	Division of event subset into activity level and solar wind parameter magnitude categories.	201

List of Figures

Figure	Page
1.1	Early visualization of the Earth's magnetic cavity (equatorial projection) (after Chapman and Ferraro, 1931).6
1.2	Noon-midnight meridian cross-section of the Earth's magnetosphere.7
1.3	Proposed sites of magnetic merging in the magnetosphere. Reconnection is believed to occur at the dayside magnetopause as well as at the distant magnetic neutral line (after Hones, 1986).18
1.4	Three dimensional cross-section of the Earth's magnetosphere (after Eastman et al., 1984).24
1.5	Schematic projection of the Chapman-Ferraro (magnetopause) currents on the Earth's magnetopause surface.25
1.6	Schematic representations of the cross-tail (neutral sheet) current in (a) a cross-tail projection, and (b) a noon-midnight meridian projection.29
1.7	Schematic representation of the ring current shown here as a projection on the equatorial plane of the magnetotail.31
1.8	Solenoidal configuration of the Birkeland (field-aligned) currents in relation to a plane parallel to and in the vicinity of the magnetotail neutral sheet (after Rostoker and Eastman, 1987).34
1.9	Distribution and flow directions of large-scale FAC (a) for weakly disturbed conditions ($ AL < 100$ nT) and (b) for active periods ($ AL \geq 100$ nT) (after Iijima and Potemra, 1976).35
1.10	Directions of Birkeland, Pedersen and Hall current flows in the auroral oval (after Rostoker and Boström, 1976).37

- 2.1 Hinging of the magnetotail and the consequent position of the neutral sheet (a) when the north geomagnetic pole is tilted toward the sun (ie: northern hemisphere summer), and (b) when the north pole is tilted away from the sun (ie: northern hemisphere winter) (after Gosling et al., 1986).47
- 2.2 Contribution to the cross-tail magnetic field component due to flaring of the tail. Projections of the field contributions on the equatorial plane are shown for (a) the northern and (b) the southern hemisphere.51
- 2.3 Ring current contributions to B_y in (a) the northern and (b) the southern hemisphere, both shown as projections onto the plane of the neutral sheet.53
- 2.4 Directions of flow for the four Birkeland current loops along with the resulting cross-tail magnetic perturbations, projected onto the cross-section of the magnetotail (after Rostoker and Boström, 1976).56
- 2.5 Scatter plot of hourly averaged tail B_y measurements as a function of simultaneously measured IMF B_y values. Data presented are those gathered by Fairfield (1979). The linear trend shown was postulated by Fairfield to represent an influence of the IMF B_y on the tail B_y component which has become known as IMF B_y penetration. From the slope of the line, 13% of the IMF B_y is proposed to penetrate the tail.58
- 2.6 Same as figure 2.5 for data compiled by Lui (1985). A 50% penetration of the IMF B_y is suggested.59
- 2.7 Twist of the magnetotail which is thought to result from a torque imposed on the tail by the IMF. The direction of twist shown corresponds to positive IMF B_y (the direction is reversed for negative IMF B_y) (after Cowley, 1981).62

Figure	Page	
2.8	Quadrants of preferred IMF B_y penetration resulting from the proposed torque exerted on the magnetotail by the IMF. Here, penetration is postulated to occur in the north-dusk and south-dawn sectors of the tail corresponding to the direction of twist of the tail shown in figure 2.7 (after Cowley, 1981).	63
2.9	Same as figures 2.5 and 2.6 but for data compiled by Tsurutani et al. (1986) for the north-dusk tail lobe. In this case, separate linear fits were made for negative and positive IMF B_y , and these suggest that 13% and 2%, respectively, of the IMF B_y penetrate the tail in this regime.	65
3.1	Sample ISEE 1 orbit plot in GSM coordinates. Shown is the (X-Y) projection for orbit 199, 1979. GSM	72
3.2	ISEE 1 magnetogram, in GSE coordinates, for hour 14, day 39 (February 8), 1979.	75
3.3	Idealized division of the tail cross-section into four quadrants which are defined according to the parities of both the X and Y components of the tail magnetic field. For example, quadrant 1 (north-dawn sector) is defined by positive B_x and positive B_y	77
3.4	Cross-sections of the geomagnetic tail illustrating schematically (a) the Russell-Brody and (b) the Fairfield model representations of the shape of the tail neutral sheet (after Gosling et al., 1986).	79
3.5	(a) Fields-of-view of the LEPEDA as referenced to the spacecraft spin axis, and (b) LEPEDA coverage of the angular distributions of the positive ion and electron intensities, projected onto the unit sphere (after Eastman et al., 1985b).	83
3.6	An example of the energy-time spectrogram format for displaying energetic particle data. This spectrogram presents data collected at low-bit rate for day 39 (February 8), 1979.	87

Figure	Page
3.7	Examples of the energy-phase angle spectrogram format for displaying energetic particle data. Presented here are data collected at low-bit rate for day 114 (April 24), 1979, at start times of (a) 11:08 and (b) 11:11 UT, respectively.89
3.8	Same as figure 3.7 but for start times of (a) 11:17 and (b) 11:38 UT, respectively'90
3.9	Same as figure 3.7 but for a start time of 11:45 UT.91
3.10	ISEE 1 magnetogram, in GSE coordinates for day 39 (February 8), 1979, hour 10.97
3.11	ISEE 1 magnetogram, in GSE coordinates, for day 39 (February 8), 1979, hour 11.98
3.12	ISEE 1 magnetogram, in GSE coordinates, for day 39 (February 8), 1979, hours 12.99
3.13	Energy-time spectrogram for day 114 (April 24), 1979.103
3.14	Distribution of the 12 geomagnetic observation stations from which northern-hemisphere AE data are gathered.108
3.15	Auroral electrojet activity levels, AU,AL,AE,AO, measured in units of nT and displayed graphically as a function of Universal Time for (a) day 39 (February 8), 1979, and (b) day 114 (April 24), 1979.110
4.1	Values of B_x plotted as a function of distance downtail for all measurements tabulated in the 1978/1979 data set.121
4.2	Same as figure 4.1 but (a) for 1978 data only, and (b) for 1979 data only.122
4.3	Scatter plots of B_x as a function of distance downtail for all samplings of (a) the CPS and (b) the PSBL from the 1978/1979 data set.126
4.4	Same as figure 4.3 but for samplings of the tail lobes.127

Figure	Page
4.5	1978 and 1979 B_x measurements plotted as a function of the AE index. 131
4.6	Histogram of all AE measurements from the 1978/1979 data set. Three categories of low ($AE \leq 150$ nT), intermediate ($150 < AE \leq 400$ nT), and high ($AE > 400$ nT) activity level are indicated. 133
4.7	Activity level as a function of B_x for all (a) CPS and (b) PSBL measurements from the 1978/1979 data set. 135
4.8	Same as figure 4.7 but for tail lobe measurements. 136
4.9	Scatter plots of B_y as a function of activity level for (a) the entire 1978/1979 data set, and (b) CPS measurements from the 1978/1979 data. 138
4.10	Same as figure 4.9 but for (a) PSBL and (b) tail lobe measurements. 139
4.11	Scatter plots of B_y as a function of distance downtail for (a) the entire 1978/1979 data set, and (b) CPS samplings. 140
4.12	Same as figure 4.11 but for (a) PSBL and (b) tail lobe samplings. 141
4.13	B_y plotted as a function of B_x for the complete 1978/1979 data set. 147
4.14	B_y as a function of B_x for (a) CPS and (b) PSBL measurements for 1978 and 1979. 149
4.15	Same as figure 4.14 except for tail lobe measurements. 150
4.16	B_y vs. B_x for a division of the 1978/1979 data into three groups based on distance downstream of the Earth. The two categories shown here are for values of X in the ranges of (a) $10 \leq X \leq 14$ Re and (b) $14 < X \leq 18$ Re (X bins #1 and #2, respectively). 153
4.17	Same as figure 4.16 but for the third range of distance downstream of the Earth given by $18 < X \leq 23$ Re (X bin #3). 154

Figure	Page
4.18 1978/1979 samplings of the CPS for X bins (a) #1, (b) #2 and (c) #3, respectively.	157
4.19 1978/1979 samplings of the PSBL for X bins (a) #1, (b) #2 and (c) #3, respectively.	158
4.20 1978/1979 samplings of the tail lobes for X bins (a) #1, (b) #2 and (c) #3, respectively.	159
4.21 ISEE 1 magnetogram for hour 14 of day 73 (March 14), 1979.	166
4.22 ISEE 2 magnetogram for hour 03 of day 126 (March 06), 1979.	169
4.23 ISEE 1 magnetogram for hour 18 of day 42 (February 11), 1979.	170
4.24 ISEE 1 magnetogram for hour 07 of day 59 (February 28), 1979.	172
4.25 ISEE 1 magnetogram for hour 10 of day 64 (March 5), 1979.	174
4.26 ISEE 1 magnetogram for hour 11 of day 90 (March 31), 1979.	175
4.27 ISEE 1 magnetogram for hour 01 of day 83 (March 24), 1979.	177
4.28 ISEE 1 magnetogram for hour 00 of day 76 (March 17), 1979.	178
4.29 B_y bias plotted as a function of Universam Time for the 302 event subset of the 1978/1979 data set. The vertical dotted line marks the vernal equinox, and the solid sinusoidal curve indicates the expected trend in B_y biases for a total field of 20 nT. The hollow diamonds represent 1978 events while the bold diamonds indicate 1979 events.	191
4.30 Histogram showing frequency of occurrence of solar wind density data. The mean value of the data is 9 cm ⁻³	197
4.31 Histogram showing frequency of occurrence of solar wind temperature data. The mean value of the data is 75×10^3 K.	198

Figure	Page
4.32 Histogram showing frequency of occurrence of solar wind velocity data. The mean value of the data is 425 km/sec.	199
4.33 Scatter plot of tail B_y (hourly averages) as a function of simultaneous hourly averaged IMF B_y for all data in the 1978/1979 data set for which IMF data was available.	212
4.34 Same as figure 4.33 but for (a) 1978 data only, and (b) 1979 data only.	213
4.35 Tail B_y plotted as a function of IMF B_y for 1978/1979 samplings of (a) the CPS and (b) the PSBL.	218
4.36 Same as figure 4.35 but for tail lobe samplings.	219
4.37 Tail B_y vs. IMF B_y for 1978/1979 samplings of the CPS, categorized into quadrants according to the definitions given in figure 3.3. Shown here are data from quadrants (a) 1 and (b) 2.	222
4.38 Same as figure 4.37 but for data from quadrants (a) 3 and (b) 4.	223
4.39 Tail B_y vs. IMF B_y for 1978/1979 samplings of the PSBL, categorized into (a) quadrant 1, and (b) quadrant 2.	224
4.40 Tail B_y vs. IMF B_y for 1978/1979 samplings of the tail lobes, categorized into (a) quadrant 1, and (b) quadrant 2.	225
4.41 Tail B_y vs. IMF B_y for samplings of (a) low and (b) intermediate AE from the 1978/1979 data set.	228
4.42 Same as figure 4.41 but for samplings of high AE.	229
4.43 Tail B_y vs. IMF B_y for samplings of the 1978/1979 data set for which the value of IMF B_z was (a) positive, and (b) negative.	230

Figure	Page
4.44 Plots of tail B_y vs. IMF B_y for data in each of the three categories of (a) positive B_y biases, (b) negative B_y biases and (c) constant, non-zero B_y during an apparent neutral sheet encounter.	232
5.1 ISEE 1 magnetogram in GSE coordinates for hour 21, day 75 (March 16), 1979.	237
5.2 Energy-time spectrogram for day 75 (March 16), 1979.	240
5.3 Energy-phase angle spectrograms for day 75 (March 16), 1979, with starting times of (a) 21:07 and (b) 21:15 UT.	241
5.4 Same as figure 5.3 but for start times of (a) 21:24 and (b) 21:32 UT.	242
5.5 Same as figure 5.3 but for start times of (a) 21:41 and (b) 21:50 UT.	243
5.6 ISEE 1 magnetogram in GSE coordinates for hour 19, day 75 (March 16), 1979.	246
5.7 A plot of the AE index for day 75, 1979.	248
5.8 ISEE 1 magnetogram in GSE coordinates for hour 03, day 59 (February 28), 1978.	250
5.9 Energy-time spectrogram for day 59 (February 28), 1978.	251
5.10 A plot of the AE index for day 59, 1978.	252
5.11 Schematic representation of the thickening of a field-aligned current layer by the addition of adjacent layers which become skewed in orientation by the magnetic perturbations which influence the new layers.	257

Chapter 1

Introduction

Magnetospheric physics is today a quite diversified and progressive science that has developed primarily through attempts at explaining observable phenomena such as the polar auroral displays and irregular fluctuations in surface measurements of the geomagnetic field. Despite early models of the magnetosphere being inferred solely from ground based magnetic observations, many fundamental concepts, including the existence of the magnetosphere as the result of the interaction of a solar plasma with the geomagnetic field, were derived through such analyses. With the advent of rocket experiments in the 1940's to study upper atmospheric regions, and of satellite technology in the 1950's, *in situ* measurements were made possible. The wealth of information thereby obtained illustrated the complexity of the terrestrial magnetosphere as a system of interrelated electromagnetic fields and plasma regimes.

Currently, data available for magnetospheric studies includes magnetic field measurements, both ground-based and *in situ*, as well as particle measurements which define the characteristics of the various plasma regimes comprising the magnetosphere. Any reliable magnetospheric model must provide agreement between observed signatures of both the magnetic and plasma (particle) data. Furthermore, all observed signatures must be explainable in the framework of such a model. Our contemporary perception of the

magnetosphere, however, is inadequate in several respects regarding agreement between signatures in the magnetic and plasma data sets corresponding to a given event in space and time. Moreover, certain magnetic signatures have been detected which appear to be in conflict with expectations based on existing models. It is the intent of this work to identify and interpret inconsistencies of these types observed in the data sets pertaining to the region of the magnetosphere known as the magnetotail. Discrepancies related to the cross-tail component of the magnetotail magnetic field will be of primary concern.

1.1 Historical Notes on the Study of Geomagnetism

The study of magnetic phenomena began many centuries ago with the discovery of the attractive and directive nature of the natural magnet, lodestone. The application to navigation of the ability of lodestone to locate what was believed to be geographic north has been authentically documented as early as the late 1100's (Chapman and Bartels, 1940). A prime observation leading to the study of the Earth's magnetic field was that a suspended magnet did not always and everywhere point to the exact geographic north pole and it was gradually recognized that this divergence was a universal phenomenon which came to be known in the early to mid 1400's as magnetic declination. Gilbert, one of the earliest researchers to quantitatively study the Earth's magnetic field, recognized in 1600 that the geomagnetic

field resembled the field of a uniformly magnetized sphere of magnetite or lodestone (terrella) (Chapman and Bartels, 1940). He proposed that the source of the Earth's field was located within the Earth, itself, in contrast to the contemporary view which attributed the magnetic alignment of lodestone to an extraterrestrial influence. Halley was also a major influence in early geomagnetic studies, having introduced in 1692 the idea of an Earth core, which moves within the solid outer crust, in an attempt to explain secular variation, or change with time at a given location, of the magnetic declination (Chapman and Bartels, 1940; Jacobs, 1963). He proposed that if such a core rotated more slowly than the outer crust of the Earth, the geomagnetic field would drift steadily westward. His theory came very close to our present understanding of the phenomenon.

Irregular and rapid fluctuations of the magnetic needle, which are now known as magnetic storms, were first associated with the northern lights in 1747 by Hiorter (Chapman and Bartels, 1940), who noted that when the magnetic needle became disturbed, the northern lights would always be observed. This conclusion led to further examination of the connection between the aurora and magnetic activity and was to form the basis of much of the geomagnetic investigation of the following years. By the nineteenth century it became clear to researchers that clues to understanding the nature of the geomagnetic field were to be found not only through investigation of the Earth's

interior structure but also of phenomena in the atmospheric regions.

1.2 The Magnetosphere

In the late 1800's and early 1900's magnetic observatories were being built in order to systematically monitor the geomagnetic field. By this point in time, researchers studying geomagnetism had become interested in determining the causes of magnetic storms which were observed as irregular fluctuations in the magnitude of surface measurements of the Earth's magnetic field. Most early theories attributed these to the action of something propagated from the sun to the Earth (Chapman and Ferraro, 1931), and this solar agent was subsequently proposed to be either some corpuscular emission or ultraviolet radiation. Birkeland in 1896 put forth the suggestion that electrons travelling toward the Earth from the sun would be deflected around the Earth's dipolar field and guided to the polar regions (Birkeland, 1908, 1913). He thus provided the first insight into the physical cause of both high latitude magnetic disturbances and the occurrence of the aurora in the polar regions. Lindemann (1919) concluded that the particles streaming from the sun must be electrically neutral in order to prevent charge build up in the Earth's atmosphere that would prevent continuous entry of further charged particles. Chapman (1923) suggested that such a plasma stream would envelope the Earth and its field

completely. The concept of a magnetic cavity as the result of the interaction of the solar particles and the geomagnetic field became firmly established with the works of Chapman and Ferraro (1931, 1932) which dealt with a new theory of magnetic storms. An early visualization of this cavity is shown in figure 1.1.

Chapman and Ferraro considered the magnetic cavity configuration as associated only with solar flares, and hence, they believed that the cavity which formed about the Earth due to the solar gas was a transient phenomenon. Studies by Biermann (1951, 1957) on the behaviour of comet tails, which conclusively showed that comet tails are always directed away from the sun independent of the direction of motion of the comet, indicated that there must be a steady efflux of matter radially and in all directions from the sun into interplanetary space. Parker (1958a, b) argued further that the flow of the *solar wind*, so named because the dynamical properties of the outward flowing gas are hydrodynamic in character, was a continuous phenomenon which extended far beyond the orbit of the Earth. Consequently, it became evident that the magnetic cavity was a permanent feature of the Earth's environment. This magnetic cavity is today known as the *magnetosphere* and attempts to determine its steady state morphology have been the focus of much study by magnetospheric physicists.

Figure 1.2 depicts a noon-midnight meridian cross section of the magnetosphere as it is visualized at the

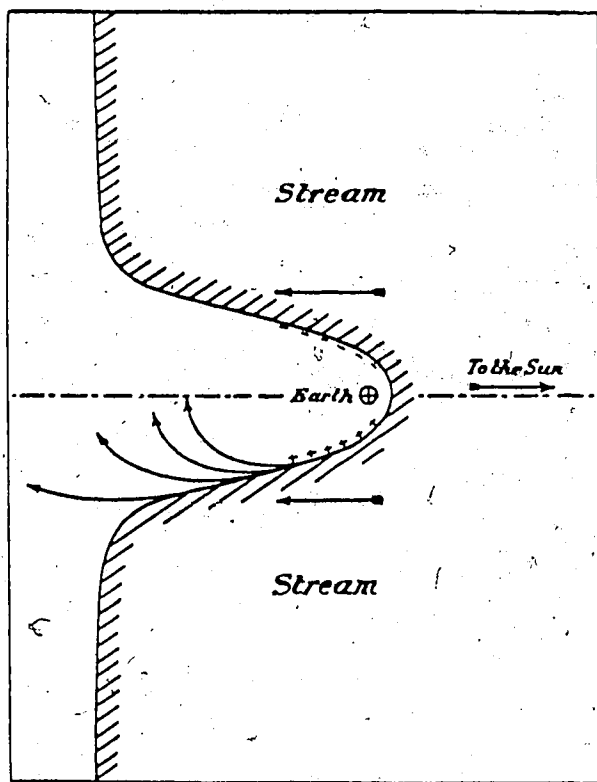


Figure 1.1 Early visualization of the earth's magnetic cavity (equatorial projection) (after Chapman and Ferraro, 1931).

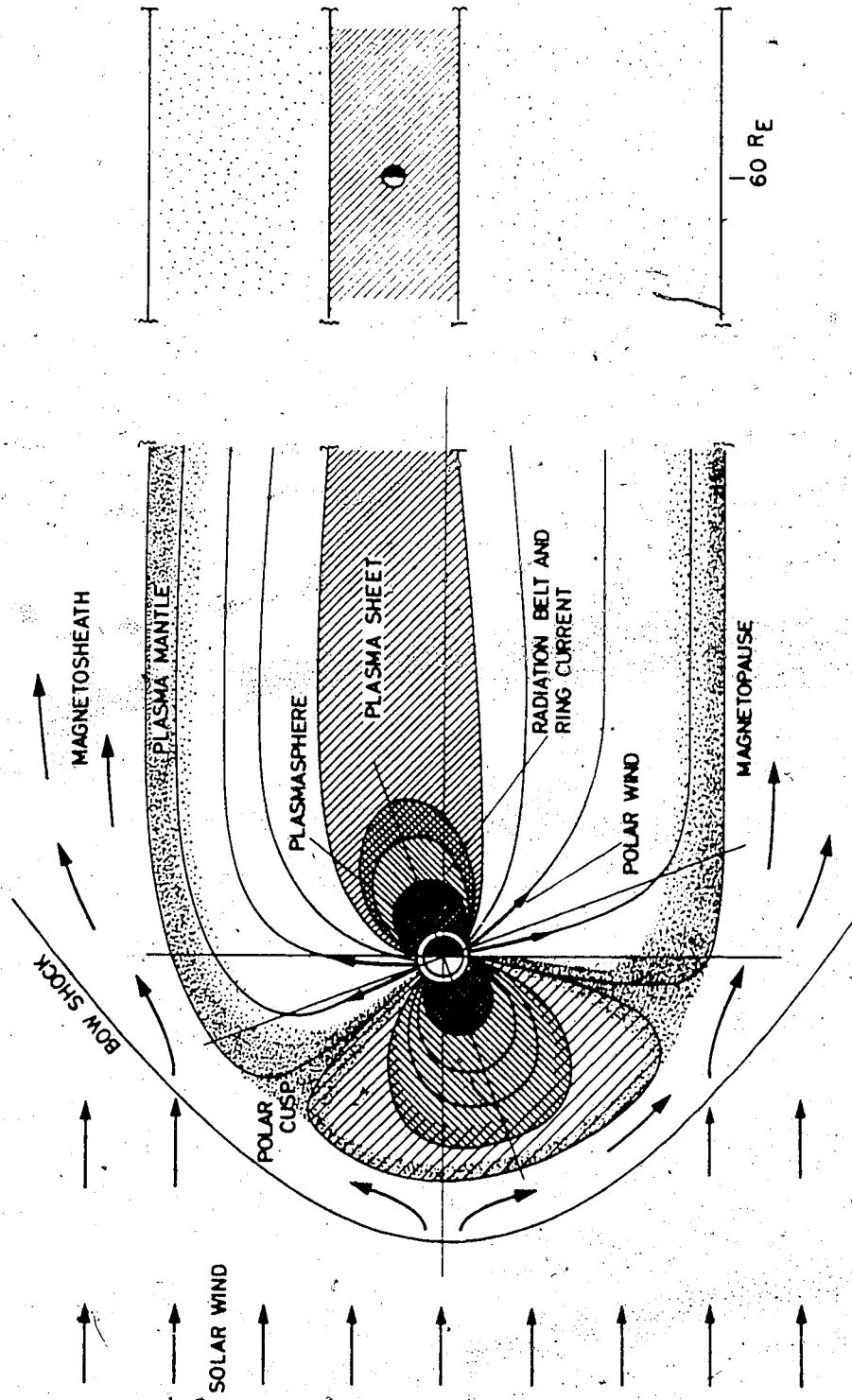


Figure 1.2 Noon-midnight meridian cross section of the earth's magnetosphere.

present time. In our current understanding, the Earth, along with its magnetic field, acts as an obstacle in the path of the supersonic, super-Alfvénic solar wind plasma emitted from the sun. The Alfvén speed is given by (Chen, 1984):

$$v_A = (B^2/\mu_0\rho)^{1/2} \quad (1)$$

where B is the total magnetic field magnitude and ρ is the mass density of the plasma. As a consequence, a standing collisionless magnetohydrodynamic shock wave, known as the *bow shock*, is created about 14 Earth radii (R_e) on the sunward side of the Earth. As the solar wind crosses through the bow shock its velocity becomes sub-sonic and sub-Alfvénic and its temperature and density increase. As a result of the density increase, and hence an increase in dynamic pressure, the frontside of the Earth's field becomes compressed. The solar plasma is deflected around the geomagnetic field forming a region of thermalized plasma known as the *magnetosheath*. The geomagnetic field lines are then pulled behind the Earth to form a roughly cylindrical comet-like tail which extends hundreds of R_e behind the Earth and which has an average diameter between 40 and 60 R_e . This extended configuration is called the *magnetotail* and it is composed of two hemispheres, the northern hemisphere consisting of sunward directed field lines and

the southern hemisphere containing anti-sunward oriented field. The oppositely directed magnetic fields are separated by a region known as the *neutral sheet*, where the magnetic field is directed perpendicular to the plane of the sheet and the field magnitude is a minimum.

The magnetosphere is separated from the magnetosheath by a boundary layer known as the *magnetopause* at which there is a pressure balance between the solar wind and the magnetosphere. The location of the magnetopause can be determined approximately by balancing the solar wind dynamic pressure (kinetic pressure of the solar wind particles) and the magnetic pressure of the geomagnetic field inside the magnetosphere. The average location of this boundary at the sub-solar point is approximately 10 Re in front of the Earth; however, it may be situated anywhere between 5 and 14 Re from the Earth's surface (Olson, 1984). The size and shape of the magnetosphere then depends directly upon the force of the solar wind blowing against it, that is, upon the velocity and mass density of the solar plasma. The magnetospheric configuration depends as well upon the magnitude and orientation of the sun's magnetic field which permeates interplanetary space and is known as the *interplanetary magnetic field* (IMF).

The plasmas found in the magnetotail are extremely tenuous. A good laboratory vacuum may have a pressure on the order of 10^{-8} torr, and this is found to be roughly eight orders of magnitude more dense than the most densely

populated region of the tail (Lui, 1987). Consequently, collisions between particles are very infrequent, with the mean free path of particles in the most dense tail plasma regime being of the order of 10^{13} km, or, 10^9 Re. The lack of collisions is indicated by the departure of the velocity distribution from a Maxwellian (Lui, 1987). Hence, the plasmas of the tail may be described as being "collisionless". However, because of the presence of magnetic fields in the tail, the particles are constrained by the magnetic field, so that the plasmas may also be described in fluid terms. Therefore, in order to understand the existence and morphology of the various plasma regimes comprising the magnetosphere, the trajectories of single particles under the influence of magnetic and electric fields, and as well, relevant fluid motions, must be discerned.

An electromagnetic field acts upon a charged particle through the *Lorentz force* which defines the equation of motion of the particle as follows:

$$\vec{F} = q(\vec{E} + \vec{v} \times \vec{B}) \quad (2)$$

where \vec{F} is the applied force, \vec{B} is the magnetic field, \vec{E} is the electric field, \vec{v} is the particle velocity and q is the electric charge. In the presence of a uniform magnetic

field, \bar{B} , where an electric field is absent ($|\bar{E}|=0$) a charged particle will exhibit simple cyclotron gyration about a magnetic field line, describing a circular orbit about a *guiding center*. This orbit is in a plane perpendicular to the magnetic field direction. In addition to this gyration, the particle drifts along \bar{B} such that the trajectory of the particle in a uniform \bar{B} field is, in general, a helix. The direction of gyration is such that the magnetic field generated by the charged particle acts to oppose the externally imposed field; hence, plasmas are diamagnetic.

If a finite electric field is introduced, an additional motion is imposed on the particle, that of a drift of the guiding center. This drift will be in a direction perpendicular to both the electric and the magnetic fields, and it is called the *convective* or *$E \times B$ drift*. Both positive and negative particles drift in the same direction under such an influence so that the plasma tends to drift as an ensemble. Consequently, the three dimensional motion of a particle in a combination of uniform electric and magnetic fields is that of a slanted helix with changing pitch.

In general, the drift velocity of a charged particle is determined according to the following relation:

$$\bar{v}_D = \frac{\bar{E} \times \bar{B}}{qB^2} \quad (3)$$

where \bar{F} is an applied force acting on the guiding center. Associated with each different force acting on the particle is a different contribution to the drift motion. The $\bar{E} \times \bar{B}$ drift is attributed to the force exerted by the electric field. Under the influence of a magnetic field which is non-uniform a particle will undergo further guiding center drifts depending on the nature of the nonuniformity of the field. When a gradient is present in the magnetic field (∇B), a *gradient drift* will occur which is oppositely directed for ions and electrons and is perpendicular to both the magnetic field and the direction of the gradient. The force in this case is given by,

$$\bar{F} = -\mu \nabla B \quad (4)$$

where μ is the magnetic moment of the particle. When the magnetic field is curved with a constant radius of curvature, a *curvature drift* will occur. Here, the force acting is the centripetal force,

$$\bar{F}_C = - \frac{mv_{\parallel}^2}{R} \hat{r} \quad (5)$$

where \bar{R} is the radius of curvature of the field directed

toward the centre of curvature, and $\hat{r} = \bar{R}/R$. The above three drifts together can be summarized by the following equation, where the first term represents the $\bar{E} \times \bar{B}$ drift, the second the gradient drift and the third, the curvature drift:

$$\bar{v} = \frac{\bar{E} \times \bar{B}}{B^2} + \frac{\epsilon_{\perp} \bar{B} \times \nabla B}{qB^2} + \frac{2\epsilon_{\parallel} \bar{B} \times \bar{R}}{qB^2 R^2} \quad (6)$$

where ϵ_{\perp} is the transverse energy associated with the gyrational motion about the field line and ϵ_{\parallel} is the longitudinal energy associated with the motion of the particle along the field line (Hines, 1963).

Under certain conditions, the fluid nature of a plasma becomes useful in understanding charged particle motions in the magnetosphere. A plasma may be considered to consist of two interpenetrating fluids, an electron fluid and an ion fluid. When a pressure (or density) gradient occurs, the guiding centres of the individual particles remain stationary, and it is the relative movement of the particles themselves with respect to each other which causes the plasma motion. In the presence of a pressure gradient (∇P) the fluid motion is that described by the *diamagnetic drift* which is defined by,

$$\bar{v}_D = \frac{\bar{B} \times \nabla P}{qnB^2} \quad (7)$$

The drift direction is perpendicular to both the magnetic field and the direction of the pressure gradient. Since ions and electrons drift in opposite directions a *diamagnetic current* ($\bar{J}_D = qn\bar{v}_D$) flows parallel to the direction of the diamagnetic drift.

The *generalized Ohm's law* is also significant in understanding the collective motion of a plasma, and it describes the electrical properties of a conducting fluid. It is obtained by taking the time derivative of the current while satisfying the MHD conditions existing in space. For low collision frequency, low temperatures and small currents (Nicholson, 1983), the generalized Ohm's law may be approximated as follows:

$$\bar{J} = g(\bar{E} + \bar{v} \times \bar{B}) \quad (8)$$

where g is the conductivity of the fluid. Under ideal MHD conditions, plasmas are considered to be collisionless, and so, the conductivity is assumed to approach infinity, since

$$g \propto \frac{1}{\text{collision rate}} \quad (9)$$

Hence, in order for current to be finite, it is necessary

that

$$\bar{E} \approx -\bar{\nabla} \times \bar{B}. \quad (10)$$

Magnetic field lines are assumed to be equipotentials; therefore, the electric field component parallel to \bar{B} becomes negligibly small ($E_{\parallel} \approx 0$), and the majority of the electric field, then, is perpendicular to the magnetic field, such that,

$$E_{\perp} \approx |-\bar{\nabla} \times \bar{B}|. \quad (11)$$

A consequence of infinite conductivity is the *frozen field condition*. Because the magnetic field is divergence-free, ($\nabla \cdot \bar{B} = 0$), flux tubes may be used to describe the magnitude and direction of the magnetic field in space. Each tube encloses a given magnetic flux, $\Delta\phi$, and the magnitude of the field at any point is equal to $\Delta\phi/\Delta A$, where ΔA is the local cross sectional area of the flux tube. Hence, at all locations,

$$|\bar{B}| \propto \frac{1}{\Delta A}. \quad (12)$$

It can be shown (see Rossi and Olbert, 1970; Nicholson, 1983) that the time rate of change of magnetic flux through a surface ΔS of the flux tube, perpendicular to the field lines, is identically zero provided that the surface moves with the fluid. While the plasma may freely flow along the direction of the magnetic field lines, any motion perpendicular to the field implies that the field lines themselves must have a component of velocity perpendicular to the field direction. Consequently, the plasma is said to be frozen to the field, and hence, it moves with the field. Conversely, as the fluid moves, the field lines move with it.

To a first approximation, the frozen field condition provides a mechanism for the formation of the magnetotail. Axford and Hines (1961) proposed that the tail is formed as a result of tangential stresses at the dayside magnetopause caused by a viscous interaction between the magnetosphere and the solar wind plasma. In this view, the magnetosphere takes on a closed, tear-drop shaped structure. However, Dungey (1961) offered an alternate approach to tail formation by employing the concept of *magnetic merging* or *reconnection* of the solar and geomagnetic field lines. This process allows for the existence of an open magnetosphere. The question of which of these processes dominates tail formation is one of ongoing debate at the present time. Although evidence for magnetic merging (particularly at the dayside magnetopause) now appears indisputable, the role of

viscous effects on magnetotail formation may also be of significance (Rostoker and Eastman, 1987). In either case, magnetic field lines at the frontside of the magnetosphere are pulled back behind the Earth by the flow of the highly conducting solar plasma which is frozen to the magnetic field. Hence, the Earth's field becomes elongated to form the magnetotail configuration.

Magnetic reconnection occurs when oppositely magnetized regions of plasma come in contact with one another. In addition to the configuration of antiparallel fields as a condition for reconnection, enhanced plasma pressure is also required to bring the field lines together. In such a region the magnetic field is very weak and the plasma and field no longer move together. Instead, the oppositely directed field lines can break and reconfigure, and since the plasma is not frozen to the field lines, it may diffuse or flow through the reconnection region. As well, when field lines are brought together, the associated magnetic field energy is dissipated through acceleration of the charged particles in the vicinity of the reconnection zone (Lui, 1987). Figure 1.3 indicates schematically how, and at what locations in the magnetosphere, magnetic merging is understood to take place.

The frozen-field condition suggests that the magnetosphere is completely impervious to the solar wind plasma, and hence, that the Earth is effectively shielded from direct influx of the solar wind with little mass and

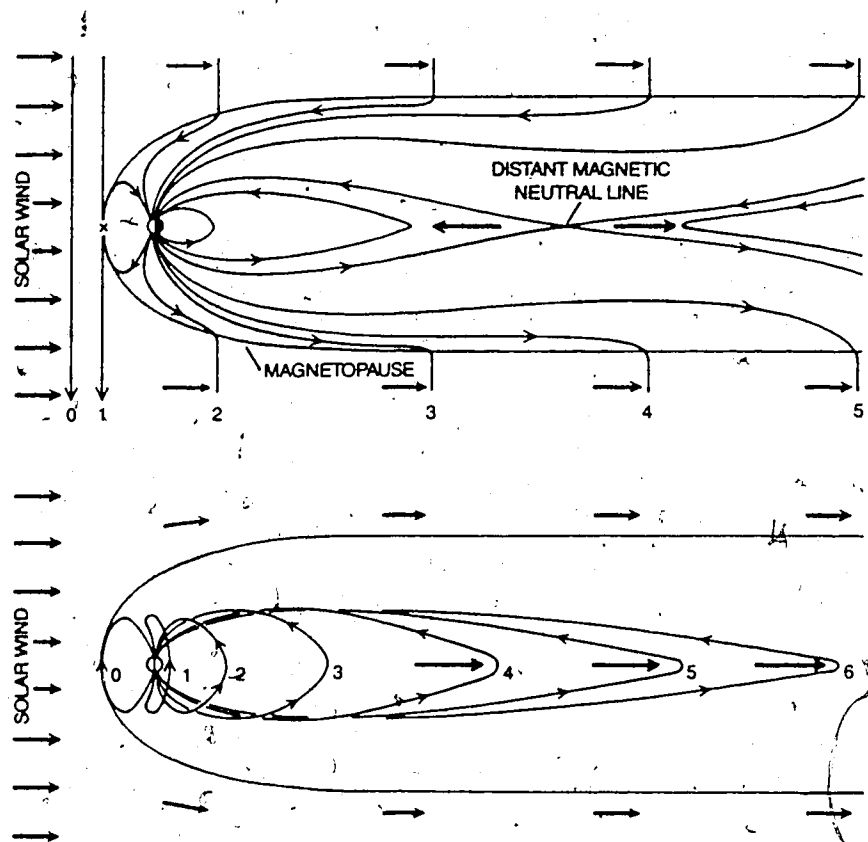


Figure 1.3 Proposed sites of magnetic merging in the magnetosphere. Magnetic merging is believed to occur at the front-side magnetopause as well as at the distant magnetic neutral line (after Hones, 1986).

momentum transfer across the magnetopause. However, such shielding is not complete, and this departure from perfect shielding is of great importance to magnetospheric dynamics. Due to the process of dayside magnetic field merging, solar plasma entry into the tail is explained, thus allowing, in part, for the formation of the plasma regimes within the magnetosphere. (An ionospheric source of plasma for the magnetosphere is also known to exist.)

As shown in figure 1.3, magnetic merging occurs at the magnetopause where the IMF, when directed southward, can merge with the northward directed geomagnetic field. Consequently, the IMF becomes coupled to the Earth's field. Field lines such as this which are connected at one end to the sun and at the other end to the Earth are known as *open field lines*, and they emanate from the high latitude regions of the Earth. These open, or merged, field lines convect across the polar cap in the anti-sunward direction through the action of the solar wind. *Closed field lines* are those which have both ends attached to the Earth, and these are connected to the Earth in the lower latitude regions. As mentioned previously, IMF field lines have both feet rooted in the sun.

In the region of field line merging at the dayside magnetopause, solar wind plasma gains access to the magnetosphere by diffusing through the reconfiguration zone across the magnetopause. Plasma may also obtain direct entry through a region known as the dayside *polar cusp* which

separates the open and closed field lines connecting to the dayside ionosphere in each hemisphere (Akasofu, 1977). Each cusp region contains what is known as a *neutral point*, or, the point at which the magnetic field is perpendicular to the magnetopause surface, and mathematically at which $|\bar{B}|=0$. At this location the concept of pressure balance is undefined, and the magnetosheath plasma readily flows to the low altitude dayside auroral regions.

Just inside the magnetopause is the *magnetospheric boundary layer* through which magnetosheath plasma enters into the magnetosphere. It consists of the *low latitude boundary layer* (LLBL) confined to the closed field lines at lower latitudes and at the flanks of the tail, and the *plasma mantle* at high latitudes located on open field lines. Just below the plasma mantle is the *lobe* region which resides on open field lines emanating from the polar cap.

The lobe is populated by very low density plasma, the energy density being dominated by the magnetic field (Lui, 1987). This region is composed of low β plasma, where β is defined as follows (Chen, 1984):

$$\beta = \frac{\text{particle pressure}}{\text{magnetic field pressure}} \quad (13)$$

The magnetospheric boundary layer plasmas, as well as the tenuous lobe plasmas, flow downtail in the anti-sunward

direction.

Plasma that has gained access to the magnetosphere through the region of field line merging enters the plasma mantle and streams downtail along high latitude open field lines in the vicinity of the Earth. However, this plasma experiences an $\bar{E} \times \bar{B}$ drift towards the mid-plane as it streams downtail (Hardy, et al., 1979), and as it moves, the plasma carries with it the magnetic field lines which are frozen to the plasma. At a location of approximately $80 R_E$ downtail a second reconnection region is believed to exist where the northern and southern tail lobe fields come together. Because the magnetic field here is very weak the location of reconnection is termed the *magnetic neutral line*.

Plasma which has convected to the location of the neutral line from the plasma mantle may be injected into a region of the magnetotail called the *plasma sheet* which is restricted to the closed field lines threading the *auroral oval*. The auroral oval is a roughly oval shaped band in the ionosphere along which the auroral arcs or active auroras are most frequently seen. This oval encircles the geomagnetic pole yet is displaced towards the night hemisphere by about 300 km. Its average diameter is approximately 4000 km, decreasing to about 3000 km when the auroras are faint and increasing to as much as 6000 km when the auroras are bright. The altitude of the lower edge of luminosity is generally 100 to 110 km, however, the altitude of the upper edge is highly variable, ranging from 400 to

1000 km (Akasofu and Kamide, 1987).

The particles in the plasma sheet are confined to the magnetosphere and they convect Earthward under the influence of an $\bar{E} \times \bar{B}$ drift. The energy density of the plasma sheet is particle dominated, thus, the plasma sheet plasmas generally have a higher β ($\beta \geq 1$) than the lobe plasmas. The plasma sheet as a whole is thinnest near midnight and its thickness increases to twice its midnight value towards the tail flanks (Lui, 1984). This regime is continually replenished with plasmas of both magnetospheric and ionospheric origins.

In recent studies the plasma sheet has been shown to consist of two distinct regions, the *central plasma sheet* (CPS) and the *plasma sheet boundary layer* (PSBL) (Eastman et al., 1984; Eastman et al., 1985a). Many studies prior to this had neglected the distinction between these two domains, making reference only to the plasma sheet. Further, the PSBL had previously been thought to exist only during periods of high magnetospheric activity; however, it is now believed to be a permanent feature of the magnetotail (Eastman et al., 1985a). The CPS maps to the region of diffuse auroras and is characterized by isotropic plasma distributions, whereas the PSBL is thought to map to the region of active or more structured auroras in the ionosphere (Rostoker and Eastman, 1987). The PSBL is characterized by anisotropic plasma distributions typified by rapidly flowing, counterstreaming ion beams. Also, broadband electrostatic noise is a typical feature of this plasma

regime (Fairfield, 1987), being absent in the lobes and present only at a reduced intensity in the CPS. The PSBL plays a major role in particle, energy and momentum transfer in the magnetosphere and is often one of the most dynamic plasma regimes. Whereas the magnetospheric boundary layer is the primary transport region for the frontside magnetosphere, the PSBL is the major region of transport for the magnetotail (Eastman et al., 1984).

The locations of all the above-mentioned plasma domains and boundaries are shown in figure 1.4 which is a three-dimensional cross-section of the Earth's magnetosphere.

1.3 Major Current Systems in the Magnetosphere

In the magnetosphere there exists a variety of current systems which are induced by the motion of charged particles under the influence of electromagnetic fields. An understanding of these current systems provides insight into the dynamics of magnetospheric processes. There are four major current systems which are of primary importance; these are the *magnetopause* (Chapman-Ferraro) currents, the *ring* current, the *cross-tail* (neutral sheet) current and *field-aligned* (Birkeland) currents. A brief description of each system follows.

The Chapman-Ferraro currents flow within the magnetopause layer and their projection on the magnetopause surface is indicated schematically in figure 1.5. They

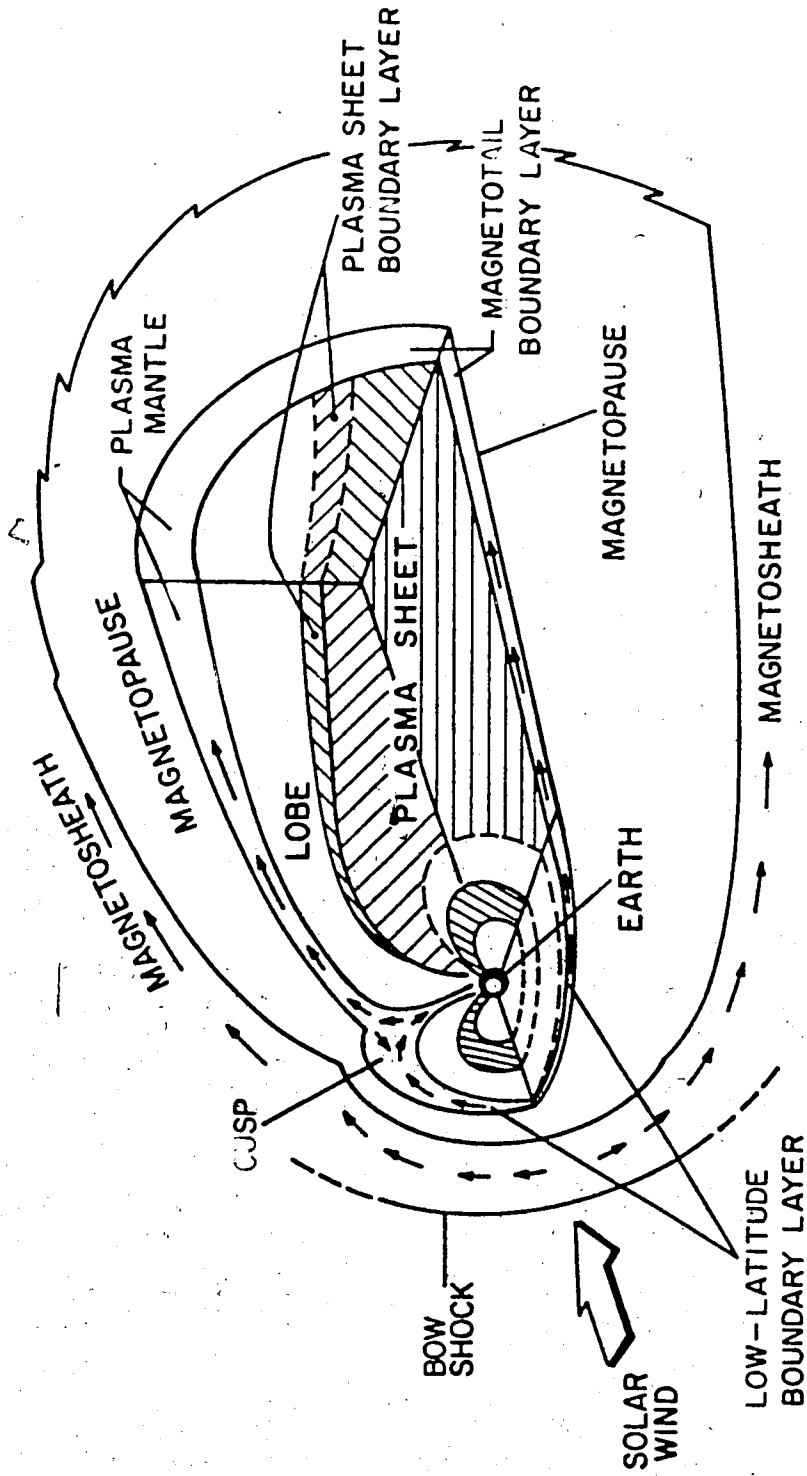
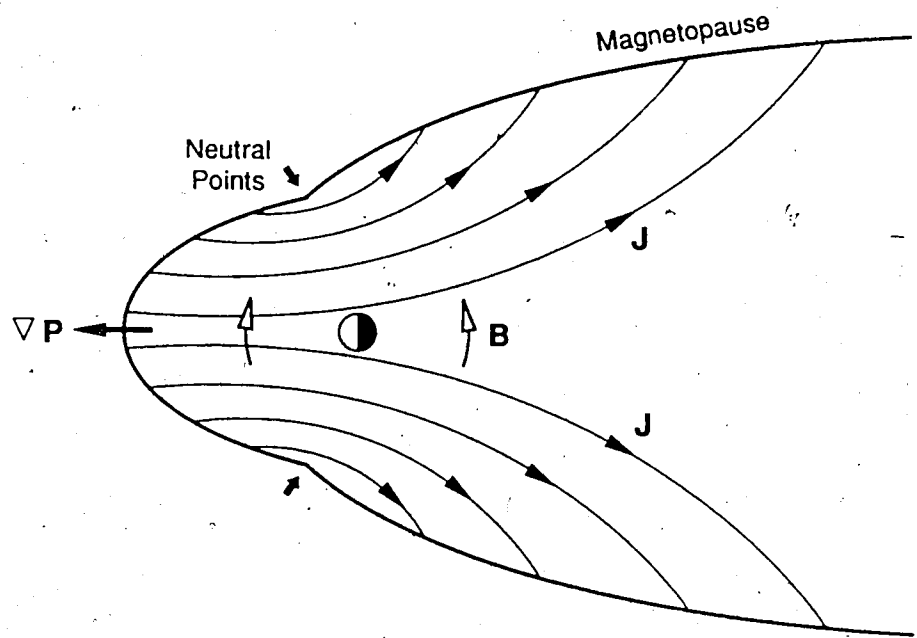


Figure 1.4 Three dimensional cross section of the earth's magnetosphere (after Eastman et al., 1984).



- ∇P Pressure gradient
B Geomagnetic field
J Chapman - Ferraro (magnetopause) currents

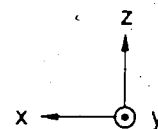


Figure 1.5 Schematic projection of the Chapman-Ferraro (magnetopause) currents on the earth's magnetopause surface.

consist of two eddy currents, one in each hemisphere centered about the respective neutral point. The current sheath has a thickness at the sub-solar point on the order of an ion gyroradius (which is dependent locally on the magnitude of the geomagnetic field). The thickness is also found to depend on the orientation of the IMF, being observed to be thicker during northward IMF than during southward IMF (Russell and Elphic, 1978). The magnetopause currents and their associated magnetic field vary with the solar wind pressure and are thus controlled by pressure gradient forces.

The magnetopause currents, which are observed to persist during both active and quiet times, can be understood in terms of the trajectories of individual solar wind particles as they interact with the geomagnetic field. When the neutral solar wind plasma encounters the Earth's field, the guiding centers of the particles experience an inertial drift due to the curvature of the magnetic field. As a result, protons and electrons drift in opposite directions, with radii of curvature proportional to their respective masses. Further, because electrons and protons have significantly different masses, the protons, being much heavier, will penetrate farther into the field than will the electrons. This leads to charge separation which produces an outwardly directed polarization electric field perpendicular to the current surface. This electric field will restrain the ions and decrease their penetration distance, causing

them to be returned in the incident direction before they have a chance to be greatly deflected in the transverse direction by the magnetic field. The electrons will gain energy in the polarization field which enhances their transverse motion due to the influence of the Lorentz force. The combined motion of the electrons and protons in opposite directions and transverse to the field direction results in the flow of Chapman-Ferraro currents in the magnetopause layer (Beard, 1964; Haerendel and Paschmann, 1982).

Because of the influence of the curvature drift which causes deflection in opposite directions of the incident particles, a component of current parallel to the magnetopause surface is introduced. A magnetic field is set up about this current component such that on the sunward side of the current sheet the magnetic field is essentially cancelled and on the Earthward side it is approximately doubled (Beard, 1960). The current layer is, in effect, an equipotential surface so that plasma cannot penetrate through the sheath. All particles execute only one gyration before being expelled from the magnetopause layer, and hence, *specular reflection* is the term used to express the inability of the particles to penetrate through to the magnetosphere. The Chapman-Ferraro currents, therefore, shield the Earth's magnetosphere, preventing solar wind particles from entering, and this results in confinement of the Earth's field within the cavity formed around the Earth (Akasofu, 1984).

Much attention has been focused on whether the magnetopause is a rotational or a tangential discontinuity. (where a rotational discontinuity is represented by a large amplitude standing Alfvén wave, and a tangential discontinuity is an equipotential current sheet with unequal particle pressures on opposite sides of the sheet (Kavanagh, 1972)). If the magnetopause is described by a discontinuity of the rotational type, a component of the magnetic field perpendicular to the boundary surface may exist, and hence, plasma can flow through the boundary at the Alfvén speed. On the other hand, if the discontinuity is tangential there can be no interconnection of the magnetic field lines between the magnetosheath and the magnetosphere. Therefore, the open model of the magnetosphere (Dungey, 1961) requires that the magnetopause be a rotational discontinuity, whereas, the closed model (Axford and Hines, 1961) favours a tangential discontinuity.

The cross-tail current is solenoidal in nature with one solenoidal type loop enclosing each of the two hemispheres in the tail, as shown in figure 1.6. The current is directed from dawn to dusk in the region of the tail mid-plane which separates the oppositely directed magnetic fields of the northern and southern hemispheres. The cross-tail current flows not only in the plane of the neutral sheet but as well throughout the plasma sheet, since currents flow wherever drifting plasma is present and gradients in plasma pressure normal to the ambient magnetic field exist. The current

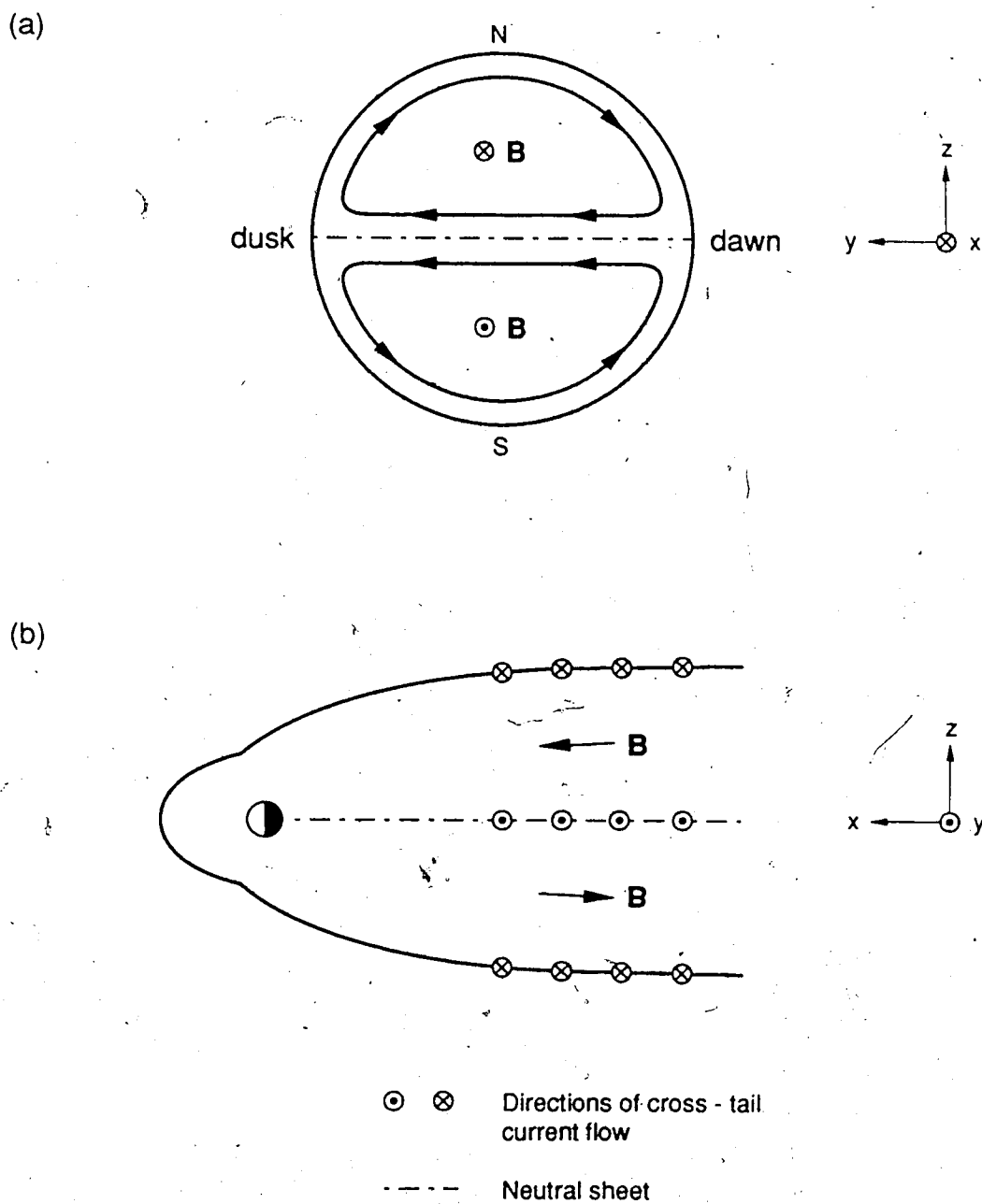


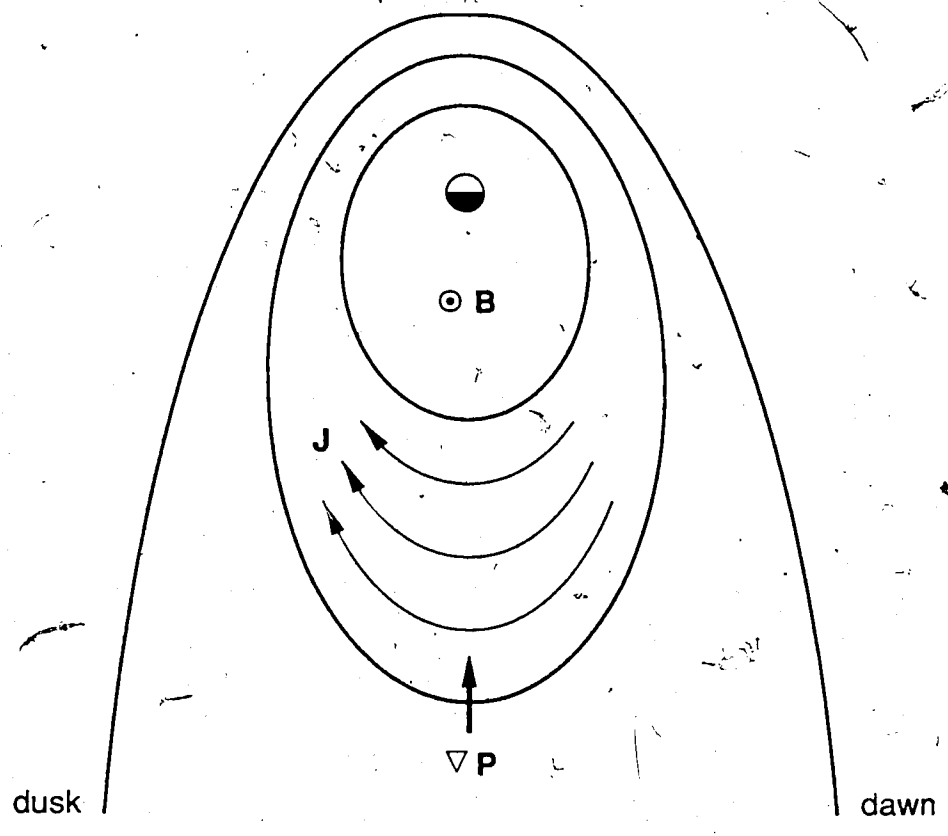
Figure 1.6 Schematic representations of the cross-tail (neutral sheet) current in (a) a cross-tail projection, and (b) a noon-midnight meridian projection.

density distribution in the neutral sheet can be calculated from the curl of the magnetic field (assuming pressure gradients are perpendicular to the the current sheet). Therefore, from Ampère's law (assuming slowly varying fields such that $\frac{\partial \bar{D}}{\partial t} = 0$), the cross-tail current may be expressed as,

$$\mu_0 \bar{J} = \nabla \times \bar{B}. \quad (14)$$

Current closure in each hemisphere is around the magnetopause, and this closure is necessary in order to explain the orientation of the magnetic field in each of the two tail hemispheres (Olson, 1984). The current may be thought of as being a source for the tail lobe magnetic field (Fairfield, 1987). The neutral sheet current persists down the length of the tail, and it is a permanent current feature.

The ring current is generated by the drift motions of charged particles in the geomagnetic field (Williams, 1985), and it is shown schematically in figure 1.7. This current is restricted to plasma trapped on the closed field lines (Voigt, 1981), and it is present during both active and quiet times. Like the cross-tail current, the ring current originates as a result of pressure gradients. There are two contributions to the overall ring current configuration, an inner component flowing eastwards and an outer component



∇P Pressure gradient
 J Ring current

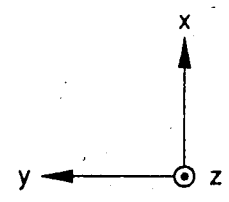


Figure 1.7 Schematic representation of the ring current shown here as a projection on the equatorial plane of the magnetotail.

flowing in a westward direction (Rossi and Olbert, 1970). The latter component greatly exceeds the former in magnitude; hence, the overall ring current flows from dawn to dusk. The total current is given by (Williams, 1985),

$$\bar{J} = \frac{\bar{B}}{B^2} \times (\nabla P_{\perp} + \frac{P_{\parallel} - P_{\perp}}{B^2} (\bar{B} \cdot \nabla) \bar{B}). \quad (15)$$

where P_{\parallel} and P_{\perp} are the components of particle pressure parallel and perpendicular to the ambient magnetic field, respectively. The Earthward edge of the tail current merges continuously into the equatorial ring current (Voigt, 1981), and as well, since the Chapman-Ferraro currents flow in the same sense as the cross-tail current, the three systems may be considered as constituents of the same current structure.

Field-aligned currents (FAC) were first proposed by Birkeland (1908) who recognized that the geomagnetic disturbances measured on the Earth's surface below the auroral regions were due to intense currents flowing horizontally in the ionosphere, and that these horizontal currents were maintained by an external source of space charge which flowed vertically into and out of the ionosphere. The vertical currents are today known as Birkeland or field-aligned currents, whereas the horizontal ionospheric components are known as the *auroral electrojets*. The existence of FAC was confirmed through satellite

magnetic field observations by Zmuda et al. (1967); however, the first direct measurements were not obtained until quite recently by Frank et al. (1981).

As their name suggests, field-aligned currents flow parallel to magnetic field lines. They form four solenoidal type loops which map from the auroral ovals in the ionosphere to the volume of space occupied by the plasma sheet, in the magnetosphere, and so couple the ionosphere to the magnetosphere. This solenoidal configuration, as predicted by Boström (1964), is shown in figure 1.8. Specific regions of FAC flow have been designated by Iijima and Potemra (1976) as Region 1 and Region 2, shown in figure 1.9, (a) and (b), for weakly disturbed conditions and active periods, respectively. The flow patterns remain basically unchanged during varying levels of geomagnetic activity, however, the auroral oval is observed to expand equatorward from the quiet-time latitude of $\approx 75^\circ\text{N}$ to lower latitudes of $\approx 50^\circ\text{N}$ during strong magnetic disturbances. In the northern hemisphere, Region 1 currents flow into the ionosphere in the morning sector and away from the ionosphere in the evening sector (Potemra, 1983), both in the region just south of the poleward edge of the auroral oval. Region 2 current directions are reversed with respect to their Region 1 counterparts, with the flow directed out of the ionosphere in the morning sector and into the ionosphere in the evening sector. However, these currents flow in the region just north of the equatorward edge of the auroral

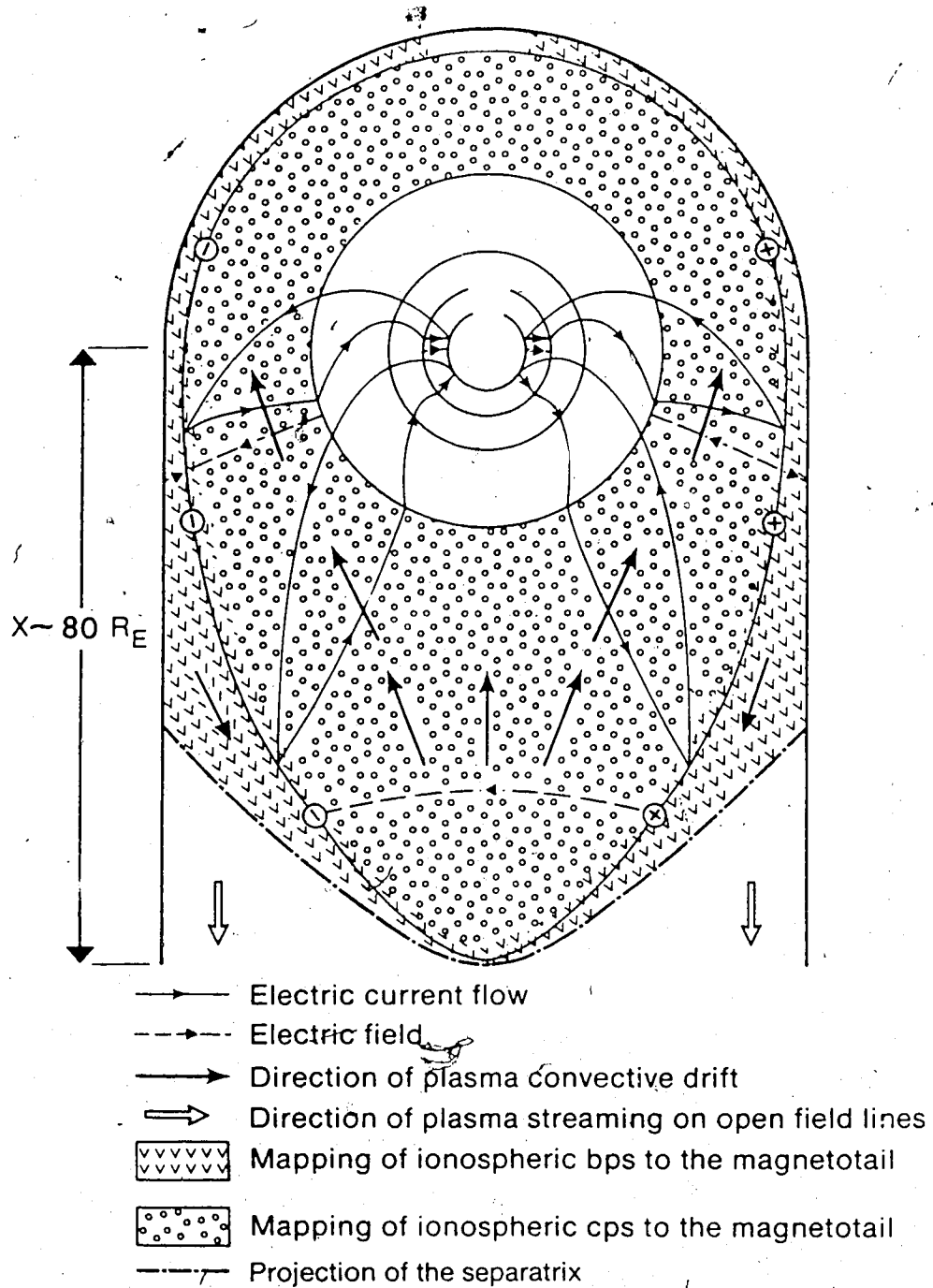


Figure 1.8 Solenoidal configuration of the Birkeland (field-aligned) currents in relation to a plane parallel to and in the vicinity of the magnetotail neutral sheet (after Rostoker and Eastman, 1987).

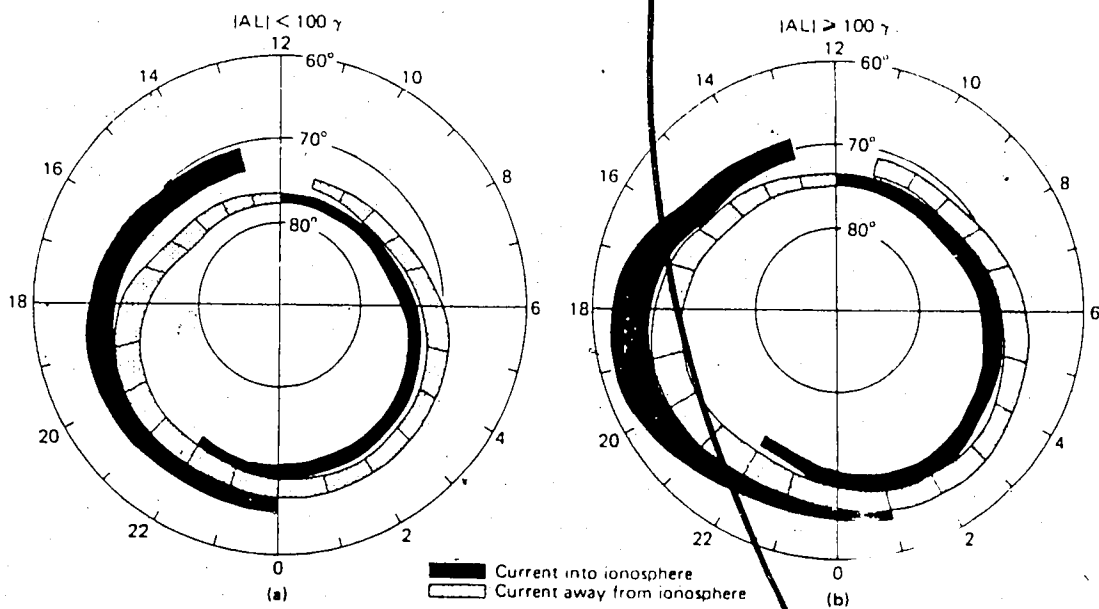
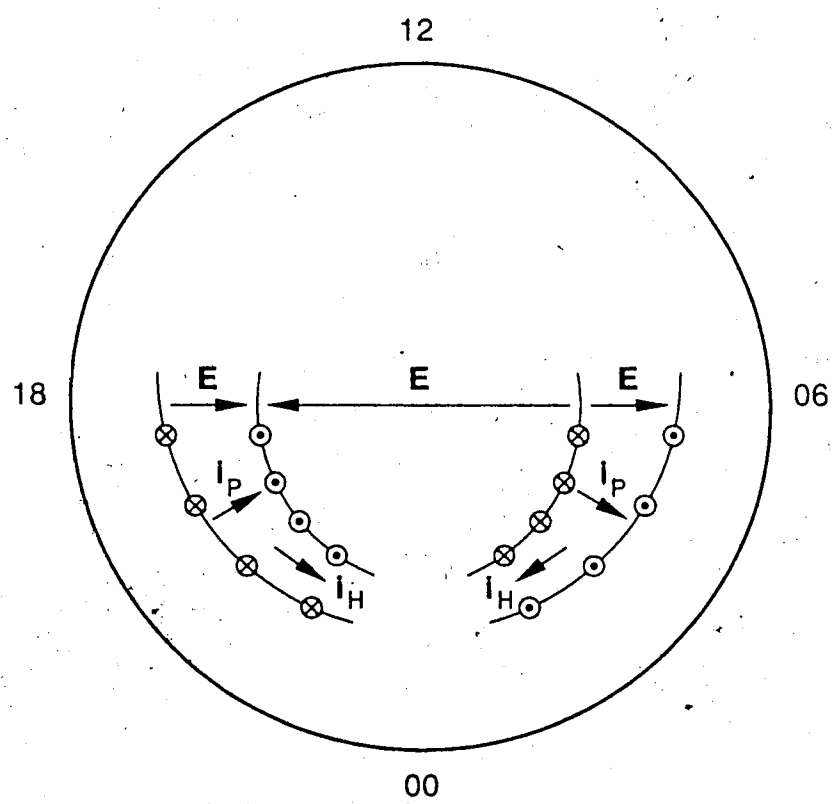


Figure 1.9 Distribution and flow directions of large-scale FAC (a) for weakly disturbed conditions ($|AL| < 100$ nT) and (b) for active periods ($|AL| \geq 100$ nT) (after Iijima and Potemra, 1976).

oval. Flow directions in the southern hemisphere mirror those of the northern hemisphere across the equator.

Each FAC current loop is closed in the ionosphere by *Pedersen* currents, which flow across the auroral oval to connect the Region 1 and 2 currents. The *Pedersen* currents flow southward in the pre-noon and northward in the post-noon regions, as seen in figure 1.10. Also indicated in this figure are the flow directions of the auroral electrojets (or Hall currents). Downward field-aligned current near local noon diverges into the ionosphere and flows horizontally in an eastward direction, forming the eastward electrojet. Downward FAC in the late morning sector diverges into the ionosphere and flows westward as the westward electrojet (Hughes and Rostoker, 1977). The eastward electrojet flows past the dusk meridian and out of the ionosphere near midnight. The westward electrojet flows past local midnight before flowing out of the ionosphere in the early evening sector. Each of the electrojets is bounded by the upward and downward flowing Birkeland current sheets. The region in the evening sector where the two electrojets flow past one another is known as the *Harang Discontinuity*. The auroral electrojets are intimately related to magnetospheric dynamics since it has been observed that a sudden intensification of the electrojets signals the onset of a magnetospheric substorm expansive phase (Kisabeth and Rostoker, 1971, 1974).



- E Electric field
- I_P Pedersen current
- I_H Hall current
- \otimes Directions of Birkeland current flow
- \odot Directions of Birkeland current flow

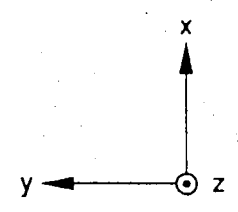


Figure 1.10 Directions of Birkeland, Pedersen and Hall current flows in the auroral oval (after Rostoker and Boström, 1976).

The generation of field-aligned currents is outlined in detail by Hasegawa and Sato (1979) and Sato (1982). Briefly, the sources of FAC may be obtained by considering the divergence of the total current density, \bar{J} . Because magnetospheric current is divergence free ($\nabla \cdot \bar{J} = 0$), it follows that,

$$\nabla \cdot \bar{J}_{\parallel} = -\nabla \cdot \bar{J}_{\perp} \quad (16)$$

where \bar{J}_{\parallel} and \bar{J}_{\perp} are the current components parallel and perpendicular to \bar{B} , respectively. Therefore, the field-aligned current sources may be determined by investigating the nature of the divergence of the cross-field current which flows perpendicular to \bar{B} (Sato, 1982).

Consider the single-fluid equation of motion (momentum equation) describing mass flow and given by,

$$\rho \frac{d\bar{v}}{dt} = \bar{J} \times \bar{B} - \nabla p + \bar{F} \quad (17)$$

where ρ is the mass density, P is the pressure, and \bar{F} represents the momentum source from the solar wind due to viscous drag and/or dayside merging. In this relationship, \bar{F}

may be neglected since it is only significant at the interface between the solar wind and the magnetospheric boundary layer. Taking the cross product of \bar{B} with equation 17, the current component perpendicular to \bar{B} is obtained:

$$\begin{aligned}\bar{J}_{\perp} &= (\bar{B} \times \nabla P) / B^2 + (\bar{B} \times \rho \frac{d\bar{v}}{dt}) / B^2 \\ &= \bar{J}_D + \bar{J}_{in}\end{aligned}\quad (18)$$

where \bar{J}_D and \bar{J}_{in} represent the diamagnetic and inertial currents, respectively. Combining equation 16 with equation 18 yields an expression for field-aligned currents:

$$\begin{aligned}J_{\parallel} &= B \int \left[\frac{\rho}{B} \frac{d(\bar{\Omega}/B)}{dt} \right. \\ &\quad \left. + \frac{2}{B^2} (\bar{J}_{\perp} \cdot \nabla B) + \frac{1}{B^2} \left(\frac{d\bar{v}}{dt} \times \bar{B} \right) \cdot \nabla \rho \right] dl\end{aligned}\quad (19)$$

where $\bar{\Omega} = (\nabla \times \bar{v})$ is the vorticity and l is the length of the magnetic field line from the ionosphere to the plane of the neutral sheet in the magnetosphere.

From the equation for parallel current it becomes evident that there are three independent sources of field-aligned current in the magnetosphere, one corresponding to each of the three terms. The first term represents the contribution to FAC resulting from local accumulations or depletions of space charge in the magnetosphere, where space charge is defined as,

$$\sigma = -\epsilon_0 \nabla \cdot \bar{B}. \quad (20)$$

Space charge is generated when there exists a component of the magnetic field parallel to the vorticity which itself results from the velocity shear of two plasmas flowing past one another with a relative velocity \bar{v} . Two such velocity shear zones at which FAC generation may occur are the solar wind-magnetosphere and CPS/LLBL interfaces.

The second source of FAC, represented by the second term in equation 19, originates in a region where a magnetic field gradient exists in the direction of a cross-field current (ie: where the pressure gradient has a component along the direction of the VB drift (Akasofu, 1984)). This source is the one most often used in the modelling of field-aligned currents.

The third FAC source resides in a region where a density gradient is present in the direction of an inertial

current. This source is often regarded as being negligible with respect to the second source discussed above. According to Sato (1982),

$$| \bar{J}_{in} / \bar{J}_D | \approx 10^{-2}. \quad (21)$$

However, it has been shown by Rostoker and Boström (1976) that inertial forces associated with the drift of plasma towards the flanks of the tail, provide sufficient energy to drive the Birkeland current system. Therefore, it is of apparent importance when investigating the generation of field-aligned currents to give careful consideration to each of the three proposed current sources, and not to neglect any one source on the basis of order-of-magnitude comparisons alone.

1.4 Thesis Objectives

Associated with each type of current system in the magnetosphere are magnetic perturbations which are superimposed on the background geomagnetic field. A quantitative magnetic field model must reproduce the observed magnetic field vector at all points in the tail. It must, therefore, include not only the field of the magnetic dipole, but also the magnetic perturbations which result from the Chapman-Ferraro currents, the ring current, the

cross-tail current, and field-aligned currents. In addition, any and all other current systems which contribute to the total magnetospheric \vec{B} field must be taken into account. In an ideal model these currents and the corresponding magnetic field configuration should represent a self-consistent response to the solar wind-magnetosphere interaction. However, such a self-consistent model of this ideal type is not available at the present time.

The present statistically derived representations of the Earth's magnetosphere do not, in all instances, reflect signatures inferred through both ground based and *in situ* magnetic field measurements. Furthermore, the magnetic signatures are not always consistent with those deduced from *in situ* energetic particle data. Through a study of both the magnetic and energetic particle data obtained via satellite in the region of the magnetotail between 10 and 23 R_E downtail, several discrepancies, not only between the two data sets themselves but also between the *in situ* magnetic field data and the present magnetospheric models, become apparent. Since an acceptable magnetospheric model must accurately characterize the processes of which observed signatures are a consequence, therefore, deviations from expected behaviour indicate that there are processes occurring in the tail to produce the observed signatures which have, to date, not been accounted for in the models. Such phenomena must be identified and the data re-interpreted in order that the magnetic and particle

signatures may be reconciled in a more consistent and realistic model of the magnetosphere.

The primary objective of this research is to identify irregularities in the statistically derived magnetospheric picture which are manifested through discrepancies not only between the magnetic and particle signatures of instantaneous observations, but, as well, through the observation of magnetic signatures expected according to model predictions. The investigation will focus on the cross-tail or dawn-to-dusk component of the magnetotail magnetic field in the particular plasma regimes of the CPS, PSBL and tail lobes. Ultimately, the identification of the primary sources of this field component is desired.

The study will begin with a description of the magnetic and particle signatures, expected according to the presently accepted models, for the regions of interest in the magnetotail. Statistical analyses of the magnetotail magnetic measurements, in conjunction with the energetic particle observations, will then be conducted. Comparison of the two data sets both with each other and with model expectations will be made and any discrepancies that are observed will be outlined. In addition, explanations will be proposed which may resolve the apparent inconsistencies between the anomalous signatures observed and the statistical models of the Earth's magnetosphere.

Chapter 2

Sources of the Cross-Tail Magnetic Field Component

Before embarking on a statistical study of the cross-tail component of the geomagnetic field it is essential first to outline what is presently known about this field component in relation to the present models. The sources of the cross-tail component and its expected behaviour must be determined. There are three major contributors to this magnetic field component, as well as one controversial yet noteworthy possibility, and these will be discussed below. However, in order to outline these clearly, it is first necessary to discuss the coordinate systems in which observations are to be ordered.

2.1 Coordinate System Definitions

There are a number of coordinate systems presently available for studies of solar-terrestrial interactions and the choice of any given system is dependent upon the nature of the investigation taking place. In this work, three different cartesian systems are of relevance to the ordering of satellite measurements with respect to the Earth and sun.

The *geocentric solar ecliptic* coordinate system (GSE) is one of the most straight forward of the various systems. (It is also referred to as the solar ecliptic or SE system). The X-axis is defined as being along the sun-Earth line with positive X in the sunward direction. The positive Y-axis is directed duskward in the plane of the ecliptic, and the

Z-axis is oriented perpendicular to the ecliptic plane with positive Z in the same sense as ecliptic north. Relative to an inertial frame of reference, the GSE system experiences a yearly rotation. In such a set of coordinates, satellite trajectories appear elliptical in shape and are therefore easily visualized. However, when dealing with measurements pertaining to the magnetotail, this system is not completely satisfactory since the structure of the geomagnetic tail, within about 12 R_e behind the Earth, is governed by the orientation of the Earth's dipole axis which is not parallel to ecliptic north.

In general, the tail may be considered as a huge windsock aligned with the direction of the solar wind. Variations in the solar wind velocity vector produce corresponding changes in tail orientation. In addition to this effect, the orientation of the tail is influenced by aberration resulting from the motion of the Earth about the sun. The near-Earth tail field structure, however, is dominated by the effect of the tilting dipole axis. The dipole tilt causes the neutral sheet to be displaced out of the ecliptic plane such that during northern summer the neutral sheet is shifted above the ecliptic and in the winter it is shifted below the ecliptic (Bowling, 1974). Beyond 12 R_e the tail orientation is influenced less strongly by the dipole tilt and is dependent mainly upon the direction of the solar wind flow. Therefore, the effect of the dipole axis on the tail is to alter its otherwise

cylindrical symmetry due to the interaction of the solar wind and the geomagnetic field. This "hinging" of the tail is shown in figure 2.1. Consequently, despite its simplicity, the GSE system does not physically order the satellite data adequately for near-Earth magnetotail studies.

A coordinate system better suited to near-Earth tail investigations is the *geocentric solar magnetospheric* (GSM) system. As in GSE coordinates, the X-axis is directed positively towards the sun along the sun-Earth line. However, the Y-axis is defined as being perpendicular to the Earth's dipole axis, or parallel to the magnetic equator. This axis is positively directed approximately duskward, although it does not point exactly towards dusk since the orientation of the magnetic equator is not fixed. The orthogonal triad is completed by projecting the Earth's dipole axis onto the Y-Z plane such that the dipole axis projection is oriented along the positive Z-axis. Consequently, the Y-Z plane rocks about the X-axis with a 24-hour period as the pole precesses. In addition, the GSM system exhibits a yearly rotation due to the motion of the Earth about the sun. The three-dimensional motion of the dipole in the GSE system has, therefore, been reduced to a two-dimensional motion in GSM coordinates, and one system may be transformed to the other by a rotation about the X-axis. Because GSM coordinates are based on the orientation of the Earth's dipole axis they more conveniently order data

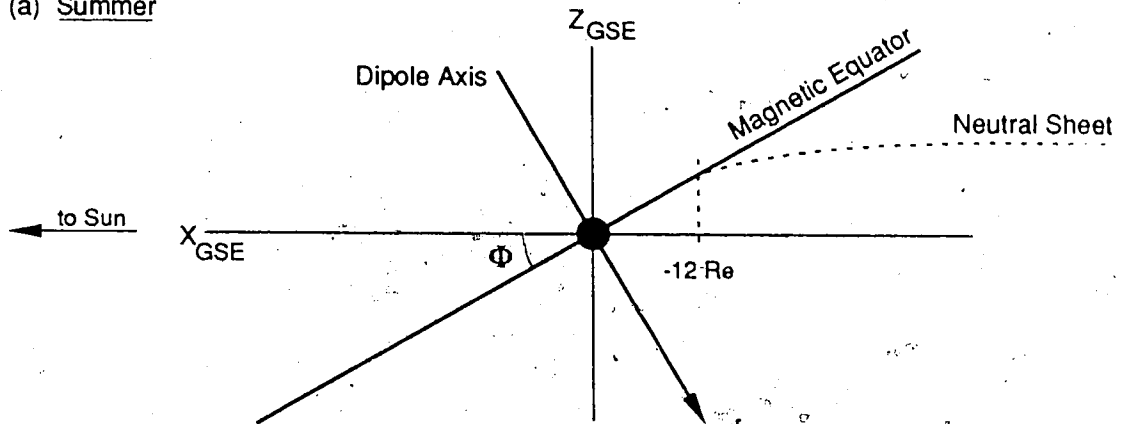
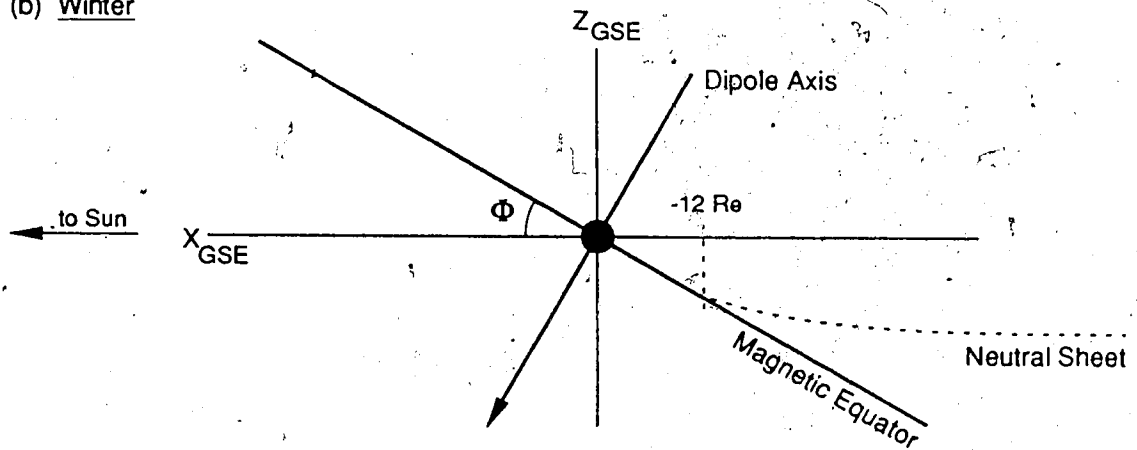
(a) Summer(b) Winter

Figure 2.1 Hinging of the magnetotail and the consequent position of the neutral sheet (a) when the geomagnetic pole is tilted toward the sun (ie: northern hemisphere summer), and (b) when the north pole is tilted away from the sun (ie: northern hemisphere winter) (after Gosling et al., 1986).

for the near-Earth tail.

Finally, the third set of coordinates in which data may be represented is the *spacecraft* coordinate system. In this system the X-axis takes on the same sense as in both the GSE and GSM systems, the Z-axis is parallel to the spin axis of the satellite, and the Y-axis completes the orthogonal triad with positive Y directed approximately downward. When the spin axis of a satellite is parallel to the direction of ecliptic north, the GSE and spacecraft coordinate systems are identical.

2.2 Hydrodynamic Tail Flare

As a result of the magnetohydrodynamic interaction of the solar wind with the Earth's magnetic field, the magnetosphere experiences a flaring effect to a distance of some 150 R_E behind the Earth (Mihalov et al., 1968; Coroniti and Kennel, 1972), after which a cylindrical shape is assumed. This flare can be compared to the flow of water around an obstacle, and is, therefore, hydrodynamic in nature.

Tail flare influences the orientation of the magnetic field in the tail. Rather than being directed predominantly in the X direction, as it would for a simplified cylindrical tail model, the magnetic field has components both in the Y and the Z directions as well as having a component in the X direction. The dawn-to-dusk component of the tail field is known also as the B_y component (the B_x and B_z components are

those aligned in the X and Z directions, respectively). Hence, tail flare is the first major source of the dawn-to-dusk component of the geomagnetic tail field and this contribution may be considered as the *background* tail B_y component.

The amount of flaring of the tail is dependent upon the conditions of the solar wind and of the interplanetary magnetic field. During intervals of southward IMF, geomagnetic activity is enhanced due to an increased interaction of the solar wind with the geomagnetic field. Such increased activity is indicative of *magnetospheric substorms* during which a large amount of energy generated through the solar wind-geomagnetic field interaction is deposited in the magnetosphere (Rostoker et al., 1980). During such phases of southward IMF, implying conditions conducive to dayside merging, compression at the frontside magnetopause is enhanced which is accompanied by a decrease in the nose radius of the magnetosphere. As the nose radius decreases, the tail field strength is found to increase which implies an increase in the transport of magnetic flux from the dayside magnetosphere to the tail (Coroniti and Kennel, 1972). Both nose shrinkage and increased tail flux require that the near-Earth magnetopause becomes flared in order to maintain the hydrodynamic pressure balance of the tail. A further consequence of the flare is that the entire tail structure must move Earthward; thus, the auroral oval shifts equatorward. Changes in the solar wind conditions,

then, govern the shape of the magnetosphere.

The effect of tail flare on the orientation of the tail magnetic field, and therefore, on the contribution to the cross-tail or B_y component, is illustrated schematically in figure 2.2, (a) and (b). In (a), the northern hemisphere field lines are projected onto the equatorial plane of the magnetosphere, whereas in (b), the southern hemisphere field lines are projected onto the equatorial plane. The total magnetic field vector is directed towards the Earth, however, it contains a component in the Y direction. In the northern hemisphere dawn sector the B_y contribution is positive, and in the northern hemisphere dusk sector the contribution is negative. In the southern hemisphere the magnetic field vector is directed anti-Earthward; hence, the B_y component in the southern hemisphere dawn sector is negative and that in the southern hemisphere dusk sector is positive. Consequently, the B_y component changes polarity in both the dusk and dawn sectors when the plane of the neutral sheet (taken for simplicity here to be the X-Y plane) is traversed. By definition of the neutral sheet as the region of field reversal between the two tail hemispheres, the tail B_y component due to tail flare must change sign, and so, be of zero or very small magnitude in the vicinity of the neutral sheet. As well, in each hemisphere, the polarity of B_y reverses across the noon-midnight meridian plane (indicated here for simplicity as the Y-Z plane).

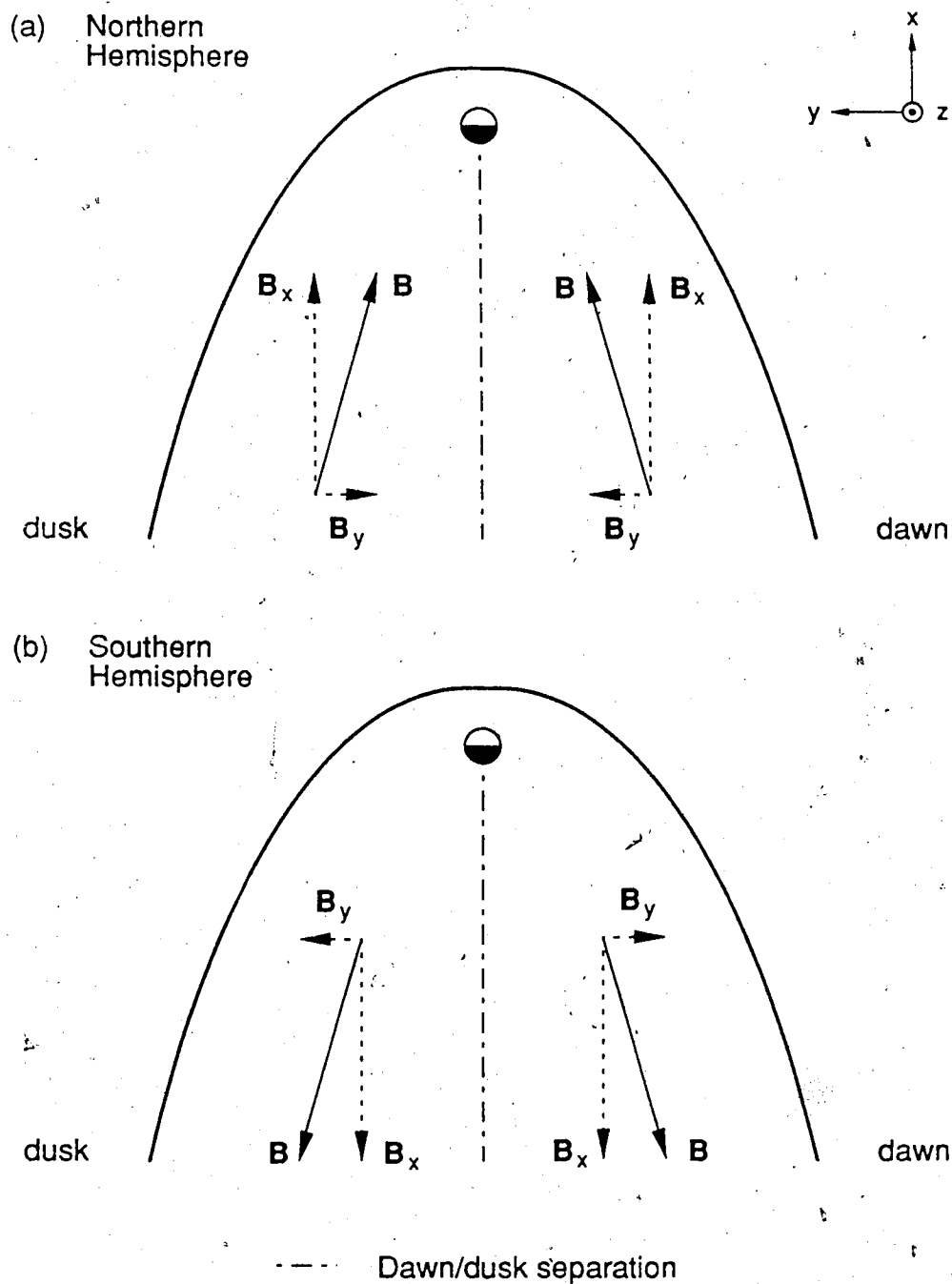


Figure 2.2 Contribution to the cross-tail magnetic field component due to flaring of the tail. Projections of the field contributions on the equatorial plane are shown for (a) the northern and (b) the southern hemisphere.

The same type of sketch may be made for a projection of the tail on the X-Z plane, which would similarly indicate contributions to the Z component of the tail magnetic field as a result of tail flare. Hence, the background magnetotail field is the result of flaring of the tail, and the configuration of the tail at any given time will govern the magnitudes of the three components of the background tail magnetic field.

2.3 Ring Current Contributions to the Magnetotail B_y Component

The ring current provides a second contribution to the B_y component of the tail field. As previously discussed, the overall ring current flows from dawn to dusk in the midplane regions of the near-Earth tail. The direction of the magnetic perturbations induced about the current flow is dependent upon the location above or below the current sheet, as indicated in figure 2.3, (a) and (b), which show projections of the northern and southern tail hemispheres, respectively, onto the plane of the neutral sheet.

Above the current sheet, in the northern hemisphere, the magnetic perturbations in the dawn and dusk sectors are positive and negative, respectively. In the southern hemisphere, the polarities reverse. Note that the perturbations due to the ring current in each of the four sectors are additive with the contributions to the B_y component resulting from tail flare. Once more, the B_y tail

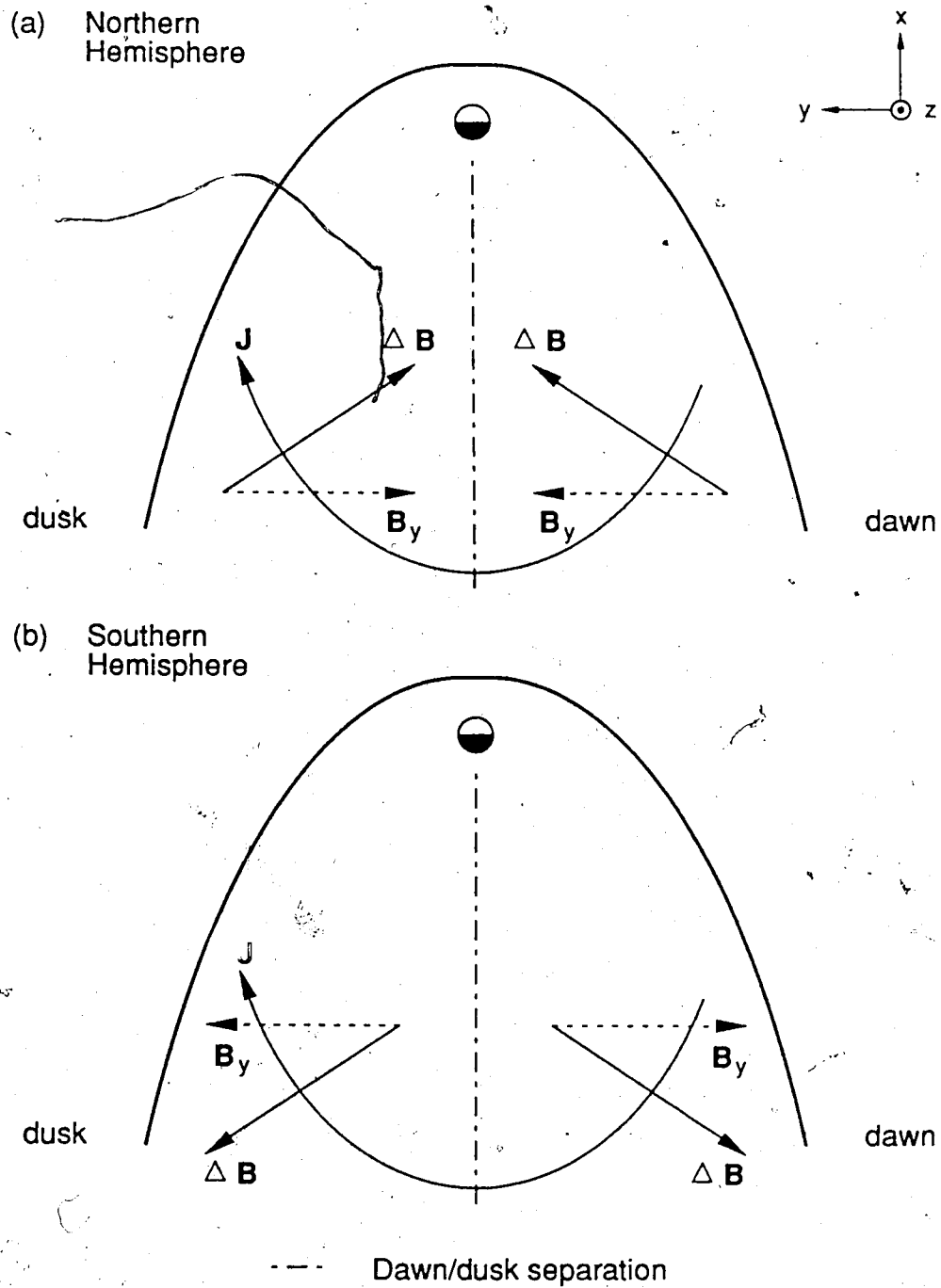


Figure 2.3 Ring current contributions to B_y in (a) the northern and (b) the southern hemisphere, both shown as projections onto the plane of the neutral sheet.

component is ideally of zero magnitude in the neutral sheet region. Also, in both situations, the polarity of the B_y perturbations change across the noon-midnight meridian plane. Contributions to the tail B_z component due to the ring current are significant at the inner edge of the current sheet and are responsible for sudden worldwide decreases in the surface magnetic field measurements which accompany the onset of magnetospheric storms (Williams, 1985).

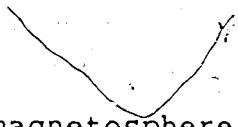
2.4 Magnetic Perturbations Due to Field-Aligned Currents

Field-aligned currents (FAC) are a third source for the cross-tail component of the tail magnetic field. As mentioned above, FAC can be thought of in terms of four solenoidal type loops, one in each of the four sectors of the tail cross section. For an idealized solenoidal current sheet configuration, no magnetic perturbations occur outside the region containing the current flow, and the only magnetic perturbations arising from such solenoids are observed within the volume occupied by the field-aligned currents (Rostoker and Boström, 1976). B_z perturbations do occur but only on a localized scale as edge effects of the main current sheets (see for example, Rostoker and Eastman, 1987). The magnetic perturbations resulting from these idealized solenoidal currents (neglecting edge effects) are indicated in figure 2.4 which depicts a tail cross sectional view typical of a distance between 10 and 30 R_E behind the

Earth. The primary magnetic perturbation resulting from the field-aligned current solenoids is oriented in the Y direction within the CPS and PSBL which are enclosed by the FAC. The lobe is situated outside the solenoidal configuration and so the magnetic perturbation in this regime, due to FAC, is negligible.

In the northern hemisphere dawn CPS the B_y perturbation due to the field-aligned currents is oriented towards the dusk, whereas that in the northern hemisphere dusk CPS is directed dawnwards. In the southern hemisphere the resulting B_y is positive in the dusk sector and negative in the dawn sector. Therefore, the polarity of the B_y perturbation reverses from dusk to dawn in each hemisphere as well as across the neutral sheet region. Once again, the perturbations in the CPS are additive with those described above resulting from both tail flare and the ring current.

2.5 IMF B_y Penetration



Assuming the Earth's magnetosphere to be an open system, that is, the interplanetary magnetic field interconnects with the geomagnetic field as described by Dungey (1961), it might be expected that the magnitude and direction of the IMF will in some manner affect the magnetotail configuration. As discussed previously, the IMF B_z component plays an important role in dayside magnetic merging and hence, in the dynamics of the tail. However, in recent years, much attention has been given to the possible

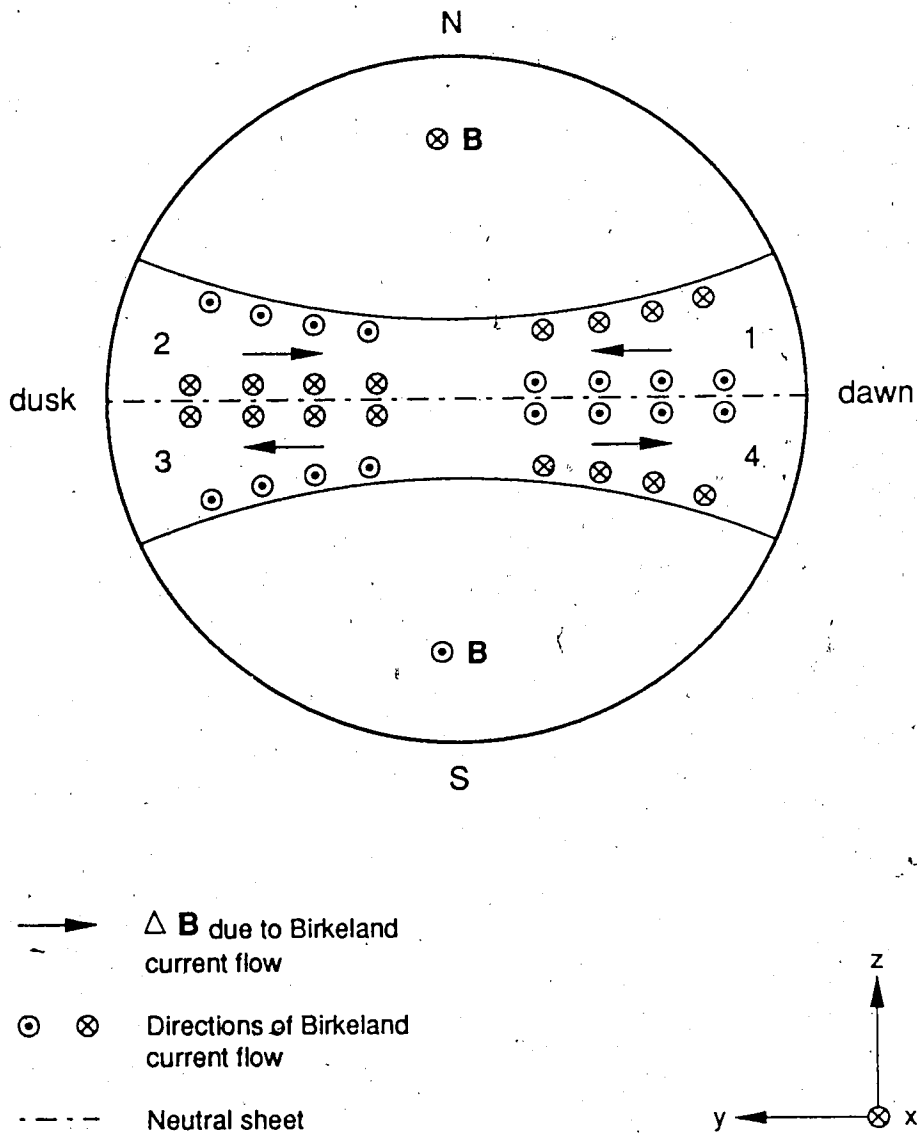


Figure 2.4 Directions of flow for the four Birkeland current loops along with the resulting cross-tail magnetic perturbations, projected onto a cross-section of the magnetotail (after Rostoker and Boström, 1976).

influence of the IMF B_y component on magnetotail structure.

Statistical analyses of magnetic field data have indicated a positive correlation between the tail B_y component and the IMF B_y component. The first of these was a statistical study of the magnetotail configuration conducted by Fairfield (1979) who used satellite magnetic field observations for all plasma regimes in the tail cross section and for locations between 22 and 33 R_e downtail. Fairfield found a linear relationship between simultaneously measured, hourly averaged values for the IMF B_y and tail B_y components. This result is shown in figure 2.5. The observed relationship has become known by the term IMF B_y penetration or *partial penetration* which suggests (that the IMF B_y field component physically penetrates the tail and hence affects the tail configuration. According to Fairfield's results, 13% of the IMF B_y is found to penetrate the tail (where this value is obtained from the slope of the linear regression curve).

Lui (1985) conducted a similar study with spacecraft magnetic measurements obtained in the plasma sheet within 30 R_e downtail. He also compiled a plot of IMF B_y as a function of tail B_y and his results are shown in figure 2.6. Lui obtained a linear relationship as well; however, his results indicate a 50% penetration of the IMF B_y into the tail. He interprets the difference between his result and that of Fairfield by suggesting that the IMF is shielded less in the plasma sheet than in the tail lobes. In a previous study,

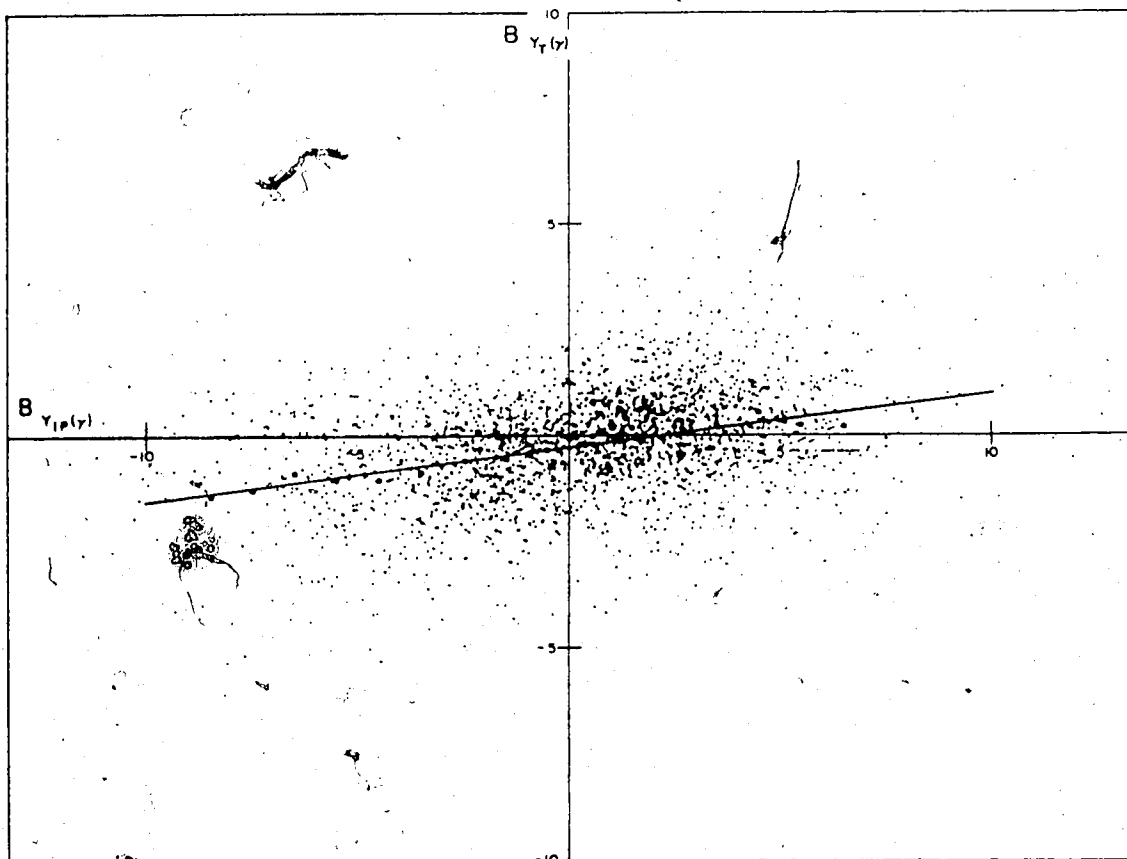


Figure 2.5 Scatter plot of hourly averaged tail B_y measurements as a function of simultaneously measured IMF B_y values. Data presented are those gathered by Fairfield (1979). The linear trend shown was postulated by Fairfield to represent an influence of the IMF B_y on the tail B_y component which has become known as IMF B_y penetration. From the slope of the line, 13% of the IMF B_y is proposed to penetrate the tail.

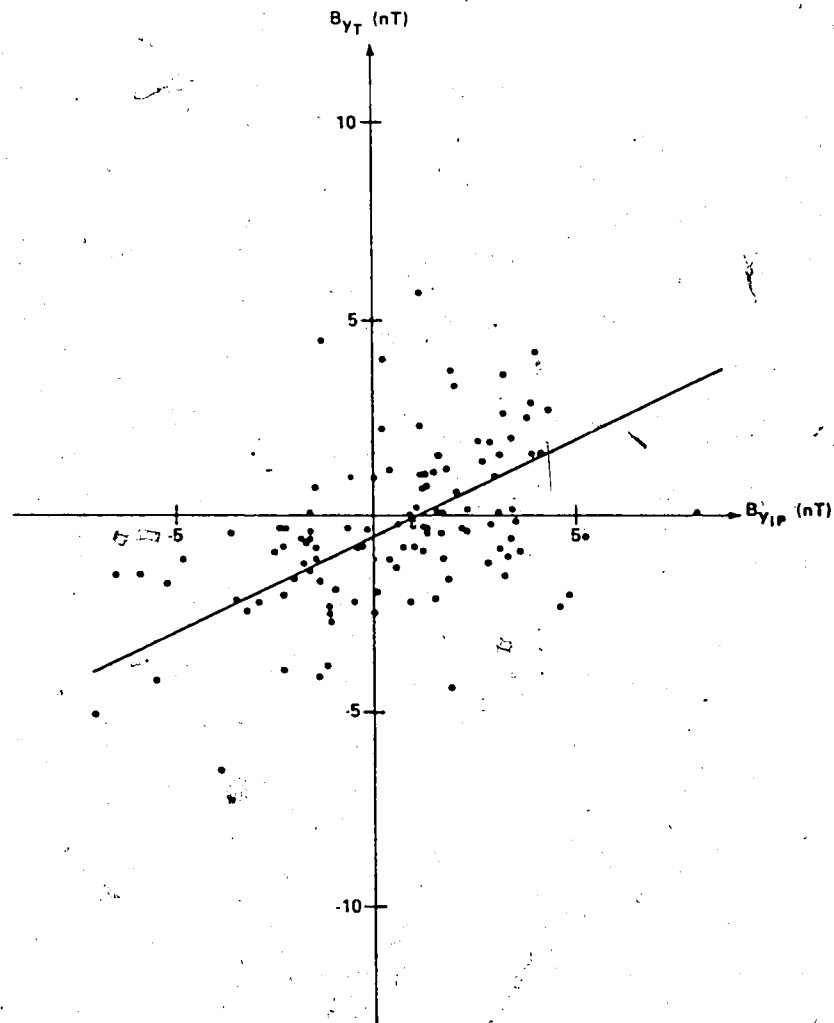


Figure 2.6 Same as figure 2.5 for data compiled by Lui (1985). A 50% penetration of the IMF B_y is suggested.

Lui (1983) found that the B_y component in the neutral sheet maintained a constant value during a sequence of neutral sheet crossings (from the above discussion of B_y sources in the tail B_y should change polarity across the neutral sheet). He attributed this to partial penetration of the IMF B_y into the tail which enhanced the tail B_y component. His findings will be investigated in chapter 4 of the present work.

Voigt et al. (1987) offer a different explanation for the enhancement of B_y in the plasma sheet. They claim that a certain fraction of the IMF B_y component is present in the tail lobes and plasma sheet, and that its presence is due to partial penetration of this IMF component into the magnetotail. However, they suggest that the presence of the IMF B_y does not lead to B_y enhancement in the plasma sheet of the tail, but rather, that a second component due to the field line shear found only in plasma dominated regimes, is the source of B_y enhancement in the plasma sheet. This shear is postulated to be due to ionospheric polar cap convection which skews high latitude plasma sheet field lines, under the influence of IMF B_y , in opposite directions in the two ionospheric polar caps. They state that the tail B_y component is largest in the centre of the plasma sheet and that it decreases monotonically towards the PSBL, reaching the minimum background field in the lobes.

Cowley (1981) discussed observations which suggest that the IMF exerts a torque on the magnetosphere about the

sun-Earth axis resulting in asymmetric addition of open flux tubes to the tail lobes about the noon-midnight meridian. The twist in the tail which results from the torque imposed by the IMF is shown in figure 2.7. Quadrants of "preferred field penetration" are proposed to be a consequence of the asymmetric addition of flux to the tail, and this is shown in figure 2.8. In this example, IMF B_y is positive, and therefore corresponds to the twist direction shown in figure 2.7; hence, penetration occurs in the north-dawn and south-dusk sectors of the tail. For negative IMF B_y the tail would be torqued in the opposite direction, and penetration of the IMF would occur in the north-dusk and south-dawn quadrants. In both situations, the polarity of the tail B_y component is then assumed to have the same polarity as the IMF B_y component, and as well, the tail B_y magnitude is similarly dependent on the magnitude of the IMF B_y . Asymmetries are suggested to occur in both open (polar cap) and closed (auroral oval) field line regimes. Sibeck et al., (1985) discuss similar observations such as tail flattening, field line twisting and field line bending, and find that these are all significant during intervals of strong IMF B_y .

Tsurutani et al. (1986) have conducted a study of the deep geomagnetic tail regions, at distances greater than 200 R_E downstream of the Earth, which involved the correlation of the IMF with the tail B_y measurements. They took into consideration a time lag between the solar wind magnetic measurements and the deep tail measurements, invoking a 60

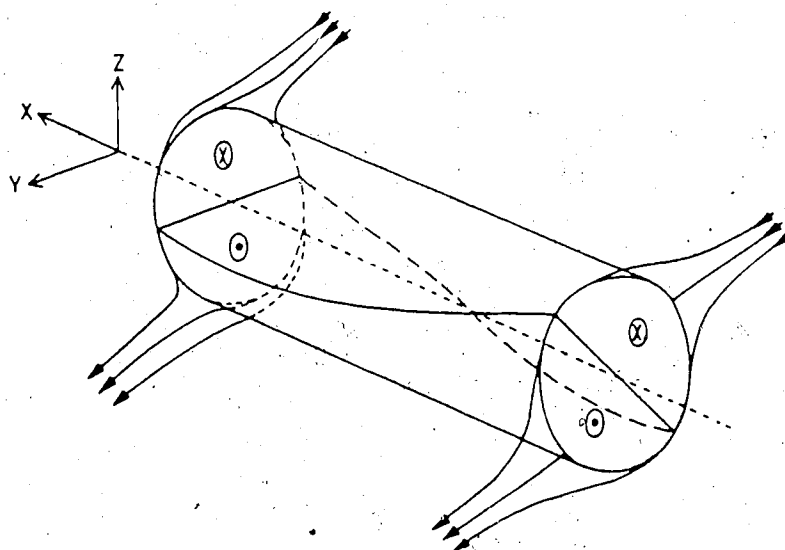


Figure 2.7 Twist of the magnetotail which is thought to result from a torque imposed on the tail by the IMF. The direction of twist shown corresponds to positive IMF B_y (the direction is reversed for negative IMF $-B_y$) (after Cowley, 1981).

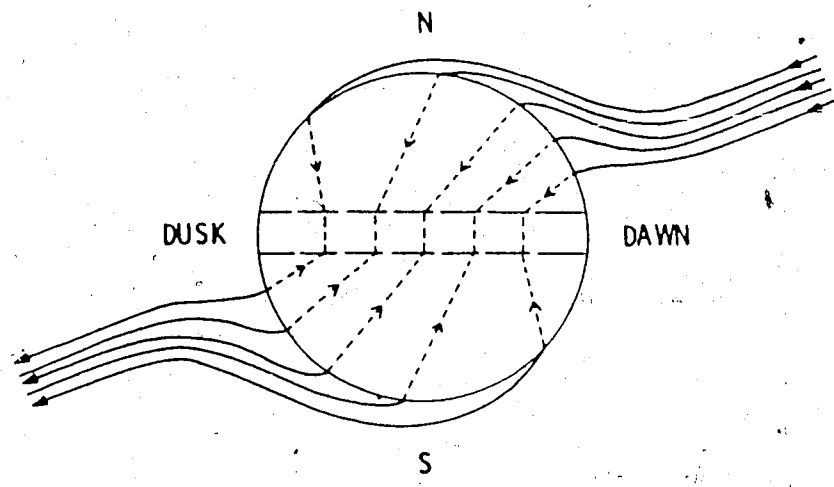


Figure 2.8 Quadrants of preferred IMF B_y penetration resulting from the proposed torque exerted on the magnetotail by the IMF. Here, penetration is postulated to occur in the north-dusk and south-dawn sectors of the tail corresponding to the direction of twist of the tail shown in figure 2.7 (after Cowley, 1981).

minute time delay of the solar wind. They plotted the ratio of IMF B_y to tail B_y for observations made in the northern hemisphere dusk tail lobe. In this case, a linear regression was made separately for positive and negative IMF B_y , as shown in figure 2.9. The results indicate a 2% penetration of the IMF B_y into the tail for positive IMF B_y , but a 13% penetration for negative IMF B_y . This is consistent with Cowley's model outlined above in that for the northern dusk lobe, penetration should be a maximum for negative IMF B_y (see figures 2.7 and 2.8). Therefore, the theory that the IMF B_y component is responsible for exerting a torque on the distant tail which causes it to be rotated and twisted is supported.

The concept of IMF B_y penetration requires further investigation before it may be accepted or refuted. However, the possibility of such an effect on tail configuration must be considered in any study of magnetotail B_y perturbations, and it will be dealt with in chapter 4 of this work.

2.6 Summary of the Contributions to B_y in the CPS, PSBL and Lobe

From the above discussion, it can be seen that the combined effects of tail flare, the ring current, and Birkeland currents, provide a specific B_y signature for each of the plasma regimes in each of the four sectors of the magnetotail cross section. (Possible contributions resulting from IMF B_y penetration will not be considered in this

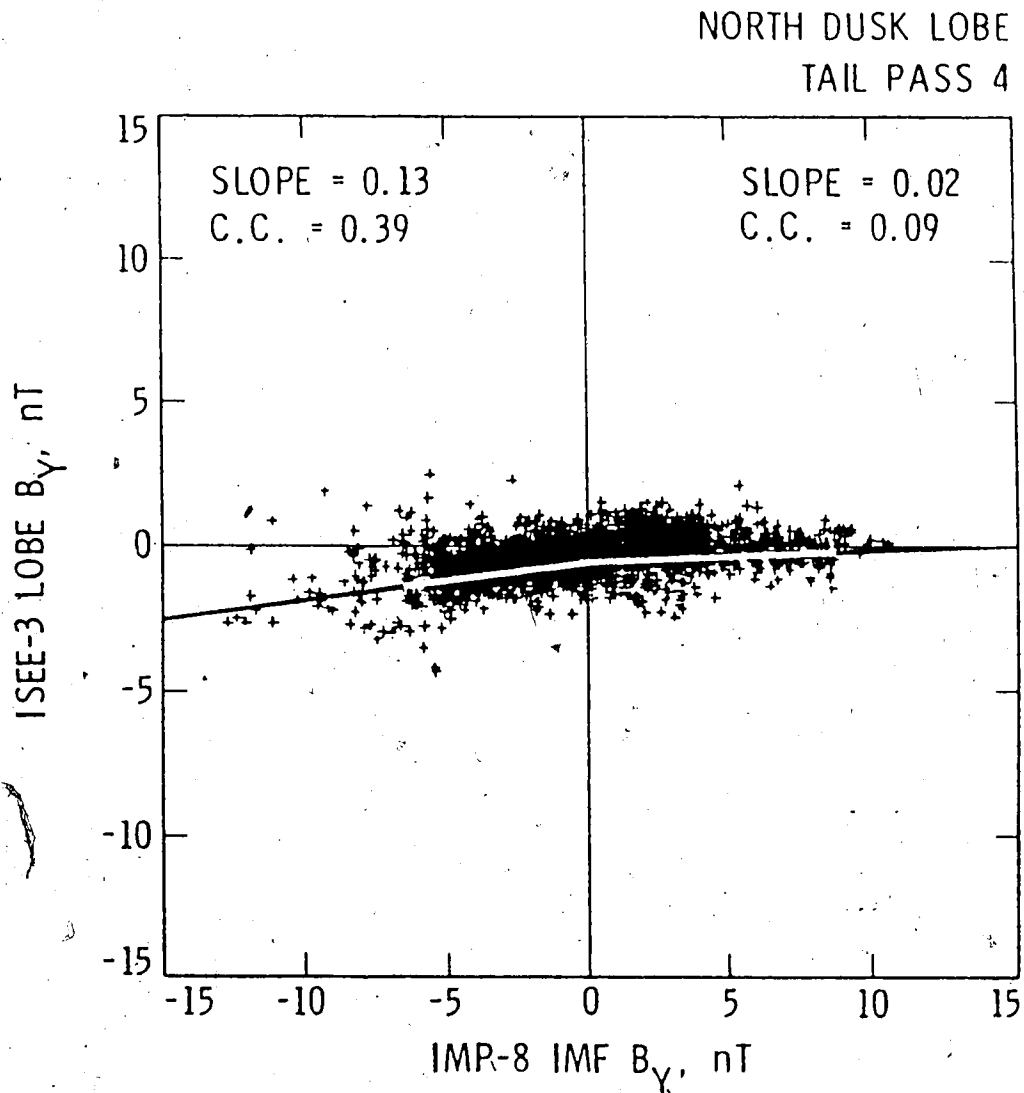


Figure 2.9 Same as figures 2.5 and 2.6 but for data compiled by Tsurutani et al. (1986) for the north-dusk tail lobe. In this case, separate linear fits were made for negative and positive IMF B_y , and these suggest that 13% and 2%, respectively, of the IMF B_y penetrate the tail in this regime.

summary due to their controversial nature.) In each sector B_y displays a given orientation or polarity which is consistent in the CPS, PSBL and tail lobes.

For example, in the northern hemisphere dawn sector, B_y is positive for all three plasma regimes; however, its magnitude varies from the CPS to the lobe, resulting from the varying contributions of the three sources. The effect of hydrodynamic tail flare is approximately constant in all three plasma regimes, providing a uniform background B_y component. The contribution from the ring current is greatest in the CPS, decreasing in magnitude towards the lobe. Perturbations due to FAC maximize in the CPS, and are negligible in the lobe. Therefore, the total B_y component has its largest value in the CPS, and its smallest value in the lobe, with the PSBL exhibiting intermediate values. The same polarity is observed in all three regions. By similar reasoning, the signatures for the other three sectors may be determined.

It is important to note that the overall B_y component changes polarity across the neutral sheet. As well, in the transition from dawn to dusk, a reversal in the polarity of B_y must take place. Therefore, a skewing of the tail magnetic field is a direct consequence of the B_y perturbations that result from the major current systems in the tail. In the northern hemisphere the various B_y perturbations in combination produce a skew of the magnetic field towards the tail axis, whereas in the southern

hemisphere the total perturbation results in a skew of the field away from the tail axis. This effect was studied by Mihalov, et al. (1968), Behannon (1970) and Rostoker and Boström (1976), who concluded that the magnetotail flares by varying degrees in planes parallel to the neutral sheet.

Chapter 3

Instrumentation and Data Presentation

The primary data base for this study consists of measurements gathered by the three-satellite International Sun-Earth Explorer (ISEE) program. The co-orbiting satellites, ISEE's 1 and 2, which carried similar instrumentation, were launched on October 22, 1977, with the fundamental objective being to collect near-Earth magnetospheric observations which could be interpreted unambiguously, both spatially and temporally. The payloads were carefully matched to facilitate comparison of the data from the two satellites, and consequently, to remove the uncertainty which arises when measurements from only one satellite are used to study the magnetospheric configuration. Observations obtained by the closely but variably configured spacecraft were intended particularly to enhance the investigation of the response to variations in solar wind parameters of the various boundaries in the magnetosphere. Determinations of the structure, motion and stability, (specifically, calculations of velocity and thickness), of boundaries such as the bow shock, magnetopause, and neutral sheet, were of foremost interest in planning the mission.

The third constituent of the ISEE mission, ISEE 3, was launched on August 12, 1978 into a halo orbit about the sun-Earth libration point, approximately 240 Re sunward of the Earth (Tsurutani, et al., 1986). It provided essential

information about the solar wind conditions which ultimately perturb the boundary structures and cause dynamic changes in the terrestrial magnetosphere. It sampled the magnetic fields and particles in the interplanetary medium approximately one hour before the corresponding plasma arrived at the Earth. Consequently, ISEE's 1 and 2 monitored dynamical processes in the magnetosphere that had been influenced by the interplanetary conditions previously observed by ISEE 3.

A total of 32 experiments were flown on the ISEE mission, 13 on ISEE 1, 7 on ISEE 2 and 12 on ISEE 3, with 5 of the experiments on ISEE 1 being duplicated on ISEE 2, consequently forming five shared studies (Ogilvie, et al., 1977b). Of central interest to this work are the *LEPEDEA* and *Fluxgate Magnetometer* experiments on ISEE's 1 and 2 used to obtain energetic particle and magnetic field measurements, respectively, as well as the *Vector Helium Magnetometer* experiment on ISEE 3 to monitor the interplanetary magnetic field. These experiments will be discussed below. In addition to the ISEE data, IMF measurements obtained by the spacecraft IMP J, and ground-based observations of auroral activity are important for the ensuing studies and will, therefore, be outlined.

3.1 Orbit Specifications for ISEE's 1 and 2

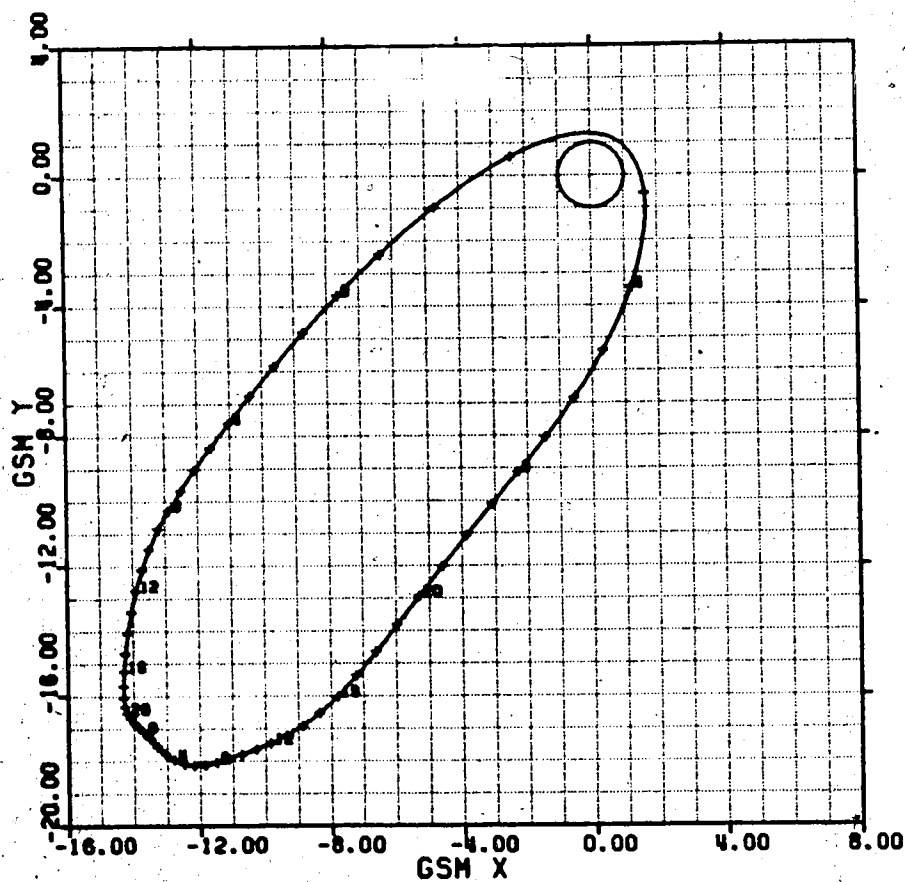
The mother and daughter satellites, ISEE 1 and ISEE 2 respectively, followed approximately the same elliptical Earth-orbiting trajectory, with ISEE 2 travelling behind ISEE 1 by a known and controllable distance, varying from 100 ± 1 km to 5000 ± 1 km. The separation distance was altered by manoeuvring ISEE 2. Perigee of the orbit was about $1.1 R_e$ (700 km above the Earth's surface), apogee was roughly $22.6 R_e$, and the orbital period was approximately 57 hours. The spin axes were aligned perpendicular to the ecliptic plane ($\pm 1^\circ$), with spin frequencies of 19.75 ± 0.05 rpm for ISEE 1 and 19.8 ± 0.1 rpm for ISEE 2, giving spin periods of approximately three seconds (Ogilvie, et al., 1977b). The orbit plane was initially inclined approximately 30° to the ecliptic such that the two satellites were farthest north of the tail mid-plane at apogee, crossing to the southern hemisphere relatively close to the Earth. As a result, preferential coverage of the northern tail hemisphere was provided. However, the plane of the orbit shifted southward by several degrees in each subsequent year (to 23° in 1978 and to 15° in 1980 (Dandouras et al., 1986)) thereby increasing the coverage of the southern hemisphere as time progressed. The spacecraft penetrated the interplanetary medium for up to three quarters of an orbital period, depending on the time of year. From mid-January to mid-June they spent most of each orbit within the tail such that at perigee the dayside magnetosphere was traversed in

the equatorial regions, and on the nightside the near-Earth tail environment was probed. For the remaining months the satellites orbited predominantly outside the magnetosphere within the solar wind.

Orbit plots for ISEE's 1 and 2 have been produced by the UCLA magnetometer group and are available on microfiche. Eleven different representations for each orbit are provided and these are described in detail by Russell et al. (1980). Of primary importance here are the orbit plots in both the GSE and GSM coordinate representations. In each coordinate system there are three plots for every orbit, depicting the three projections in the X-Y, X-Z and Y-Z planes. In either system, any two of these provide enough information to determine the spatial location of the satellite. As well, X-Z and Y-Z and plots which present the neutral sheet location in GSM coordinates according to the two models of Russell and Brody, (1967) and Fairfield (1980) are of interest.

Figure 3.1 is a sample orbit plot in the GSM coordinate system for a typical tail traversal by ISEE 1. (The corresponding ISEE 2 plot is almost identical except for a shift in time.) This figure shows the $(X-Y)_{GSM}$ projection for orbit 199, 1979. The orbit number, satellite specification, and time of perigee (day 38, hour 20:08) are indicated at the top of the plot. The grid spacing on both axes is one R_e and each plot displays a 24 by 24 R_e region of space which is shifted from plot to plot in order to

ISEE-A ORBIT 199
PERIGEE 79 38 2008



UCLA MAY 20 1980

Figure 3.1 Sample ISEE 1 orbit plot in GSM coordinates. Shown is the (X-Y)_{GSM} projection for orbit 199, 1979.

contain the orbit. The satellite trajectory is marked with a cross at each hour and every four hours the *Universal Time* is specified. The same format is also used for the other two GSM projections. Note that the irregular shape of the orbit results from the "rocking effect" of the GSM coordinate system about the X-axis, as described in section 2.1.

Universal Time (UT), also known as Greenwich mean time, is defined as the local time at the meridian of zero geographic longitude (ie: Greenwich, England). Local time at the geomagnetic north pole is obtained by adding to the value of Universal Time the number of 15° longitude sectors (each representing one hour of Universal Time) between Greenwich longitude and that of the geomagnetic north pole (this value is obtained by measuring longitude west of Greenwich). The north geomagnetic pole is located 4.65 hours west of Greenwich, therefore, approximately 5 hours must be added to the hour in Universal Time of a particular magnetic observation made by a satellite in order to be able to determine the orientation of the geomagnetic axis for the given magnetic event. In this work all events will be referenced in Universal Time.

3.2 Measurement and Display of the Tail Magnetic Field

The instrumentation onboard the ISEE 1 and 2 spacecraft included identical UCLA fluxgate magnetometers which simultaneously measured the three orthogonal components of the magnetic field in the spacecraft coordinate system

(equivalent to GSE coordinates for the ISEE satellites since their spin axes are oriented in a direction perpendicular to the ecliptic plane). These instruments are described by Russell (1978). A wide dynamic range was required for the magnetometers since the magnetic field magnitude near the Earth is greater by a factor of 10^4 than that in the mid-tail regions (at perigee $|\bar{B}| \approx 50,000$ nT whereas at apogee $|\bar{B}| \approx 20$ nT). Two commandable ranges chosen for the instruments were $\pm 8192 \pm 1/4$ nT, and $\pm 256 \pm 1/128$ nT.

The magnetic field measurements obtained by ISEE 1 and 2 were processed by the UCLA magnetometer group, and magnetograms with a sampling interval of either 64 seconds or 4 seconds are available on microfiches. The latter format is employed in this study. Figure 3.2 shows the ISEE 1 magnetogram for hour 14, day 39, 1979, corresponding to a segment of the orbit reproduced in figure 3.1 above. Figure 3.2 displays the UCLA magnetogram which gives the components of the magnetic field in spacecraft (GSE) coordinates. Four panels are displayed on each magnetogram, one corresponding to each of the three magnetic field components, B_x , B_y , and B_z , and the fourth representing the total magnetic field magnitude, $|\bar{B}_T|$ (from top to bottom, respectively). The abscissa represents field magnitude measured in nanoteslas and accurate to ± 1 nT, and the ordinate indicates Universal Time in hours.

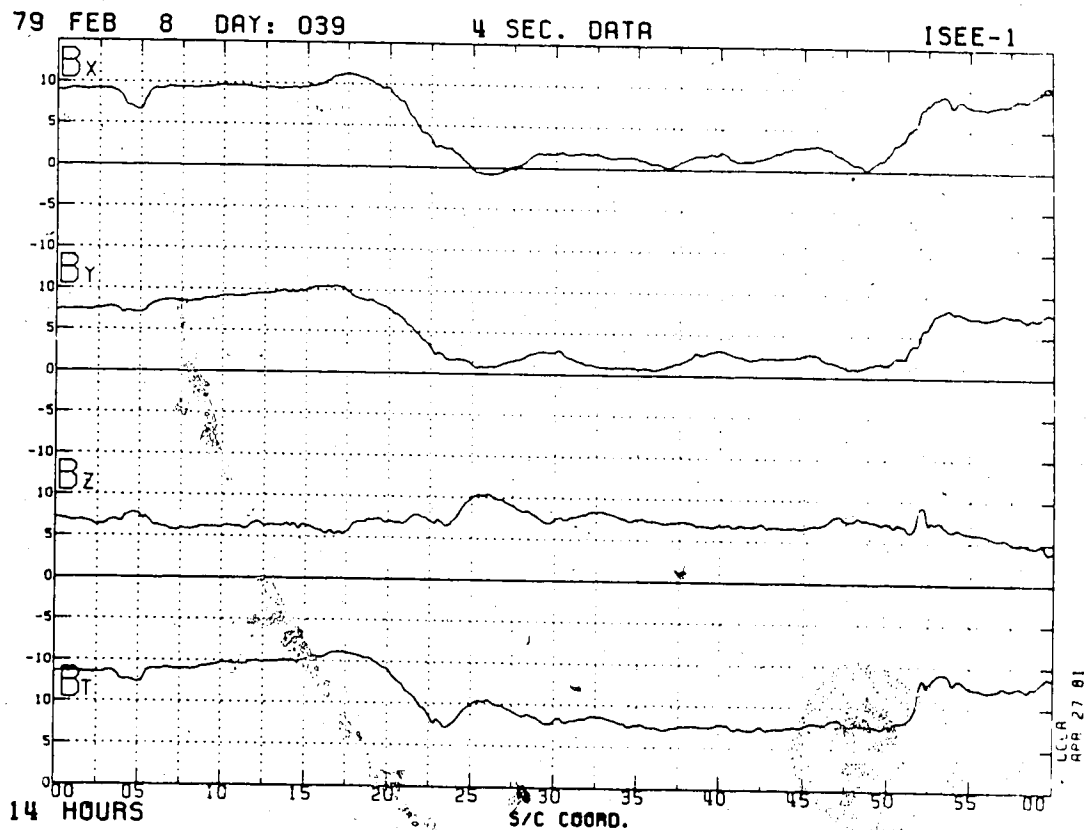


Figure 3.2 ISEE 1 magnetogram, in GSE coordinates, for hour 14, day 39 (February 8), 1979.

3.3 Magnetic Signatures of the CPS, PSBL and Lobe

Satellite magnetograms provide the magnitude and direction, as well as a qualitative character of the magnetic field being observed by the spacecraft. According to the polarity of the B_x component, determination of whether the satellite is situated in the northern or southern hemisphere may be made since B_x has a positive polarity in the northern hemisphere and a negative polarity in the southern hemisphere for all plasma domains. Similarly, the polarity of the B_y component dictates whether the satellite is situated in the dusk or the dawn sector of the tail, as discussed in section 2.6. Consequently, four "quadrants" may be defined in the tail cross-section according to the polarities of B_x and B_y , as shown in figure 3.3.

This regional division of the tail cross-section into quadrants is, however, somewhat simplistic in that the actual shapes and positions of the transition zones between the northern and southern hemispheres, as well as between dusk and dawn, are not this clearly defined. The dawn-to-dusk transition is thought to lie closer towards dusk than dawn by $\approx 3^\circ$ as a result of aberration of the tail (Behannon, 1970). As well, there has been much discussion of a curved or warped neutral sheet (Russell and Brody, 1967; Bowling, 1974; Fairfield, 1980; Voigt, 1984; and Gosling et al., 1986). In particular, the Russell-Brody and Fairfield models for determining the shape of the neutral sheet are of

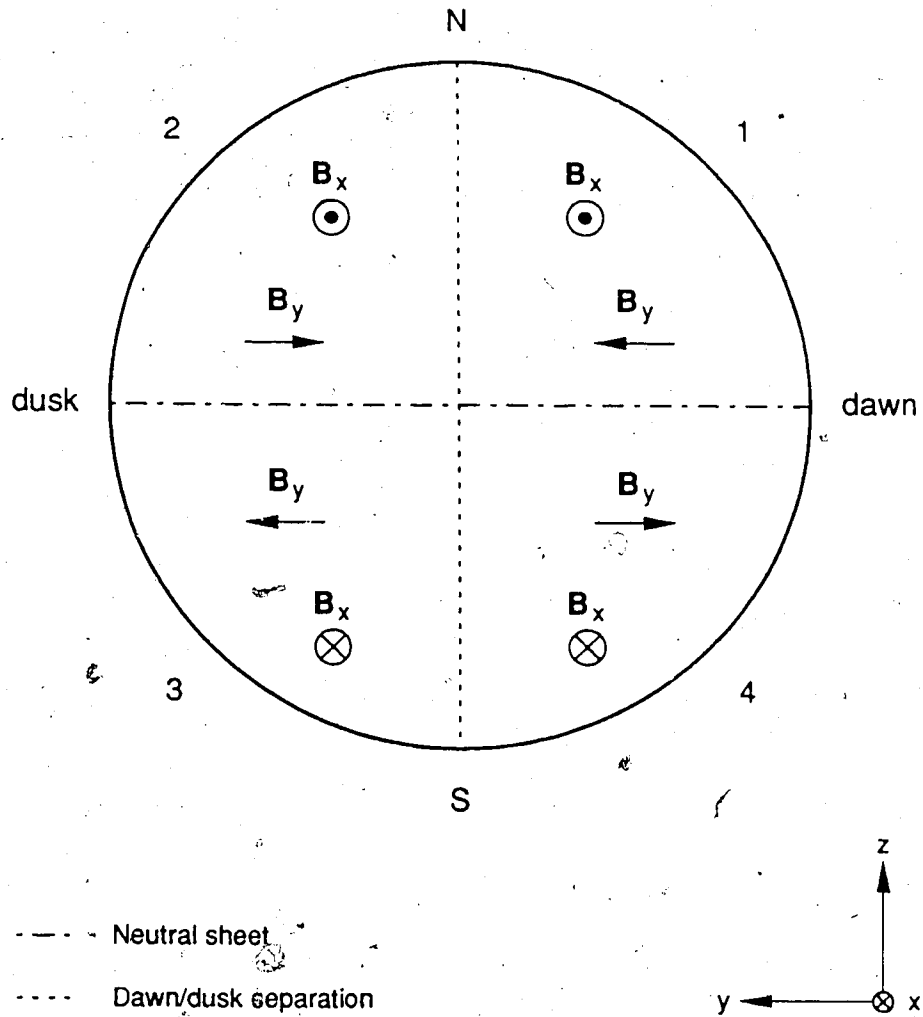
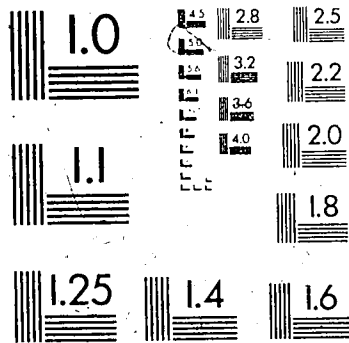


Figure 3.3 Idealized division of the tail cross-section into four quadrants which are defined according to the polarities of both the X and Y components of the tail magnetic field. For example, quadrant 1 (north-dawn sector) is defined by positive B_x and positive B_y .

2



interest, since in both cases the neutral sheet position has been calculated for the ISEE 1 and 2 satellites throughout 1978 and 1979. The calculated positions are available on microfiche in terms of orbit plots in the GSM coordinate system.

The basis of any neutral sheet model is that an equal amount of magnetic flux must be present in each of the two tail hemispheres. In the Russell-Brody model, the neutral sheet is represented by a curved surface which touches the X-Y plane at the edges of the tail and which is farthest from the X-Y plane near the central axis of the tail. At all times, the neutral sheet position depends on the continually changing orientation of the dipole axis (if the dipole were aligned perpendicular to the X-Y plane then the neutral sheet would coincide with the X-Y plane). In the region of the tail for which $|Y| \geq 11 R_e$ and $X \geq -30 R_e$, the Russell-Brody model may be schematically represented as in figure 3.4(a) (which gives the shape of the neutral sheet that is appropriate when the geomagnetic pole is tilted towards the sun; that is, during northern hemisphere summer). The Fairfield model also represents the neutral sheet as an arched surface, shown schematically in figure 3.4(b), which crosses the solar magnetospheric equatorial plane near the flanks of the tail $\approx \pm 18 R_e$ from the tail axis. In this model, the shape and position of the neutral sheet do not vary significantly with increasing distance downtail. In addition, Fairfield reports that the neutral sheet tends to

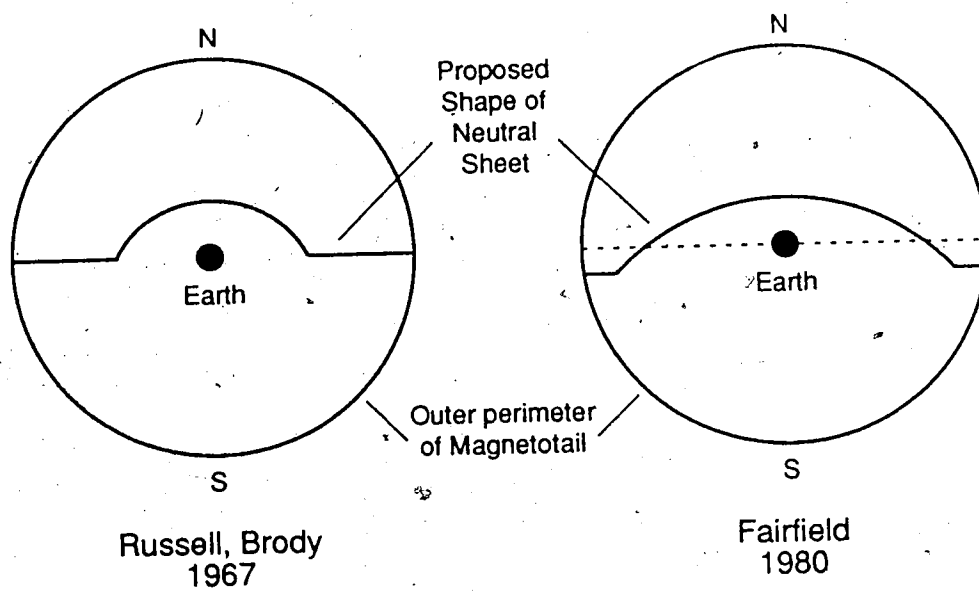


Figure 3.4 Cross-sections of the geomagnetic tail illustrating schematically the (a) Russell-Brody and (b) Fairfield model representations of the shape of the tail neutral sheet (after Gosling et al., 1986).

be slightly nearer the tail mid-plane during intervals of intense magnetospheric activity.

The transition zones shown in figure 3.3 strictly represent an idealization, and the question of their actual shapes and locations is of minor importance in the following studies. However, the above definitions of northern vs. southern hemisphere and dusk vs. dawn according to B_x and B_y polarities remain valid.

General guidelines from the statistical magnetospheric model may be outlined according to which specification of the plasma regime being sampled by the satellite may be attempted. In either hemisphere, the B_x component increases in magnitude towards the tail lobe, since in this region, the field is most tail-like, and hence, B_x is largest in magnitude here. The B_z component, on the other hand, is very weak in the lobes. Towards the CPS the field lines become more dipolar in nature; thus, the magnitude of B_x decreases and that of the B_z component increases. Therefore, B_x is smallest in magnitude in the CPS, and at the neutral sheet, whereas the B_z component is largest in magnitude near the centre of the CPS and normally exhibits a positive polarity there. In the PSBL, both B_x and B_z are of intermediate magnitudes. The magnitude of B_y is very weak in the zone separating dusk and dawn, undergoing a polarity change there, whereas it is larger towards the flanks of the tail. The magnitude of this field component also decreases towards the lobe. In terms of character of the magnetic trace, lobe

traversals provide smooth or quiet traces, the PSBL is characterized by noisy traces with small, rapid field fluctuations, and the traces for the CPS are also comparatively regular (Elphic et al., 1985). However, these field characteristics are not always observed, nor are they definitive.

In combination, the above signatures form the basis of the geomagnetic tail field model incorporating the CPS, PSBL and lobe plasma regimes. It must be emphasized that these signatures present a statistical and idealized picture of a rather dynamic magnetotail. Additional information is required for accurate plasma regime identification, and such is provided by energetic particle measurements.

3.4 Energetic Particle Detection and Presentation

The instrument employed on ISEE's 1 and 2 to collect observations of plasma characteristics was a quadrispherical low energy proton and electron differential energy analyser, or, LEPEDEA. This instrument was developed by the University of Iowa space physics group and it has provided the first three dimensional plasma flow measurements in the magnetosphere and magnetosheath. Previous instruments had been limited to measurements of bulk flow in a plane perpendicular to the spacecraft spin axis. Due to the capability of the LEPEDEA to obtain entire velocity distributions for low energy protons and electrons, direct measurements of current in the magnetosphere and at the

magnetopause became possible.

The LEPEDA is described in detail by Frank et al. (1978a). It is essentially an electrostatic analyser incorporating 14 continuous-channel electron multipliers which together are capable of determining the directional intensities of both electrons and positive ions arriving at the satellite from all but two percent of the unit sphere. The ions are assumed to be primarily protons (Eastman et al., 1985b). The instrument contains seven pairs of detectors, each consisting of an electron detector and an ion detector. The seven sets are oriented at different angles of incidence, incremented in altitude as shown in figure 3.5(a). The ranges in polar angle θ , or latitude, (measured in degrees from the spin axis), of the seven individual fields-of-view are 9-18, 18-39, 39-71, 71-109, 109-141, 141-162 and 162-171 degrees where north is represented by $\theta=0^\circ$. Only the charged particles with incident polar angles lying within the 9 degree half-angle cones centered about the spin axes (both 0° and 180°) are not sampled by the LEPEDA. Because each satellite spins about its axis, seven latitudinal bands are swept out on the unit sphere, as indicated in figure 3.5(b). Thus, the angular distributions of positive ion and electron intensities in the seven directions are measured separately and simultaneously with the fan-shaped field-of-view configuration of the LEPEDA.

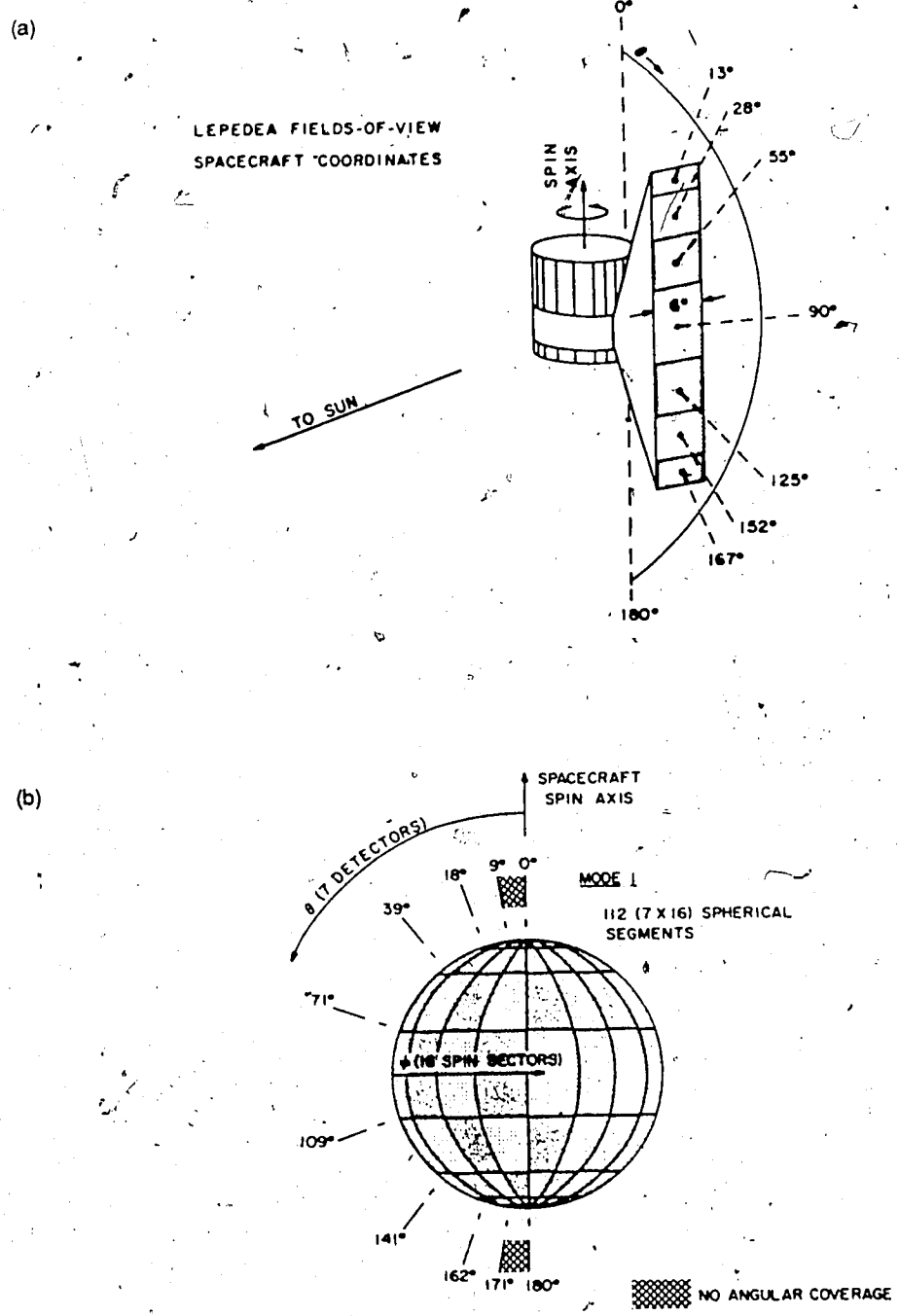


Figure 3.5 (a) Fields-of-view of the LEPEDA as referenced to the spacecraft spin axis, and (b) LEPEDA coverage of the angular distributions of the positive ion and electron intensities, projected onto the unit sphere (after Eastman et al., 1985b).

The energetic particle data were collected at either a high- or a low-bit rate. At low-bit rate each azimuthal band is incremented into 16 equal and contiguous sun-referenced sectors; however, at high-bit rate the LEPDEA is slaved to the spacecraft clock, and the spin period is then divided into 12 equal angular segments. The number of energy passbands sampled depends on the data mode in use. At low-bit rate 64 passbands are sampled, spanning the full energy range of the instrument, and at high-bit rate only the highest 32 levels including energies above 215 eV are sampled. In high-bit rate mode each instrument cycle requires 128 seconds for completion (32 energy levels x 4 seconds per level). Starting at the lowest energy, each detector sweeps through all azimuthal angles before stepping up to the next highest energy level, such that 12 sectors are sampled during each three second spin period and at each energy. Further, all seven polar angles are sampled simultaneously by the corresponding proton and electron detectors, consequently, the LEPDEA covers the full solid angle range during each three second spin period at each energy level. In low-bit rate mode the time required for a complete instrument cycle is about eight minutes (64 energy levels x 8 seconds per level) with 16 azimuthal sectors being sampled.

The LEPDEA has an energy range of $1 \text{ eV} \leq E/q \leq 45 \text{ keV}$ with an energy resolution of $\Delta E/E = 0.16$ or 16%. The intensity thresholds (or minimum intensities detectable) for

positive ions are 7×10^3 and 1.5×10^{-1} $(\text{cm}^2\text{-sec-sr-eV})^{-1}$ at 1 eV and 45 keV, respectively. The corresponding electron threshold intensities are 2×10^4 and 4×10^{-1} $(\text{cm}^2\text{-sec-sr-eV})^{-1}$ at 1 eV and 45 keV, respectively. The maximum ion and electron intensities within the ranges of the LEPEDA are a factor of 3×10^5 greater than the above corresponding thresholds (Ogilvie et al., 1977b).

A Geiger-Mueller (GM) counter was also included in the plasma instrumentation. It has a collimated conical 40° field-of-view directed perpendicular to the spin axis of the spacecraft, providing measurements in the vicinity of the satellite midplane. The GM tube is sensitive to electrons with $E \geq 45$ keV and protons with $E \geq 600$ keV.

Energetic plasma measurements obtained from the LEPEDA are available in two graphic, colour-coded forms, the *energy-time* (E-t) spectrogram and the *energy-spin phase angle* (E- ϕ) spectrogram, and these were both processed by the Iowa space physics group. The identification of a particular plasma regime is usually unambiguous when using the three-dimensional E- ϕ spectrograms; however, interpretations based on the two-dimensional E-t spectrograms must rely on lower spatial and temporal resolution, and therefore, short excursions from one plasma regime to another may not be detectable. Consequently, although the E-t spectrograms provide information adequate for general surveying purposes, the E- ϕ displays provide finer detail and are useful for more precise event analyses.

An example of the energy-time spectrogram format is shown in figure 3.6. At the top of each spectrogram the name of the satellite which collected the data, as well as the day number and year, are given. This spectrogram presents energetic particle data for day 39, 1979. The first four panels display positive ion responses obtained by that detector which is centered on the equatorial plane of the spacecraft. The responses are averaged over four "look" directions or quadrants of view which are, from top to bottom, sunward (V), dawnward (<), anti-sunward (\wedge) and duskward (>). The bottom panel represents azimuthally averaged electron spectra, sampled by the equatorially-centered electron detector. The vertical axes represent logarithmic energy scales (\log_{10}) in units of electron volts and the horizontal axes indicate both Universal Time (in hours), and the location of the spacecraft in solar ecliptic (GSE) coordinates, where R_{SE} is the geocentric radial distance to the satellite (measured in Earth radii), θ_{SE} is the solar ecliptic latitude, and ϕ_{SE} is the solar ecliptic longitude (both measured in degrees). Note that the start of first hour of each day is denoted by 00, and the end of the last hour by 24. The color code on the side provides a logarithmic indication of flux intensity, encompassing a range of four orders of magnitude, with red representing high detector responses and blue, low responses. This scale is used for displaying the number of counts per accumulation interval at both low- and high-bit

National Library
of Canada

Canadian Theses Service

Bibliothèque nationale
du Canada

Service des thèses canadiennes

NOTICE

AVIS

THE QUALITY OF THIS MICROFICHE
IS HEAVILY DEPENDENT UPON THE
QUALITY OF THE THESIS SUBMITTED
FOR MICROFILMING.

UNFORTUNATELY. THE COLOURED
ILLUSTRATIONS OF THIS THESIS
CAN ONLY YIELD DIFFERENT TONES
OF GREY.

LA QUALITE DE CETTE MICROFICHE
DEPEND GRANDEMENT DE LA QUALITE DE LA
THESE SOUMISE AU MICROFILMAGE.

MALHEUREUSEMENT, LES DIFFERENTES
ILLUSTRATIONS EN COULEURS DE CETTE
THESE NE PEUVENT DONNER QUE DES
TEINTES DE GRIS.

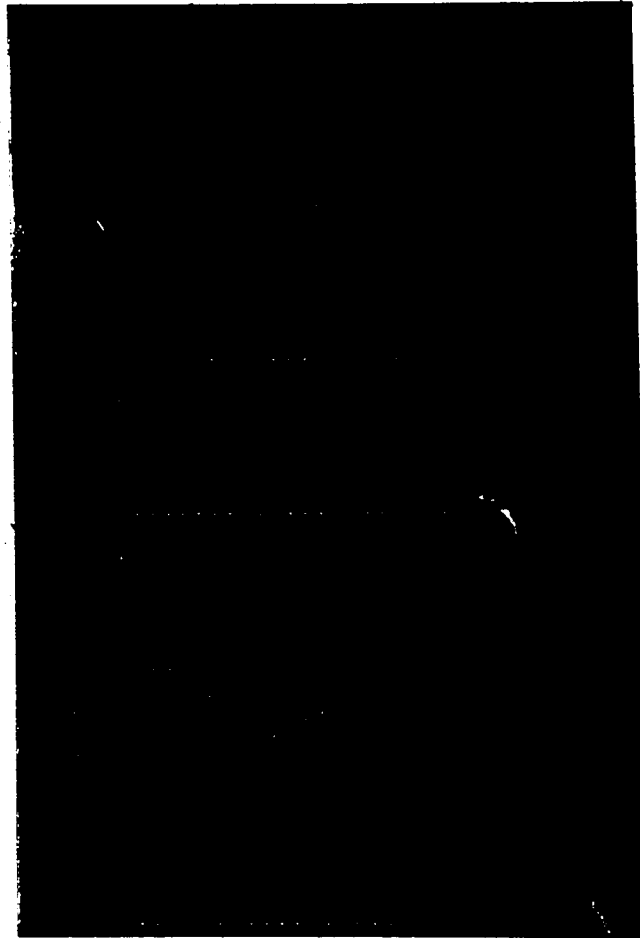
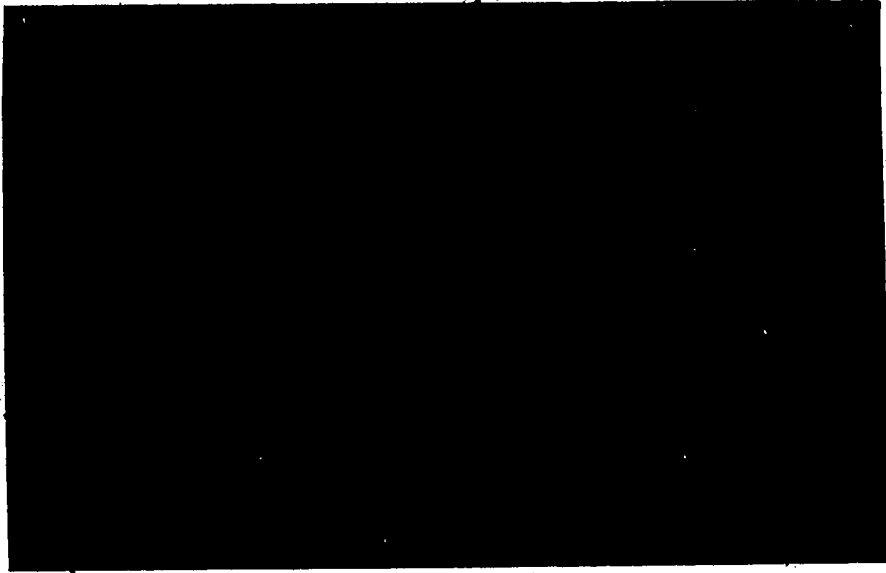


Figure 3.6 An example of the energy-time spectrogram format for displaying energetic particle data. This spectrogram presents data collected at low bit-rate for day 39 (February 8), 1979.

rates; therefore, no units are given since the accumulation times for the two modes are different (Frank, et al., 1978b). At high-bit rate six hours of data are shown on a spectrogram whereas at low-bit rate 24 hours are presented. The data for figure 3.6 were recorded at low-bit rate; therefore, 24 hours of data are displayed.

E- ϕ spectrograms for selected time intervals during day 114, 1979, are shown in figures 3.7, 3.8 and 3.9. The start time, satellite specification, radial distance from the Earth, day and year for each sequence is given at the top of the display. There are fifteen panels per plate, each representing a three-dimensional particle response array. The first seven indicate ion distributions, denoted by 1P-7P, the last seven show electron distributions, denoted by 1E-7E, and the center panel displays high energy particle responses measured by the Geiger-Mueller counter. The detectors are numbered sequentially beginning with the polar detector which has a field-of-view centered at the satellite polar angle of 13° and ending with that centered about the polar angle of 167° . For each detector, responses are plotted as a function of spacecraft spin angle (ϕ), with each frame displaying observations for 16 azimuthal sectors as marked on the abscissa. Since the spin axis is nearly perpendicular to the ecliptic plane, the abscissa may be interpreted as the solar ecliptic longitude with one frame width representing a 360° rotation of the satellite. The sides of each panel represent fluxes approaching the

(a)



(b)

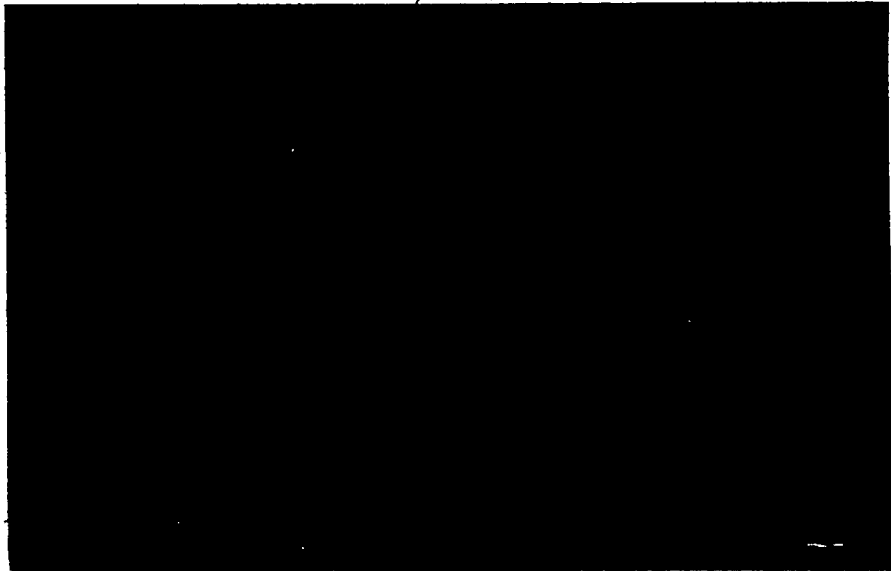


Figure 3.7 Examples of the energy-phase angle spectrogram format for displaying energetic particle data. Figures 3.7(a) and (b) present data collected at low bit-rate for day 114 (April 24), 1979, at start times of 11:08 and 11:11 UT, respectively.

(a)



(b)

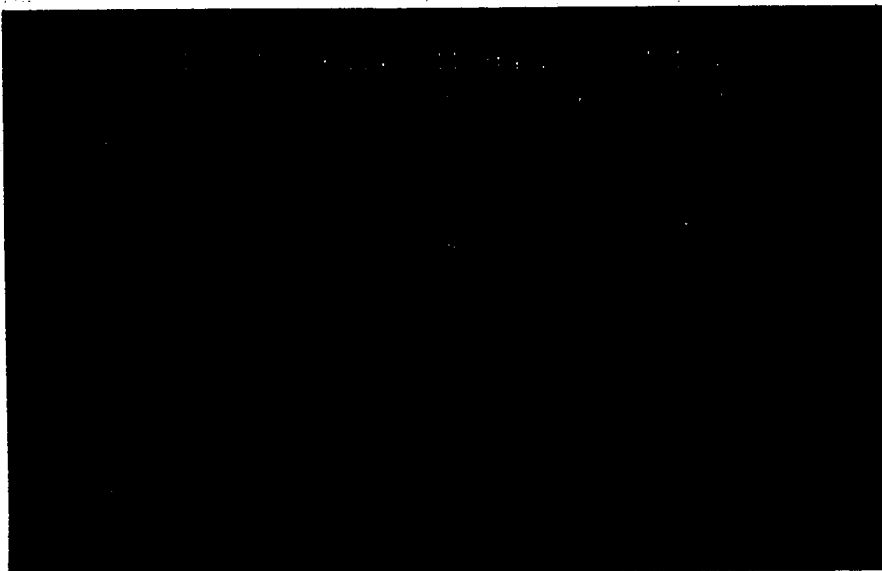


Figure 3.8 Same as figure 3.7 but for start times of (a) 11:17 and (b) 11:38 UT, respectively.



Figure 3.9 Same as figure 3.7 but for a start time of 11:45 UT.

satellite in the Earthward direction while the center of each panel represents anti-Earthward directed fluxes. For the electron and ion response frames, values of \log_{10} of the particle energy (in units of electron volts), are given along the ordinate. For the GM frame, the ordinate represents Universal Time and the energies of the detected particles are not specified.

All frames within the energy-phase plots, including the GM frame, display responses sequentially in time from bottom to top. The colour code shows a logarithmic measure of flux intensity in units of \log_{10} of the sensor count rate. A vertical band of large responses near the center of each GM frame arises from solar X-rays (Eastman et al., 1984). It is important to note that detector 7E on ISEE 1 has deteriorated since the launch of the spacecraft, and therefore, the display of electron fluxes in the corresponding frame of each E- ϕ spectrogram is not reliable. Also, there is an enhancement of electrons at low energies in the 5E frame which is due to secondary electrons and photoelectrons resulting from the instrument-spacecraft configuration (Eastman et al., 1985b).

3.5 Energetic Particle Signatures in the CPS, PSBL and Lobe

The primary particle signatures of the CPS, PSBL and lobe, which are the regions of interest in this work, have been outlined by Eastman et al. (1984) and Eastman et al. (1985a, b). According to Eastman et al. (1985b) the only

reliable criterion for identifying the CPS is the occurrence of quasi-isotropic velocity distributions for both ions and electrons. Two distinct isotropic ion components, one of high energy (hot) and one of low energy (cold), are commonly observed. The high energy ion component in the CPS is most frequently observed towards the center of the plasma sheet (in latitude, azimuth and radial distance). The occurrence of the two components has been correlated with the level of geomagnetic activity, the cold component being observed to dominate the PS during periods of low activity, while the hot component is observed when activity levels are high (Eastman et al., 1985b). Often, however, the particle spectrograms will indicate a transition from one component to the other, with no corresponding ground-based indication of a change in geomagnetic activity.

The PSBL is characterized by significant anisotropies in the particle velocity distributions, which often include both high and low energy components. Counterstreaming high-energy ion beams with energies of $1 \text{ keV} \leq E \leq 45 \text{ keV}$ are typically observed. As well, anti-sunward flowing ion beams of $E \leq 1 \text{ keV}$ are common in the PSBL. According to Williams (1981), the counterstreaming ion distributions are the result of near-Earth mirroring of ion beams which have been accelerated towards the Earth from a source region roughly 80 to 100 R_E downtail. Consequently, these energetic ion beams are field-aligned. High speed ion flows are confined to the PSBL, not being observed in either the CPS

or the lobe (Decoster and Frank, 1979). Enhanced flow speeds frequently appear in the PSBL during periods of high activity; however, significant flow speeds also occur in the PSBL during periods of extended quiescence.

The tail lobes are identified by the occurrence of very low plasma densities which generally are not isotropically distributed. Frequent intervals of low energy ion responses (≤ 0.5 keV), especially a low energy anti-sunward ion component, are characteristic of the tail lobes. The PSBL also contains a low energy ion component which is often indistinguishable from the related low energy ion component observed in the lobes. Ions of $E \geq 5$ keV are not observed in the lobe plasma domain, but low energy (soft) electron spectra are typical.

During the onset of a magnetospheric substorm, a sudden reduction in energetic particle flux intensity is often observed. This is a typical signature of substorm activity, and it is known as a *plasma sheet dropout*. A dropout is interpreted as indicating the exit of the observing satellite from the CPS through the PSBL and into the lobe as the plasma boundaries move past the spacecraft due to a thinning of the plasma sheet in response to the occurrence of the magnetospheric substorm (Dandouras et al., 1986). During the substorm recovery phase, the satellite may experience a return to the CPS from the lobe, via the PSBL, as the plasma sheet again expands and the boundaries move past the satellite. Plasma sheet distributions at the heart

of the CPS show no significant change in plasma flow near the onset of a substorm, however, counterstreaming ion beams are observed in the PSBL at this time. During high activity, the plasma sheet can be very thin and it is, therefore, not always detectable, especially in the E-t spectrogram format. However, according to Dandouras et al. (1986), although even weak substorms can produce large perturbations of the plasma sheet, the thickness of the plasma sheet can also locally remain unaffected by intense substorm activity.

3.6 Sample Event Analyses

The GSE magnetogram shown in figure 3.2 features magnetic field signatures typical of the CPS. Positive polarity of the B_x and B_y components suggests that the satellite is located in the dawn sector of the northern hemisphere, with the magnitudes of these components being characteristic of the CPS regime. As well, a positive B_z component is expected in the vicinity of the tail mid-plane within about 30 R_e downtail. From orbit plots it can be determined that ISEE 1 is situated at $X_{GSE} = -14.2 R_e$, $Y_{GSE} = -13.3 R_e$ and $Z_{GSE} = +5.5 R_e$. During the interval of 14:25 to 14:50 the satellite appears to be in the vicinity of the neutral sheet since both the B_x and B_y components exhibit magnitudes of only one or two nT. Further, within this time interval B_z increases slightly, indicating that the satellite is closer to the neutral sheet than at the start and end of hour 14. According to the magnetogram, ISEE 1

appears to spend the entire hour within the CPS since neither PSBL or lobe signatures are apparent.

The magnetograms in figures 3.10, 3.11 and 3.12, for hours 10, 11, and 12 of day 39, 1979, may be interpreted as indicating a traversal of ISEE 1 from the lobe through the PSBL to the CPS. From the start of hour 10 until approximately 11:30, the magnitude of the B_x component is ≥ 20 nT, the magnitude of B_y is ≈ 10 nT, and the B_z component magnitude is very small. These signatures indicate that the field lines are tail-like, with the field being oriented predominantly in the X direction. This suggests that the satellite is located within the lobe regime. Because both B_x and B_y are positive in polarity, the northern hemisphere dawn sector is being sampled. Further, since the traces of all three components are generally smooth and steady in nature, a quiet or relatively non-dynamic plasma domain is being observed by the satellite, which, in this case, is the lobe (Slavin et al., 1985).

Between 11:30 and 11:55, the component traces become somewhat turbulent, and exhibit an increased noise level. This is indicative of the more dynamic plasma regime of the PSBL. Fluctuations in the magnetogram traces, particularly in the B_y component (transverse to the background field), can be attributed to FAC flowing in the PSBL (Elphic et al., 1985). As well, because the B_x component magnitude has decreased whereas those of the B_y and B_z have increased, the spacecraft appears to be somewhat closer to the midplane of

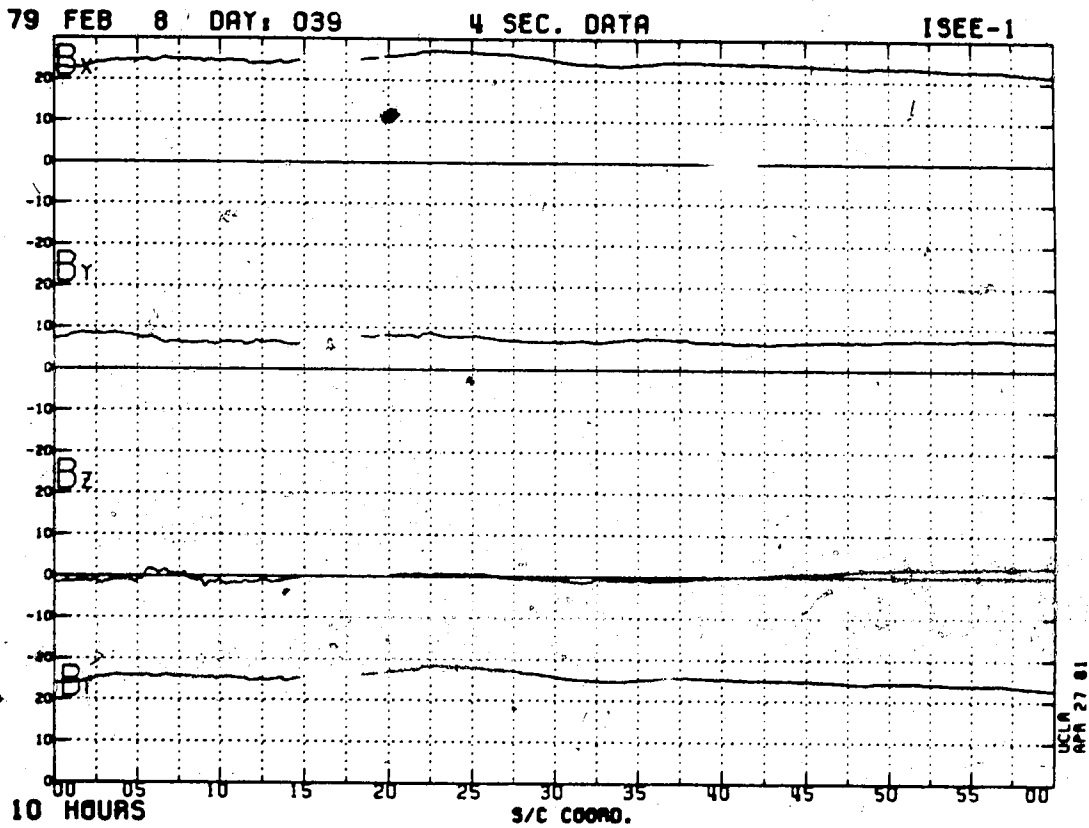


Figure 3.10 ISEE 1 magnetogram, in GSE coordinates, for day 39 (February 8), 1979, hour 10.

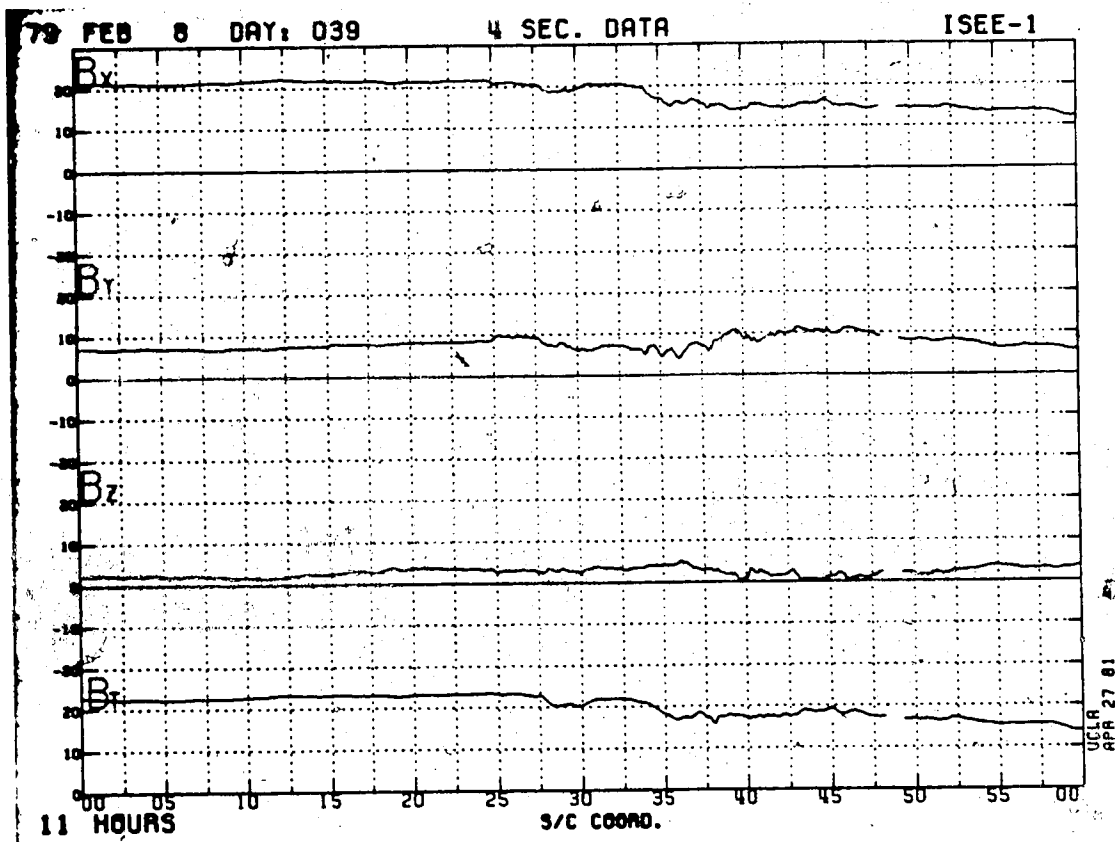


Figure 3.11 ISEE 1 magnetogram, in GSE coordinates, for day 39 (February 8), 1979, hour 11.

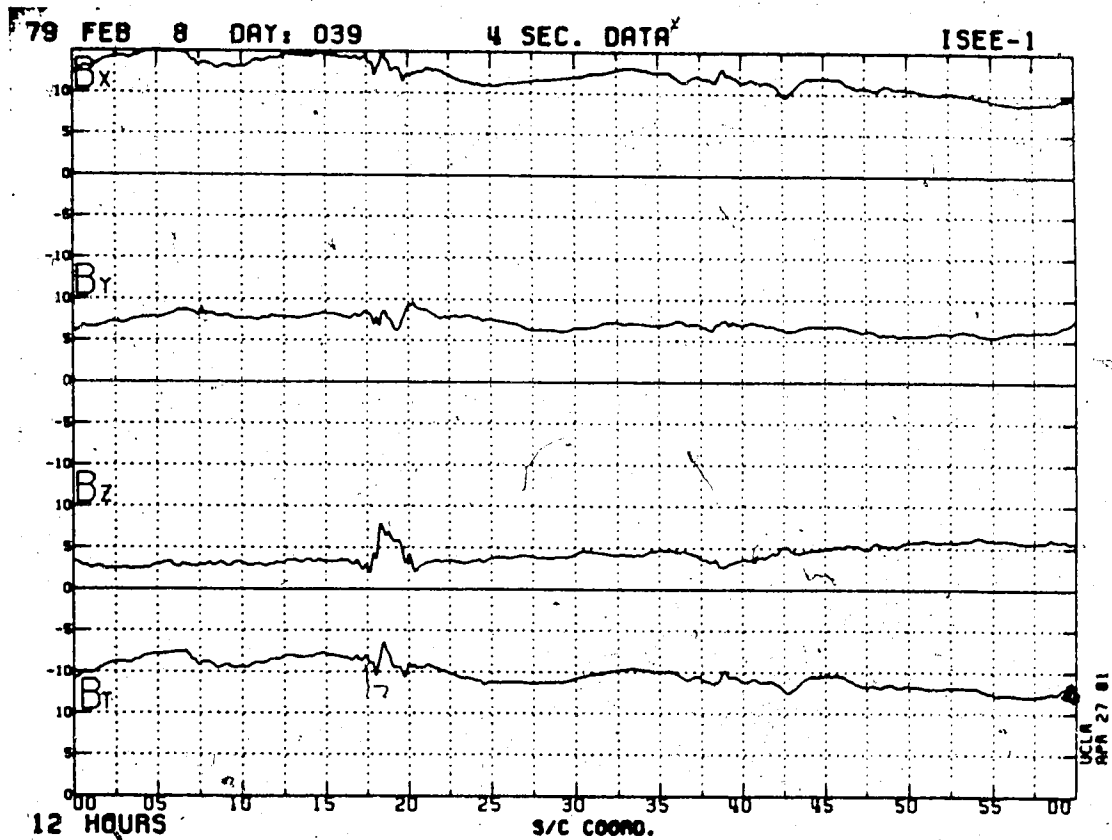


Figure 3.12 ISEE 1 magnetogram, in GSE coordinates, for day 39 (February 8), 1979, hours 12.

the tail. Together, these signatures would suggest that the PSBL has been encountered. Note, however, that the observed magnetic signatures are not always apparent in a PSBL crossing.

Finally, between 11:55 and the end of hour 12, the magnetic signatures are similar to those described for hour 14, day 39, 1979. The further decrease in magnitude of the B_x component accompanied by a continued increase in magnitude of the B_y and B_z components indicates that the satellite has entered the CPS, and it gets closer to the neutral sheet as the hour progresses.

The three plasma regimes of the CPS, PSBL and lobe, are clearly illustrated in the E-t spectrogram of figure 3.6. The top four ion response panels indicate high-energy, isotropic ion fluxes ($0.5 \text{ keV} \leq E \leq 10 \text{ keV}$), for the time interval of hour 7 to hour 9, as well as for hours 13 through 19, inclusive. During these intervals, the particle data indicate that ISEE 1 was situated within the CPS, thereby confirming the prior interpretation of the magnetogram of figure 3.2 which suggested that the spacecraft was located in the CPS for the whole of hour 14. Note that the energetic particle data can only indicate which plasma domain is being sampled; therefore, from the E-t spectrogram one cannot distinguish between the northern and southern hemispheres within the plasma sheet, nor can one identify the neutral sheet region.

It is also clear from the E-t spectrogram that the interval of time between the start of hour 10 and the end of hour 12 represents a traversal of ISEE 1 from the lobe through the PSBL and into the CPS, as was described above with respect to the magnetograms of figures 3.10, 3.11 and 3.12. The lobe is evident from the general absence of both ion and electron responses from approximately 10:10 until the first part of hour 11 (a low-intensity, low-energy electron component, with $E \leq 0.5$ keV, is present). At approximately 11:30 the satellite detected a distinct anti-Earthward flow of ions ($E \leq 1$ keV), and as well, the ion distributions in the four look-directions become anisotropic, indicating that ISEE 1 has encountered the PSBL. Near the end of hour 12, ion responses appear isotropic in nature, suggesting that the central plasma sheet has been entered. ISEE 1 then remained clearly within the CPS until approximately the end of hour 19. Hence, the E-t particle signatures for this particular example confirm the interpretation of the magnetograms in figures 3.10, 3.11 and 3.12.

Prior to 10:10 (the beginning of the lobe encounter) ISEE 1 appears to have been located within the CPS, evidenced by the occurrence of isotropic responses for the ions in each of the top four panels of the E-t spectrogram. However, according to the spectrogram, the PSBL signature is absent. This suggests that the spacecraft experienced a rapid traversal from the CPS to the lobe, and such a

transition is indicative of plasma sheet thinning which accompanies a magnetospheric substorm.

A second example of such a sequence of events is shown in figure 3.13 which represents the E-t spectrogram for day 114, 1979. These data were collected at high-bit rate, providing enhanced coverage of each plasma regime encountered. At approximately 11:00 ISEE 1 sampled the CPS, as indicated by the isotropic ion responses in the upper four panels of the spectrogram. The energy range of the ions spans from 100 eV to 45 keV. By about 11:15 the spacecraft had abruptly entered the lobe region ($E \leq 1$ keV), where it remained for about half an hour. The PSBL is not easily distinguished in the crossing from CPS to lobe. However, the PSBL was distinctly encountered just after 11:30, as evidenced by the anisotropic ion distributions ($E \geq 10$ keV) at this time.

It is clear from the E-t spectrogram that a coarse survey of the plasma regimes sampled by a satellite is possible; however, greater detail is desired for more accurate analyses. Such detail is available from the energy-phase angle spectrogram format, as illustrated below. Data for the E- ϕ spectrograms of figures 3.7, 3.8, and 3.9 were collected at high-bit rate, consequently each instrument cycle required 128 seconds to complete. Figure 3.7(a) is the E- ϕ spectrogram corresponding to the beginning of the sequence of events described in the discussion of the E-t spectrogram for day 114, 1979, hour 11. The start time

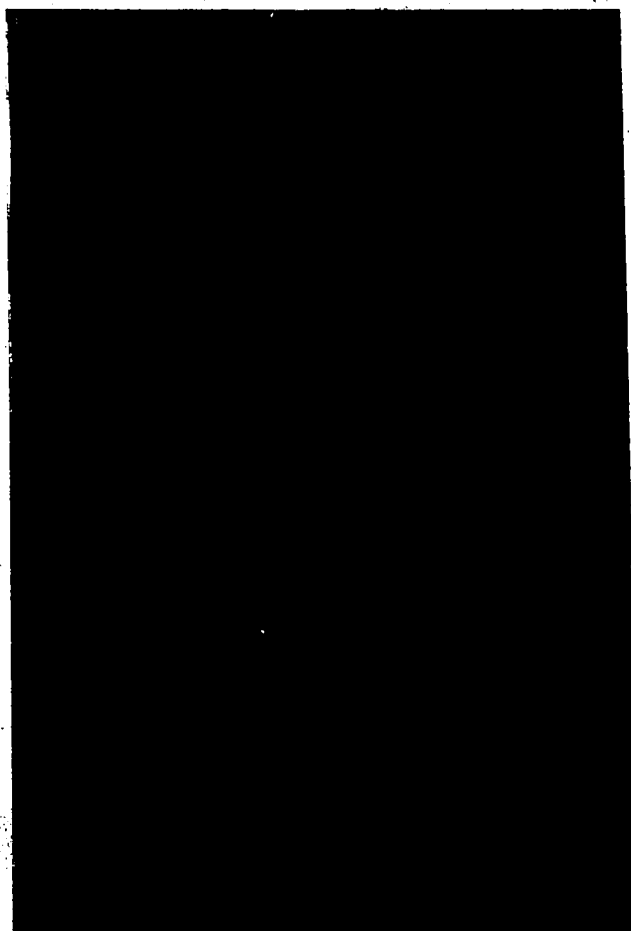


Figure 3.13 Energy-time spectrogram for day 114 (April 24), 1979.

for the spectrogram is 11:08.54 UT. This set of frames indicates that ISEE 1 was situated within the CPS, which, as in the E-t display, is characterized by generally isotropic ion and electron distributions ($100 \text{ eV} \leq E_{\text{ions}} \leq 45 \text{ keV}$, $E_{\text{electrons}} \leq 10 \text{ keV}$). The detector responses are nearly independent of azimuth and altitude for both species of particles.

In figure 3.7(b) (start time of 11:11.02), anisotropies become evident especially in the electron distributions for detectors 3E, 4E and 5E. Particle intensities in the Earthward and anti-Earthward directions dominate these frames, and such bi-directional flows are indicative of a PSBL encounter. Most of the ions with energies $\leq 1 \text{ keV}$ seen in the previous frame are no longer evident, with only the higher energy ions being observed.

By 11:17.25 (figure 3.8(a)) the distinctly low intensity of both ions and electrons indicates that the spacecraft has entered the lobe. Essentially no ions are observed at the energies displayed on the E-t spectrogram; however, soft, anisotropic electron spectra ($E \leq 1 \text{ keV}$) are evident. Note the enhancement of low energy electrons in frame 5E resulting from the spacecraft-instrument configuration, as mentioned previously. The satellite is still situated within the lobe at 11:38.43, as shown in figure 3.8(b), which is unchanged in character from the previous set of frames in figure 3.8(a).

At approximately 11:45.60 (figure 3.9), ISEE 1 re-encounters the PSBL as indicated by anisotropic distributions particularly evident in the ion response frames where high energy ions ($E \geq 10$ keV), are observed flowing primarily in the Earthward direction. The electrons, as well, are anisotropic in nature. Hence, it is clear from this discussion that the $E-\phi$ representations of the energetic particle data provide considerable information for detailed event analyses, as evidenced by the appearance of the PSBL signature at 11:11.02 which was not visible in the corresponding $E-t$ spectrogram.

3.7 Measurement of the IMF and Solar Wind Plasma Parameters

The ISEE 3 instrumentation includes a Vector Helium Magnetometer (VHM) which made continuous observations of the interplanetary magnetic field near one A.U. while the satellite was in its halo orbit (see Frandsen et al., 1978). The magnetometer sensor is mounted at the end of a three meter boom to remove it from on-board sources of interference. It measures three steady state components of the ambient magnetic field in spacecraft coordinates, and from these, the total field magnitude is calculated.

IMF magnetic field measurements are published in the Interplanetary Medium Data Book - Supplement 3A (Couzens and King, 1986). These data were obtained not only from ISEE 3 (until June of 1982) but also from ISEE 1 (when it's orbit passed through the solar wind) and from the satellite, IMP J

(IMP 8). The latter spacecraft was placed in a geocentric orbit of low eccentricity with major and minor axes of approximately 40 and 30 R_e respectively, and with an orbital period of 12.5 days. Six to eight days of each IMP J orbit were spent within the solar wind. When both ISEE 3 and IMP J measurements are available for a given interval of time, the IMP J data are used since IMP J was situated closer to the Earth than was ISEE 3 while in its halo orbit. However, ISEE 3 data were preferentially chosen to ISEE 1 observations due to the availability of additional parameters measured by ISEE 3.

The Interplanetary Medium Data Book tables include hourly averages of the following quantities: the total magnetic field (nT), the three components of \bar{B} (nT) in the GSM coordinate system, solar wind bulk speed (km/sec), solar wind density (cm^{-3}), and solar wind temperature (1000 °K). As well, specification of the satellite used to obtain each average is given. The parameter of greatest interest to this study is the magnitude of the IMF B_y component which has been correlated with the magnitude of the tail B_y in order to study the concept of IMF B_y penetration.

3.8 The Auroral Electrojet Indices

The term "Auroral Electrojet Indices" (Davis and Sugiura, 1966), incorporates a set of four indices denoted by AU, AL, AE and AO, which together provide a quantitative measure of the global electrojet activity in the auroral

zone as a function of Universal Time. These indices are derived from the horizontal component (H) of variations in the geomagnetic field at roughly one dozen ground-based observatories located within the auroral zone in the northern hemisphere. The location of these stations is shown in figure 3.14. The AU index represents the largest value of the horizontal magnetic component from all the stations for each sampling interval, whereas the AL index signifies the lowest value recorded. For a given time interval, therefore, both an upper and lower envelope are defined from a superposition of the H plots obtained from all the ground-based magnetic observatories. The AE index proper, is derived by taking the difference between the AU and AL indices, whereas the AO index represents the mean value of AU and AL.

Physically, the AU and AL indices represent the magnitudes of the strongest current densities of the eastward and westward auroral electrojets, respectively. In the ideal situation of infinite ground-based spatial coverage, the AU and AL envelopes would represent at each epoch the maximum positive and negative deviations of the H component which occur in the auroral oval. Stations to the east of midnight contribute the most to the AL index whereas those west of midnight contribute to the AU index. The AE index provides a measure of the overall electrojet activity level, or the total maximum amplitude of the eastward and westward electrojets. The AO index is considered to be a

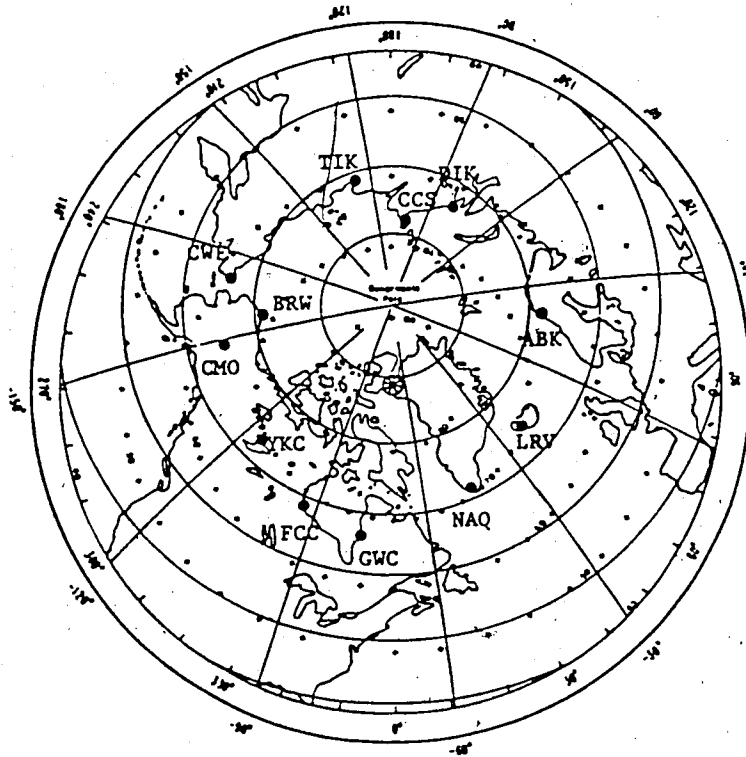


Figure 3.14 Distribution of the 12 geomagnetic observation stations from which northern-hemisphere AE data are gathered.

measure of the equivalent zonal current.

The auroral electrojet indices are processed by the World Data Center C2 for Geomagnetism and published in a series of Auroral Electrojet Indices Data Books (Kamei and Maeda; 1981, 1982). The electrojet data are presented either in tabular or graphical format. Four tables are compiled for each month, one corresponding to each of the four electrojet indices. Values of hourly averages, calculated from all available data from all stations, are recorded. The graphical presentation is displayed in figure 3.15(a) which shows the auroral electrojet activity for day 39, 1979, corresponding to the E-t spectrogram of figure 3.6. Values of the four electrojet indices, AU, AL, AE, and AO, are plotted (in units of nT) as a function of Universal Time.

A rise in the magnitude of the AE index is indicative of the onset of a magnetospheric substorm, and alternately, a decrease in AE signifies the beginning of the recovery phase. By this definition, substorm onsets are observed to occur in figure 3.15 (a) at approximately 9:45, 16:00 and 23:00, UT. The substorm event beginning at 9:45 and ending at about 10:45 corresponds to the passing of the ISEE 1 spacecraft from the CPS to the PSBL and then to the lobe, and back to the CPS via the PSBL (as discussed in section 3.3) and this is indicative of the plasma sheet thinning during a magnetospheric substorm. The dropout at the start of the event sequence is very rapid, consequently the PSBL signature is not observed in the E-t spectrogram. A similar

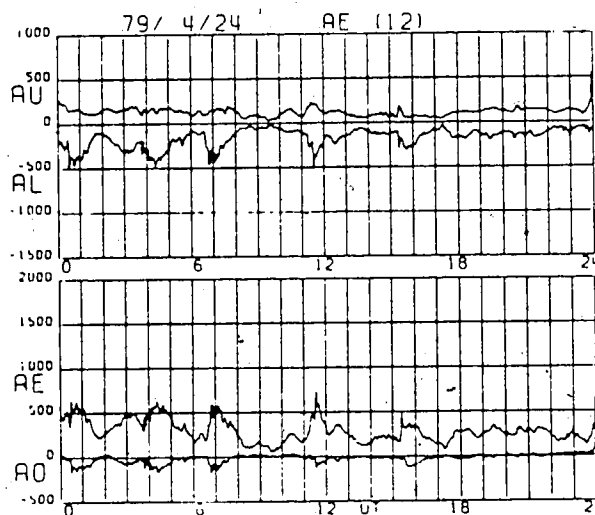
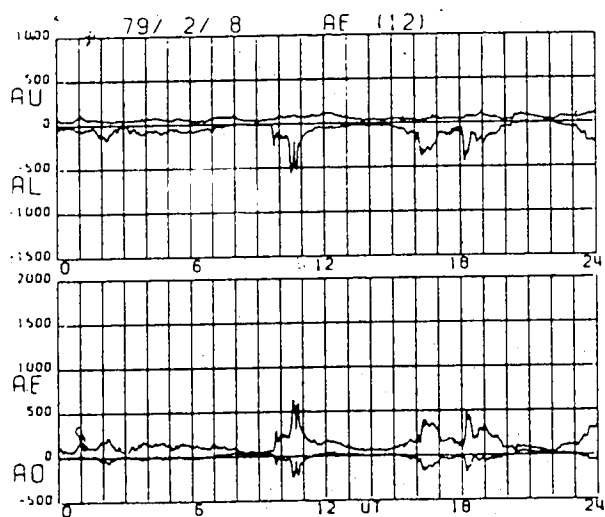


Figure 3.15 Auroral electrojet activity levels, AU,AL,AE,AO, measured in units of nT and displayed graphically as a function of Universal Time for (a) day 39 (February 8), 1979, and (b) day 114 (April 24), 1979.

interpretation may be made for day 114, 1979, hour 11 when the corresponding activity records are incorporated in the analysis (see figure 3.15(b)).

The absence of the substorm signature on the auroral electrojet magnetograms is not necessarily a definitive indication of geomagnetic quiescence. When magnetic activity is high, the auroral oval expands southward, often beyond the detection range of the magnetic observatories, and as a result, the associated substorm may not be evident in the AE index. Similarly, substorms often are rather localized events and if one occurs at a location not directly above any of the magnetic observatories, the variations in the H component at the recording stations may be small, therefore indicating a low level of activity. Consequently, although a sharp rise in AE is always indicative of substorm activity, the absence of the substorm signature does not always signify low activity, since a localized event may be taking place, or alternatively, since the auroral oval may have expanded out of the range of the observing stations.

Chapter 4

Statistical Studies Involving B_y

The initial research for the ensuing studies of the cross-tail component of the magnetospheric magnetic field entailed a systematic and comprehensive investigation of the magnetograms constructed from *in situ* observations made by ISEE 1. Of primary interest to these studies is the region of the tail between 10 and 23 R_E behind the Earth and containing the CPS, PSBL and tail lobe regimes. The satellite traversed this spatial domain predominantly from mid-January to mid-June in both 1978 and 1979. Magnetograms in GSE coordinates corresponding to times during which the spacecraft was located within this domain were examined.

The magnetic field signatures of the CPS, PSBL and lobe, according to the present models and applicable to distances downtail between 10 and 23 R_E , were outlined in section 3.3. Using the magnetic signatures as a guideline, the 1978 and 1979 ISEE 1 magnetograms were analysed by comparing observed magnetic signatures with those expected from the statistically derived magnetospheric models. In addition, an attempt was made in the analyses to identify the magnetotail plasma regime being sampled by the spacecraft. Both magnitude and polarity of mainly the B_x and B_y magnetic field components, as well as the characters of the field traces, were considered in the plasma domain specification. PSBL and neutral sheet encounters were of particular importance in studying the magnetograms.

From preliminary consideration of the magnetograms alone, without reference to the corresponding energetic particle data, it was frequently observed that the simultaneous traces of the three magnetic field components together did not identify a distinct plasma regime, the observed traces collectively indicating signatures which do not conform with those outlined in the statistically derived models. The failure of any one of the three magnetic traces to fit the standard patterns suggests that physical processes, of which the atypical signatures are a consequence, are ongoing in the tail that have not been accounted for in the statistical models. Identification of such discrepancies, as well as explanations for their occurrence, is essential in order for a more precise, unified model of the magnetosphere to be constructed.

One prominent example of magnetotail field component traces contradicting the average and expected patterns concerns the cross-tail component, B_y , sampled when ISEE 1 appears to be in the vicinity of the neutral sheet as defined by a polarity reversal in the B_x component. Ideally, a neutral sheet encounter is identified by a change in polarity of the B_x component, accompanied by a simultaneous change in polarity of the B_y component. However, the B_y component frequently exhibits a non-zero magnitude at a time coincident with a change in polarity of the B_x component, and this is in conflict with the present models. Cases of non-zero B_y at an "apparent" neutral sheet encounter were

observed to follow two patterns. In the first situation non-zero B_y appears unchanged across the neutral sheet. In the second scenario, a baseline shift seems to occur such that if the zero baseline of B_y was shifted either positively or negatively by a specific amount, the apparent neutral sheet crossing would be accompanied by the B_y behaviour expected according to the statistical models.

The second phase of research involved a comparison of the magnetograms with the corresponding energetic particle spectrograms, the intent being to verify the magnetogram interpretations. The energetic particle signatures for the plasma regimes of interest were discussed in section 3.5. Through a comparative analysis of the two data sets, it became evident that frequently the plasma regime suggested by the magnetogram was in contradiction with that indicated by the particle data. Often, the magnitudes and characters of the traces for each of the magnetic field components did not agree with those expected from the model for the plasma regime specified by the spectrograms. The frequency of disagreement between the two data sets was significant, indicating further that the statistically derived models of the magnetotail do not adequately incorporate deviations from the average configuration of the magnetosphere. The existence of such deviations requires that the present models be updated to provide consistency between the various sets of observations. As well, processes which statistically occur infrequently enough to be neglected in a general

picture of the tail nevertheless play a significant role in magnetospheric dynamics and must be included in the models.

An important issue is raised by the occurrence of discrepancies such as described above: can either of the two data sets be reliably used to identify the correct plasma regime being sampled by the satellite? Furthermore, can the discrepancies between the predictions of plasma regime being sampled, from the particle and magnetic field data, be reconciled? In the following sections, the usefulness of both the energetic particle and magnetic field data sets will be discussed in this regard. As well, the primary discrepancies which were observed between magnetic field component traces on a given magnetogram will be investigated.

4.1 Use of Energetic Particle Spectrograms for Identification of the Plasma Regime Being Sampled

That the magnetosphere was composed of a number of distinct plasma regimes was determined through the detection of energetic particles with varying characteristics in different spatial domains. As a prime example, the existence of the PSBL was inferred through study of energetic particle observations (Eastman et al., 1985a). The distinctive set of criteria outlined in section 3.5, according to which the CPS, PSBL and tail lobe regimes may be clearly differentiated, are for the most part, diagnostic. Since the plasma regimes incorporated into the magnetospheric models

are each defined according to such a set of energetic particle signatures, the energetic particle spectrograms necessarily provide sufficient information to identify precisely the plasma regime being observed by the satellite.

In practice, the analysis of an energetic particle spectrogram is not in every case straightforward since particle distributions sometimes appear quite complex rather than conforming with the typical characteristics of a given domain. In such instances, a careful investigation of the spectrograms in conjunction with various other plasma data sets (such as observations obtained through the noise and APL fast particle experiments, both on ISEE 1), may be required in order to obtain a reliable interpretation. However, the majority of spectrogram analyses are straightforward and the plasma regime being sampled is definable with a high degree of certainty. In the 1978/1979 data set applicable to the present studies, the number of one-hour intervals during which ISEE 1 was clearly situated within one of the CPS, PSBL or tail lobes, according to the energetic particle signature definitions, approaches 2000. Therefore, despite the existence of occasional events which are difficult to interpret, the energetic particle spectrograms generally provide an unambiguous determination of the plasma regime being sampled by the satellite.

Such reliability of a data set is an important consideration regarding accurate plasma regime identification. Since no obvious irregularities have been

encountered in the particle spectrogram investigations, and furthermore, since contradictory interpretations of the $E-t$ and $E-\phi$ spectrogram representations have not been observed, energetic particle spectrograms may be reliably employed in determining the plasma regime being traversed by the observing satellite. Consequently, the identification of plasma regimes based on analysis of the energetic particle spectrograms will be considered as definitive in the following studies.

4.2 The Inadequacy of Employing Magnetic Field Data Alone for Magnetotail Plasma Regime Identification

In order for the magnetic field data to be used independently for determining the plasma domain being sampled by the satellite, a sufficient set of diagnostic criteria is required according to which an unambiguous identification may be made. Furthermore, the plasma domain defined by the magnetic signatures must be in agreement with the domain suggested by the coincident plasma data. It will be shown in this section that no such set of magnetic criteria can, in fact, be compiled. The inability of the magnetic data to provide accurate identification of the plasma regime being sampled by the satellite is the focus of this section, and it will be studied here using a statistical approach.

4.2.1 Data Selection Criteria

The following criteria for data selection were employed to obtain a consistent and reliable data set. The energetic particle spectrograms (E-t format) were first scanned to select intervals of time, each of approximately one hour in duration, for which the satellite was situated in one of the CPS, PSBL or lobe for the entirety of the hour or majority thereof (≈ 45 minutes or more). The indication of plasma regime being sampled, according to the particle signatures, was assumed as definitive. For each hour selected, the position of the spacecraft in GSE coordinates, hourly averages of the three GSE magnetic field component magnitudes, as well as the corresponding hourly averages of IMF B_y , IMF B_z , and AE index were tabulated. Hourly averages of both B_x and B_y were obtained by determining the respective field component magnitudes at five minute intervals from the GSE magnetograms from which the mean values were calculated. Hourly averages of the IMF were obtained from the Interplanetary Medium Data Book (Couzens and King, 1986). Because hourly averages are employed, transient or short temporal effects of much less than one hour in duration necessarily remain unaccounted for in the following statistical studies.

A total of 1075 data points for 1978 were collected according to the above selection process, and 790 were tabulated for 1979, providing a combined set of 1865 points. Only hours for which both magnetic and plasma data were

available were included. AE values were available for all hours selected, however, IMF data were not available for a large portion of 1978 and some hours in 1979. The hours for which the IMF data were not available were nevertheless included in the data set. Only hours during which ISEE 1 was located between -10 and -23 Re downtail were considered. In the cross-tail direction any values of Y were acceptable providing that the satellite was not encountering the LLBL, and similarly, all Z values were acceptable for which the magnetospheric boundary layer or the interplanetary magnetic field were not being sampled. Limits to both these coordinates, therefore, are variable, depending on temporal changes in magnetotail structure.

Several comparisons were considered in attempting to decide upon criteria from the magnetic field data which could be used to accurately determine the plasma regime being sampled. A description of each study and the subsequent results are given below.

4.2.2 $|B_x|$ as a Function of Downtail Distance

The first study attempts to define whether or not a relationship exists between the magnitude of the B_x component and distance downtail of the observing satellite. A series of seven plots are shown to illustrate not only the variation of $|B_x|$ with X for the plasma domains of the CPS, PSBL and lobe, but also to indicate the spatial sampling range of ISEE 1.

Figure 4.1 displays all data available for 1978 and 1979 (1865 points), as chosen by the criteria outlined above, whereas figures 4.2, (a) and (b), show the data for years 1978 and 1979, respectively. During the two years the northern hemisphere received greater coverage than did the southern hemisphere (1581 positive B_x vs. 265 negative B_x measurements). This is a consequence of the satellite orbit which resulted in preferential sampling of the northern regions of the tail, particularly in 1978. (Note that 19 points for which $|B_x|=0$ nT are not included in either hemisphere). Recall that the inclination of the orbital plane with respect to the ecliptic plane decreased from about 23° in 1978 to approximately 15° in 1980 (Dandouras et al., 1986). Hence, during 1979 southern hemisphere coverage was greater than during 1978 (235 vs. 30 points). This is evident from figures 4.2 (a) and (b). The general absence of points, then, for large X and negative B_x represents uneven satellite coverage and does not have any further interpretable significance. This must be kept in mind when analyzing the remaining B_x vs. X graphs, and it is perhaps more meaningful to base any conclusions on the northern hemisphere data alone. It is noteworthy also that the nature of the plotter is such that if several points occur with identical ordinate and abscissa values, only one point appears on the graph. Hence, it is not possible to comment on the density of points, since one point may in fact represent several samplings.

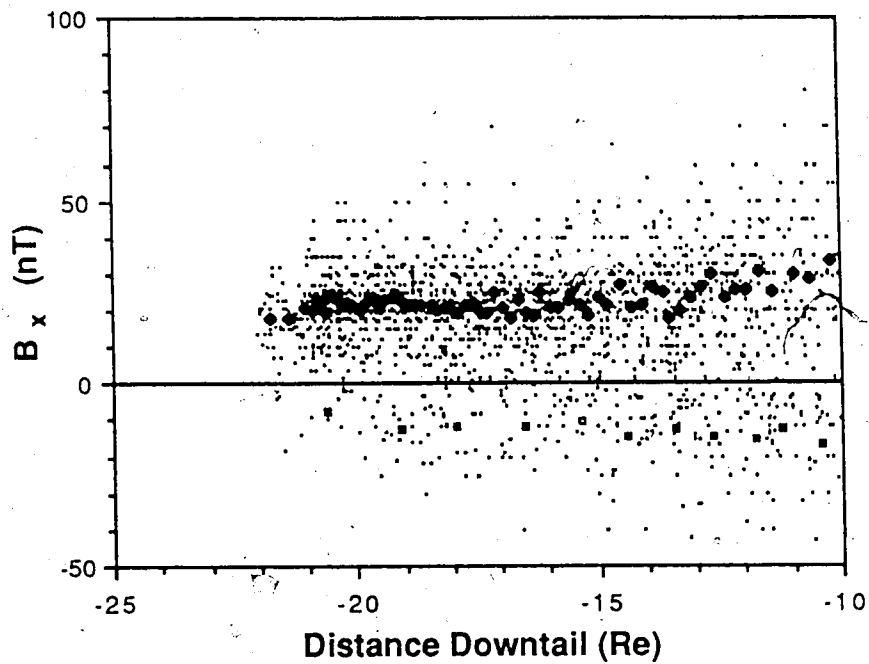


Figure 4.1 Values of B_x plotted as a function of distance downtail for all measurements tabulated in the 1978/1979 data set.

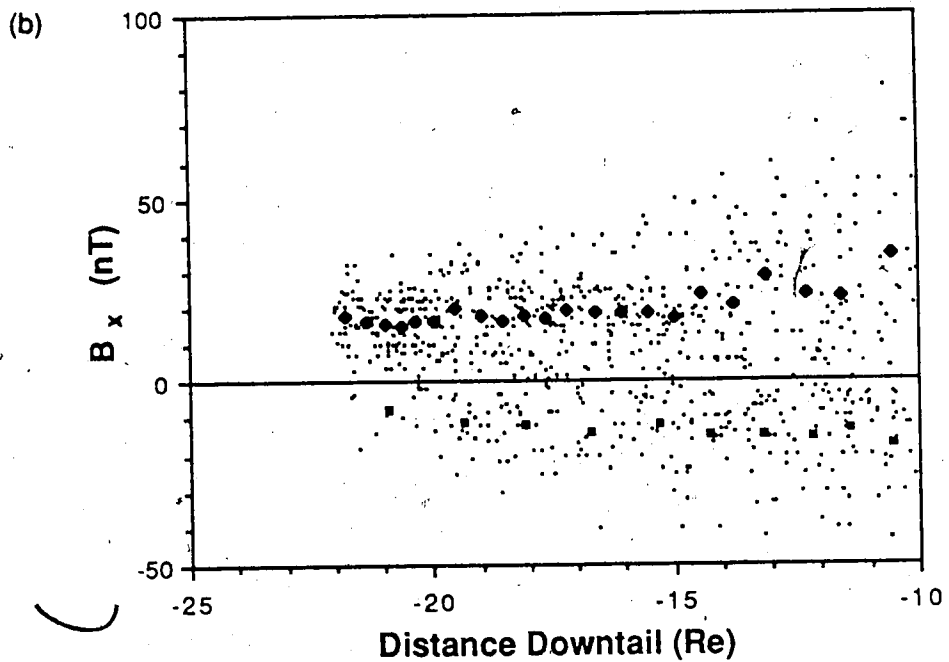
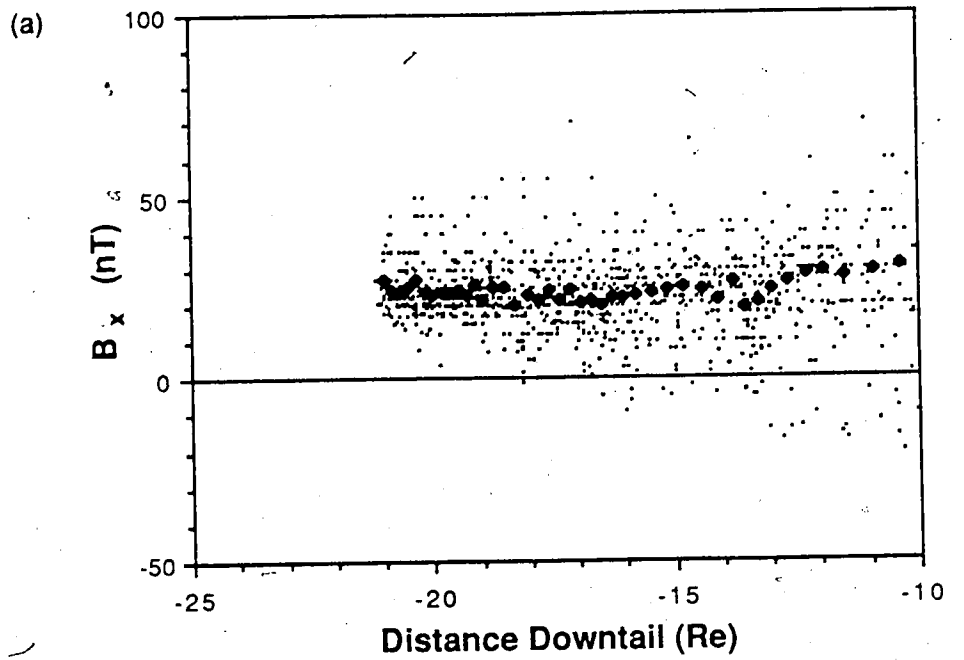


Figure 4.2 Same as figure 4.1 but (a) for 1978 data only, and (b) for 1979 data only.

A second observation may be made from figures 4.1 and 4.2 concerning the overall distribution of points. Considering primarily data for the northern hemisphere, it is evident in figure 4.1 that $|B_x|$ is approximately constant for all values of the X coordinate. Quantitatively, this statement is justified by the trend apparent in the distribution of the bold diamonds in this figure: Each diamond represents the mean value of 25 northern hemisphere B_x measurements, selected consecutively according to the magnitude of the X coordinate. Note that this averaging technique takes into account all raw data points, therefore, although several measurements of one (X, B_x) pair may only appear as one point on the scatter plot of the raw data, such multiple samplings will be accounted for in the averaging process. Since the mean values for the northern hemisphere fall in a roughly horizontal band of limited thickness, it can be concluded that the range of B_x magnitudes observed is relatively independent of distance downtail between -10 and -23 Re. Similarly, 25-point B_x averages for the southern hemisphere data are indicated in figure 4.1 by the bold squares. Here, as well, $|B_x|$ is also roughly constant for all X values.

In the raw data for both hemispheres, there is a slight tendency for large B_x to occur closer to the Earth, but this is expected since the magnitude of the geomagnetic dipole field maximizes at the Earth's surface (specifically, at the poles), and decreases as the inverse of the cube of the

radial distance from the surface. Near the Earth the contribution from the dipole field dominates the magnetic observations, whereas, farther downtail the contribution to the field due to the cross-tail current becomes more dominant. Since the field due to the cross-tail current does not decrease in magnitude with increasing downtail distance at the same rate as does the dipole contribution, a leveling off in the magnetic field magnitude observed by ISEE 1 is expected, and this is reflected in figure 4.1. However, according to the figure, it appears that the total field has already become dominated by the tail field by $-10 R_E$ downtail and that the effect of the dipole is minimal at this distance.

In figure 4.2 (a) the lack of data for large X and small β_x in the northern hemisphere is satellite orbit dependent. Since ISEE 1 crossed from high northern altitude at apogee to low southern altitude at perigee, it sampled the lobe most frequently when situated farther downtail, and the CPS at locations closer to the Earth. This of course assumes, according to the statistical models, that small values of B_x are expected to be observed mainly in the CPS, especially since $|B_x|$ is small in the vicinity of the neutral sheet. Taking into account only the northern hemisphere data, no distinct increase in $|B_x|$ towards the Earth is apparent. This is again illustrated quantitatively by the relatively constant magnitude of the 25-point averages of B_x values shown by the bold diamonds. In

contrast, the 25-point averages of the northern hemisphere 1979 data, represented by the bold diamonds in figure 4.2 (b), indicate a slightly more noticeable decrease in $|B_x|$ for larger values of X . Once more, this result may be explained in terms of satellite orbit. Since in 1979 the plane of the ISEE 1 orbit shifted to a lower altitude, the CPS would be sampled more frequently near apogee in 1979 than in 1978. The mean of northern hemisphere measurements of B_x for the 1979 data is 20.2 nT which is somewhat lower than the 1978 mean of 24.1 nT. Finally, since little of the 1978 data corresponds to southern hemisphere samplings, the 1979 southern hemisphere data can be interpreted as per figure 4.1.

Consider next plots of B_x vs. X for each of the three plasma regimes of interest in this work. Both 1978 and 1979 data are combined for each region and graphed in figures 4.3, (a) and (b), and 4.4, which display the CPS, PSBL and lobe data, respectively. For figures 4.3 (b) and 4.4, only the data available for the northern hemisphere will be analysed, since southern hemisphere coverage of the PSBL and lobe is not sufficient for reliable analysis.

In figure 4.3 (a) the distribution of northern hemisphere CPS B_x values remains approximately constant for all X , and this is verified by the trend evident in the 25-point B_x averages (again, represented by bold diamonds) which lie in a distinctly horizontal band. The mean B_x for the northern hemisphere CPS as a whole is 16.8 nT. Most

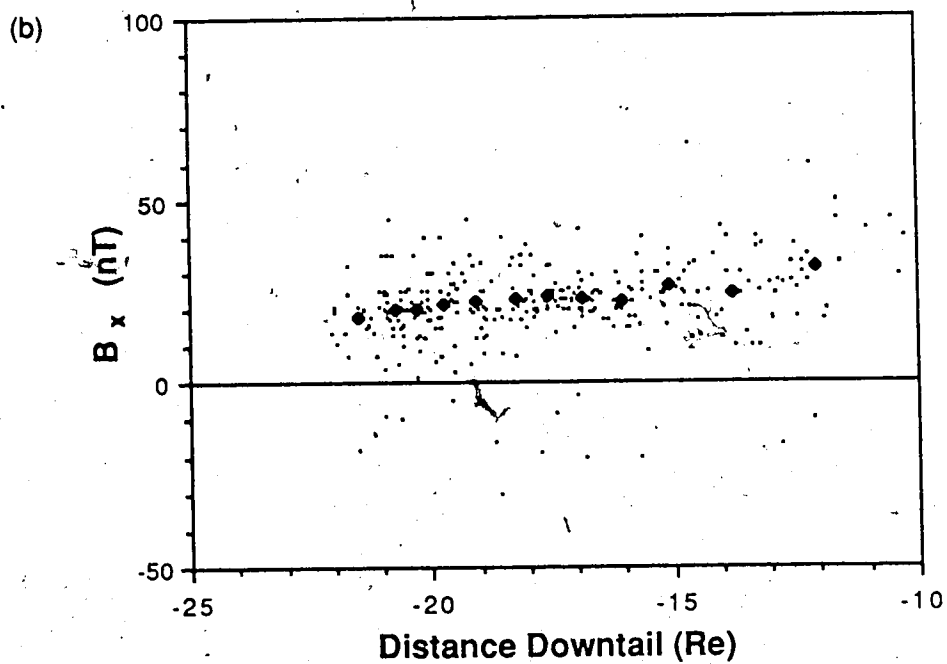
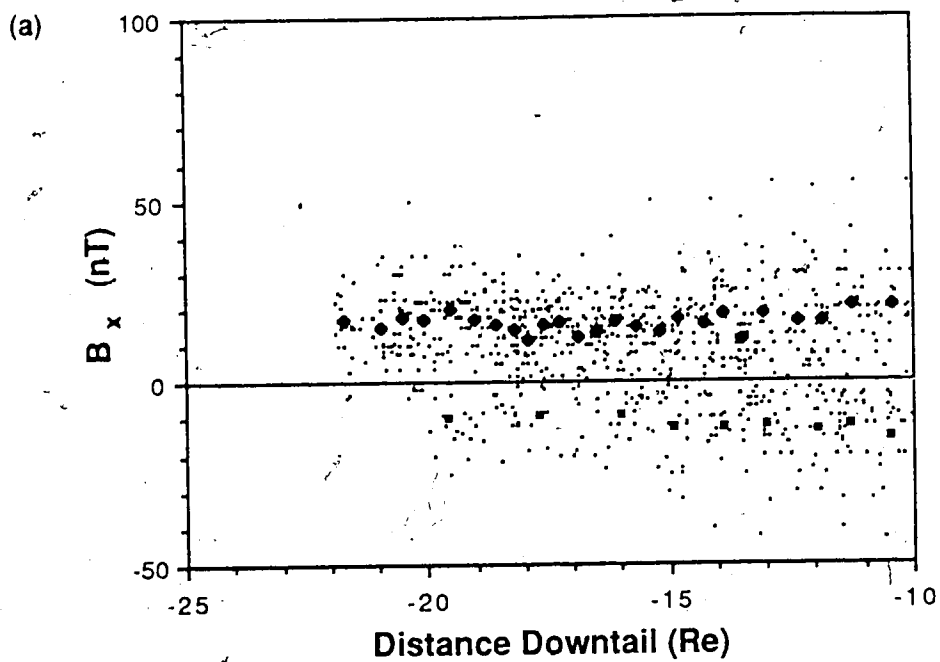


Figure 4.3 Scatter plots of B_x as a function of distance downtail for all samplings of (a) the CPS and (b) the PSBL from the 1978/1979 data set.

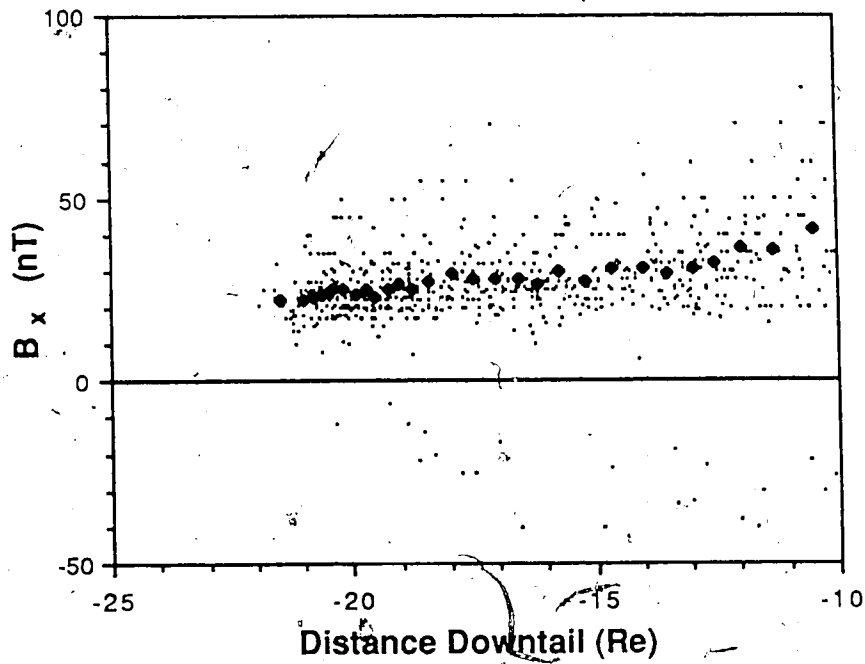


Figure 4.4 Same as figure 4.3 but for samplings of the tail lobes.

points ($\approx 95\%$) lie in the range of $0 < B_x < 35$ nT. Several points with B_x values between 35 and 60 nT are observed and these mainly occur towards smaller values of $|X|$. The existence of many very low B_x values indicates the frequency of neutral sheet encounters. The southern hemisphere CPS data comprise the majority of the 1978/1979 southern hemisphere measurements, and hence, their interpretation corresponds to that of the southern hemisphere data in figure 4.1 (the mean B_x value for the southern hemisphere CPS is -11.6 nT, which differs slightly from that for the entire 1978/1979 data set).

Similarly, figure 4.3 (b), representing PSBL samplings, does not indicate a significant increase in $|B_x|$ as $|X|$ decreases. For this plasma regime, $\approx 95\%$ of the B_x measurements lie in the range $0 < B_x \leq 40$ nT, with the remainder of measurements (with magnitudes up to 65 nT) occurring primarily towards smaller $|X|$. The 25-point averages of northern hemisphere B_x show a slight increase in magnitude towards lower values of $|X|$, with the overall mean northern hemisphere B_x value being 23.3 nT. From the raw data, it is also apparent that the PSBL is encountered less frequently closer to the Earth, and this is a direct consequence of satellite orbit.

Finally, the plot of B_x vs. X for the lobe regime (figure 4.4), indicates that the majority (95%) of values of B_x lie within the range of $15 < B_x < 55$ nT. As well, all values within this range may occur at any distance between 10 and

23 Re downtail. However, as is shown by the 25-point northern hemisphere B_x averages (represented by bold diamonds) there is a slight tendency for larger B_x values to occur closer to the Earth, and as with the PSBL, the lobe also appears to be sampled less frequently nearer the Earth. The overall mean B_x value of the northern hemisphere lobe for the 1978/1979 data set is 27.9 nT.

The main conclusion which can be drawn from figures 4.3 and 4.4 is that there exists a range of B_x values which occurs at all downtail distances between -10 and -23 Re and in all three plasma regimes. Considering the northern hemisphere only, values of $15 \leq B_x \leq 35$ nT are encountered by ISEE 1 in each of the CPS, PSBL and lobe and at all sampled distances downtail. For the northern hemisphere, 57% of all CPS measurements, 80% of all PSBL samplings and 83% of all lobe values fall within this range. This strongly implies that it is impossible to determine which plasma regime is being sampled by the satellite on the basis of $|B_x|$ alone. In both the CPS and the lobe the magnetic field character is typically smooth; hence, when a value of B_x between 15 and 35 nT is encountered there is no criterion available from the magnetic traces by which to distinguish the two regions. In addition, although the presence of short period magnetic fluctuations may be the distinguishing factor between the PSBL and CPS or lobe when B_x lies in the 15 to 35 nT range, the fluctuating or noisy character is often absent in a PSBL magnetic trace, frequently due to the rapid passing of the

spacecraft through this regime. Consequently, based on magnitude and character of B_x , the plasma regime being sampled cannot uniquely be identified.

4.2.3 $|B_x|$ and $|B_y|$ as Functions of AE

An interesting observation is evident in figure 4.3 (b) which involves the existence of very low magnitudes of B_x occurring at various downtail distances. Small values of B_x (≤ 10 nT) are indicative of the neutral sheet region, and hence, of the CPS. What process or set of circumstances can produce values of northern hemisphere $B_x \leq 10$ nT in the PSBL? As well, several B_x values with small magnitudes (≤ 10 nT) also occur in the lobe (figure 4.4), and this is not typical according to the statistical magnetospheric models.

As discussed in section 3.8, substorm activity may be associated with perturbations of the normal plasma sheet configuration. Can such activity result in atypical values of B_x being observed in the PSBL as well as the lobe? An investigation of activity level with respect to the B_x component was conducted in order to determine whether or not a correlation exists between activity level and unusually low values of B_x in these two plasma regimes.

Figure 4.5 presents all AE data from both the northern and southern hemispheres in 1978 and 1979, graphed as a function of corresponding B_x values. The AE data were binned into intervals of 50 nT, and each AE datum was plotted at the midpoint of its respective bin (ie: as a multiple of

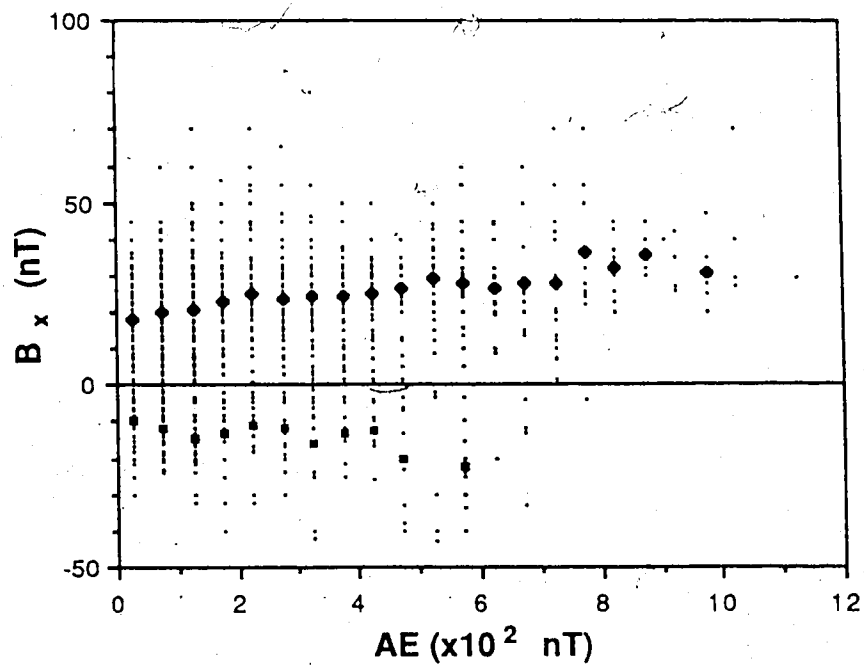


Figure 4.5 1978 and 1979 B_x measurements plotted as a function of the AE index.

25 nT), rather than as a raw measurement. The mean values of both northern and southern hemisphere B_x measurements for each 50 nT interval of AE were separately computed, and these are indicated by bold diamonds in the northern hemisphere, and by bold squares in the southern hemisphere. Averages were only computed for AE bins in which more than 5 values of B_x were recorded.

In each hemisphere the mean values of B_x exhibit a slight increase in magnitude as $|AE|$ increases. Considering the northern hemisphere data alone (since southern hemisphere coverage is less complete) the occurrence of very high AE appears to correspond to a limited range of $+B_x$. The significance of this exception is inconclusive due to the low frequency of occurrence of high AE values, as seen in figure 4.6, which displays the occurrence frequency of AE values, grouped into 50 nT bins, for the entire 1978/1979 data set. 51.4% (959 values) of the AE observations have magnitudes ≤ 150 nT, 31.2% (582 values) have magnitudes in the range $150 < AE \leq 400$ nT, and the remaining 17.4% (324 values) of the AE values exhibit magnitudes > 400 nT. These three divisions will be considered in this work to represent low, intermediate and high activity ranges, respectively. Consequently, since high activity measurements comprise the minority of AE observations, perhaps a larger data set is desirable in order to determine whether very high activity corresponds to all observed values of B_x (as is the case with the low and medium activity levels), or only to higher

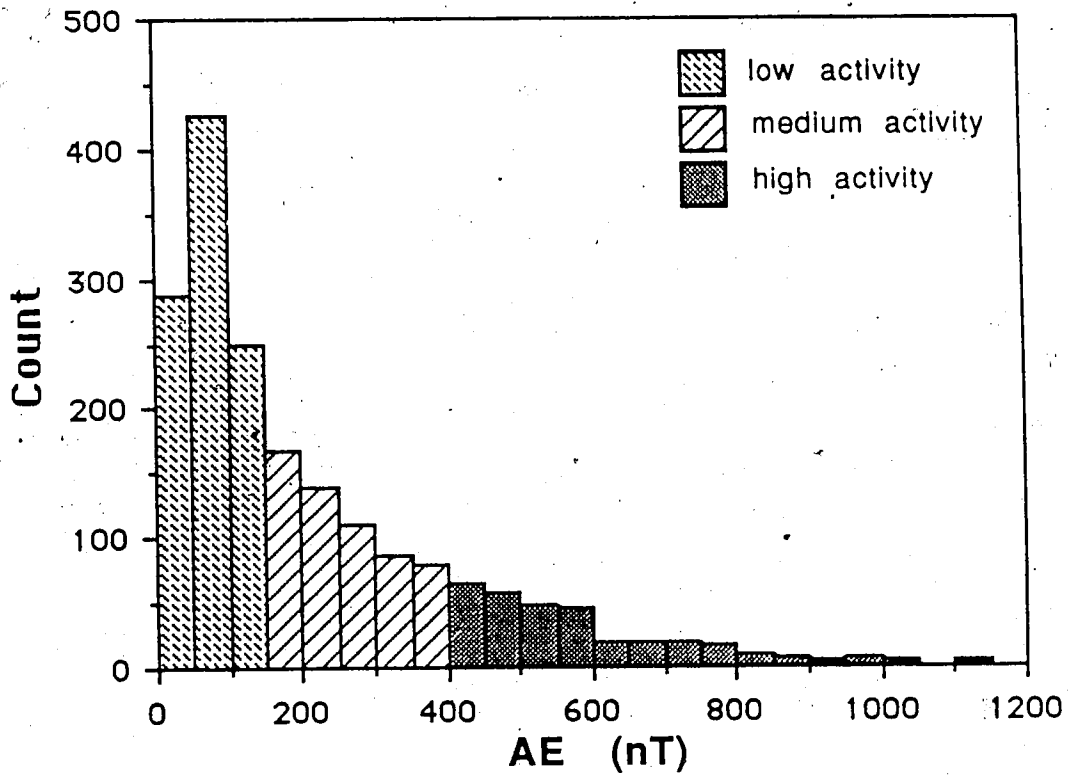


Figure 4.6 Histogram of all AE measurements from the 1978/1979 data set. Three categories of low ($AE \leq 150$ nT), intermediate ($150 < AE \leq 400$ nT), and high ($AE > 400$ nT) activity level are indicated.

B_x magnitudes.

Figures 4.7, (a) and (b), and figure 4.8 illustrate activity level as a function of B_x for the CPS, PSBL and lobe regimes, respectively. The bold diamonds in each of these figures represent the mean value of B_x in each 50 nT AE interval for the northern hemisphere whereas the bold squares in figure 4.7 (a) represent southern hemisphere mean values in each AE bin. (Southern hemisphere PSBL and lobe means have not been computed due to inadequate data coverage in these regimes). Again, means were only calculated for AE bins in which there were more than 5 B_x measurements. In the CPS and PSBL, the mean values of B_x remain approximately constant for all levels of magnetospheric activity. Consequently, the magnitude of B_x in the CPS and PSBL regimes appears to be independent of the magnitude of the AE index, since all levels of AE (ie: low, intermediate, and high) coincide with samplings of these two plasma domains. However, in the lobe a slight trend towards increasing B_x magnitudes with larger values of AE is evident, as was seen in figure 4.5 for the northern hemisphere measurements.

Finally, because all levels of activity (as defined by figure 4.6) are observed to coincide with the unusually low B_x values in the PSBL and lobe, it cannot be concluded that perturbations of the plasma sheet during substorm activity (indicated generally by high AE) are the cause of measurements of low B_x magnitude in these plasma regimes.

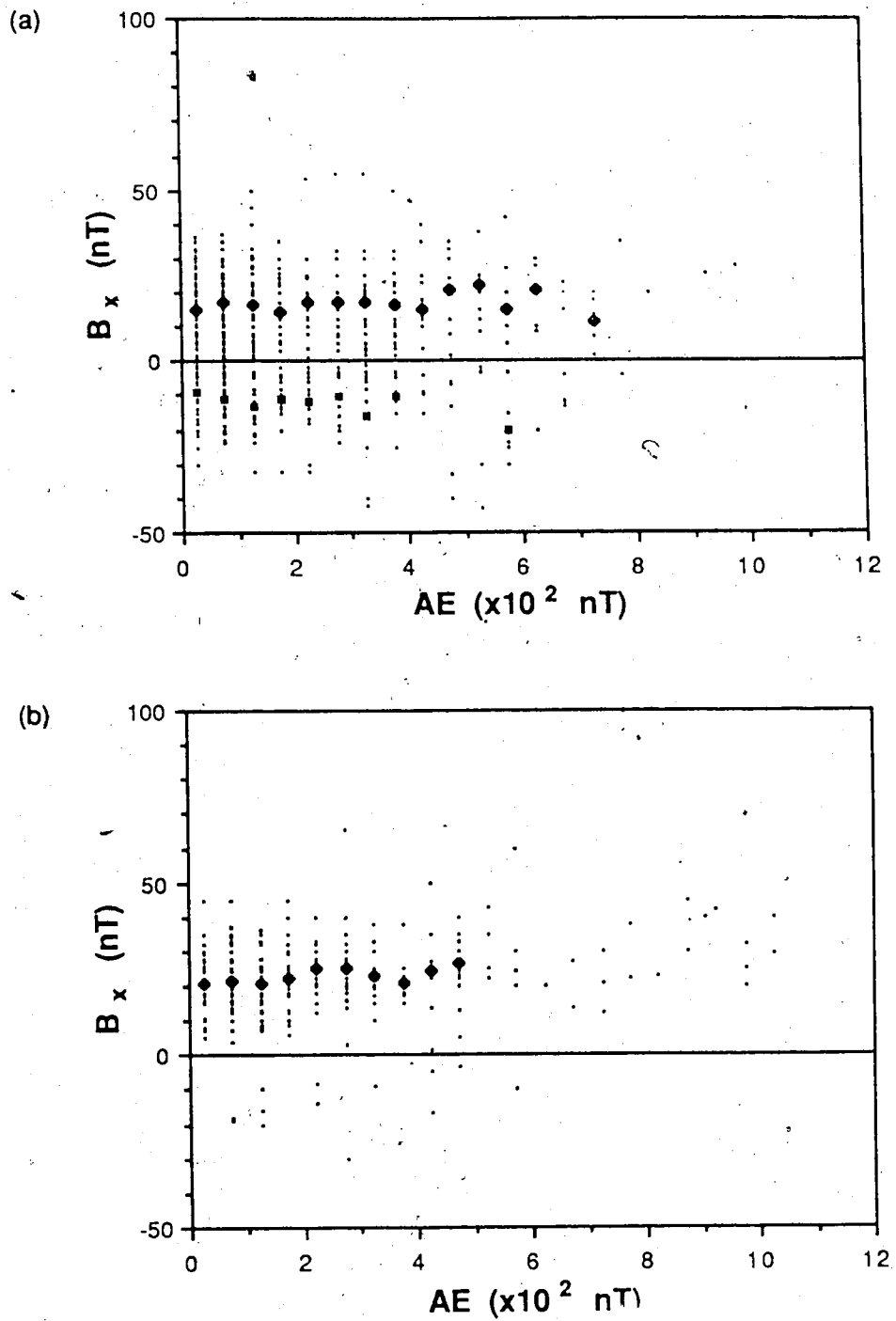


Figure 4.7 Activity level as a function of B_x for (a) CPS and (b) PSBL measurements from the 1978/1979 data set.

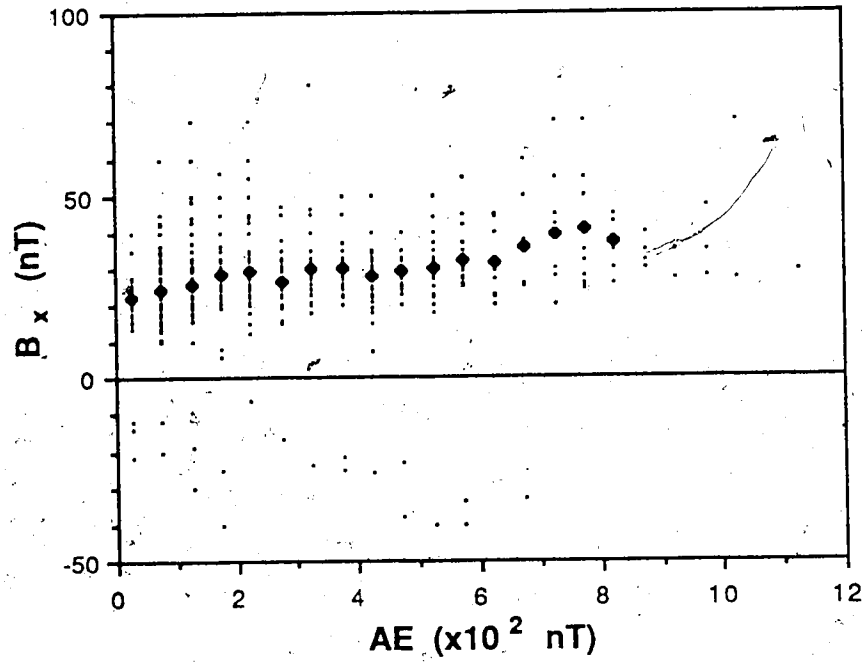


Figure 4.8 Same as figure 4.7 but for tail lobe measurements.

For completeness, similar plots to those of AE vs. B_x for the CPS, PSBL and lobe were constructed for activity level as a function of corresponding B_y data (the complete data set, with both northern and southern hemisphere values, is used here). These are shown in figures 4.9, (a) and (b), and 4.10, (a) and (b), which present AE data as a function of B_y for all regions together, and for the CPS, PSBL and lobe, respectively. In each plot, all B_y measurements corresponding to each 50 nT AE interval and for both hemispheres together are averaged and displayed on the graphs, at the midpoint of each bin, by bold squares. The approximately constant value of B_y in each figure for all levels of AE, quantitatively indicates that no distinct relationship exists between the magnitude of the cross-tail magnetic field and the level of magnetospheric activity.

4.2.4 $|B_y|$ as a Function of Downtail Distance

To further substantiate that the usefulness of magnetic field data in distinguishing between plasma domains is quite limited, plots of B_y vs. X were compiled for the three plasma regimes. Figure 4.11 (a) includes all available data for 1978 and 1979, whereas figures 4.11 (b) and 4.12, (a) and (b), represent samplings, for both 1978 and 1979, of the CPS, PSBL and lobe, respectively. In these graphs, positive B_y may be considered to represent measurements made in both the northern hemisphere dawn and southern hemisphere dusk sectors, whereas negative B_y represents both the northern

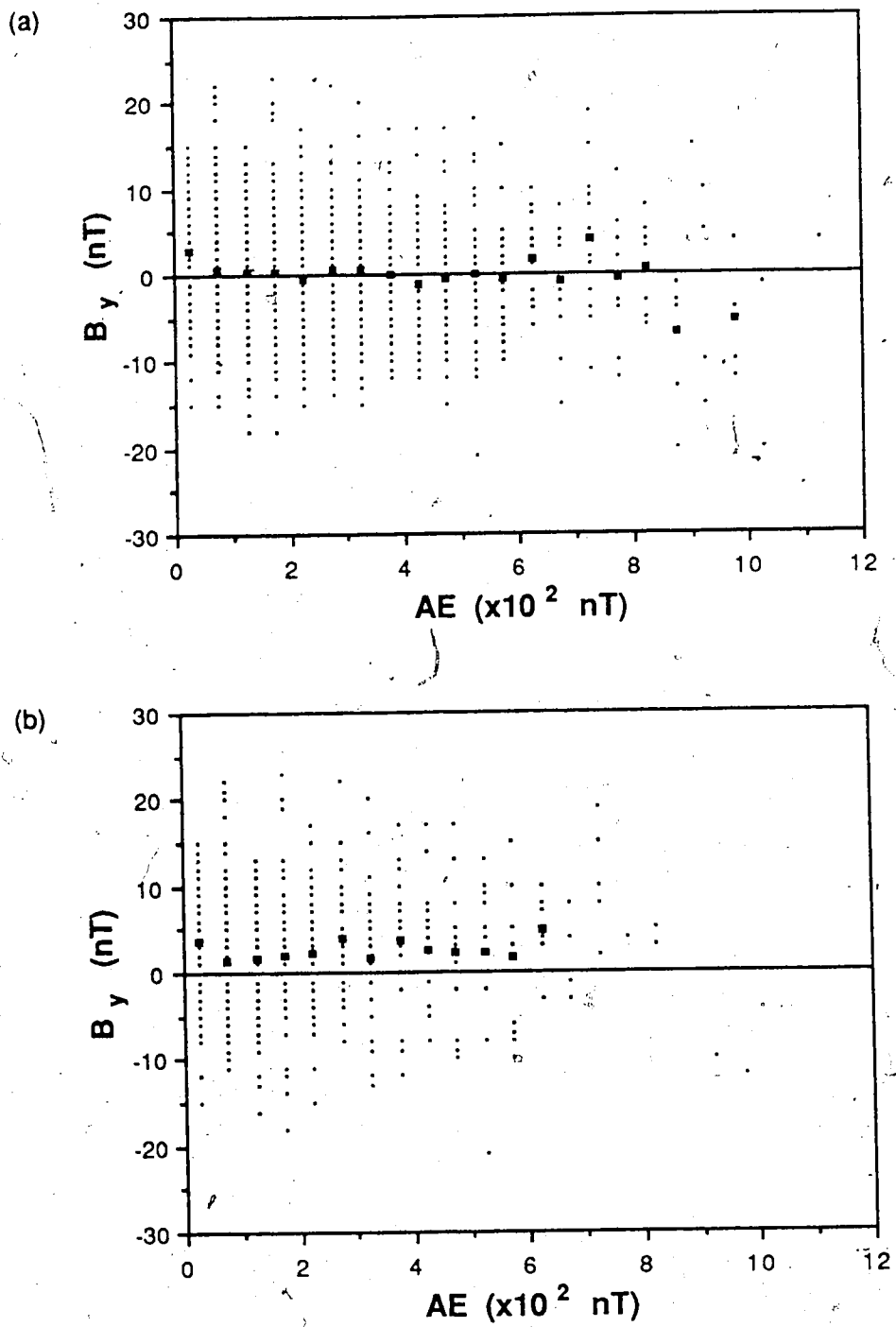


Figure 4.9 Scatter plots of B_y as a function of activity level for (a) the entire 1978/1979 data set, and (b) CPS measurements from the 1978/1979 data.

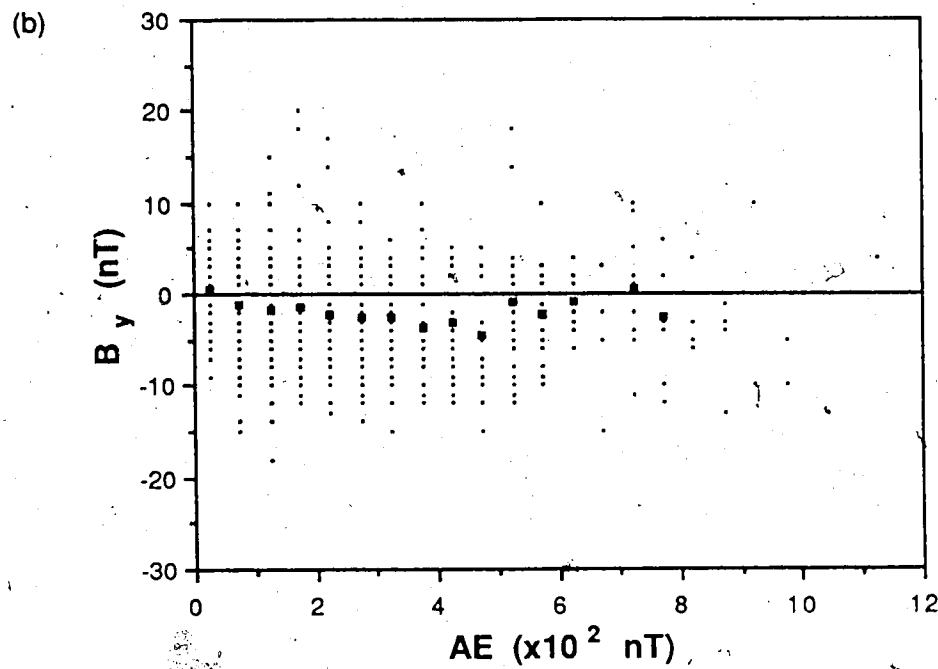
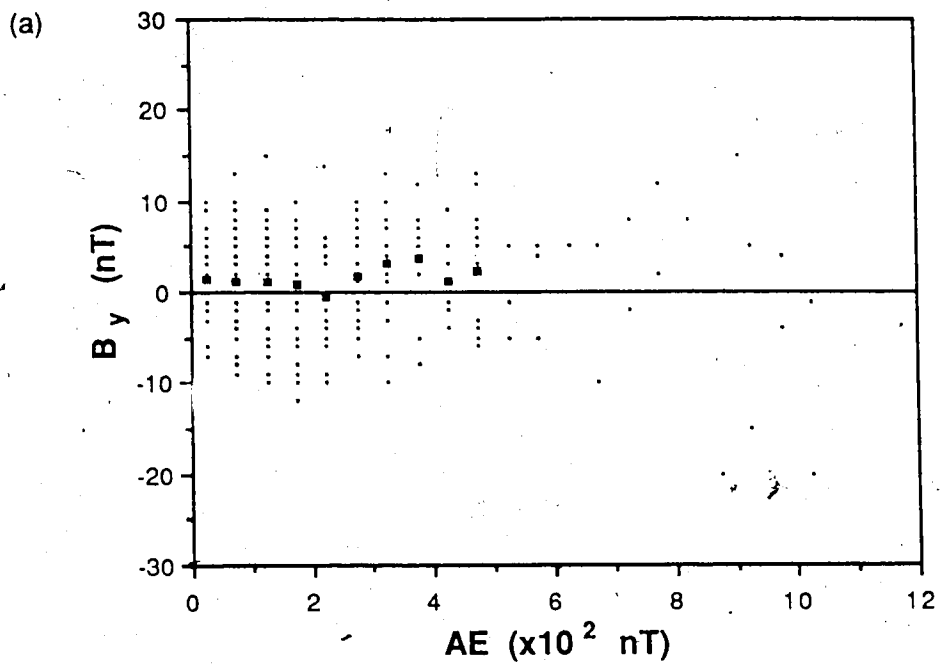


Figure 4.10 Same as figure 4.9 but for (a) PSBL and (b) tail lobe measurements.

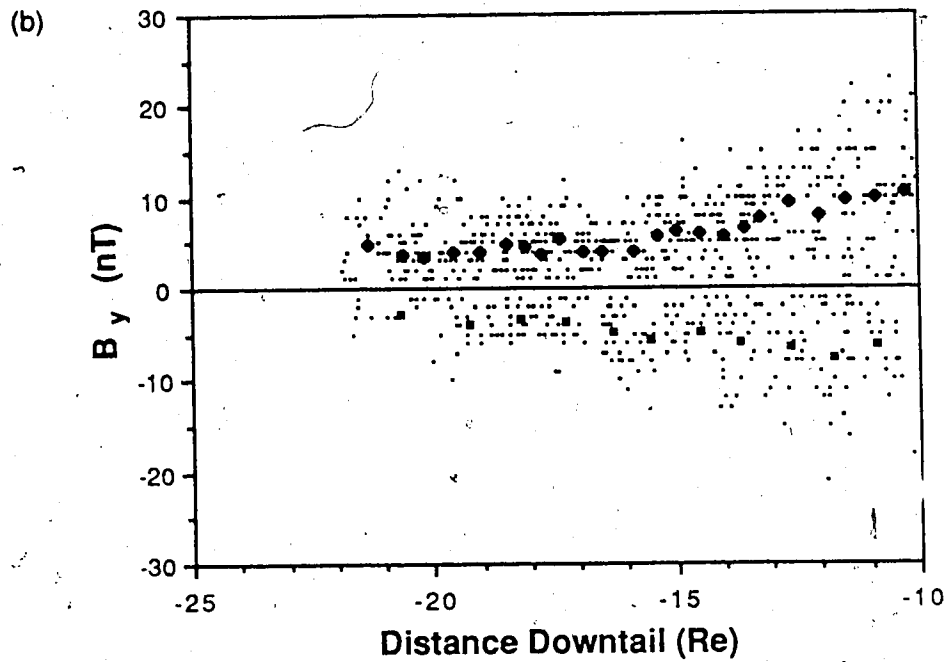
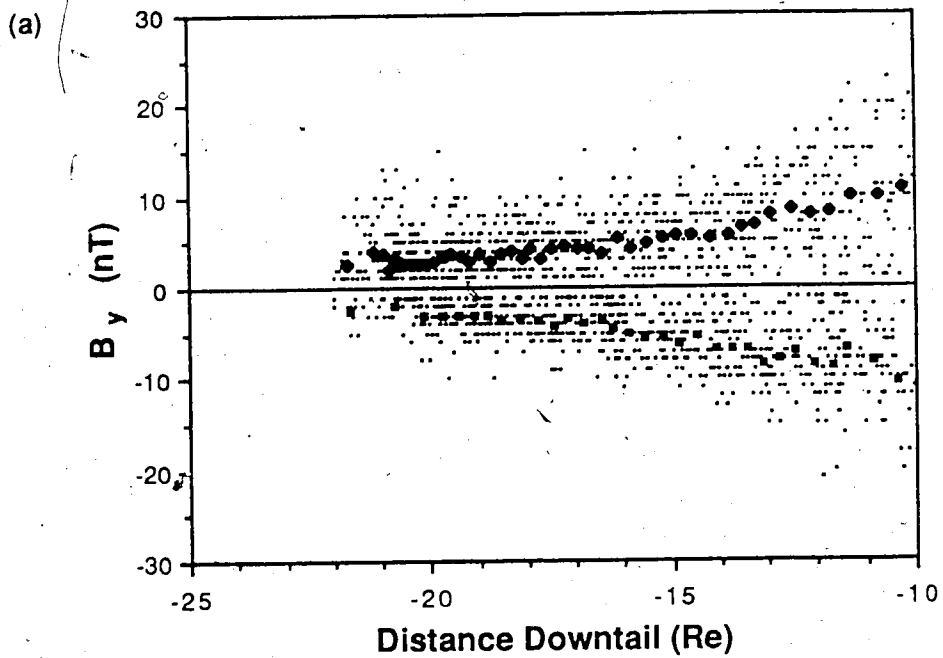


Figure 4.11 Scatter plots of B_y , as a function of distance downtail for (a) the entire 1978/1979 data set, and (b) -CPS samplings.

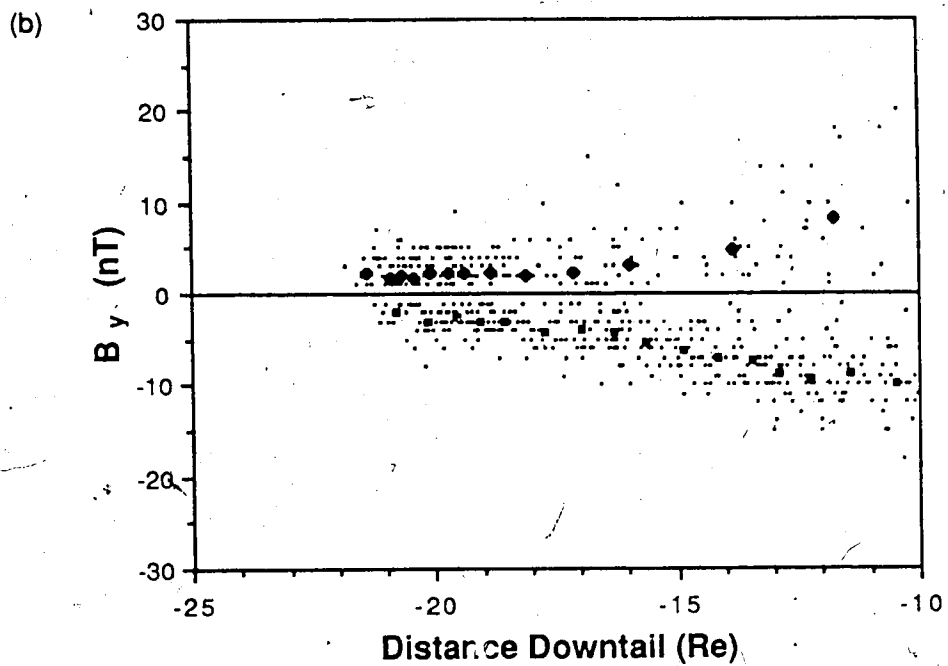
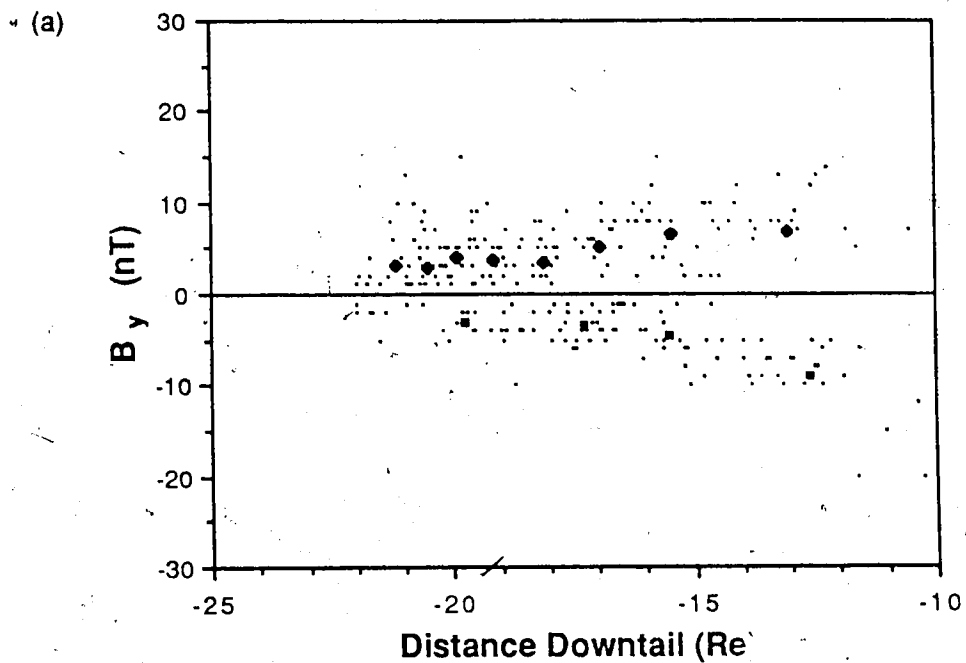


Figure 4.12 Same as figure 4.11 but for (a) PSBL and (b) tail lobe samplings.

hemisphere dusk and southern hemisphere dawn sector observations (recall figure 3.3). A connection may be made between the magnitude of B_y and the Y coordinate, with larger values of B_y corresponding to larger Y. This follows from the fact that the background B_y field component results from hydrodynamic tail flare which maximizes near the flanks of the tail and closer to the Earth (Mihalov et al., 1968). $|B_y|$ consequently decreases towards the zone dividing the dusk and the dawn, since in this vicinity B_y must change polarity.

As with the B_x vs. X plots, nonuniform satellite coverage is apparent, although this observation is not as distinct here. In figure 4.11 (a), it is evident that negative B_y is sampled less frequently than positive B_y , particularly at large distances downtail (760 $-B_y$ measurements were recorded compared with 1105 $+B_y$ samples, whereas none of the hourly averaged values of B_y in the data set had magnitudes of 0 nT). The northern hemisphere dawn quadrant was traversed more frequently than was northern hemisphere dusk (978 values for the dawn as opposed to 622 values for the dusk). In addition, the southern hemisphere was sampled less completely than was the northern hemisphere, and although the southern hemisphere dawn quadrant was traversed somewhat more often than southern hemisphere dusk (138 dawn vs. 127 dusk values), the difference is not enough to override the trend set by the northern hemisphere observations. Therefore, analysis based

on positive B_y samplings is perhaps more reliable than that based on negative B_y measurements.

Consider the portion of the graph corresponding to positive B_y . The majority of points (95%) lie in the range $0 < +B_y \leq 13$ nT. The bold diamonds represent 25-point $+B_y$ averages for consecutive values of the X coordinate. These mean values lie in an approximately horizontal pattern, for distances less than $-16 R_e$ behind the Earth, which suggests that the magnitude of $+B_y$ is approximately independent of distance downtail between -16 and $-23 R_e$. For this region, the overall mean value of $+B_y$ is 3.4 nT. Similarly, the bold squares represent 25-point averages of $-B_y$ values, which again lie in a roughly horizontal pattern. The overall mean value of B_y for distances downtail between -16 and $-23 R_e$ is -3.4 nT. As well, 95% of the $-B_y$ values lie in the range of $-11 \leq B_y < 0$ nT. For both positive and negative B_y , a trend towards larger B_y magnitudes closer to the Earth is observed, which would be expected since the effect of tail flare is largest near the Earth. That this trend does not distinctly continue as distance downtail increases indicates the existence of processes which cause the value of B_y to be greater in magnitude than expected due to flare alone.

Next, consider separately data for each of the three plasma regimes under investigation. S encounters for 1978 and 1979 are shown in figure 4.11 (b). The overall distribution in this plot resembles that observed in figure 4.11 (a). The 579 $+B_y$ measurements are relatively evenly

distributed in terms of the X coordinate, whereas the 265 $-B_y$ samples appear at a lower frequency particularly at large X. Beyond $-16 R_e$ downtail, the magnitudes of the $+B_y$ 25-point averages are approximately constant (total mean value for these X values is 4.2 nT); however, due to the smaller number of $-B_y$ samplings, the constancy of the $-B_y$ 25-point averages is somewhat less clear (the total mean value of $-B_y$ for $X \leq -16 R_e$ is -3.7 nT). 95% of all measurements of $+B_y$ lie in the range $0 < +B_y \leq 13$ nT for all values of X, whereas 95% of $-B_y$ values lie in the range $-11 \leq -B_y < 0$ nT for all X. Again, larger values of both positive and negative B_y (up to ± 23 nT) tend to occur at values of X closer to the Earth.

In figure 4.12 (a), which presents the PSBL data for 1978 and 1979, 95% of all observations lie in the region $-10 \leq B_y \leq 10$ nT (recall that no hourly averages of $|B_y| = 0$ nT were obtained). Satellite coverage near the Earth for this region is sparse, again suggesting that the PSBL is less frequently encountered in the vicinity of the Earth due to the nature of the satellite orbit. The 25-point positive and negative B_y averages do not provide reliable interpretations due to the small number of raw data points displayed (206 $+B_y$ and 105 $-B_y$ values). Negative B_y particularly is relatively infrequently sampled, and therefore provides little in the way of significant information.

In the lobe, (figure 4.12 (b)), both positive and negative B_y values have a tendency to be somewhat smaller

than in the CPS and PSBL, with 95% of positive B_y values lying in the range $0 < B_y \leq 8$ nT and 95% of negative B_y values lying in the range $-11 \leq -B_y < 0$ nT. This is expected since the lobe lies outside the FAC solenoids, and hence, the main magnetic field component is necessarily B_x . The lobe is encountered near the Earth more frequently than is the PSBL, and frequency of $-B_y$ values is much greater for the lobe than for both the CPS and the PSBL (390 lobe vs. 265 CPS and 105 PSBL values). The $+B_y$ 25-point averages are roughly constant beyond -16 Re downtail whereas the magnitudes of the $-B_y$ 25-point averages tend to decrease slightly more as X increases. The overall $+B_y$ mean value in the lobe for $X \leq -16$ Re is 2.1 nT whereas that for $-B_y$ in this spatial range is -3.3 nT. Once again, the larger values of B_y which do occur are observed closer to the Earth.

Through the B_y vs. X studies it has been determined that values of the cross-tail magnetic field component (both positive and negative B_y) in the range of $-10 \leq B_y \leq 10$ nT (where $|B_y| \neq 0$ nT) occur in all three plasma regimes and at all distances downtail. Note that 89% of all CPS values, 96% of all PSBL and 94% of all lobe measurements fall within this range.

4.2.5 $|B_y|$ as a Function of $|B_x|$

Conclusions reached in the above studies may be further investigated through a comparison of simultaneously measured B_x and B_y values. Figure 4.13 is a plot of all available

1978 and 1979 data for the three regions under consideration. This representation may be interpreted as showing observations made in each of the four quadrants of the tail cross section as defined in figure 3.3. Several points of interest require discussion. Limited southern hemisphere (negative B_x) coverage, due to the nature of the spacecraft orbit, is once again evident. That the majority of southern hemisphere points were obtained in 1979 is not obvious from this particular graph. A large range of combinations of the two parameters of B_x and B_y is apparent, indicating that corresponding to a given value of B_x is a large range of B_y values.

The most striking feature of figure 4.13 is that the data are ordered in the form of a large "X" which is filled with measurements both to the right and left of the X (in terms of the X coordinate), but for which there is a distinct absence of points both above and below the X shape (in terms of positive and negative B_y). Careful consideration of this result suggests that, in actuality, it indicates what would be expected from the statistical magnetospheric models. When $|B_x|$ is small one would predict that the satellite is in the vicinity of the neutral sheet in the CPS. According to the models, $|B_y|$ should also be small near the neutral sheet. Consequently, the X pattern observed in figure 4.13 generally satisfies the model predictions in that when $|B_x|$ is small, so is the corresponding $|B_y|$. However, according to figure 4.13 values

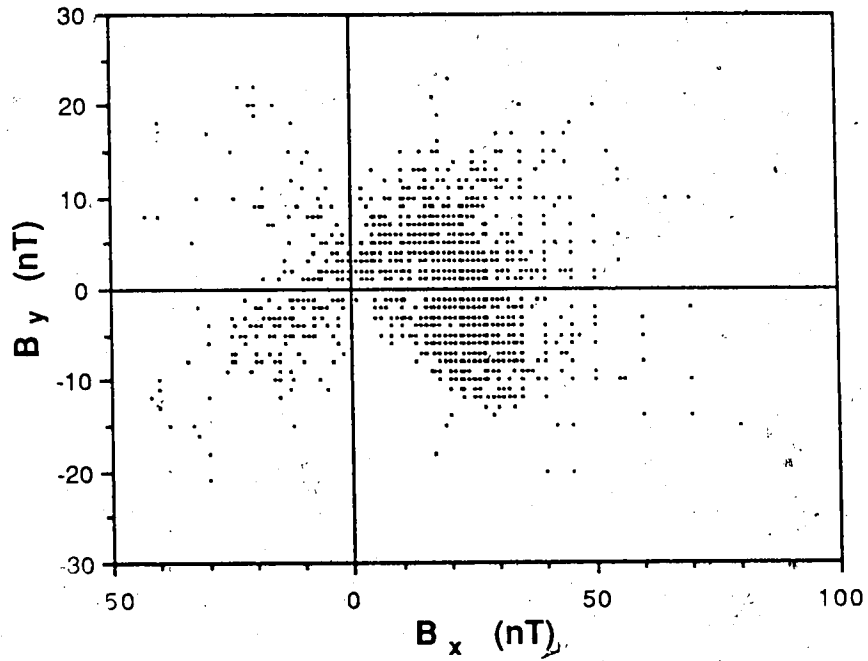


Figure 4.13 B_y plotted as a function of B_x for the complete 1978/1979 data set.

of B_y , as large as 10 nT are also observed to correspond to $|B_x|=0$, in contrast to what is expected. This observation will be dealt with in detail in following sections.

Figures 4.14, (a) and (b), and 4.15 present 1978 and 1979 data for the CPS, PSBL and lobe, respectively. CPS observations follow the same overall trend as seen in figure 4.13. As mentioned earlier, 19 measurements of $|B_x|=0$ nT were made, and of these, 17 appear in figure 4.14 (a), indicating that the majority of occurrences of $|B_x|=0$ do take place in the CPS, and likely at the neutral sheet (the remaining two values of $|B_x|=0$ appear in figure 4.14 (b) for PSBL samplings). Caution must be used, however, in making this statement because only hourly average values were used to compile the graphs for these studies. As will be seen on a smaller time-scale analysis in following studies, the occurrence of $|B_x|=0$ is not necessarily indicative of a neutral sheet encounter, although on the time frame of one hour, such would appear to be the indication from a statistical point of view. From figure 4.14 (a) it is also evident that many combinations of B_x and B_y exist in the CPS, and that no specific diagnostic set of combinations may be chosen from this figure which can uniquely identify the plasma regime being sampled.

Figures 4.14 (b) and 4.15, which display the PSBL and lobe encounters, respectively, also indicate that a great variety of B_x vs. B_y combinations are observed within these plasma domains. Southern hemisphere coverage is minimal for

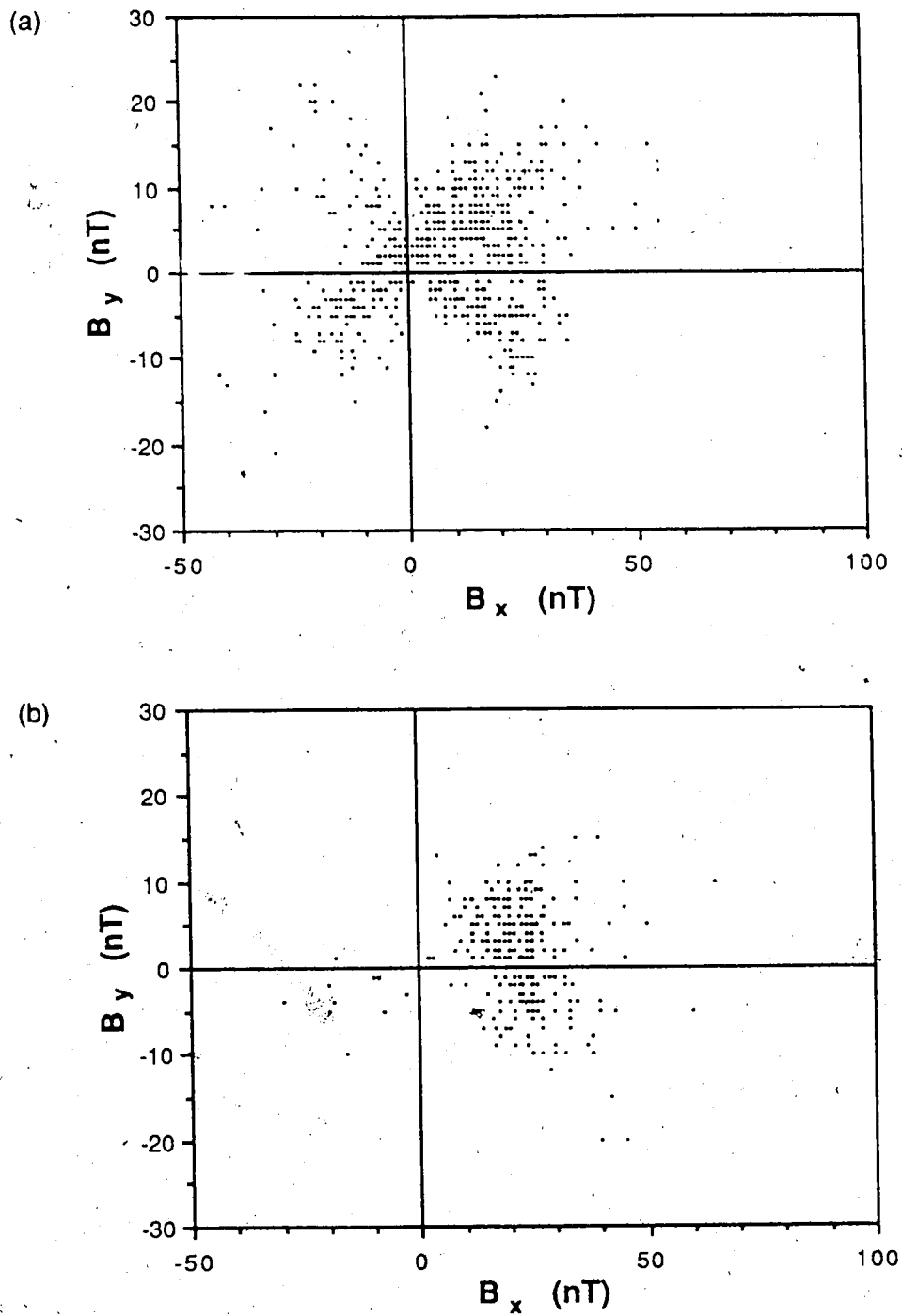


Figure 4.14 B_y as a function of B_x for (a) CPS and (b) PSBL measurements for 1978 and 1979.

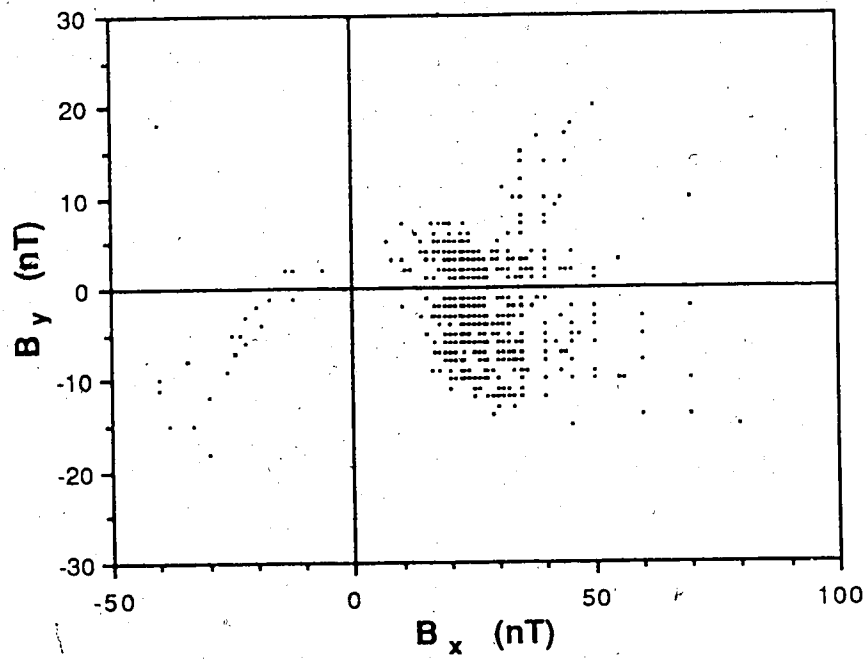


Figure 4.15 Same as figure 4,14 except for tail lobe measurements.

both regions, however, for the northern hemisphere data, the distribution of points in each case is quite variable. Values of $B_x \leq 10$ nT are not typically expected to be encountered in either the PSBL or the lobe according to the statistical tail model, although such points are in fact observed.

From the three individual plots of CPS, PSBL and lobe data (figures 4.14, (a) and (b), and 4.15, respectively), it may be noted that a certain range of B_x vs. B_y points are encountered in each of the three regions. Considering the northern hemisphere only (because of greater satellite coverage), a significant number of points in the ranges of $15 \leq B_x \leq 35$ nT and $-10 \leq B_y \leq 10$ nT occur in each of the CPS, PSBL and lobe (48% of all CPS values, 78% of all PSBL and 79% of all lobe measurements fall within these limits). This further substantiates the conclusion made from the B_x vs. X and B_y vs. X studies that magnitudes of the tail magnetic field components alone cannot be used to determine which of the three plasma regimes in question is, in fact, being sampled by the satellite.

A final comparison of B_x vs. B_y involves analysis of the data in three groups based on downtail distance from the Earth. Three X bins are chosen for this purpose, $10 \leq X \leq 14$ Re, $14 < X \leq 18$ Re, and $18 < X \leq 23$ Re, which are labeled bins #1, #2 and #3, respectively. For each bin, data from both years and all three plasma regimes are plotted, and these are shown in figures 4.16, (a) and (b), and 4.17 in ascending order of X

bin. Consider again only the northern hemisphere where coverage is more complete. The total number of northern hemisphere points in each bin are 370, 554 and 657 for bins #1, #2 and #3 respectively.

A distinct pattern is observed in each of the three plots. Data for the X bin nearest the Earth (bin #1) shows the largest amount of variability in distribution of both B_x and B_y ; however, a noticeable absence of points occurs in the region of approximately $8 \leq B_x \leq 30$ nT, and $-5 \leq B_y \leq 5$ nT, which is indicated on the graph by solid lines enclosing this region. In the second (intermediate) X bin, the distribution in B_x and B_y magnitudes is somewhat decreased from that observed nearer the Earth, and the "hole" in the distribution for the first X bin has been filled in to a certain degree, although there is still an absence of points in the small region of about $8 \leq B_x \leq 20$ nT and $0 \leq B_y \leq 3$ nT, shown again by the solid lines. Finally, the data in the third X bin shows the least variation in B_x and B_y magnitudes of the three X bins, and the "hole" in the distribution seen in the first two bins has been filled completely.

The "hole" in the distribution can be explained in terms of satellite coverage. Recall that B_y changes polarity in the transition from dusk to dawn; hence, the observation of low values of B_y suggest that this transition zone is being sampled. Due to the nature of the satellite orbit, this zone is not often encountered near the Earth (ie: in the region of $10 \leq |X| \leq 14$ Re). Here, the satellite

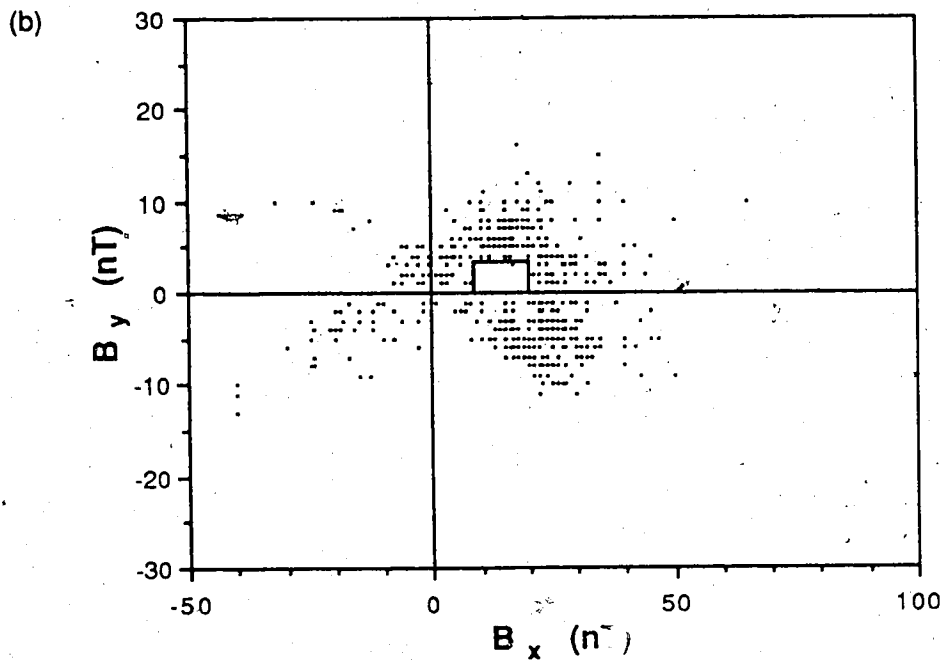
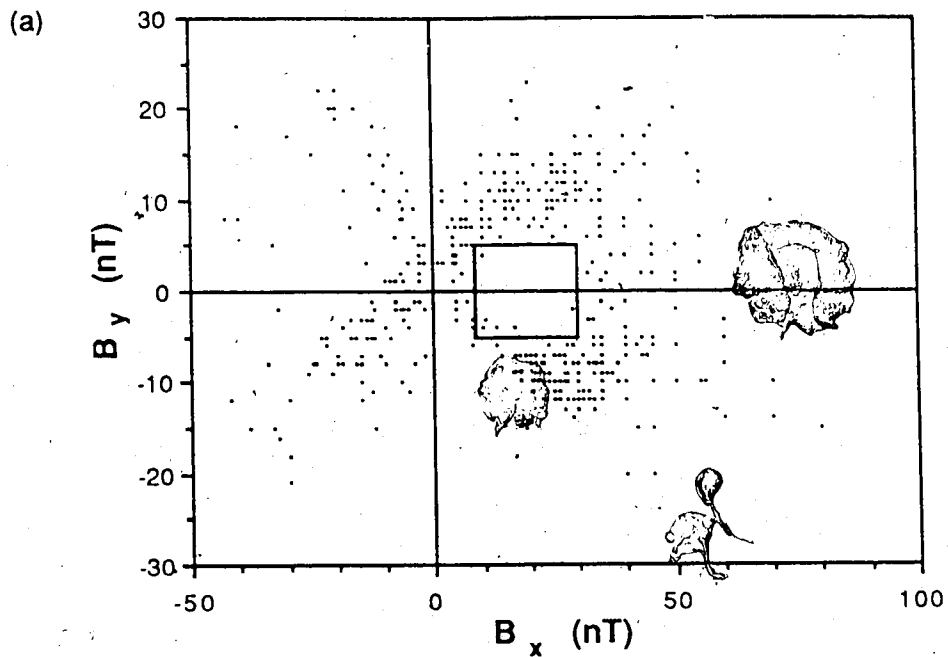


Figure 4.16. B_y vs. B_x for a division of the 1978/1979 data into three groups based on distance downstream of the earth. The two categories shown here are for values of X in the ranges of (a) $10 \leq |X| \leq 14$ Re and (b) $14 < |X| \leq 18$ Re (X bins #1 and #2, respectively).

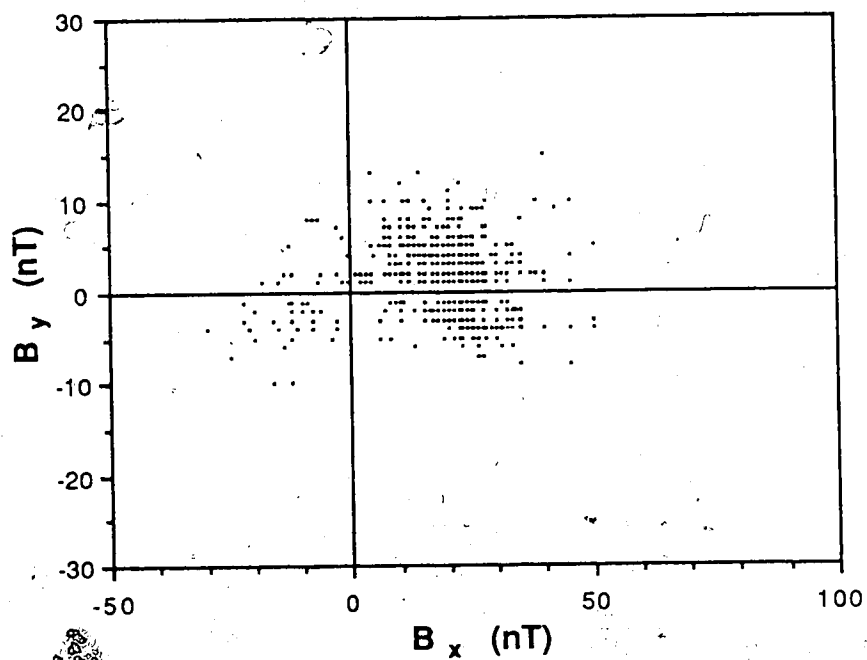


Figure 4.17 Same as figure 4.16 but for the third range of distance downstream given by $18 < |X| \leq 23$ Re (X bin #3).

preferentially samples the flanks of the magnetotail as it prepares to swing around the Earth. However, for distances downtail in the range $18 < |X| \leq 23 R_e$, the transition region from dusk to dawn is frequently sampled, and therefore, low values of B_y are observed for this X bin. At intermediate distances the frequency of low B_y sampling is increased from that near the Earth. It is apparent, then, that as distance downtail increases, the dawn to dusk transition region is more frequently encountered, as observed in figures 4.14, (a) and (b), and 4.15.

In these figures, the range of values observed earlier to persist in each of the three plasma regimes, that is, $15 \leq B_x \leq 35$ nT and $-10 \leq B_y \leq 10$ nT (northern hemisphere only), is found to occur in each bin. However, it is also evident that as distance downtail increases, a different B_y range is dominant in each X bin. For the bin representing values of X nearest the Earth, larger B_y values tend to be recorded, and as distance downtail increases, the magnitude of the B_y measurements tends to decrease. Despite this tendency for B_y to increase in magnitude towards the Earth, there still remain too many combinations of $|B_x|$ and $|B_y|$ in each X bin and in each region to define a specific set of criteria from which the plasma regime being traversed by the satellite may be uniquely and unambiguously determined.

For completeness, plots of B_x vs. B_y for the different plasma regimes in each of the three X bins outlined above were constructed. Figure 4.18 presents 1978 and 1979 data in

the three X bins for the CPS (283, 324 and 237 points for bins #1, #2 and #3, respectively), figure 4.19 shows data for the PSBL for both years (45, 113 and 153 points for bins #1, #2 and #3, respectively), and figure 4.20 shows days lobe observations for 1978 and 1979 (177, 208 and 328 points for bins #1, #2 and #3, respectively). The general trends observed in figures 4.16, (a) and (b), and 4.17 prevail for each plasma regime. This distribution of points is always most varied in the bin representing $10 \leq X \leq 15$ Re and it decreases as X increases. Largest values of B_x occur in the lobe and smallest values of B_x are seen in the CPS. However, the ranges of $15 \leq B_x \leq 35$ nT and $-10 \leq B_y \leq 10$ nT are all apparent in each of the plasma regimes. As well, the "hole" in the distribution of data points observed in figures 4.16 (a) and (b) persists in each of the three plasma domains.

4.2.6 Summary

The preceding statistical studies, which employed particle spectrograms to identify the plasma regime being sampled, have clearly illustrated that corresponding to each plasma regime in question are many combinations of the X and Y magnetic field component magnitudes. Because of the diversity of these combinations it is not possible to select a finite set of criteria based on field magnitude by which to uniquely define each plasma domain. Specifically, the grey zone of $15 \leq B_x \leq 35$ nT and $-10 \leq B_y \leq 10$ nT is apparent in each of the plasma regimes (northern hemisphere only). As

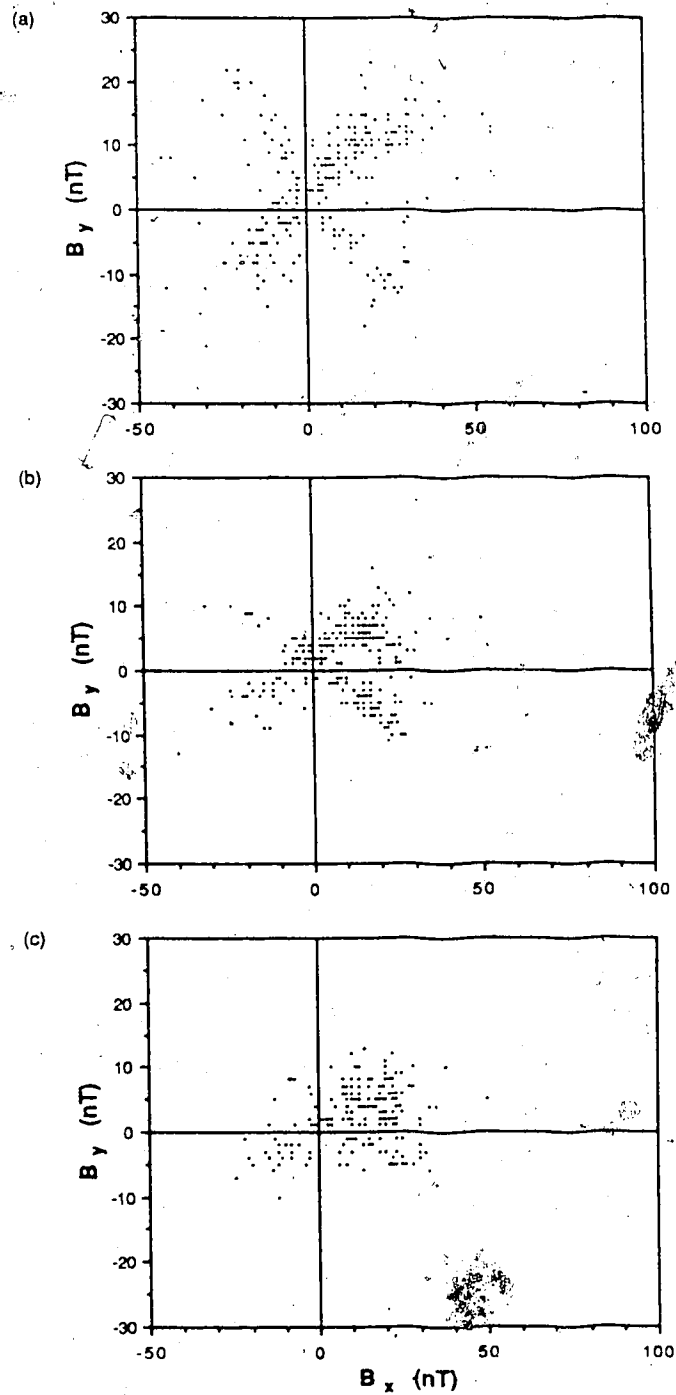


Figure 4 18 1978/1979 samplings of the CPS for X bins (a) #1, (b) # and (c) #3, respectively.

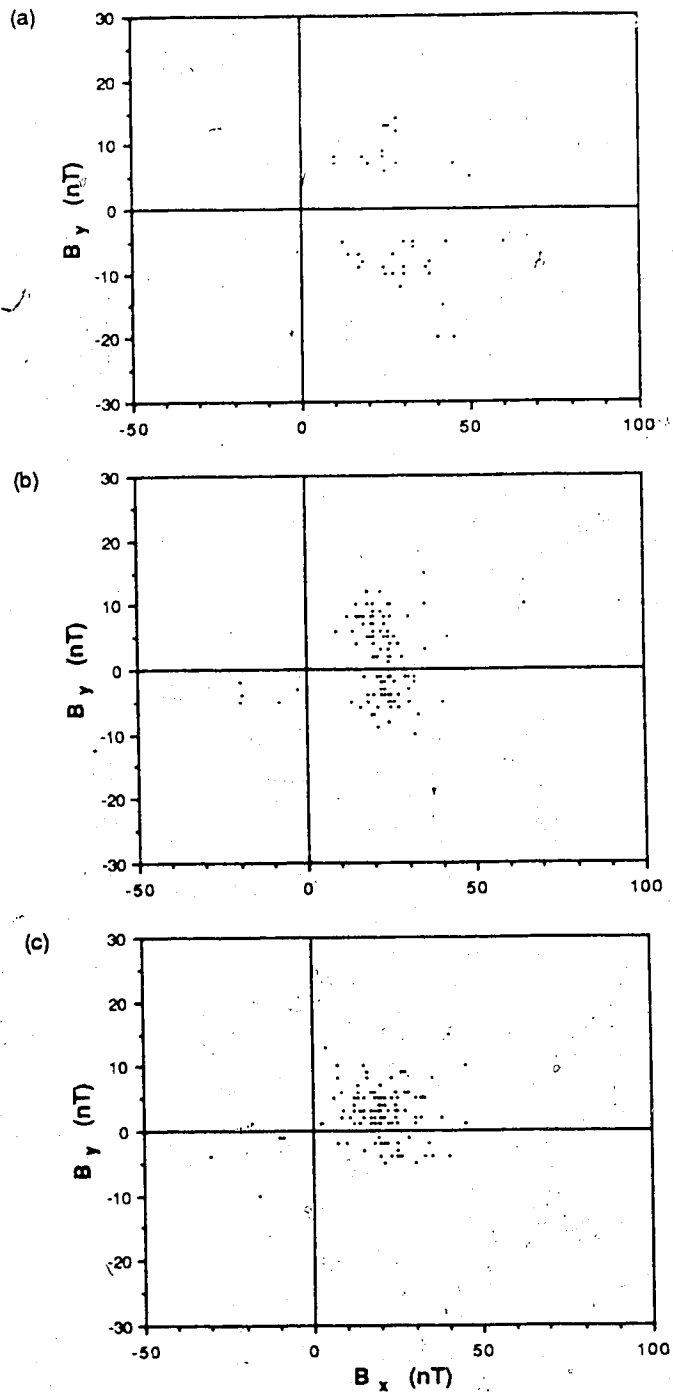


Figure 4.19 1978/1979 samplings of the PSBL for X bins (a) #1, (b) #2 and (c) #3, respectively.

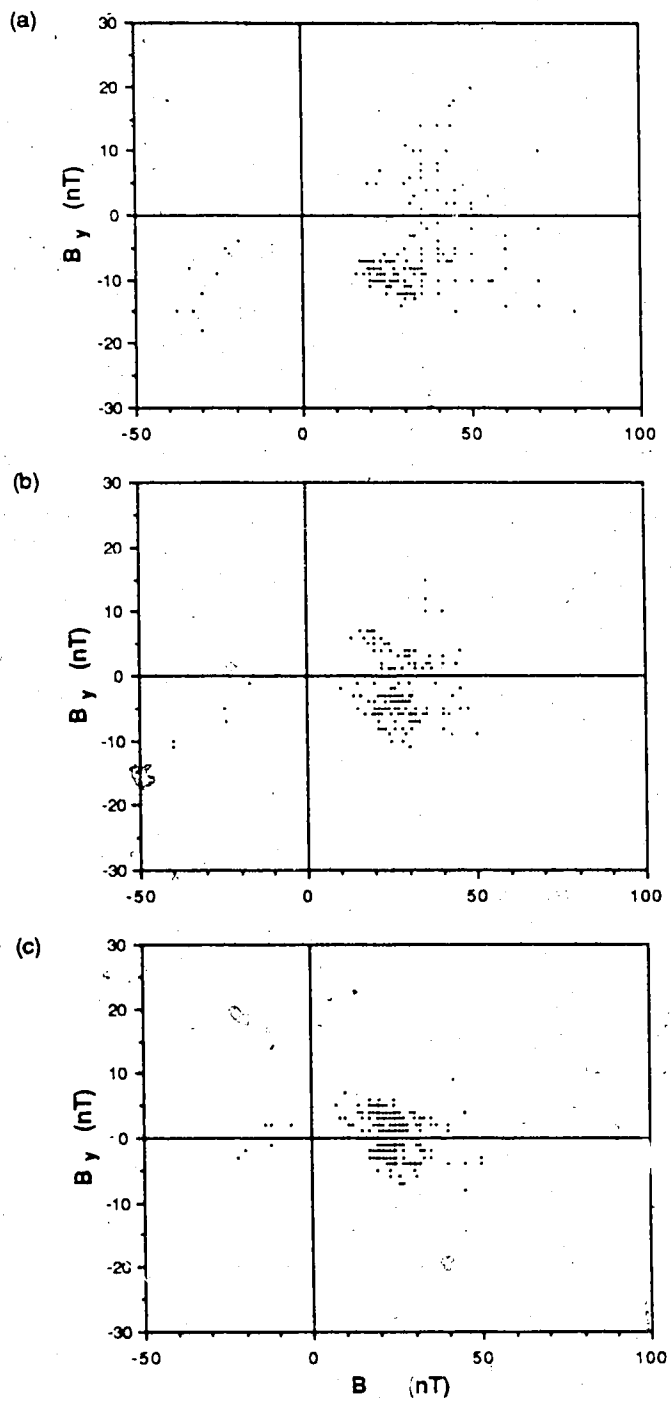


Figure 4.20 1978/1979 samplings of the tail lobes for X bins (a) #1, (b) #2 and (c) #3, respectively.

well, the lack of association between the magnitude of each field component trace and either ground based activity level (except perhaps in the lobe) or location of the satellite in the magnetotail in terms of spatial coordinates (ie: distance downtail) further impedes the attainment of criteria by which to distinguish the CPS, PSBL and tail lobes. It is clear that on the basis of magnetic data alone, no set of reliable criteria can be outlined according to which accurate and unambiguous determination of the plasma regime being sampled by ISEE 1, whether it be the CPS, PSBL or lobe, may be made.

4.3 Non-zero B_y at the Neutral Sheet

As a result of irregularities observed in studying the *in situ* magnetograms obtained by ISEE 1, the choice of magnetic signatures for defining a neutral sheet encounter in the statistical magnetospheric models has demanded some investigation. Strictly speaking, both the B_x and B_y field components must simultaneously change polarity when the neutral sheet is crossed. Some researchers (ie: McComas and Russell, 1984) have ignored the occurrence of a non-zero B_y magnitude coincident with an approximately zero-magnitude B_x component, and have chosen to identify such events as neutral sheet encounters on the basis of the B_x magnitude alone. As will be seen in chapter 5, the practice of overlooking a non-zero magnitude B_y signature concurrent with zero-magnitude B_x may lead to incorrect identification

of the region of the tail being sampled by the satellite, which further results in erroneous analysis of magnetospheric processes.

A statistical approach will again be employed in the following study of apparent neutral sheet encounters. Here, "apparent" will be used to indicate events which are considered to be neutral sheet encounters when only the nature of the B_x component is considered, and without regard to the simultaneous B_y signature. From the data set utilized in section 4.1, all hours during which at least one occurrence of $|B_x| \approx 0 \pm 1$ nT was observed were tabulated, providing a total of 302 such hours. (Note that the ± 1 nT uncertainty is quoted in order to incorporate the degree of accuracy to which any component trace of an ISEE 1 magnetogram can be read). For each data entry, the simultaneous B_y magnitude, the plasma regime being sampled, and as well, the hourly averages of the AE index, IMF B_y , and solar wind velocity, density and temperature were recorded.

The 302 selected hours were subdivided into four categories, according to the nature of the B_y component signature, as follows:

1. *Zero B_y Bias* (Well-Defined Neutral Sheet Encounter): both B_x and B_y simultaneously exhibit magnitudes of 0 ± 1 nT.
2. *Positive B_y Bias*: a zero-baseline shift towards positive B_y is observed such that B_y is more positive than it should be when $|B_x| = 0 \pm 1$ nT.

3. *Negative B_y Bias*: a zero-baseline shift towards negative B_y is observed such that B_y is more negative than it should be when $|B_x|=0\pm 1$ nT.

4. *Constant, Non-zero B_y at an "Apparent" Neutral Sheet Encounter*: the B_y component typically exhibits an approximately constant magnitude during the transition through $|B_x|=0\pm 1$ nT.

Due to the limited accuracy of the magnetic traces mentioned above, any event for which $|B_y|\leq 2$ nT coincident with $|B_x|=0$ nT will be classed as a well-defined neutral sheet encounter, or zero B_y bias event. This range of ± 2 nT takes into account the ± 1 nT uncertainty in reading each of the B_x and B_y traces. The time corresponding to $|B_x|=0$ nT is considered to be the actual time of the encounter, that is, the B_x component is, in effect, deemed accurate in order to simplify analyses.

Of the 302 hours in which the X component of the magnetotail magnetic field exhibited a magnitude of 0 nT, only 27.2% (or, 82 events), involve unquestionable neutral sheet encounters according to the above criteria. 41.7%, or 126, of the total number of entries are cases of positive B_y biases, 4.6% (14 events) exemplify negative B_y biases, and the final 26.5% (80 cases) represent constant, non-zero B_y magnitudes coincident with zero-magnitude B_x values.

These results illustrate that a significant number of events for which $|B_x|=0$ nT are not representative of neutral sheet encounters in compliance with the strict definition

outlined in the statistically derived magnetospheric models. This raises several queries regarding neutral sheet identification, particularly in studies presented in the literature. How have researchers dealt with the 73% of $|B_x| \approx 0$ nT events where $|B_y| \neq 0$ nT? As evidenced by published works, the issue of constant, non-zero B_y magnitude at an "apparent" neutral sheet crossing has not been discussed in much detail and that of positive and negative B_y biases has not, to the knowledge of the author, been addressed. Are such events, then, being included as neutral sheet encounters proper despite their contradicting the neutral sheet definition? As noted above, there is evidence to suggest that this is, in fact, the case. Is it, therefore, acceptable to term events which exhibit B_y biases or constant, non-zero B_y magnitude as legitimate neutral sheet encounters? If so, the discrepant B_y behaviour must be explained in terms of physical processes ongoing in the magnetotail. Alternatively, such occurrences may not, in reality, represent legitimate neutral sheet encounters, in which case these magnetic events must be re-analysed and the circumstances which result in the B_x component having a "zero" magnitude at a location other than the neutral sheet must be identified.

Events representing each of the four categories of B_y behaviour at the "apparent" neutral sheet are given in table 4.1. In this table are listed the following information for each of the events to be discussed: position of the

Table 4.1 : Events Representing Each of the 4 Categories of By Behaviour at the Neutral Sheet

Hour/Day/Year	X (Re)	Y _{GSE} (Re)	Z _{GSE} (Re)	Y _{GSM} (Re)	Z _{GSM} (Re)	Plasma Regime	(B _y) _{GSE} Bias (nT)	(B _y) _{GSM} (nT)	Z _{NSRFB} (Re)	Z _{NSF} (Re)
14/39/1979	-14.2	-13.3	+ 5.5	-14.0	+ 3.2	CPS	0	- 1.0	+ 2.2	+ 2.7
14/73/1979	-20.6	- 7.5	+ 4.3	- 8.2	+ 2.0	CPS	0	- 1.0	+ 1.3	+ 1.2
3/126/1979	-18.7	+12.0	+ 3.0	+ 9.6	+ 7.5	CPS	+ 4	- 0.4	+ 7.5	+ 7.2
18/42/1979	-12.0	-17.1	+ 3.3	-17.0	- 3.2	CPS	+ 4	+ 0.4	- 3.3	- 3.3
10/64/1979	-16.0	-11.9	+ 2.4	-12.0	+ 0.2	CPS	- 4	- 1.0	+ 0.3	+ 1.2
11/90/1979	-21.5	- 2.3	+ 3.4	- 2.7	+ 3.0	CPS	- 8	- 8.9	+ 2.0	+ 2.0
01/83/1979	-21.6	- 3.4	+ 4.3	- 5.0	+ 2.0	CPS	NA	-12.6	+ 2.5	+ 2.5
00/76/1979	-20.9	- 6.8	+ 3.9	- 7.8	- 0.5	CPS	NA	+14.4	+ 0.3	+ 0.3

* value corresponding to time of neutral sheet encounter

satellite in both GSE and GSM coordinates, plasma regime being sampled, magnitudes of the observed $(B_y)_{\text{GSE}}$ bias (when applicable) and of $(B_y)_{\text{GSM}}$ at the time of the neutral sheet encounter, as well as the distance of the observing satellite from the neutral sheet as predicted by both the Russell-Brody and Fairfield models.

An example of a magnetogram illustrating a well-defined neutral sheet encounter was shown in figure 3.2 in section 3.2 (February 8 (day 39), 1979, hour 14). A second similar case is shown in figure 4.21. In this instance, a neutral sheet "crossing" (a crossing from one hemisphere to the other), is displayed. ISEE 1 crosses the neutral sheet from the northern to the southern hemisphere dawn sector at about 14:28 UT and then back to the northern hemisphere at about 14:36 UT on March 14 (day 73), 1979. For this event, both the B_x and B_y components change polarity at the same instant.

In both of the above examples, the magnitudes of B_x and B_y simultaneously approach zero as the neutral sheet is encountered, and this is accompanied by a concurrent increase in the magnitude of the positive B_z component. As well, the B_x and B_y traces tend to follow very similar patterns, the component magnitudes increasing and decreasing proportionately and correspondingly in time (ie: they track one another). The plasma regime being sampled by ISEE 1 during these events is the CPS within which neutral sheet encounters are expected to be observed. However, as is

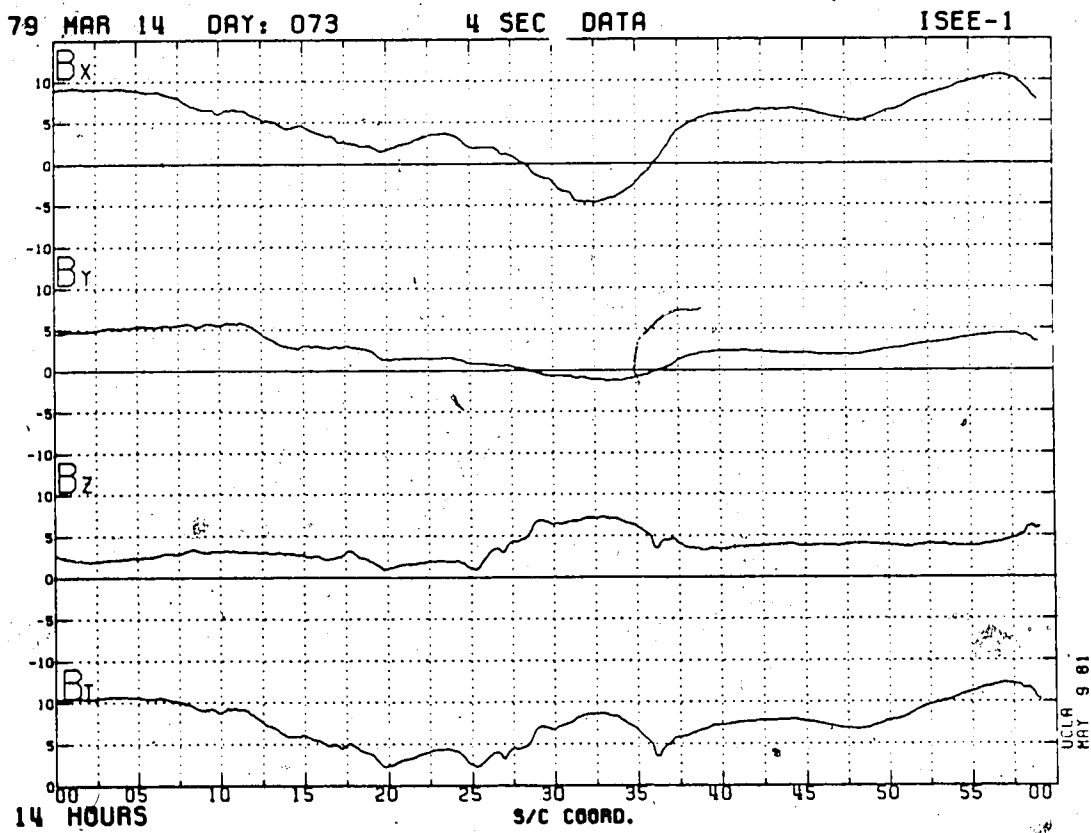


Figure 4.21 ISEE 1 magnetogram for hour 14 of day 73 (March 14), 1979.

evident from the statistics quoted above, clear-cut neutral sheet encounters of this nature are not frequently observed.

A final comment regarding these two events concerns the predictions of the distance from the satellite to the neutral sheet determined according both the Russell-Brody and Fairfield models (see table 4.1). For hour 14 of day 39 the two models suggest, respectively, that ISEE 1 situated 2.2 and 2.7 R_E above the neutral sheet, whereas, for hour 14 of day 73, distances below the neutral sheet of 1.3 and 1.2 R_E are predicted from the two models, respectively. In both cases the model predictions provide some confirmation that the neutral sheet is in fact being encountered since the predicted values of neutral sheet location are comparable to the position of the satellite.

In approximately 46% of all occurrences of $|B_x|=0$ nT, the shape of the B_y trace very closely resembles that of the B_x trace, and an appropriate positive or negative B_y baseline adjustment could bring the two traces into alignment such that a well-defined neutral sheet encounter would result. The majority of the B_y baseline biases are positive in sign; that is, B_y is more positive than it should be at the neutral sheet. In the data set for this study, such positive biases range in magnitude from the minimum of +3 nT (the limit of accuracy of the magnetograms) to +17 nT.

Examples of positive B_y biases are shown in figures 4.22 (day 126, 1979, hour 03), and 4.23 (day 42, 1979, hour

18), which both indicate a bias of approximately +4 nT. On day 126, hour 03 the observing satellite (in this case, ISEE 2) was located in the northern hemisphere dusk sector, and the plasma regime being sampled was the CPS. In such a location, the B_y component should be of negative polarity. At about 3:35, the time of the approach to the neutral sheet according to B_x , the B_z component magnitude maximizes, as is expected at the neutral sheet. Consequently, it would appear that B_y has been positively biased, and if the B_y trace were shifted in a negative direction by about 4 nT then the three magnetic component traces would illustrate the expected signatures when the satellite is situated in the northern hemisphere dusk CPS. On day 42, hour 18 the CPS of the southern hemisphere dawn sector was being traversed by ISEE 1. Both B_x and B_y are of negative polarity for the majority of the hour, as expected for this quadrant, however, $|B_y|$ is more positive than it should be, especially at 18:25 which appears to be the time of the neutral sheet encounter according to the magnitude of B_x . Consequently, B_y appears again to have been positively biased. Note that in this example $|B_z|$ does not increase as the neutral sheet is approached, and although not the expected signature, this is frequently observed.

When the predictions of neutral sheet location suggested by the Russell-Brody and Fairfield models are considered for these two events, the neutral sheet is estimated to be located about 7.5 R_e below and 3.3 R_e above

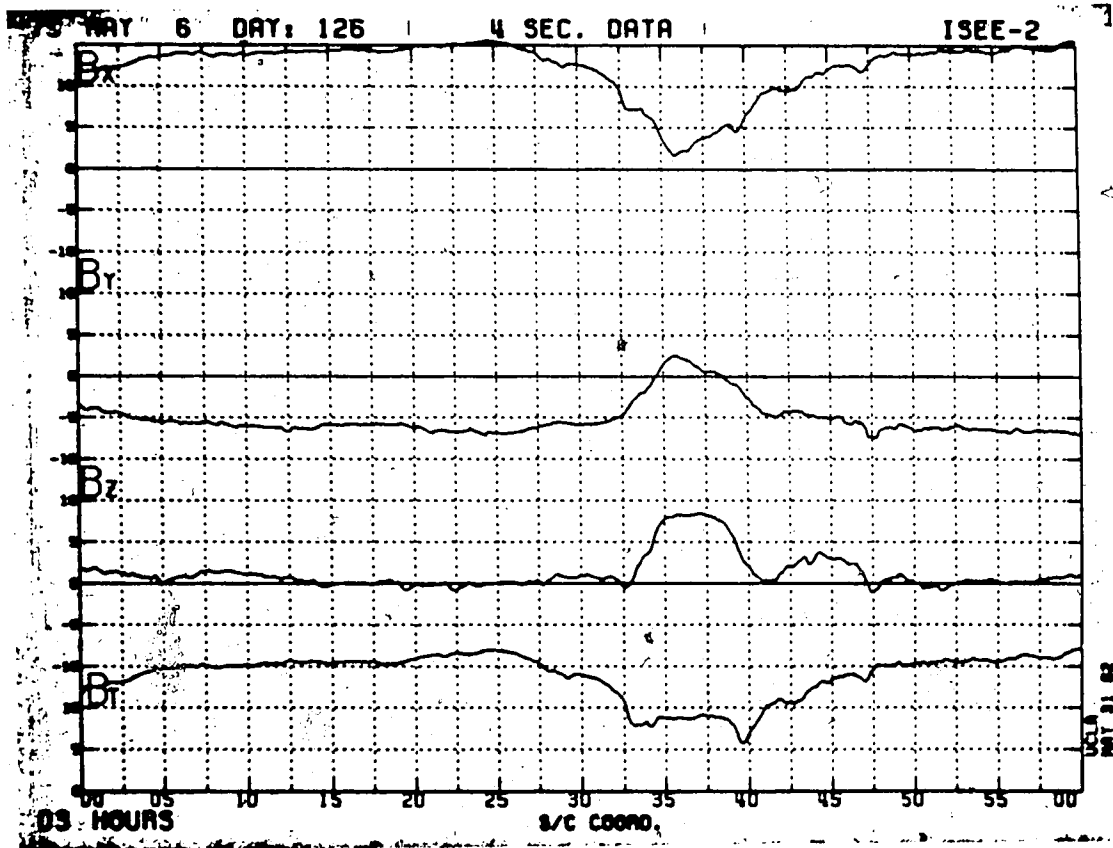


Figure 4.22 ISEE 2 magnetogram for hour 03 of day 126 (March 06), 1979.

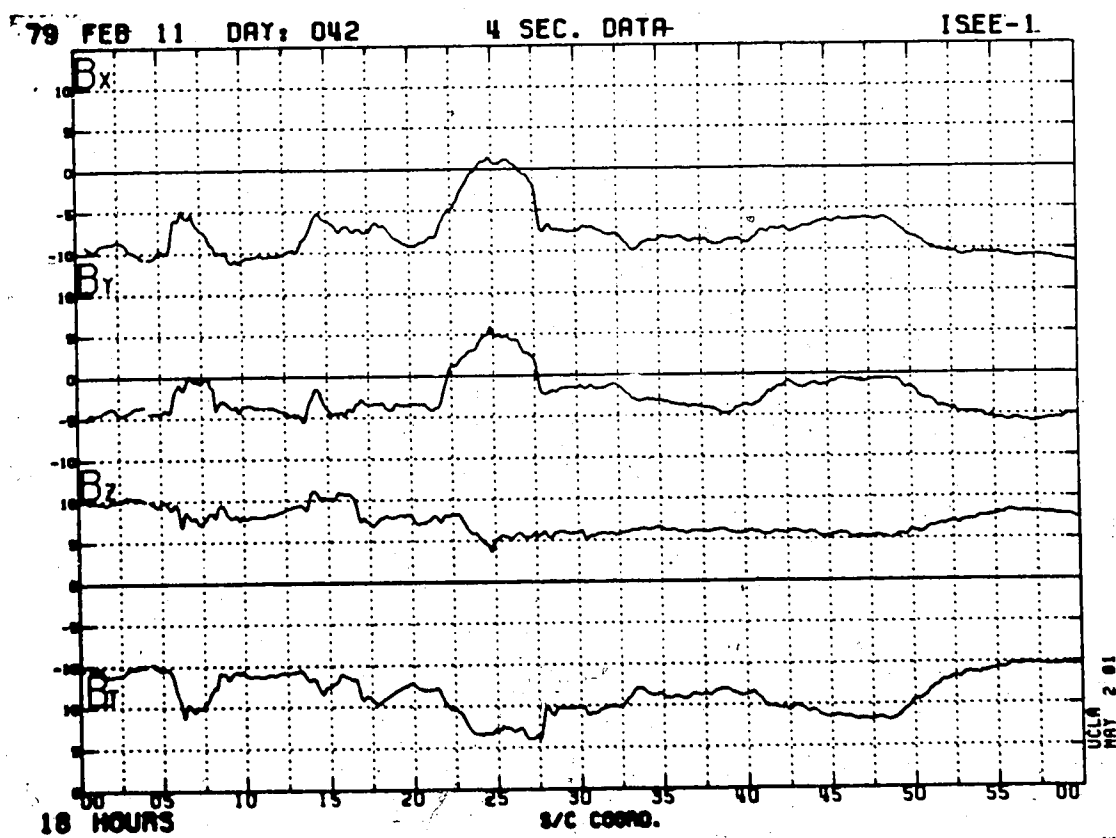


Figure 4.23 ISEE 1 magnetogram for hour 18 of day 42 (February 11), 1979.

the satellite for hour 03 of day 126 and hour 18 of day 42, respectively (the two models are in close agreement). These values do not clearly support to the magnetogram interpretations made above which suggest that the neutral sheet is being encountered.

Typically, a B_y baseline bias appears to pertain to the entire hour in question (as in the above two cases). However, in some instances the value of the baseline shift may be different for one part of the hour than for another. This is illustrated in figure 4.24 which shows the ISEE 1 magnetogram for hour 07 of February 28 (day 59), 1979 during which time the satellite was sampling the CPS of the dawn sector of the tail, crossing back and forth from northern to southern hemisphere. Each time ISEE 1 crosses the neutral sheet, B_y is expected to change polarity simultaneously with B_x . Three neutral sheet crossings are thus observed during this hour. A positive B_y bias is maintained throughout the hour; however, the respective B_y biases decrease in magnitude from +7 nT at approximately 7:07 to +5 nT at 7:17 and to +1 nT at about 7:30. Therefore, the temporal duration of any given bias may range from several minutes to more than an hour. For this event the Russell-Brody and Fairfield models predict the distance from the satellite to the neutral sheet to be +0.7 and +2.3 R_E , respectively. The first of these values does agree with the corresponding magnetogram analysis; however, the second provides little support for the interpretation that the satellite is near

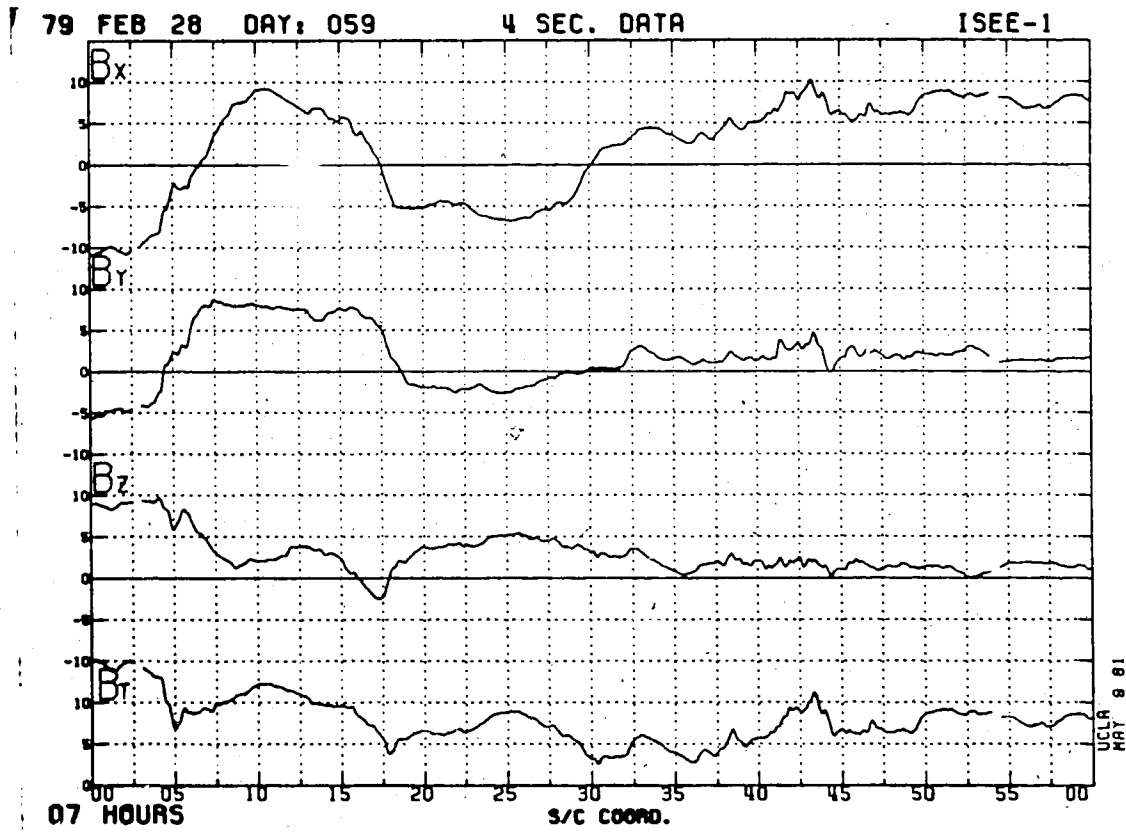


Figure 4.24 ISEE 1 magnetogram for hour 07 of day 59 (February 28), 1979.

the neutral sheet.

Only 14 examples of negative B_y baseline biases have been observed in the data set. For these events, baseline shift magnitudes vary from -3 to -10 nT. Figures 4.25 (day 64, 1979, hour 10) and 4.26 (day 90, 1979, hour 11), show two examples of negative B_y baseline shifts, the first representing a bias of -4 nT and the second of -8 nT. In each case, B_z increases as B_x approaches zero nT, supporting the expectation that B_y should also approach zero nT as the neutral sheet is encountered. For both events ISEE 1 was situated within the northern hemisphere dawn sector of the tail, therefore, B_y should exhibit positive polarity during both hours. As well, the central plasma sheet was being sampled throughout each hour as indicated by the simultaneous energetic particle spectrograms. The Russell-Brody and Fairfield neutral sheet position predictions provide reasonable support for the magnetogram interpretations in the first case, however less so in the second. For hour 10 of day 64 the Russell-Brody and Fairfield models indicate that ISEE 1 is situated 0.3 and 1.2 R_e above the neutral sheet, respectively, whereas for hour 11 of day 90 the two models both suggest that the satellite is about ~~two~~ 2.0 R_e above the neutral sheet. Furthermore, since both B_y traces closely follow the trends of the corresponding B_x traces it is clear that a negative bias in the B_y components has resulted in the B_y magnitudes being more negative than they should be. A shift towards

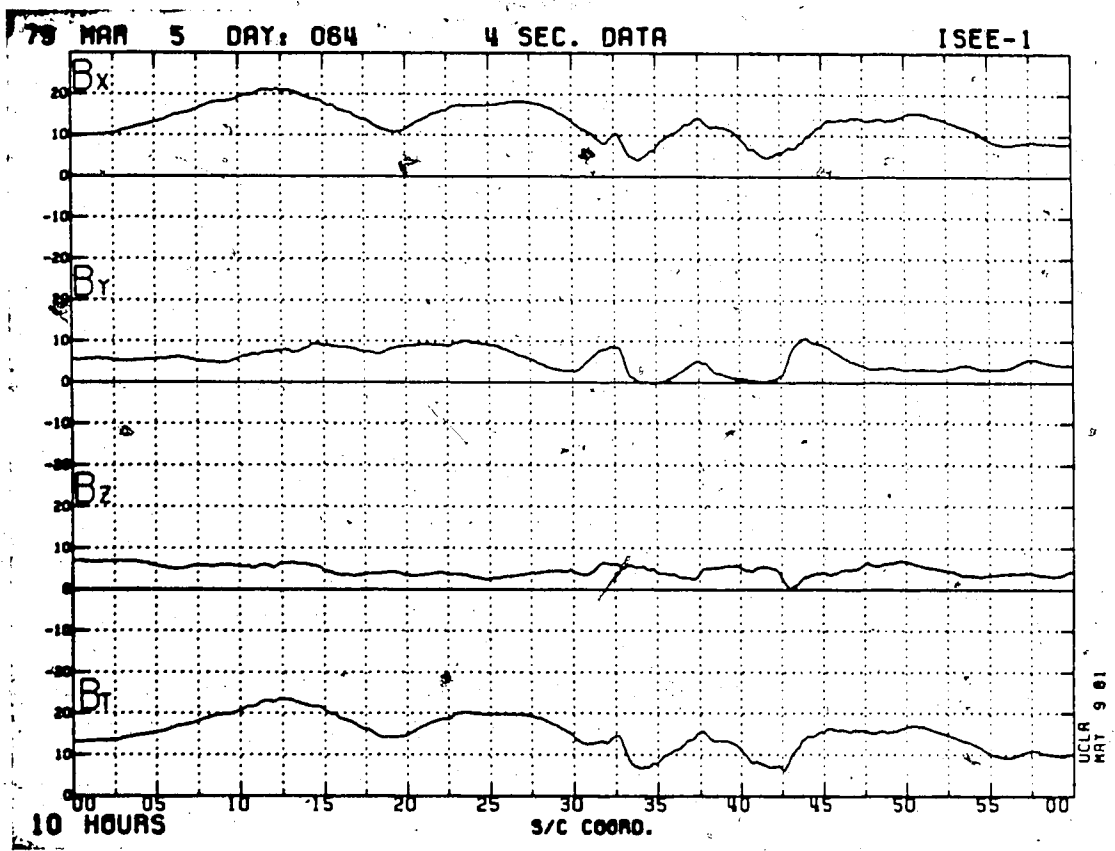


Figure 4.25 ISEE 1 magnetogram for hour 10 of day 64 (March 5), 1979.

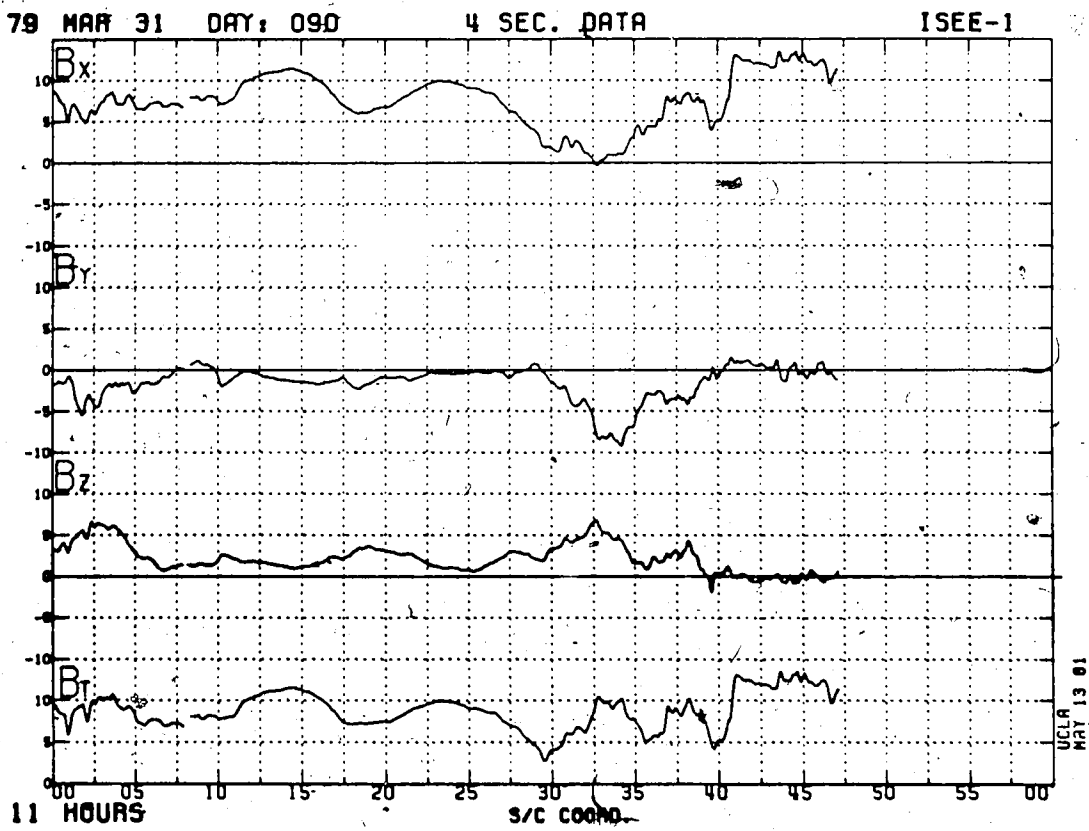


Figure 4.26 ISEE 1 magnetogram for hour 11 of day 90 (March 31), 1979.

positive B_y in each example would produce the magnetic signatures expected when ISEE 1 is located within the northern hemisphere dawn CPS.

Finally, examples of constant, non-zero B_y coincident with $|B_x| = 0 \pm 1$ nT are given in figures 4.27 and 4.28 which are ISEE 1 magnetograms for March 24 (day 83), 1979, hour 01, and March 17 (day 76), 1979, hour 00, respectively. In figure 4.27, B_y remains approximately constant and negative in polarity throughout the entire hour, despite B_x changing polarity four times. During this hour ISEE 1 was located in the CPS of the northern hemisphere dawn sector. In figure 4.28 B_y maintains a constant positive magnitude during four apparent neutral sheet crossings identified according to the B_x component. During this hour ISEE 1 was again situated within the CPS of the dawn sector in the northern hemisphere. In both events, B_y clearly does not respond to the changing polarity of the B_x component as ISEE 1 encounters what appears to be the neutral sheet. For hour 01 of day 83 the distance to the neutral sheet predicted by the Russell-Brody and Fairfield models is $+2.6 R_e$ in both cases, whereas for hour 00 of day 76 a value of $+0.3 R_e$ is obtained from both models. In the second instance, this value is small which indicates that the neutral sheet models appear accurate in this case.

If all occurrences of $|B_x| = 0$ nT do in fact represent legitimate neutral sheet encounters, then how may both positive and negative B_y baseline shifts, as well as

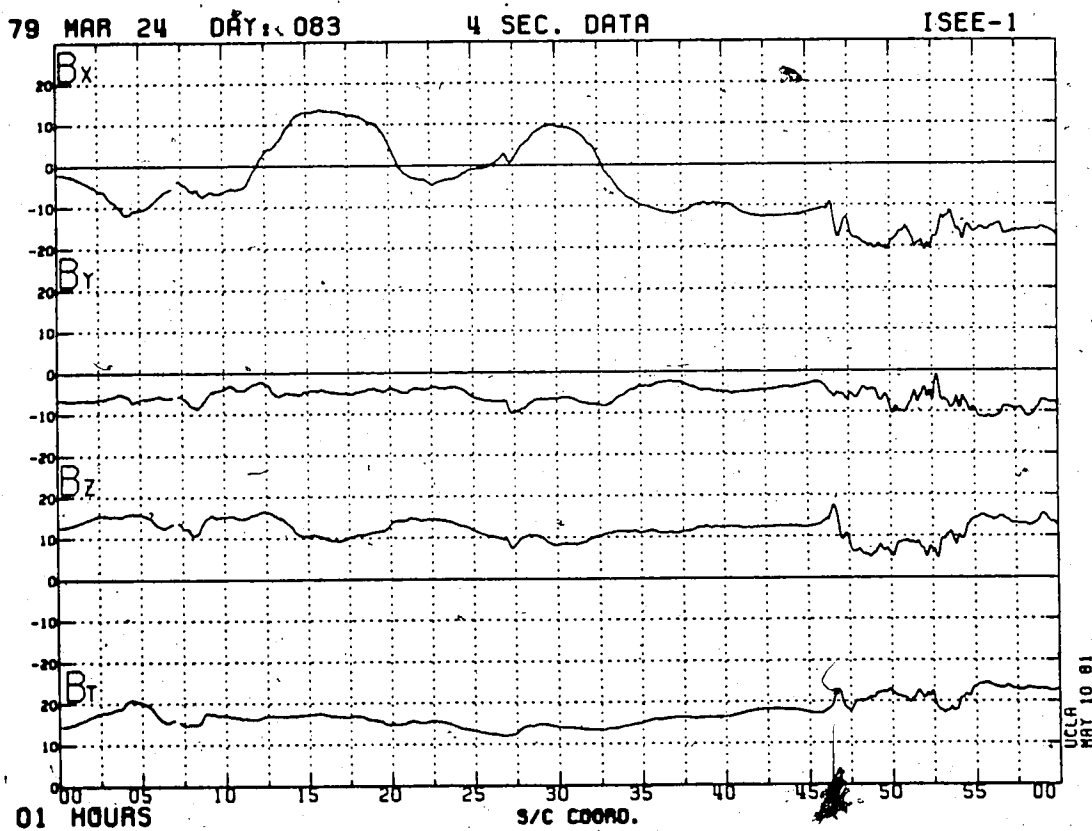


Figure 4.27 ISEE 1 magnetogram for hour 01 of day 83 (March 24), 1979.

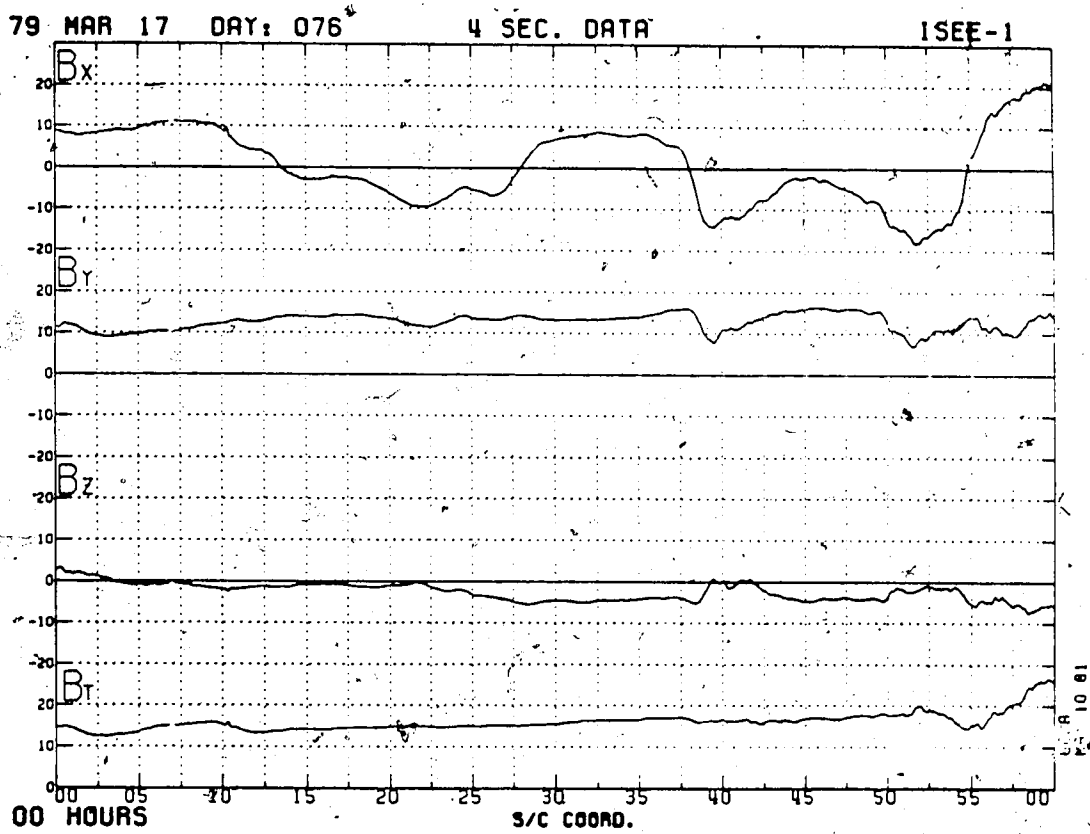


Figure 4.28 ISEE 1 magnetogram for hour 00 of day 76 (March 17), 1979.

constant, non-zero B_y at the neutral sheet, be understood? It is unlikely that there exists one all-encompassing explanation for the three scenarios. However, two mechanisms by which the discrepant B_y behaviour may possibly be explained require investigation. The first of these deals with both daily and seasonal sun-Earth geometry, and the second with the dependence of magnetotail magnetic field magnitudes on either the level of magnetospheric activity or on variations of one or more of the solar wind parameters. These will be discussed individually in the following two sections.

4.4 The Relationship Between Sun-Earth Geometry and B_y Biases

Both the seasonally varying tilt of the Earth, and as well, the diurnal change in orientation of the geomagnetic axis relative to the Earth's spin axis with respect to a fixed coordinate system (either GSE or GSM) significantly influence the magnitudes of the magnetotail magnetic field components. The spin axis of the Earth is oriented at an angle of 23.5° with respect to ecliptic north, while the geomagnetic axis is inclined to the axis of rotation by an angle of approximately 11.5° , with the north geomagnetic pole being located at 78.5°N , 70°W and the south geomagnetic pole at 78.5°S , 110°E . The maximum angle between the geomagnetic axis and ecliptic north, therefore, is 35° , with the minimum angular separation being 12° .

During the northern hemisphere winter the magnetotail is deflected southward, in the GSE coordinate system, in response to the seasonal tilt of the Earth's spin axis, while in the northern hemisphere summer the tail is deflected northward (recall figure 2.1). At the time of either the winter or summer solstice the spin axis is tilted entirely in the $(X-Z)_{\text{GSE}}$ plane; consequently, no twist of the tail about the X-axis in the $(Y-Z)_{\text{GSE}}$ plane results from the orientation of this axis. However, as the Earth revolves about the sun after the winter solstice, the orientation of the spin axis begins to introduce a twist of the magnetic field configuration in the $(Y-Z)_{\text{GSE}}$ plane about the X axis, which maximizes at the vernal equinox. At the vernal equinox the effect of the spin axis tilt is a rotation entirely in the $(Y-Z)_{\text{GSE}}$ plane, with no accompanying rotation in the $(X-Z)_{\text{GSE}}$ plane.

Consider the effect of the changing orientation of the rotation axis on the magnetic field (in GSE coordinates) observed by a satellite when it is located in the vicinity of the neutral sheet. A consequence of the orientation of the spin axis is a positive enhancement of the B_y component magnitude between the winter and summer solstices (ie: spring season), and a negative enhancement of B_y between the summer and winter solstices (ie: autumn). Positive B_y enhancement increases in magnitude between the winter solstice and the vernal equinox. At the time of the vernal equinox, the twist or rotation of the magnetic configuration

about the X-axis is a maximum, and therefore, the positive enhancement of B_y is also maximized. After the equinox, the positive enhancement again decreases until the minimum effect of the summer solstice axis orientation is reached. In such a scenario, the B_y component in springtime is always enhanced in the positive sense with respect to that B_y magnitude which would exist if the spin axis was parallel to ecliptic north. In the fall season the B_y component becomes more negative as a result of the spin axis tilt.

Also, when the satellite is in the vicinity of the neutral sheet, a positive enhancement of the magnetic field component in the X_{GSE} direction occurs between the vernal and autumnal equinoxes (ie: summer) followed by a negative enhancement of B_x between the autumnal and vernal equinoxes (ie: winter) due to the Earth's tilting rotation axis. The maximum positive B_x enhancement occurs at the summer solstice and the maximum negative enhancement at the winter solstice, with smooth variations occurring throughout the intervening months. Throughout the year, $|B_z|$ is always reduced, as a result of spin axis tilt, from the value it would have if the rotation axis was parallel to ecliptic north.

In addition to the above influence on the magnetic field components, the diurnal precession of the geomagnetic axis about the geographic axis produces a rotation of the tail in both the $(X-Z)_{GSE}$ and $(Y-Z)_{GSE}$ planes, and therefore induces alterations (which vary with the changing time of

day), in the GSE magnetic field component magnitudes. As the spin axis changes position throughout the year with respect to the GSE coordinate reference frame, the resulting effects on both the B_x and B_y magnitudes due to the geomagnetic axis position also change. For a field line projected on the $(X-Z)_{GSE}$ plane at the time of the winter solstice with the satellite located near the neutral sheet, the geomagnetic axis is aligned in the plane containing the spin and Z_{GSE} axes at local midnight in the time frame of the geomagnetic north pole. In this situation, the effect of the geomagnetic axis tilt enhances the effect due to the orientation of the rotation axis (since at this time the Earth is essentially tilted with respect to ecliptic north by a total angle of 35°). However, at local noon at the geomagnetic north pole, the effect of the geomagnetic axis will subtract from that due to the spin axis since the total angle of the Earth's tilt with respect to ecliptic north is reduced to 12° .

In general, then, the B_y perturbations due to the diurnal precession of the geomagnetic axis about the spin axis will vary in magnitude and they will either add to or subtract from those perturbations resulting from spin axis tilt depending on the time of year and hour of the day. In the most extreme situations, the magnetic field components may be reduced or enhanced due to the geomagnetic axis tilt by as much as 50% of that effect due to the spin axis orientation alone.

According to the above analysis, it may be suggested that from the winter solstice to the vernal equinox an increase or positive bias in the B_y component of the magnetic field (in GSE coordinates) would be observed which maximizes at the equinox and which has 24 hour periodicity due to the geomagnetic axis tilt. This would be followed by a decrease in positive bias, again with an oscillation in bias magnitude every 24 hours, until the summer solstice is reached. Throughout the spring season, then, all B_y traces should be positively biased, and it should be possible to systematically apply a correction factor to all B_y observations such that the positive bias could be removed from the data in order to restore all B_y traces to those which would be observed if the rotation and geomagnetic axes of the Earth were aligned with the direction of ecliptic north.

A question which is raised by the above discussion concerns the choice of coordinate system which is most appropriate for displaying and analysing satellite observations of the magnetospheric magnetic field. In this study, magnetograms constructed for the GSE coordinate system were employed due not only to their availability but as well, because energetic particle spectrograms were recorded in GSE, or spacecraft, coordinates. However, use of the GSM system for ordering *in situ* magnetic data is widespread in the literature. (Recall that the +Z coordinate in the GSE system is aligned with ecliptic north whereas

$+Z_{\text{GSM}}$ is the projection of the geomagnetic axis of the Earth on the Y-Z plane, and in both orthogonal systems, $+X$ is directed from the Earth to the sun). Consequently, when specifically discussing biases in the B_y component resulting from the changing orientations of the spin and geomagnetic axes, perhaps a coordinate system such as the GSM system, which automatically incorporates these effects, is better suited for ordering the ISEE data.

In the vicinity of the Earth, where the dipole contribution to the total magnetic field is a maximum, the variations in magnetic field component magnitudes due to the continual change in orientation of the spin and geomagnetic axes, are best accounted for in the GSM system. In fact, the $(B_y)_{\text{GSM}}$ component necessarily represents the un-biased cross-tail component since it is calculated in the frame of reference of the dipole axis. On the other hand, no biases in the $(B_x)_{\text{GSE}}$ component occur since in both coordinate systems the B_x component is identical. In GSM coordinates, changes in the magnitudes of B_y and B_z are complimentary. That is, an increase in B_y is accompanied by a decrease of the same magnitude in B_z . Conversely, if $|B_y|$ decreases by a given amount, $|B_z|$ will increase by this same amount.

At larger distances downtail, the effect on the magnetic field configuration due to the direction of the solar wind flow increases (recall that the tail is "hinged" at $\approx -12 R_e$ downtail), and as well, other processes may begin to affect the tail orientation (such as the torque on the

tail resulting from IMF influences, discussed by Cowley (1981)). The effect of the dipole tilt may become less significant as $|X|$ increases, and therefore, the GSE system may become increasingly more appropriate as the system in which, to order the *in situ* magnetic measurements. At intermediate X values a coordinate system which combines the GSM and GSE systems is perhaps desirable. Unfortunately, since no accurate measure of the changing orientation of the tail field with increasing distance downstream of the Earth is available, it is difficult to quantify the appropriateness of one system with respect to any other.

The overall trends in B_y biases expected to influence the $(B_y)_{GSE}$ field component will be investigated using the results of a computer program which calculates these biases. The GSM coordinate system will be considered here to represent the un-biased magnetic field configuration, since it incorporates the position of the geomagnetic axis. The program determines the relative GSE components of a unit magnitude magnetic field vector in GSM coordinates which represents the field observed by a satellite when it is positioned at the neutral sheet. That is, for an idealized neutral sheet encounter, $|\bar{B}| = (|B_z|)_{GSM} = 1$ and $(|B_x|)_{GSM} = (|B_y|)_{GSM} = 0$. Also, because the X component of the field in both coordinate systems is identical, then $(B_x)_{GSE} = (B_x)_{GSM} = 0$ at the neutral sheet. Since $|B_y|$ is also expected to be approximately zero at the neutral sheet, then the value of $(B_y)_{GSE}$ obtained through the calculations

represents the B_y bias in terms of a fraction of the total magnetic field magnitude. Biases calculated in this way will represent the maximum possible bias in $(B_y)_{GSE}$ which can result from the spin and geomagnetic axes orientations. Note that no conclusions may be drawn from these calculations regarding either the change in bias with downtail distance of the satellite, or the effects on B_y due to any possible torque exerted on the tail by the IMF.

The program listing is given in appendix A. The algorithm is based on a series of coordinate transformation matrices outlined by Russell (1971). Essentially, the transformations from GEI (geocentric equatorial inertial) to GSE coordinates, and from GEI to GSM coordinates are required in order to calculate the transformation from GSM to GSE coordinates. Both the method and notation used in this program identically follow those used by Russell; therefore, further details will be omitted here.

A second version of the program (listed in appendix B), is a modification of version one, and it calculates the unbiased B_y component (ie: $(B_y)_{GSM}$). In this case, the time of the event (UT) as well as the day and year, and the three magnetic field component magnitudes measured by the satellite in the GSE system, are the input parameters.

From the output of version one of the program (appendix A), it is evident that the magnitude of the B_y bias at the neutral sheet in GSE coordinates changes throughout the day and as the year progresses (recall that bias values are

calculated as a fraction of a total field of 1 nT). At the winter solstice (\approx day 356 for 1979) the B_y bias at the neutral sheet may be positive or negative in sign depending on the time of day (ie: depending on whether the effect of the geomagnetic axis tilt adds to or subtracts from that of the spin axis tilt). The maximum positive and negative biases on this day are essentially the smallest maximum biases observed throughout the year (except that they are equalled at the summer solstice). This is expected since at the winter solstice the spin axis is aligned in the $(X-Z)_{GSE}$ plane and consequently the only contributions to B_y arise through the dipole axis tilt. The maximum positive bias for day 356 is +0.22 which occurs at \approx hour 23 UT, whereas the maximum negative bias has a value of -0.21 which occurs at \approx hour 11 UT. These results are also expected. For the winter solstice, the maximum positive bias occurs at 18:00 in the local time frame of the geomagnetic north pole (the maximum positive bias of the day is expected when the dipole is oriented towards dusk). The maximum negative bias occurs at 6:00 in the time frame of the geomagnetic north pole (the maximum negative bias is expected when the dipole axis is tilted towards dawn). Minimum positive and negative biases of ± 0.2 occur at hours 17:00 UT and 5:00 UT respectively, which translate to local times at the geomagnetic north pole of 12:00 and 0:00 respectively, and this also confirms expected results. Variations in bias throughout the day are smooth and periodic.

Negative biases are expected in 1979 until mid-January. By January 15 the negative biases, which occur for only selected hours depending on the combined effects of axes orientations, have become negligibly small. After this time only positive biases are observed until approximately 25 days prior to the summer solstice (\approx day 147, near the end of May). Therefore, throughout the spring season only positive biases are expected to be observed in the $(B_y)_{GSE}$ measurements. The magnitude of the positive biases maximizes at the vernal equinox (\approx day 80). The maximum positive bias of +0.57 occurs on this day at hour 23 UT, whereas the minimum positive bias of +0.21 occurs at hour 11 UT. These times correspond to hour 18 and hour 6, respectively, in the local time frame of the geomagnetic north pole, and therefore provide the expected results since the maximum positive bias at the vernal equinox should occur when the dipole axis is tilted towards dusk, and similarly, the minimum positive bias at this time should occur when the dipole is oriented towards the dawn. As well, the minimum positive bias at the equinox is of approximately the same magnitude as the maximum positive bias at the solstice.

Finally, between the summer and winter solstices B_y biases mirror those which occur between the winter and summer solstices, except that the polarity is reversed such that negative biases prevail in the autumn season (the maximum negative bias occurs at the autumnal equinox and it equals the magnitude of the maximum positive bias which

occurs at the vernal equinox).

The maximum positive bias (which occurs at the vernal equinox) has a value of +0.57, and this number represents the positive increase in B_y , from the expected $B_y=0$ at the neutral sheet, for a total field magnitude of unity. Hence, for a total field of, for example, 10 nT at the neutral sheet, a maximum B_y bias of approximately 6 nT may be observed in the $(B_y)_{GSE}$ data. In other words, for a measurement of $(B_y)_{GSM}$ of zero magnitude, a maximum $(B_y)_{GSE}$ component magnitude of 6 nT should be observed in the data due to the influence of the spin and geomagnetic axes tilts, and this would occur at the vernal equinox.

Consequently, from the B_y bias calculations, it may be noted that for the data set employed in the studies of this chapter, which incorporate events throughout the spring season (mid January to mid June), positive biases in $(B_y)_{GSE}$ will predominate when ISEE 1 is located at the neutral sheet. Furthermore, a B_y bias of approximately 60% of the total tail field is the maximum bias that can occur as a result of spin and geomagnetic axes orientations. Negative biases are possible only for the early part of January and beyond the end of May. These negative biases are observed for only some hours of the day, and as well, their magnitudes are very small. Therefore, negative B_y biases of any appreciable size (>2.0 nT) observed in the spring between mid-January and early June are not explainable within this framework.

Now that the trends in B_y biases due to spin and geomagnetic axes tilts have been established, it may be determined whether or not it is possible for these expected trends to account for positive B_y biases observed in the magnetotail magnetic field measurements during the spring season. In terms of long range temporal expectations, since the sampling rate of the ISEE 1 magnetometer is about four seconds, the existence of any diurnal as well as seasonal shifts in B_y should be readily visible in the data. However, there is no indication of either a seasonal or a daily trend in B_y biases, as is evident in figure 4.29 which is a plot of B_y bias as a function of both time of day and year for the 302 events in the data set of section 4.3. An inspection of the graph reveals no distinct seasonal increase in positive bias towards the equinox, which is marked in the figure by the vertical dotted line. The expected trend in bias, for a total field of 20 nT, is indicated by the solid sinusoidal curve. However, the magnitudes of the positive biases vary randomly throughout the season with no distinct bias maximum being apparent at any time. Furthermore, events exhibiting negative B_y biases, ones for which B_y is constant and non-zero at the apparent neutral sheet, and as well, examples of well-defined neutral sheet encounters, also appear randomly throughout the data set. If a systematic variation in positive B_y bias was to occur, then one would not expect to observe any well-defined neutral sheet encounters near equinox since the magnitude of the B_y

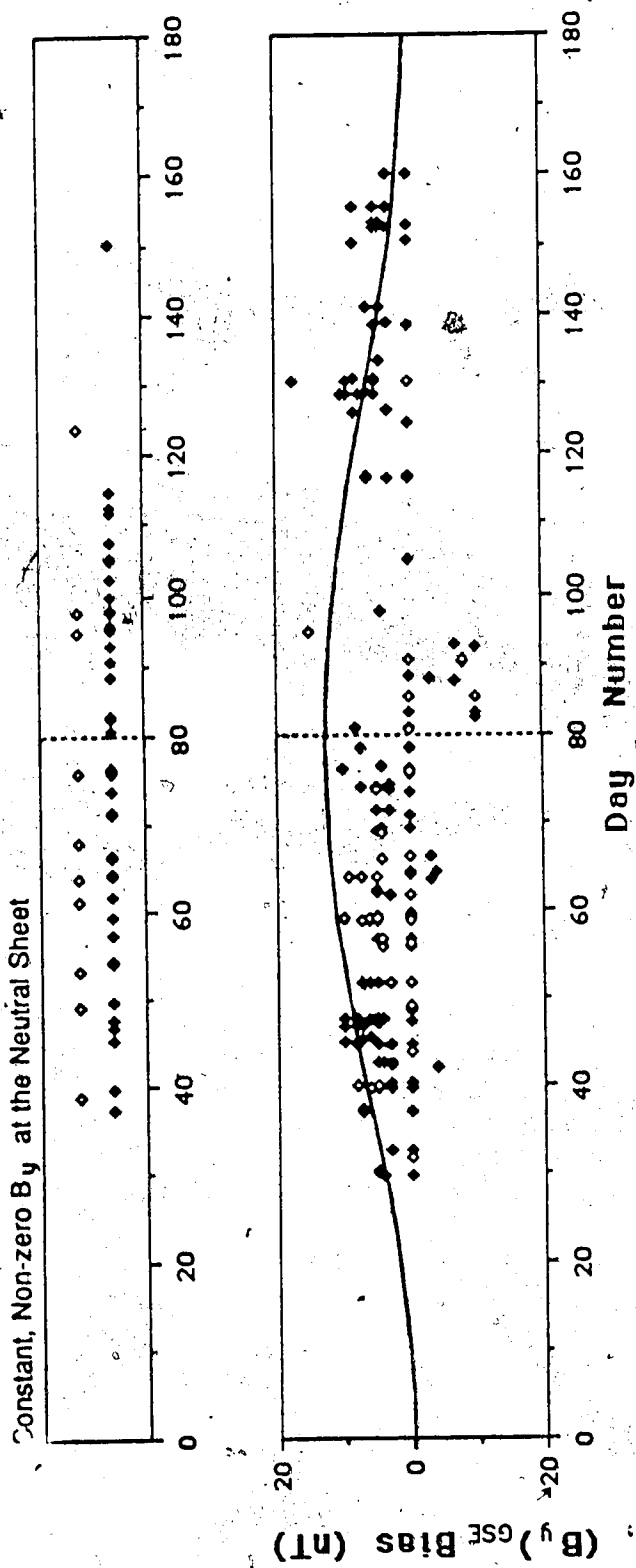


Figure 4.29 B_y bias plotted as a function of Universal Time for the 302 event subset of the 1978/1979 data set. The vertical dotted line marks the vernal equinox, and the solid sinusoidal curve indicates the expected trend in B_y biases for a total field of 20 nT. The hollow diamonds represent 1978 events while the bold diamonds indicate 1979 events.

component would always be larger than it should be at this time of year. Clear-cut neutral sheet encounters are, however, observed near the spring equinox. It appears, then, from these observations, that the steady variations of the tilting Earth's axes do not adequately account for the occurrence of positive B_y baseline shifts.

In order to partially understand why the expected results do not evidently agree with observation, the assumptions made in calculating the magnitudes of the expected B_y biases require consideration. The results of the program which calculates the B_y biases represents a first order approximation to those biases which would occur if a more realistic model of the geomagnetic tail were to be incorporated in the modelling routine. The program, as it stands, considers the Earth's magnetosphere to be an idealized dipole of infinite extent which is unaltered by the solar wind. The effects on the B_y biases, therefore, due to temporal and spatial fluctuations in the magnetotail configuration, are not reflected in the calculations, and as well, no indication is given regarding how the B_y biases change with increasing distance downtail. Consequently, the program results are best used as guidelines according to which trends in B_y biases may be investigated.

It is of interest in the framework of the foregoing analysis to study specific magnetic events included earlier in this chapter in order to determine whether or not the influence of the spin and geomagnetic axes orientations is

great enough to produce biases which occur in actual magnetogram observations.. Of particular importance is the question of whether or not it is possible to account for the magnitudes of the B_y biases observed through straight forward alterations in tail geometry resulting from varying orientations of both the rotation and geomagnetic axes.

Recall the data listed in table 4.1, which includes the calculated value of $(B_y)_{GSM}$ for the six B_y bias events in question (ie: two events for each of positive, negative and zero- B_y biases). Consider first the biases and satellite locations for the two positive B_y bias events. On day 42, 1979, hour 18, which lies approximately half way between the winter solstice and the vernal equinox, ISEE 1 was located relatively close to the Earth. For the neutral sheet encounters of this event (ie: 18:24 and 18:26), $(|B_y|)_{GSE} = +4$ nT (ie: a bias of +4 nT). On day 126, 1979, hour 03, which is roughly half way between the vernal equinox and the summer solstice, ISEE 1 was located farther downtail at $X = -18$ Re. For the neutral sheet encounter of this event (ie: 3:36), $(|B_y|)_{GSE} = +2.5$ nT coincident with $(|B_x|)_{GSE} = +2.0$ nT. However, since the satellite was located in the northern hemisphere dusk sector at this time, the polarity of B_y should be negative. Consequently, the B_y trace appears biased by +4.5 nT. In comparing these two situations it may be noted that the difference in downtail distance of the observing satellite did not result in a larger bias for day 42 than for day 126 as might be

expected. Rather, both events are approximately equally displaced temporally from the equinox, (ie: one before and one after), and so, the effect of the Earth's spin axis tilt should be comparable in each case.

For the event of day 42, the calculated value of $(|B_y|)_{\text{GSM}}$ is $+0.4$ nT, and for that of day 126 $(|B_y|)_{\text{GSM}} = -0.4$ nT. In both cases the calculated $(B_y)_{\text{GSM}}$ magnitudes approach 0 nT as is expected at the neutral sheet, and on day 126 $(B_y)_{\text{GSE}}$ is negative as it should be in the northern dusk sector. Therefore, for these two examples, the positive B_y biases observed in the $(B_y)_{\text{GSE}}$ traces can be attributed, at least in principle, to the choice of coordinates in which the magnetic data were presented.

Consider next the two negative B_y bias events listed in table 4.1. For the neutral sheet encounter at 11:33 on day 90 (March 31), 1979, $(|B_y|)_{\text{GSE}} = -8$ nT (ie: bias of -8 nT is observed), whereas on day 64 (March 5), 1979, at both 10:34 and 10:42, $(|B_y|)_{\text{GSE}} = -4$ nT (-4 nT bias). However, since the two events both take place in the late spring, negative biases are not expected. The $(|B_y|)_{\text{GSM}}$ values calculated for the two events are -8.9 and -1.0 nT for day 90 and day 64, respectively. In both cases, $(|B_y|)_{\text{GSM}}$ is of non-zero magnitude at the apparent neutral sheet, and for the event of day 64, B_y is even more biased in a negative sense after the transformation to GSM coordinates. Consequently, the choice of coordinate system cannot be considered as the cause of the negative biases, and

therefore, some physical process must be in operation to produce the anomalous B_y field magnitudes.

Finally, the influence of the orientation of the spin and geomagnetic axes must be considered for the two examples of well-defined neutral sheet encounters (or zero- B_y biases) on days 39, 1979 (hour 14 UT) and 73, 1979 (hour 14 UT). A value of $(|B_y|)_{\text{GSM}} = -1.0$ nT is calculated for both spring season events, respectively. Only minimal differences appear between the magnitudes of the B_y field components in the two coordinate systems. The effects of both the spin and geomagnetic axes/orientations at the times of these events are relatively small, essentially lying within the error margins of the magnetograms. Therefore, it is evident that the observation of neutral sheet crossings proper are physically possible even when axes tilt effects are taken into account.

So, from the preceding analyses, it has been shown that some positive B_y biases can be physically explained in terms of the influence of the diurnal and seasonal variations in the orientation of both the Earth's rotation and geomagnetic axes. On the contrary, negative B_y biases observed in the late spring season, cannot be understood in this framework. Therefore, some other processes ongoing in the magnetotail must be the source for the occurrence of such biases. In addition, neutral sheet encounters in the true sense may be observed regardless of the existence of biases due to axes orientations. Note that the question of constant, non-zero

B_y during an apparent neutral sheet encounter is not addressed by the above considerations.

4.5 Investigation of Solar Wind Influence on Atypical B_y Signatures at the Neutral Sheet

Ultimately, it is the solar wind which shapes magnetospheric structure; consequently, it might be expected that an examination of variations in solar wind parameters should provide insight into the occurrence of atypical B_y signatures observed in the magnetotail by ISEE 1. In addition, the level of geomagnetic activity might be expected to reflect anomalous tail B_y behaviour since the magnetospheric configuration is influenced by fluctuating activity levels. A quantitative investigation will be made here of the variations of solar wind velocity, density and temperature, as well as the AE level, for the four classifications of B_y signatures outlined in section 4.3. This will be followed by a study which attempts to determine whether or not any relationship exists between the IMF B_y and the cross-tail magnetic field component.

Histograms showing independently the frequency of occurrence of each of the three solar wind parameters for the data set selected in section 4.3 are given in figures 4.30, 4.31 and 4.32. Arithmetic mean values for each parameter were calculated to be 425 km/s for solar wind velocity, 9 cm^{-3} for solar wind density, and $75 \times 10^3 \text{ }^\circ\text{K}$ for solar wind temperature. For each histogram, the arithmetic

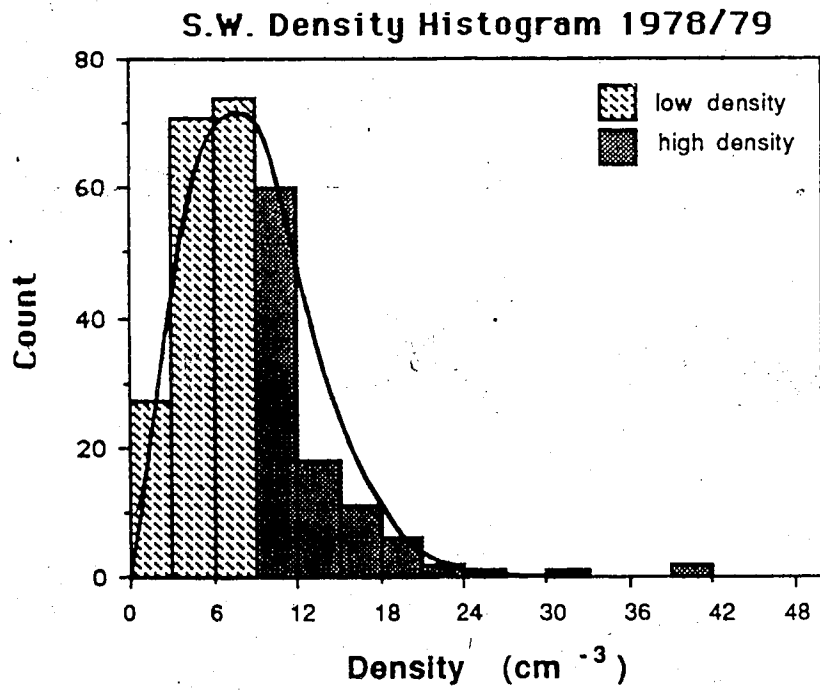


Figure 4.30 Histogram showing frequency of occurrence of solar₃ wind density data. The mean value of the data is 9 cm^{-3} .

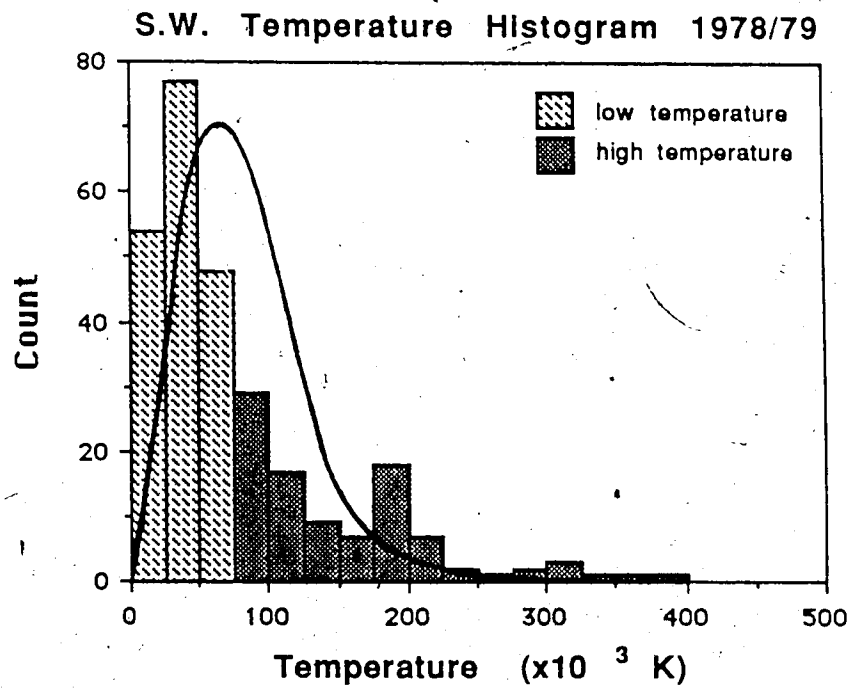


Figure 4.31 Histogram showing frequency of occurrence of solar wind temperature data. The mean value of the data is 75×10^3 K.

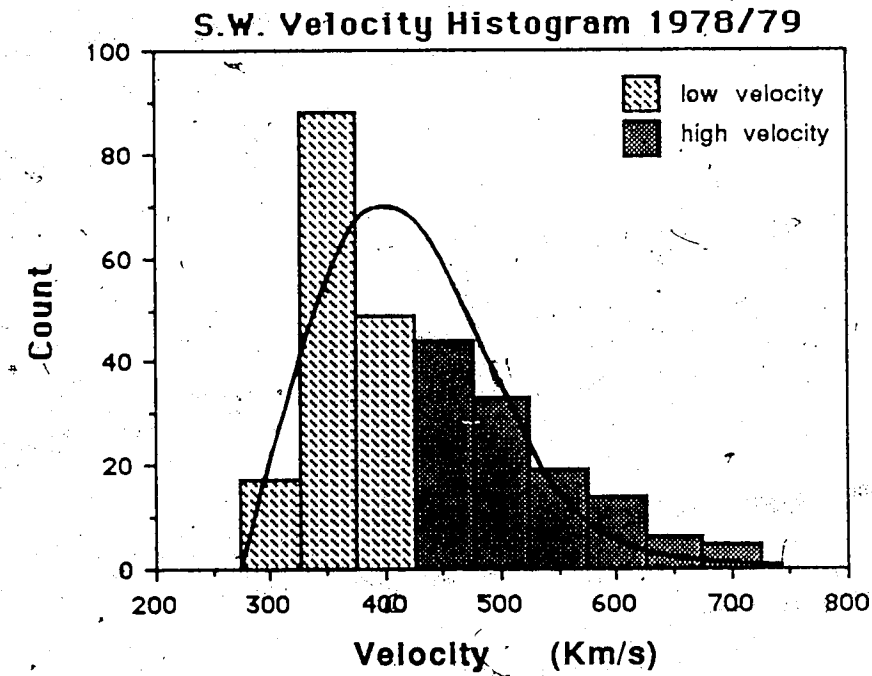


Figure 4.32 Histogram showing frequency of occurrence of solar wind velocity data. The mean value of the data is 425 km/sec.

mean of the respective parameter measurements was chosen to represent the boundary between low and high parameter magnitude. The two magnitude categories are indicated on each graph by different patterns of shading.

Table 4.2 summarizes the percentage of events in the two categories of low and high parameter magnitude for each of the four classifications of B_y behaviour at the neutral sheet discussed at the start of section 4.3. In addition, the corresponding B_y values, categorized into low, intermediate and high activity (as per section 4.2.3), are included in the table. Note that the total number of events is different for each of the three solar wind parameters considered since data gaps resulting from non-continuous satellite tracking are present. Of the 302 events compiled in the data set for section 4.3, only 276 events are accompanied by solar wind velocity measurements, solar wind density data is available for 274 events, and 278 solar wind temperature values are recorded, with an AE index measurement being available for all 302 events.

From a division into the two magnitude bins of all observations of a given parameter in one of the B_y classifications, any irregularities which may exist in the distribution will become apparent. Such irregularities may be significant in identifying a possible source for the atypical B_y signature being studied. For example, an unusually large proportion of high magnitude parameter observations may suggest an association between that

Table 4.2 : Division of Event Subset into Activity Level and Solar Wind Parameter Magnitude Categories

	AE		Density		Temperature		Velocity	
	low $0 < AE \leq 150$ nT	intermediate $150 < AE \leq 400$ nT	low $\leq 9 \text{ cm}^{-3}$	high $> 9 \text{ cm}^{-3}$	low $\leq 75 \times 10^3$ K	high $> 75 \times 10^3$ K	low ≤ 425 Km/s	high > 425 Km/s
Positive By biases	67.5% of 126	23.8% of 126	56.0% of 116	44.0% of 116	77.6% of 116	22.4% of 116	77.8% of 117	22.2% of 117
Negative By biases	28.6% of 14	35.7% of 14	78.6% of 14	21.4% of 14	28.6% of 14	71.4% of 14	21.4% of 14	78.6% of 14
Zero By biases	63.4% of 82	25.6% of 82	71.4% of 70	28.6% of 70	74.0% of 73	26.0% of 73	50.7% of 71	49.3% of 71
By constant, non-zero at Neutral Sheet	48.8% of 80	37.5% of 80	64.9% of 74	35.1% of 74	42.7% of 75	57.3% of 75	32.4% of 74	67.6% of 74
Overall	59.6% of 302	28.5% of 302	63.5% of 274	36.5% of 274	64.7% of 278	35.3% of 278	55.8% of 276	44.2% of 276

parameter and the unusual B_y behaviour. However, if the distribution of observations into the two magnitude bins is comparable to an expected distribution then it appears unlikely that the parameter in question significantly influences the cross-tail magnetic field component.

It has already been shown in section 4.2.3 that no apparent correlation between the magnitude of the AE index and that of either $|B_x|$ or $|B_y|$ has been observed. This does not necessarily discount the possibility that the occurrence of a particular classification of B_y signatures may be dependent on the magnitude of AE. However, the percentages of AE observations in the three magnitude bins listed for the B_y categories of well-defined neutral sheet encounters, positive B_y biases, and constant, non-zero B_y at the apparent neutral sheet tend to support the conclusion that AE and $|B_y|$ are uncorrelated. Since low, intermediate and high magnitude ranges were defined in figure 4.6 so as to include in each category 51.4%, 31.2% and 17.4% of all observations, respectively, then any subset of events should statistically fill the three bins according to these proportions if the subset represents a random sampling. For each of these three B_y classifications the maximum percentage occurs in the low AE magnitude bin and the minimum percentage in the high AE magnitude bin as expected from the distribution in figure 4.6. The percentages quoted, however, indicate that a larger proportion of events than expected coincide with low AE for both neutral sheet

encounters proper (17% more) and positive B_y bias events (12% more), whereas for the classification of constant, non-zero B_y at the neutral sheet, the intermediate AE bin holds 7% more events than expected. Only for the category of negative B_y biases do the observed percentages not follow the same trend set by figure 4.6, with the maximum percentage of events occurring in the medium and high AE ranges followed by a lower percentage in the low AE range. Whether or not this deviation from the expected trend is significant is uncertain since only a small number of events (14) fall into the negative B_y bias category. The number of values in the low, medium and high magnitude bins are 4, 5 and 5, respectively, consequently, no meaningful conclusions can be drawn from the distribution of negative B_y biases. In general, then, little evidence to support a correlation between AE magnitude and the presence of anomalous B_y signatures at the neutral sheet has been obtained.

Consider next the percentages of points in each magnitude category for the three solar wind parameters in question. In order to interpret these results, a standard is required to which the observed percentages may be compared. Such a standard may be obtained by analysing the occurrence frequency histogram for each solar wind parameter in terms of a probability distribution model which represents the experimental distribution. The solar wind density observations may be represented by the Poisson distribution (Parratt, 1961) which is defined according to:

$$f(k) = P(k; \mu) = \frac{\mu^k e^{-\mu}}{k!} \quad (22)$$

where P is the probability, μ is the mean of the mathematical model distribution, and k is the classification interval index (k marks the center point of each interval, and the first interval is denoted by $k=0$). Note that this distribution is a function of only one parameter, the mean μ , and the value of μ therefore determines the nature of the frequency distribution curve. The experimental mean, m , for the solar wind density histogram is 9 cm^{-3} which translates to $\mu=2.5$ (midway between bin $k=2$ and bin $k=3$). The Poisson distribution curve for $\mu=2.5$ is superimposed on the solar wind density histogram of figure 4.30. Note that equation 22 gives the normalized probability, therefore, P must be multiplied by N , the total number of events, before the probability curve is plotted.

One criterion which must be met for the Poisson distribution to represent a good fit to a set of experimental data is that the mean value, μ , must lie within one value of k to the right of the most probable value of k , k_0 , which represents the classification interval most frequently sampled. For the model distribution with $\mu=2.5$, $k_0=2$. For the solar wind density histogram $k_0=2$ as well,

therefore, the mean of 2.5 falls within the required limit. Clearly, the Poisson distribution represents a good fit to the solar wind density experimental data.

Consequently, the number of measurements expected in each of the two magnitude categories (low and high) can be determined according to the model distribution. The Poisson cumulative distribution is calculated using the following equation:

$$\sum_k P(k; \mu) \equiv \sum_k (\mu^k e^{-\mu}) / k! \quad k=0, n \quad (23)$$

where the summation is stopped at the desired value of n . Note that the total cumulative probability approaches unity as n approaches infinity. It is of interest to determine the percentages of events likely to fall within the two magnitude categories of low and high, and for the solar wind density data these values may be obtained by calculating the summations from $k=0$ to $k=2$, and from $k=3$ to $k=13$, respectively. The results from these two summations indicate that the probability of a solar wind density observation falling within the low density category is 0.65 and that of a similar observation falling within the high density category is 0.35, giving a total probability of unity, which indicates that the number of events in the data set of interest is sufficient for such a statistical analysis.

Therefore, 65% of all observations of solar wind density are expected to be of low magnitude, whereas the remaining 35% are expected to be of high magnitude, if the data are accurately represented by a Poisson distribution. From table 4.2, 173 low density and 101 high density values (total of 274) are observed, giving a proportionality of 63%:37% which is reasonably close to the expected result.

The histogram for solar wind temperature (figure 4.31) may be analysed using the same technique. The experimental mean, $m=75 \times 10^3$ °K, representing the separation line between low and high temperature, again lies intermediate to the bins denoted by $k=2$ and $k=3$. Therefore, the model mean is given by $\mu=2.5$ as was the case for the solar wind density data. The Poisson distribution superimposed on figure 4.31 is identical to that applicable to the solar wind density histogram. Consequently, 65% of all observations are expected to fall in the low temperature category, with the remaining falling in the high temperature category. The solar wind temperature data, however, are not as well represented by a Poisson frequency distribution as are the solar wind density data. The most probable classification interval in this case is $k_0=1$, and the mean, μ , falls farther to the right of k_0 than one value of k . However, the observed percentages of measurements falling within the low and high temperature categories are 65% and 35%, respectively, and this is in agreement with the expected proportionality for a Poisson distribution with $\mu=2.5$.

Therefore, the experimental proportionality provides a valid standard according to which observed percentages of events in the two magnitude categories and for each classification of B_y signatures may be compared.

In figure 4.32 the experimental mean value of $m=425$ km/sec also falls between the bins specified by $k=2$ and $k=3$, and this corresponds to $\mu=2.5$. The relevant Poisson distribution curve is superimposed on the histogram. The model distribution approximately fits the data, however, the fit is not as good as might be desired. The mean value falls 1.5 classification intervals away from k_0 , and therefore, the desired criterion for an accurate fit is not satisfied. The Poisson distribution for $\mu=2.5$ provides a cumulative probability of 65% that an observation of solar wind velocity will fall in the low velocity category, and a 35% probability of obtaining a high velocity measurement. Experimentally, 56% of the measurements of solar wind velocity fall in the low magnitude category whereas the remaining 44% fall in the high magnitude category.

Finally, the observed percentages of low and high magnitude of each solar wind parameter and for each of the four classifications of B_y behaviour at the neutral sheet may be analysed with respect to the proportionalities expected from the Poisson distribution which approximates the distributions of the experimental data. In each case, if the proportion of low to high observations is comparable to that expected from the Poisson distribution relevant to the

solar wind parameter in question, then it can be concluded that the B_y behaviour is independent of that solar wind parameter. However, when the observed percentages differ greatly from the expected proportionality, a relation between the solar wind parameter and the classification of B_y behaviour may be implied. A threshold value of 15% will be chosen such that if the difference between the experimental and expected percentages is $\leq 15\%$ it will be considered that no relationship exists.

Consider first the solar wind density proportionalities. For all four classes of B_y behaviour, the maximum percentage falls in the low density category as predicted by the Poisson distribution. An expected 65% of events in the class of constant, non-zero B_y at the neutral sheet is observed, whereas 56% of the positive B_y biases, 79% of the negative biases and 71% of the neutral sheet encounters proper correspond to low magnitude densities. Consequently, the magnitude of solar wind density appears to be unrelated to the occurrence of atypical B_y behaviour at the neutral sheet, since all the above values fall within 15% of the expected percentage from the Poisson distribution.

Such is not the case with the results for solar wind temperature data. For both positive and zero biases, 78% and 74% of all events in the respective category fall in the low temperature range, and these values lie within the 15% uncertainty limit. In contrast, only 29% of negative bias

events, and 43% of events in the constant, non-zero B_y category fall in the low magnitude range (ie: 36% and 22% lower, respectively, than expected). This indicates that perhaps these two categories of B_y behaviour are dependent on the magnitude of solar wind temperature, and in particular, on high temperature values. Again, however, for the category of negative B_y biases, the small number of events (14) renders the reliability of this result questionable.

Similarly, 78% of positive bias events coincide with low magnitudes of solar wind velocity, a value which is 13% higher than expected. 51% of zero-bias events fall within the low magnitude solar wind velocity category, and this is 14% lower than expected (although, this value still represents the majority of events for this B_y classification). However, the percentages of events in the low magnitude category for both negative biases and constant, non-zero B_y at the neutral sheet are 21% and 32%, respectively, which are 44% and 33% lower, respectively, than the expected proportionality. It consequently appears that these two categories of B_y behaviour are also dependent on solar wind velocity, specifically on high velocity values.

Again, care must be taken in basing conclusions on the small sample size of negative B_y biases. Only 14 occurrences of negative biases were observed for which solar wind parameter measurements were available. Nevertheless, the

consistency in the three solar wind parameter sets is interesting. However, the tendency for observations of constant, non-zero B_y at the apparent neutral sheet to occur coincidentally with higher values of solar wind velocity and temperature may be legitimate since the sample size of 74 (75) events should be large enough to give a reliable indication of trends in the data. Hence, some evidence for attributing irregular tail B_y behaviour to variations in the solar wind parameters of temperature and density has been gained, and this perhaps warrants future investigation with the employment of a larger data base.

4.5.1 IMF B_y Penetration

One final solar wind parameter which must be considered as a possible contributor to atypical tail B_y signatures is the B_y component of the IMF, which may in some way influence the cross-tail magnetic field component of the magnetotail, as discussed in section 2.5 in the context of IMF B_y penetration.

The validity of the proposed theories mentioned in section 2.5 will be investigated here through a study of the data set compiled according to the criteria outlined in section 4.2.4. IMF B_y values are not available for all events in the master data set since communication with ISEE 3 (the satellite which collected much of the solar wind data) was intermittently disrupted, particularly in 1978, resulting in gaps in the data. Only events for which both

tail B_y and IMF B_y values were present are applicable when analyzing the effects, if any, of the IMF on the magnetotail field. The data set for the following analysis consists of 414 events from 1978 and 745 events from 1979, for a total of 1159 data entries. Recall that hourly averages of each parameter are employed.

First, consider a statistical comparison of tail B_y and IMF B_y , similar to those conducted by Fairfield (figure 2.5) and Lui (figure 2.6). Figure 4.33 is a scatter plot of tail B_y vs. IMF B_y for all the 1978 and 1979 events, while figures 4.34, (a) and (b), are plots of these two parameters for 1978 and 1979, respectively. In figure 4.33, the scatter in the data is quite substantial and there appears to be no strong indication of a direct correlation between the two parameters. However, a slight tendency is noted for the occurrence of a greater number of points with tail B_y and IMF B_y of the same sign than of opposite signs, suggesting some trend in the data exists. Because of the high degree of scatter in the data, the question of whether or not this trend is significant must be addressed in order to test the validity of the IMF B_y penetration theory.

A technique involving *principal component analysis* (Hotelling, 1933; Jolliffe, 1986), will be used here in order to quantify the appropriateness of conducting a linear regression analysis for a scatter plot of two variables. In the linear regression calculations it is assumed that the independent variable is accurate (ie: that its values have

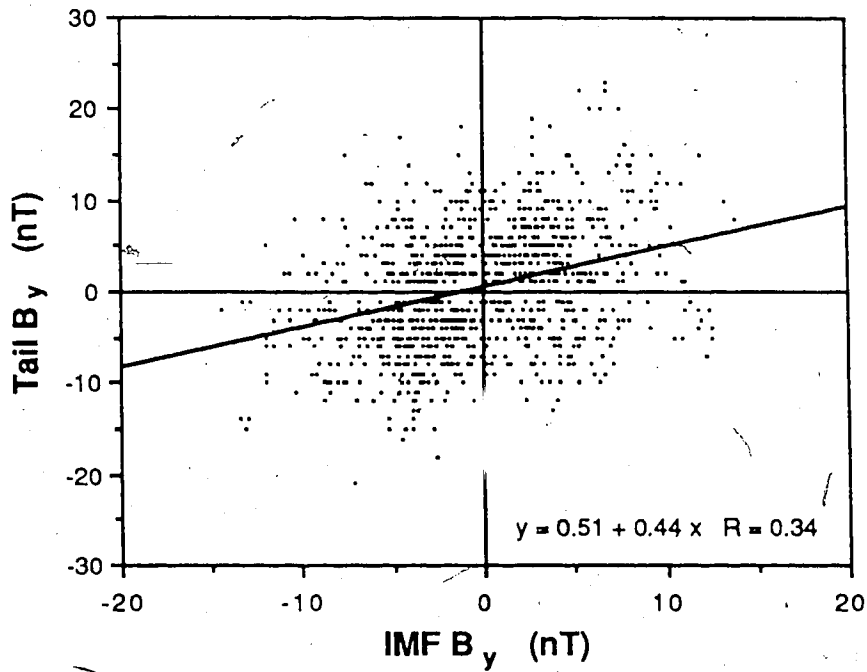


Figure 4.23 Scatter plot of tail B_y (hourly averages) as a function of simultaneous hourly averaged IMF B_y for all data in the 1978/1979 data set for which IMF data was available.

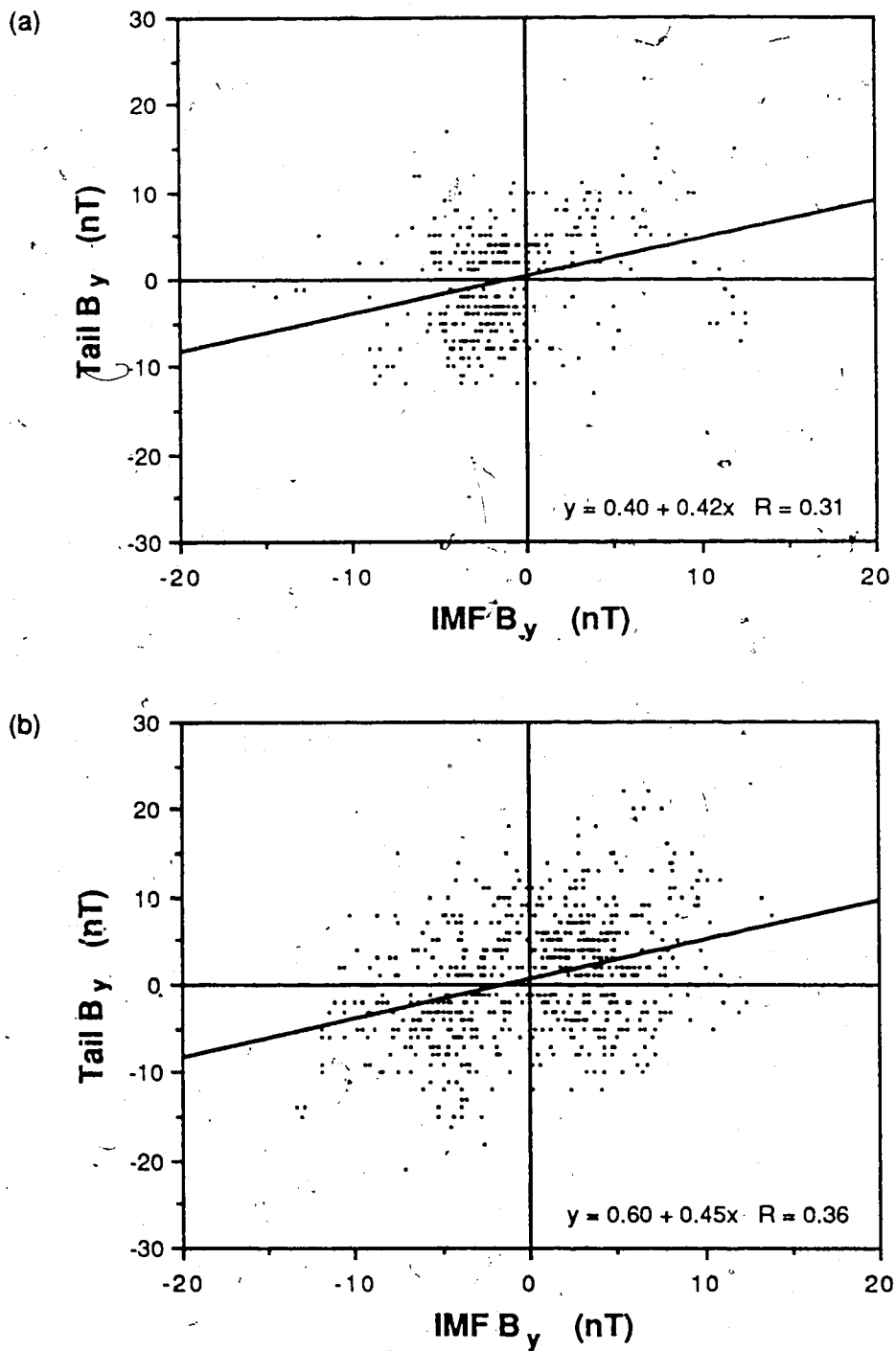


Figure 4.34 Same as figure 4.33 but for (a) 1978 data only, and (b) 1979 data only.

associated with them no uncertainty). However, this is not the case in the present studies since both tail and IMF B_y measurements contain some degree of uncertainty. The uncertainty in the independent variable is taken into account by the principle component method, and hence, comment on the validity of any apparent linear trend in the data set may be made with the results from this technique.

Essentially, the principle component technique "fits" an ellipse about the scattered data, and the shape of the ellipse is then analysed in order to determine whether or not it is appropriate to discuss a linear correlation between the two variables. Two eigenvalues, λ_1 and λ_2 , are measures of the major and minor axes lengths, respectively, and their ratio gives an indication of how well the data is represented by a linear relationship. If the ratio of λ_1/λ_2 is very large then the data is well represented by a linear relationship; however, if this ratio is very small (approaches unity) then the scatter in the data is very substantial (the ellipse approaches a circular shape) and a linear regression analysis cannot be justified. If the ratio gives an intermediate result then some degree of linearity in the data is present. As well, two eigenvectors may be calculated, from which the ratio of the components $V(2,1)/V(1,1)$ gives the slope of the linear fit to the data. This slope should correspond to that obtained through the standard linear regression technique.

For all studies conducted in this section, the ratio of λ_1/λ_2 will be determined in order to test for the significance of fitting a linear regression curve to the data. If the ratio gives a value greater than or equal to 2, it will be assumed that there is some degree of validity in conducting a linear regression analysis; however if the ratio gives a value of less than two it will be assumed that the tail and IMF B_y data are not clearly linearly related (J. Samson, private communication).

For figure 4.33 the ratio of λ_1/λ_2 gives a value of 2.42 which suggests that although the two parameters do not vary in a distinctly linear fashion, a slight trend is evident. Consequently a linear regression analysis has been conducted for these data for the purpose of comparison with the results of Fairfield and Lui. According to the best linear fit, a slope of 0.44 and a regression coefficient of 0.34 are obtained from the regression line, which is displayed on the graph in the form $y=b+mx$ (where y refers to the tail B_y and x refers to the IMF B_y) The value of the slope represents, according to the theory of IMF B_y penetration, the percentage of IMF B_y thought to penetrate the tail, which in this case is 44%. However, the small magnitude of the regression coefficient suggests that the raw data is poorly represented by the linear relationship shown. In addition, there does not appear to be any merit in fitting two separate regression curves to this data, one for positive and one for negative IMF B_y , as was done by

Tsurutani et al. (1986). This indicates that on the gross scale there is no evidence for varying degrees of IMF B_y penetration depending on the polarity of the IMF B_y component. In general, then, because of the significant degree of scatter in figure 4.34, although a slight linear trend is apparent, little in the way of convincing evidence is provided from this figure for the existence of a distinct relationship between the B_y components of the magnetotail and IMF.

The plots of B_y vs. IMF B_y for 1978 and 1979 data individually also show only slight linear trends. This statement is supported by the ratios of λ_1/λ_2 , which give values of 2.52 and 2.40 for figures 4.34 (a) and (b), respectively. There is a definite absence of data points in the quadrant of the 1978 graph for which tail B_y is negative and IMF B_y is positive; however, because of the irregular availability of IMF measurements during the early part of the year, any significance of this observation is questionable. Linear regression curves have been included for both plots, and according to the best linear fits, 45% and 43% of the IMF B_y component is suggested, according to the theory, to penetrate the tail for the 1978 and 1979 data, respectively. However, the regression coefficients are again low (0.31 for 1978 and 0.36 for 1979), and owing to the large amount of scatter in the data, the justification for regression analyses is somewhat tenuous.

Lui (1985) postulated that the IMF is shielded less in the plasma sheet than in the tail lobes, and consequently, found from his results that the degree of IMF B_y penetration was greater in this plasma domain (he includes both the CPS and PSBL in his use of the term "plasma sheet"). Further, he attributed the occurrence of what is known in this work as constant, non-zero B_y at the "apparent" neutral sheet to IMF B_y penetration which allowed for the enhancement of the tail B_y magnitude. In order to investigate these hypotheses, consider the independent scatter plots of tail B_y vs. IMF B_y for the CPS, PSBL and tail lobe plasma regimes; shown in figures 4.35, (a) and (b), and 4.36, respectively, each of which includes both 1978 and 1979 data. The values of λ_1/λ_2 for these graphs are, respectively, 2.48, 2.17 and 2.41, suggesting some degree of linearity in all three cases. Linear regression curves are also included in these three figures, and these suggest a 39% penetration of the IMF B_y component in the CPS, 32% in the PSBL, and 45% in the tail lobes, assuming validity in the theory of penetration (the respective regression coefficients are 0.28, 0.36 and 0.40 for the CPS, PSBL and lobe). According to these results, if penetration was to occur, it would be a maximum in the tail lobes, in contrast to Lui's conclusions.

Ideally, in order to draw reliable conclusions from figures 4.35, (a) and (b), and 4.36, each plasma domain should be represented by the same number of data points, and the size of the data set should be quite large. Of the three

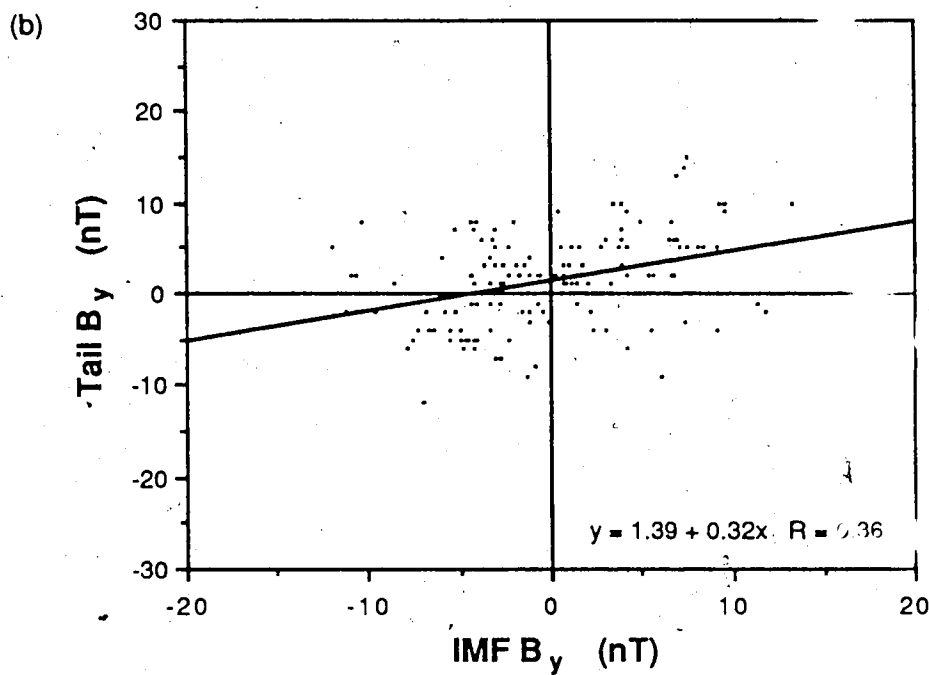
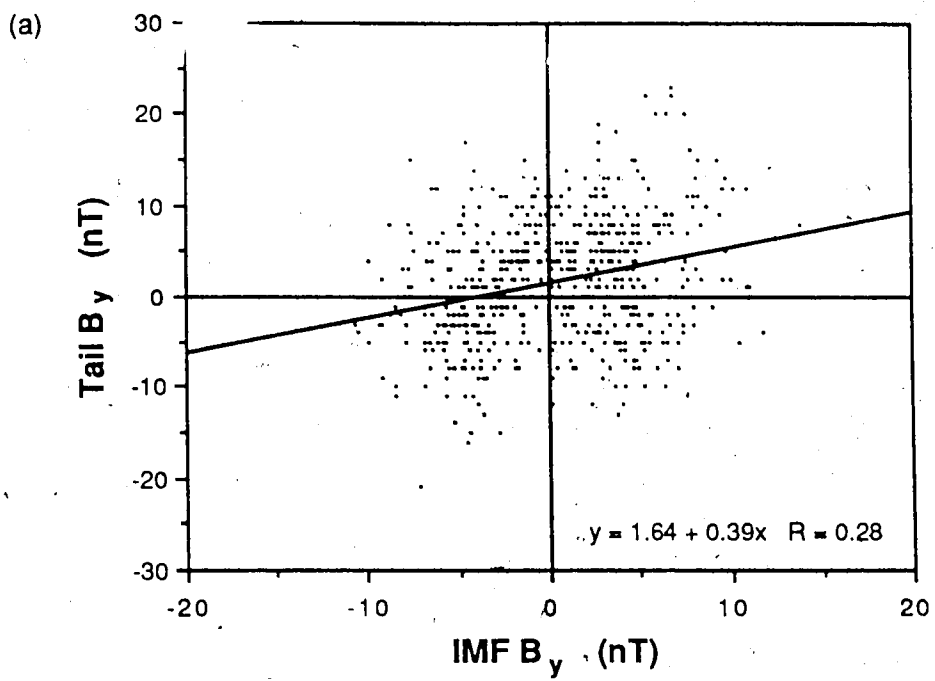


Figure 4.35 Tail B_y plotted as a function of IMF B_y for 1978/1979 samplings of (a) the CPS and (b) the PSBL.

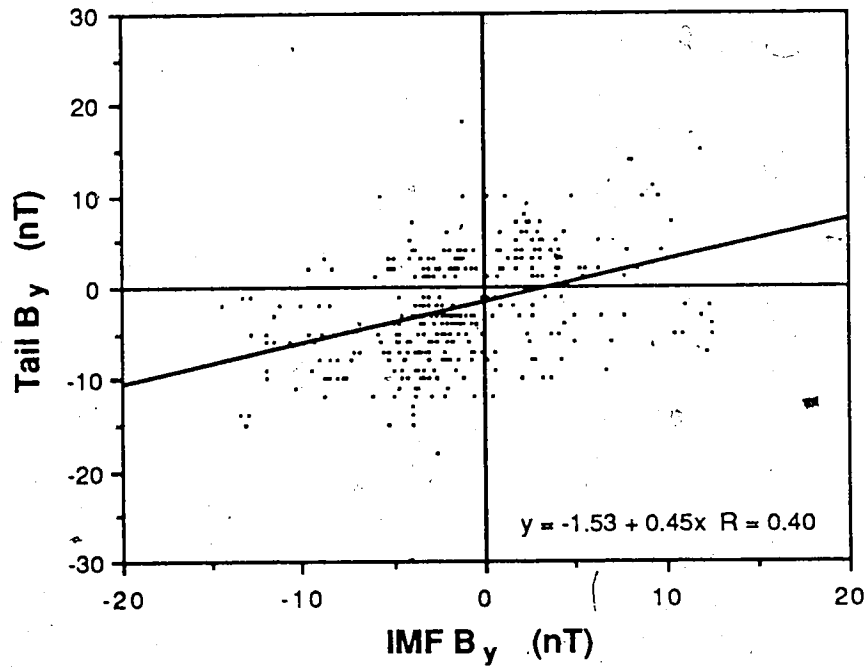


Figure 4.36 Same as figure 4.35 but for tail lobe samplings.

plasma regimes, the tail lobe appears to indicate the most distinct linear trend according to the value of the regression coefficient (followed by the PSBL); however, the value of λ_1/λ_2 suggests that the degree of linearity is slightly lower for the lobe than for the CPS and noticeably lower for the PSBL. In addition, as with the PSBL, the number of points representing the lobes is smaller than that representing the CPS. Since the three regimes are not equally represented, interpretations of both the linear regression and principal component analyses are somewhat uncertain, and it is not clear which of the three plots provides the most justifiable linear trend, and consequently the most reliable slope value. From the results presented here, Lui's postulate concerning greater IMF B_y penetration in the plasma sheet does not appear to be supported. Hence, his attributing constant, non-zero B_y at the neutral sheet to such increased penetration in this region remains unsubstantiated from these studies.

In order to investigate the hypothesis put forth by Cowley (1981) regarding the existence of preferred quadrants in the tail in which penetration of the IMF B_y component is most likely to occur, the 1978 and 1979 data for the CPS, PSBL and tail lobe regimes are divided into quadrants as defined in figure 3.3. Tail B_y vs. IMF B_y values are plotted in figures 4.37, (a) and (b), and 4.38, (a) and (b), for quadrants 1, 2, 3 and 4 of the CPS, respectively, in figures 4.39, (a) and (b), for quadrants 1 and 2 of the PSBL,

respectively, and in figures 4.40, (a) and (b), for quadrants 1 and 2 of the tail lobes, respectively. Note that limited data are available in quadrant 4 for the CPS, and no data are available in quadrants 3 and 4 for either the PSBL or tail lobes. This is the direct result of uneven spatial satellite coverage of the tail by ISEE 1 (recall the discussion of section 4.2).

Consideration of the regression analyses conducted for each of these figures indicates that IMF B_y penetration, as postulated, is not well supported in either quadrant. The suggested percentages of IMF B_y penetration in the CPS would be 0%, 19%, 29% and 15% for quadrants 1, 2, 3 and 4 respectively. The corresponding regression coefficients are 0.00, 0.2, 0.23 and 0.16. However, if there is any validity in the theory, quadrants 2 and 3 would then appear to be those of "preferred penetration", suggesting that the north-dusk and south-dusk quadrants are being influenced most by the IMF B_y component. This is in contrast to what is expected from the penetration hypothesis. Recall from figure 2.8 that preferred penetration in quadrants 1 and 3 is expected for negative IMF B_y , whereas preferred penetration is expected to occur in quadrants 2 and 4 for positive IMF B_y .

According to the principal component analyses, values of λ_1/λ_2 are 1.56, 2.73, 2.20 and 1.46 for quadrants 1, 2, 3 and 4 of the CPS, respectively. These support that the most justifiable linear trends occur in quadrants 2 and 3, and

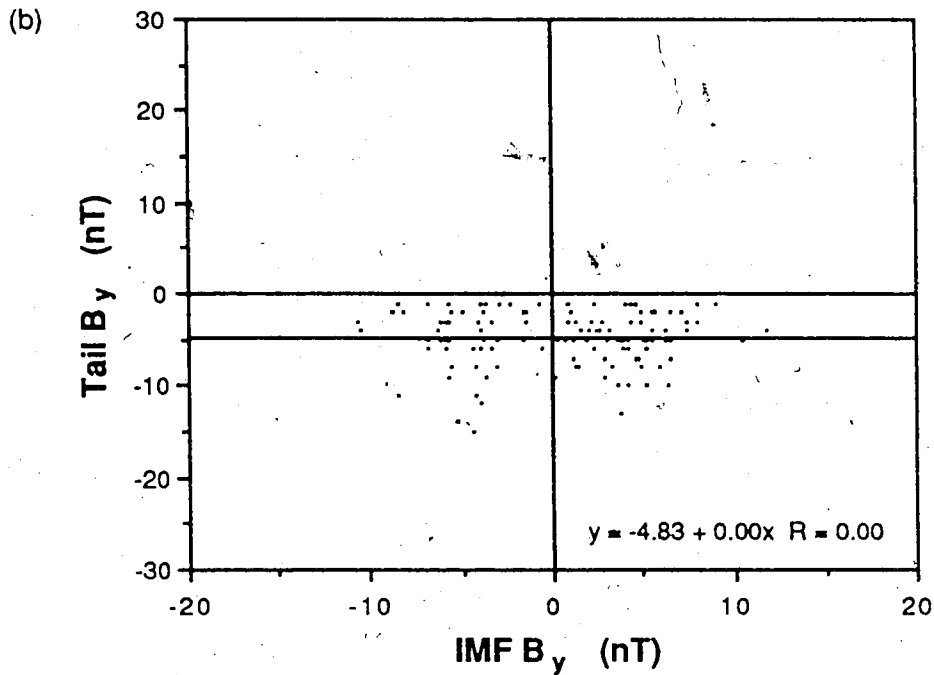
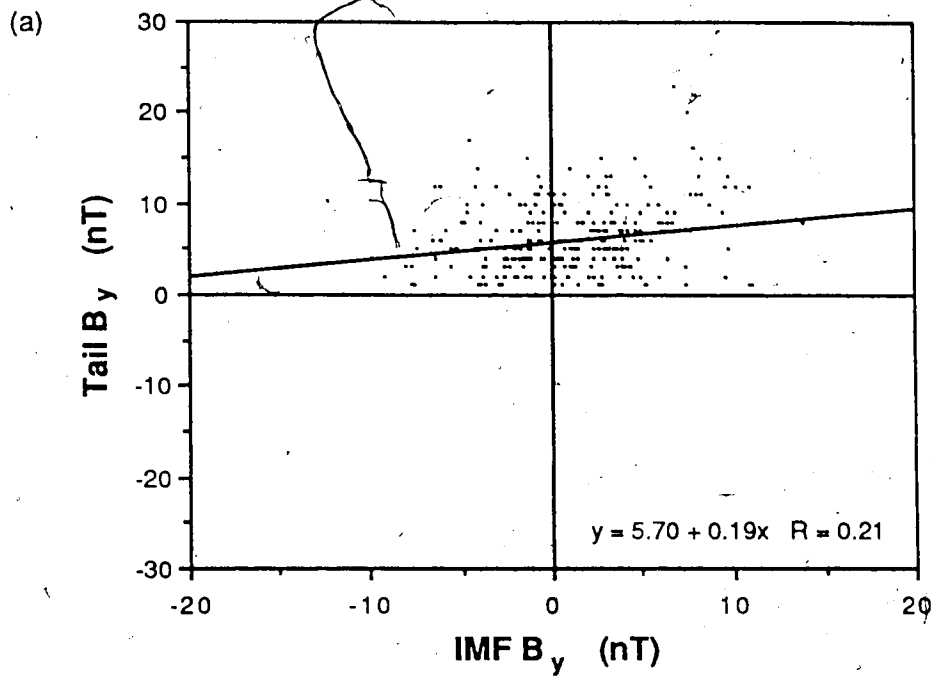


Figure 4.37 Tail B_y vs. IMF B_y for 1978/1979 samplings of the CPS, categorized into quadrants according to the definitions given in figure 3.3. Shown here are data from quadrants (a) 1 and (b) 2.

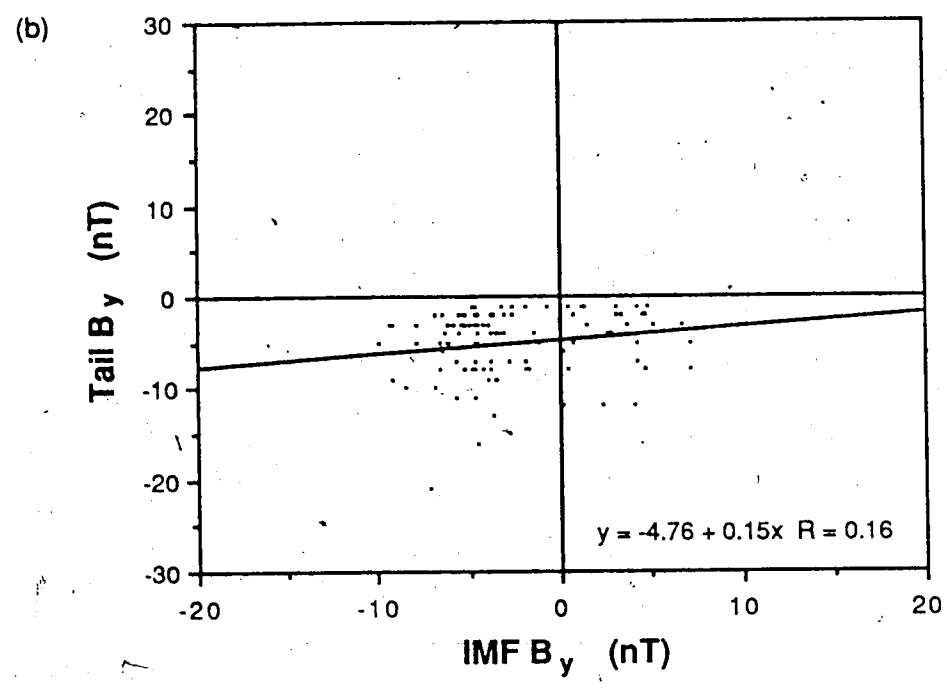
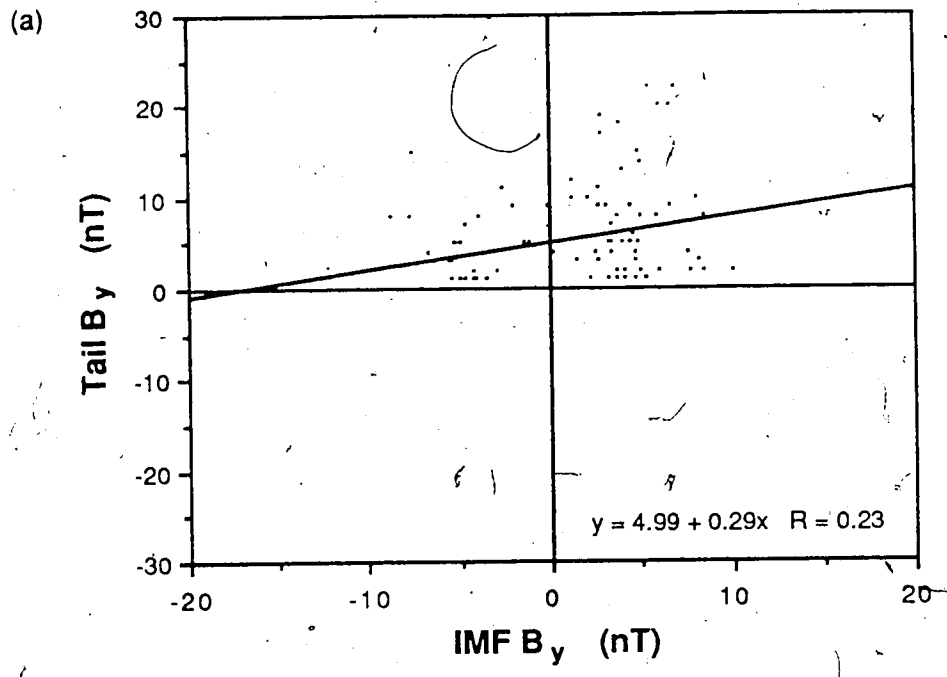


Figure 4.38 Same as figure 4.37 but for data from quadrants (a) 3 and (b) 4.

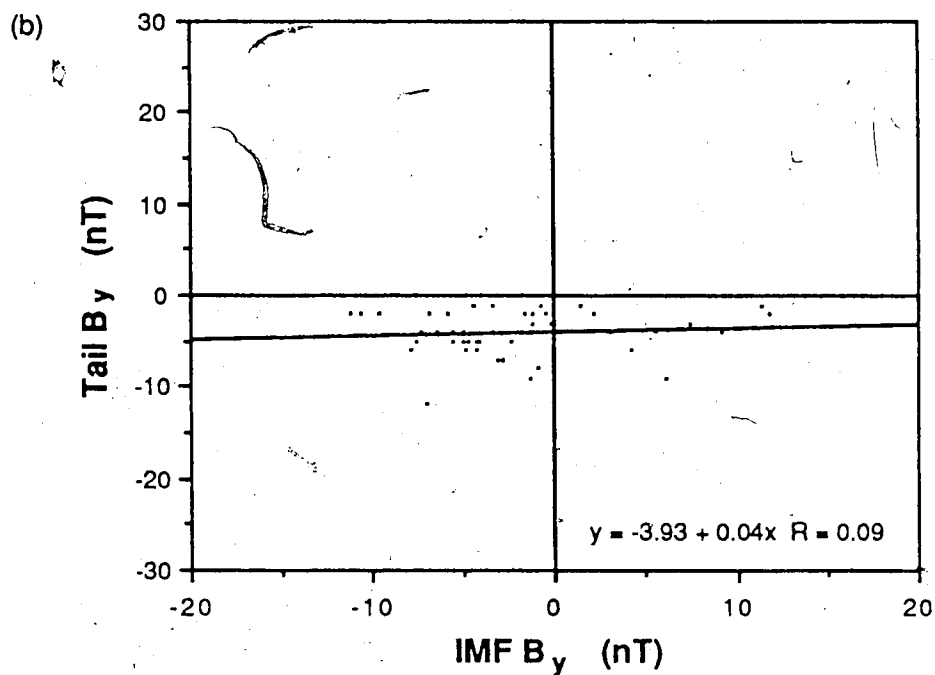
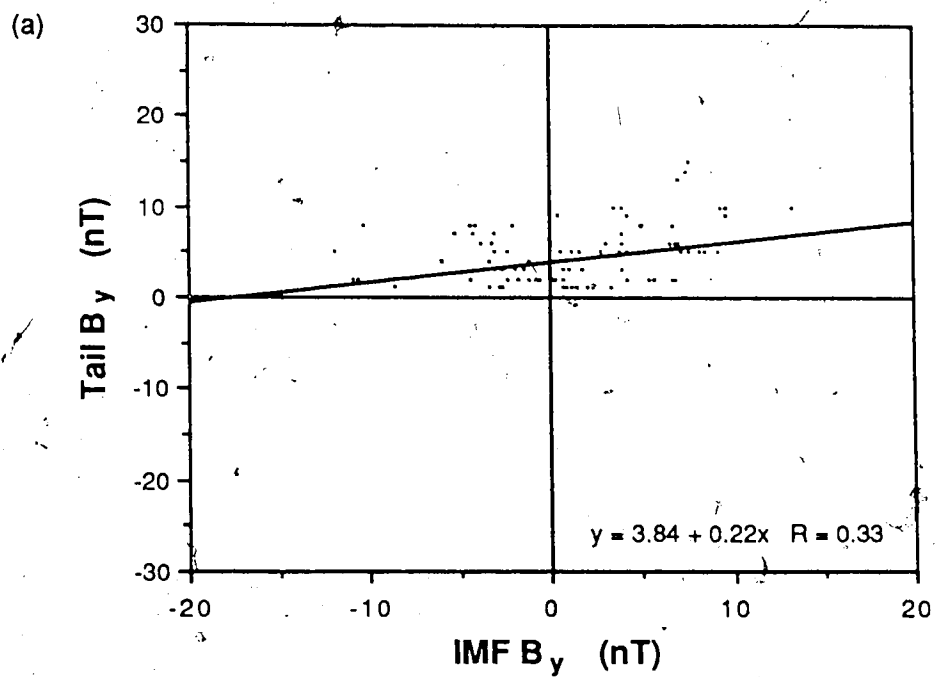


Figure 4.39 Tail B_y vs. IMF B_y for 1978/1979 samplings of the PSBL, categorized into (a) quadrant 1, and (b) quadrant 2.

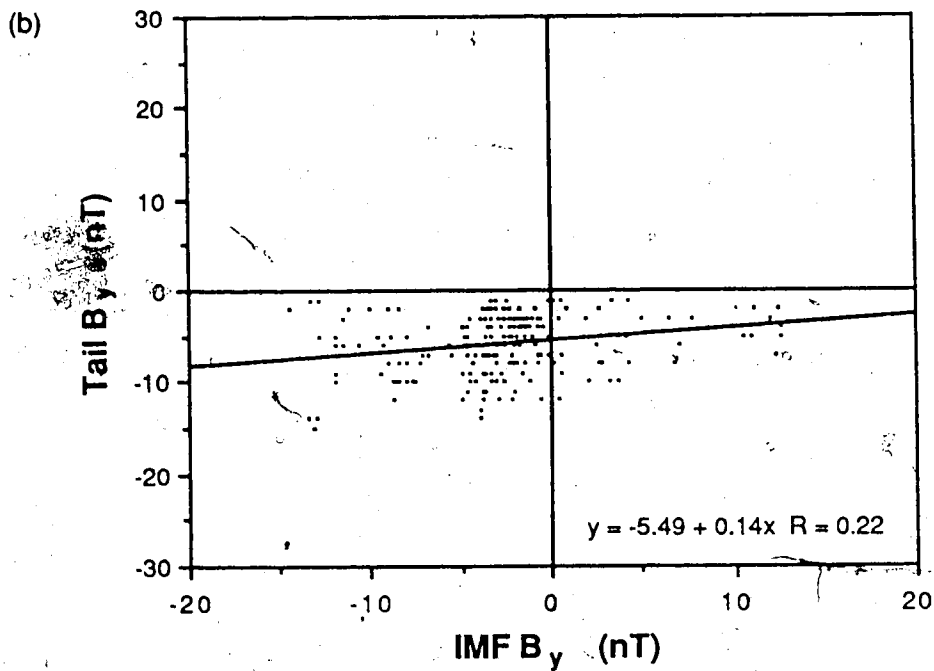
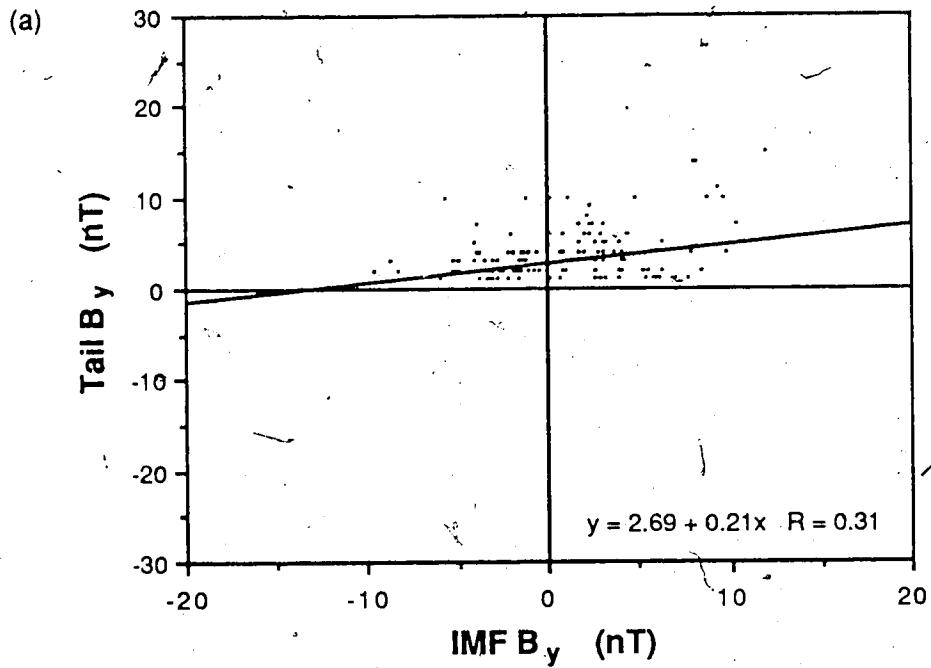


Figure 4.40 Tail B_y vs. IMF B_y for 1978/1979 samplings of the tail lobes, categorized into (a) quadrant 1, and (b) quadrant 2.

that the tail and IMF B_y parameters are poorly correlated in quadrants 1 and 4. Note that the results of the principal component analyses are in agreement with those of the linear regression calculations.

In the PSBL, the linear regression curve for quadrant 1 suggests a 22% penetration of the IMF B_y with a regression coefficient of 0.33. Quadrant 2, on the other hand, appears to allow only 4% penetration according to the hypothesis (regression coefficient of 0.09). In the lobe, the percentage of IMF B_y penetration in quadrant 1 would be 21% (regression coefficient of 0.31) and in quadrant 2 the penetration percentage would be 14% (regression coefficient of 0.22) if penetration actually occurs. Note that in these two plasma regimes, the linear regression results indicate that the lowest percentage of penetration of the IMF B_y would occur in quadrant 2. Values of λ_1/λ_2 are 2.92 and 4.87 for quadrants 1 and 2 of the PSBL, and 2.69 and 2.67 for quadrants 1 and 2 of the lobe, and these all suggest that linear trends are better justified in these two plasma regimes than in the previously discussed studies for the four-quadrants of the CPS.

Because of the very low values of the regression coefficients, and as well, the small magnitudes of the slopes obtained for each of the above quadrant analyses, the indication that penetration may occur preferentially in certain quadrants remains somewhat inconclusive. In the near-Earth regions of the magnetotail, then, evidence for

preferred penetration is minimal; however, this does not discount the possibility that preferred penetration (if penetration occurs at all) might take place in the distant tail, which was the region of focus in the study conducted by Tsurutani et al. (1986).

Next, consider the possibility of a dependence of the proposed IMF B_y penetration on either the polarity of the IMF B_z component, or similarly, on the magnitude of magnetospheric activity defined by the AE index. Both northward and southward turnings of IMF B_z (ie: a change from negative to positive polarity or vice versa), are known to be accompanied by increases in magnetospheric activity (Rostoker, 1983) which in turn are frequently reflected by increases in the magnitude of the AE index. Figures 4.41, (a) and (b), and 4.42 represent scatter plots of tail B_y vs. IMF B_y data for low, intermediate, and high activity, respectively (as defined in section 4.2.3), and figures 4.43, (a) and (b), are scatter plots of the two B_y parameters for positive and negative IMF B_z , respectively. The regression analyses for these studies show values of apparent IMF B_y penetration (followed by the corresponding regression coefficient, R) of 41% (R=0.32), 59% (R=0.42) and 25% (R=0.19) for low, intermediate and high activity respectively, and 36% (R=0.30) and 57% (R=0.38) for positive and negative IMF B_z , respectively. Values of λ_1/λ_2 are 2.30, 3.09, and 2.07 for low, intermediate and high AE, respectively, and 2.05 and 3.13 for positive and negative

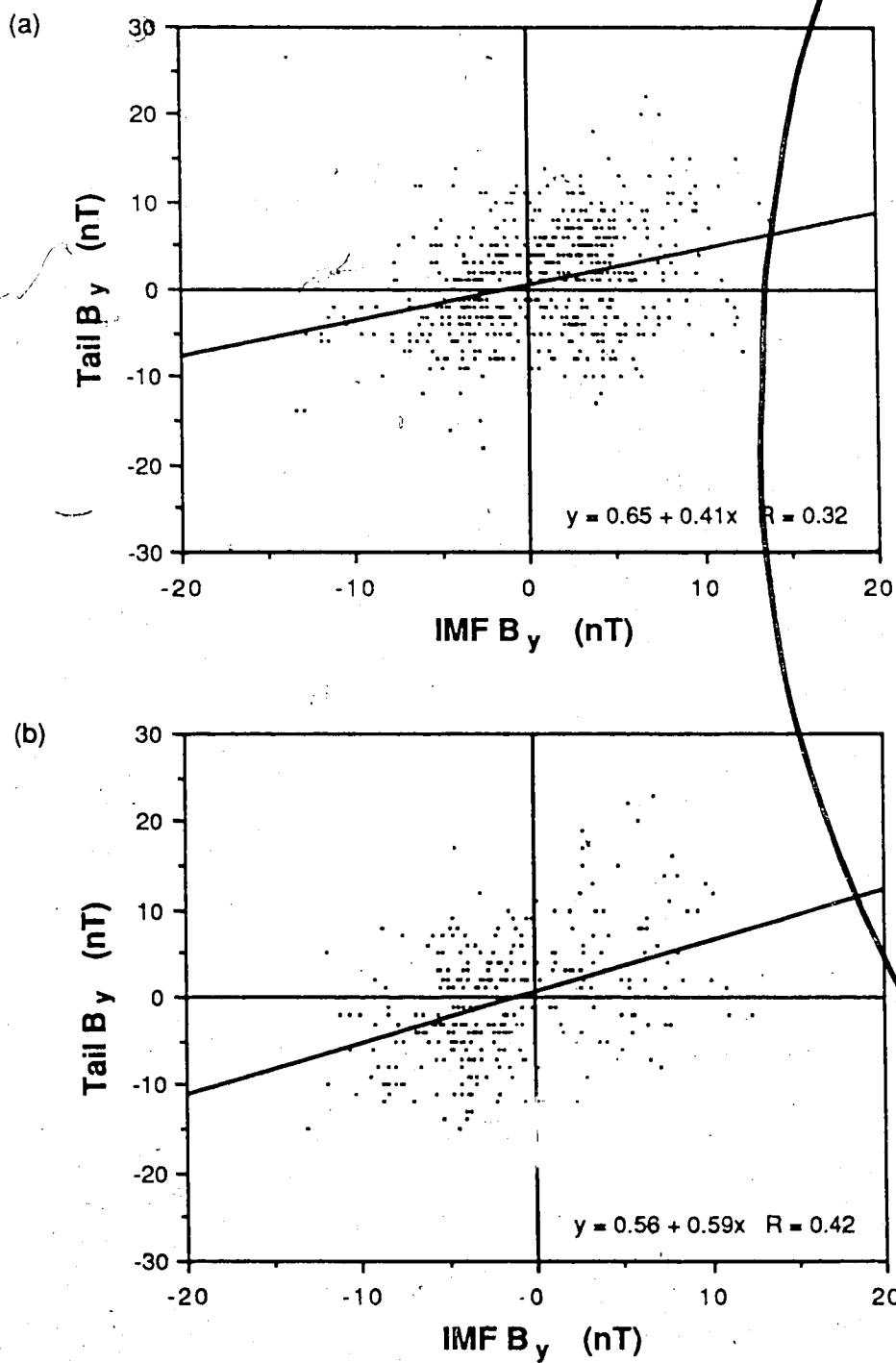


Figure 4.41 Tail B_y vs. IMF B_y for samplings of (a) low and (b) intermediate AE from the 1978/1979 data set.

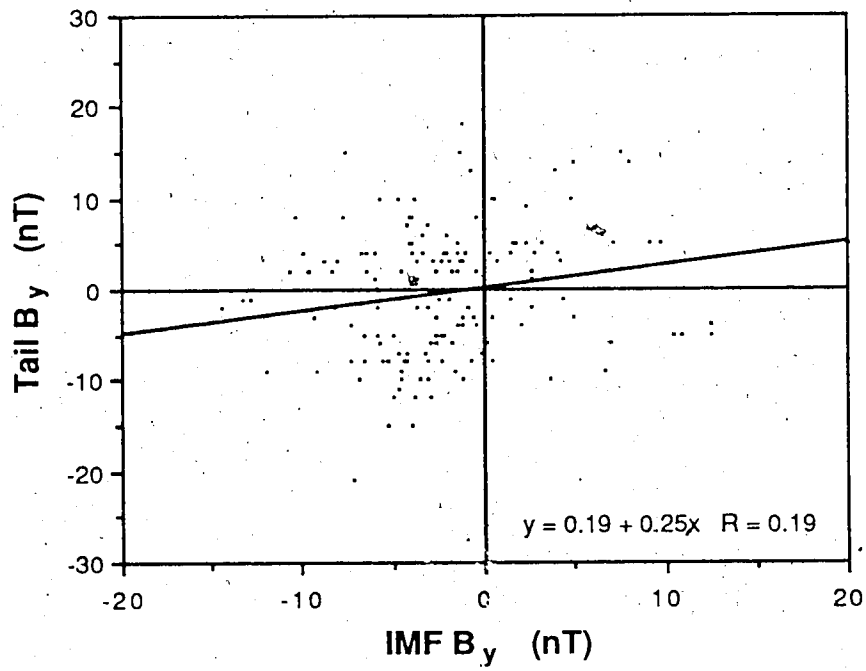


Figure 4.42 Same as figure 4.41 but for samplings of high AE.

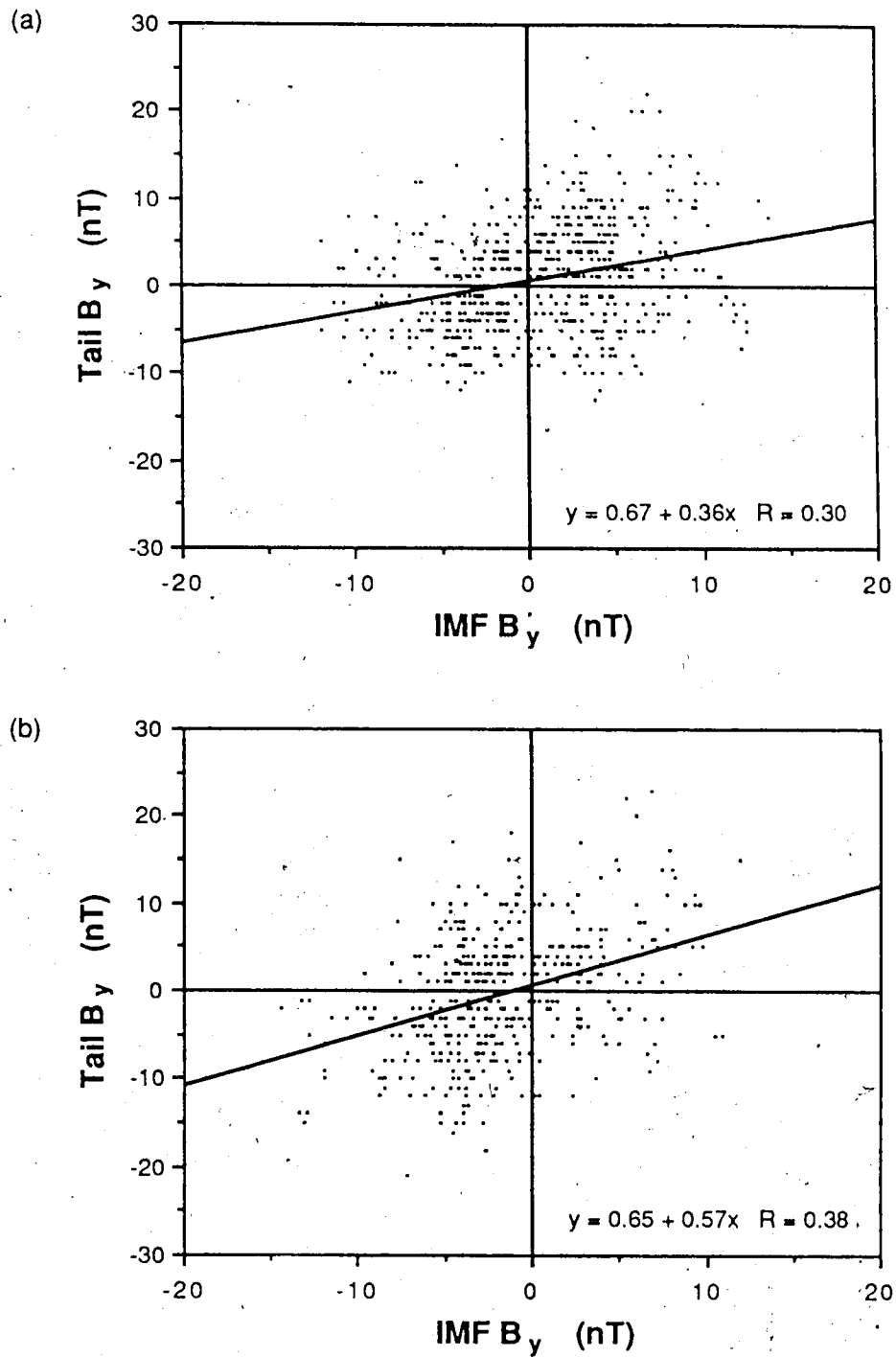


Figure 4.43 Tail B_y vs. IMF B_y for samplings of the 1978/1979 data set for which the value of IMF B_z was (a) positive, and (b) negative.

IMF B_z , respectively. In all five graphs the scatter in the data is substantial (regression coefficient values again are low); however, some support is given to a linear relationship between the two variables according to the principal component analysis technique. The suggested percentages of IMF B_y penetration for both intermediate activity and negative IMF B_z are larger than any observed in earlier analyses, and their reliability is supported by the values of λ_1/λ_2 obtained for these two cases.

Finally, the question of IMF B_y penetration may be considered in the context of the four categories of atypical tail B_y behaviour at the neutral sheet outlined earlier in section 4.3. Although when considering the entire data set there appears to be only minimal evidence to support the proposed influence of the IMF B_y component on tail B_y magnitudes, it is possible that for a specific subset of the data there may be some validity to the theory. With this in mind, plots of IMF B_y vs. tail B_y were constructed for the data in each of the three categories of positive B_y biases, negative B_y biases and constant, non-zero B_y at an apparent neutral sheet encounter, and these are shown in figures 4.44 (a), (b) and (c), respectively.

In the case of positive B_y biases (figure 4.44(a)) no linear trend indicating IMF B_y penetration is evident. Most of the 110 tail B_y values in this figure are positive (which is to be expected due to the nature of the bias), and although more points occur for positive than for negative

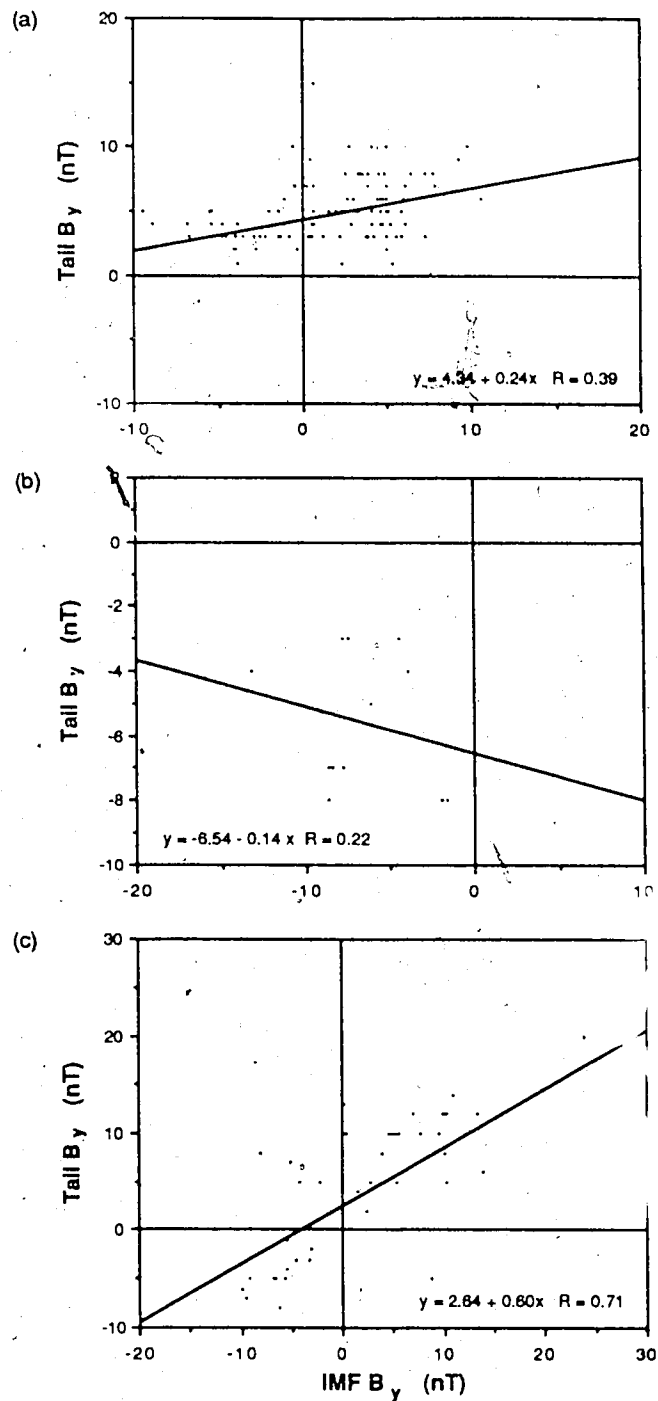


Figure 4.44 Plots of tail B_y vs. IMF B_y for data in each of the three categories of (a) positive B_y biases, (b) negative B_y biases and (c) constant, non-zero B_y during an apparent neutral sheet encounter.

IMF B_y , the scatter in the data is substantial. The linear regression analysis for these data suggests that 24% ($R=0.39$) of the IMF B_y would penetrate the tail. Figure 4.44(b) indicates that for each of the 12 data points in the category of negative B_y biases, both tail B_y and IMF B_y are of the same (negative) polarity. This perhaps suggests that IMF B_y does in fact influence the tail B_y component; however, the data set is so small that the result cannot be considered as conclusive.

The final plot, which displays the data for constant, non-zero B_y at the apparent neutral sheet (figure 4.44(c), indicates that for most of the 55 data points both IMF B_y and tail B_y are of the same polarity, whether it be positive or negative. Only five points lie in the quadrants for which the two parameters are of different sign. This result, therefore suggests the possibility of some validity in the IMF B_y penetration theory. From the linear regression analysis conducted for this figure, 60% of the IMF B_y appears to penetrate the tail. Since the regression coefficient has a relatively large value in comparison with all previous coefficients ($R=0.71$), this result is the only one which provides justification for the hypothesis of IMF B_y penetration. As well, since most of the events in this category of constant, non-zero B_y at the neutral sheet represent CPS samplings, the apparent linear trend here also tends to support Lui's suggestion that B_y enhancement at the neutral sheet may be a consequence of IMF B_y penetration.

However, once again, the data set is not as large as might be desired, and consequently, caution should be taken when drawing conclusions from this result.

Values of λ_1/λ_2 for these final three plots were calculated to be 3.6, 4.3 and 6.1 for positive biases, negative biases and constant, non-zero B_y at the neutral sheet, respectively. Each of these values is larger than the threshold value of 2, and consequently, the linear trends which appear are justifiable, especially for the last two categories of B_y behaviour at the neutral sheet. In particular, the value of λ_1/λ_2 for constant, non-zero B_y events clearly supports the linear trend observed in this data, and therefore, provides the only reliable evidence for the IMF B_y hypothesis.

Finally, the values of IMF B_y for the classification of well-defined neutral sheet encounters (ie: for which $|B_y|=0$), range from -7.9 to +8.0, and are relatively evenly distributed between positive and negative IMF B_y (45% and 55%, respectively, of the 65 events in this category for which IMF B_y values were available). This indicates that the IMF B_y component appears to have little or no influence on well-defined neutral sheet encounters.

As a last note, because cases do exist in each B_y category for either polarity of IMF B_y , then regardless of statistics and any possible validity of the IMF B_y penetration hypothesis, the cases which do not conform with the theory require explanation, and the sources of the

anomalous B_y behaviour must be identified in order for the magnetotail configuration to be adequately understood.

Chapter 5

Distortion of the Magnetotail Magnetic Field by Large-Scale Field-Aligned Currents

In this chapter further investigation into the causes of non-zero B_y at an "apparent" neutral sheet encounter (ie: where $|B_x| \approx 0$ nT) will be conducted. As will be demonstrated, the term "apparent" is the key to understanding such events, since many of these do not, in fact, represent neutral sheet encounters. Rather, the X component of the magnetotail magnetic field has been reduced to zero magnitude, at a location other than the neutral sheet, as a consequence of the presence of large-scale field-aligned currents which are capable of producing perturbation magnetic fields that can severely distort the normal tail magnetic field configuration. Details of the mechanism by which $|B_x|$ may be reduced to zero will be discussed following a case study of an event such as described here.

5.1 Case Study: Day 75, 1979

Consider the ISEE 1 magnetogram for day 75 (March 16), 1979, hour 21, shown in figure 5.1. GSE coordinates are used to display the magnetic field traces in this representation. For this event, ISEE 1 was situated in the northern hemisphere, dawn sector of the tail at a location specified by $X_{GSM} = -21$ Re, $Y_{GSM} = -7.2$ Re, and $Z_{GSM} = 0.5$ Re. The Russell-Brody and Fairfield models for determining the position of the neutral sheet, both indicate that the

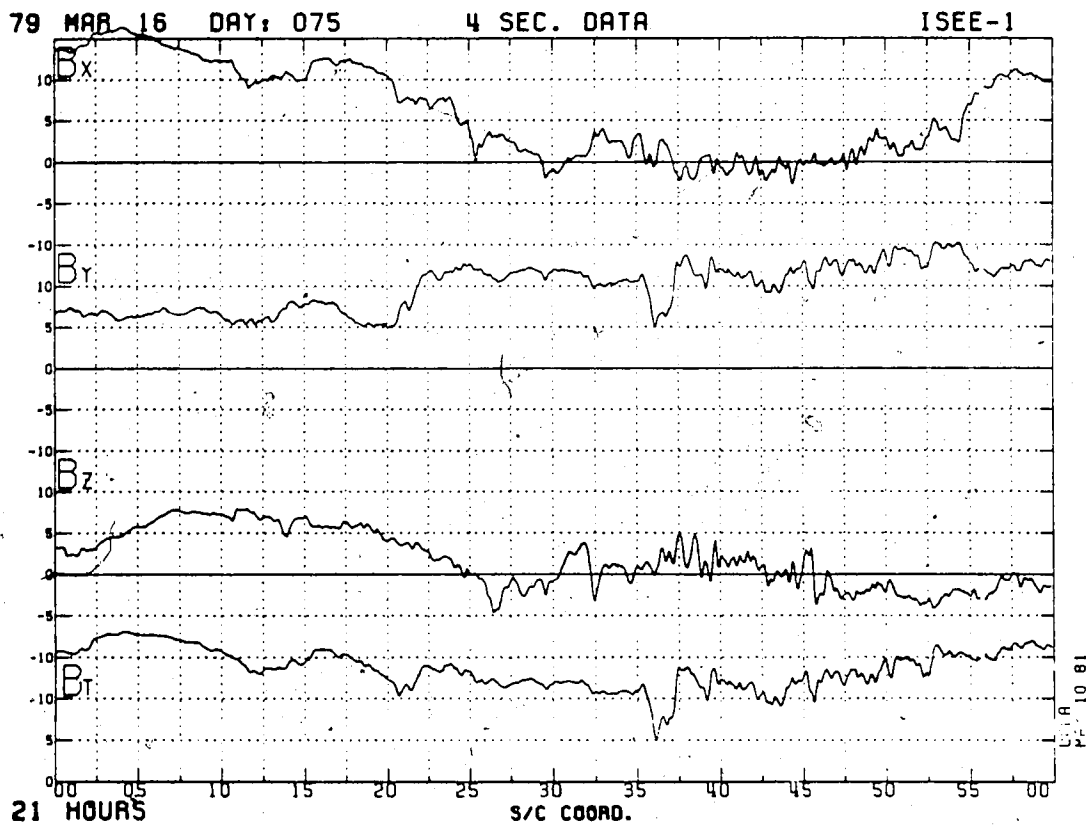


Figure 5.1 ISEE 1 magnetogram in GSE coordinates for hour 21, day 75 (March 16), 1979.

neutral sheet was located at $Z_{\text{GSM}}=0.0$ Re, and this suggests that ISEE 1 was in the vicinity of the neutral sheet at this time.

In figure 5.1, the B_x component magnitude is observed to decrease from ≈ 15 nT at the start of hour 21 to ≈ 0 nT by 21:30. ISEE 1, therefore, appears to encounter the neutral sheet at 21:30 as indicated by the magnitude of B_x at this time. This interpretation further suggests that the satellite remains in the vicinity of the neutral sheet for the next 20 minutes, until about 21:50, when the magnitude of the B_x component begins to increase. However, the B_y trace for this hour displays a rather unusual signature for a supposed neutral sheet encounter. Not only does B_x remain positive in polarity for the entire hour but, as well, B_y actually increases from between 6 - 7 nT observed from 21:00 until about 21:20, to a maximum positive value of ≈ 12 nT at 21:30, that is, at the time of the apparent neutral sheet encounter (a value of $|(B_y)_{\text{GSM}}| \approx 9$ nT was calculated for this time). The B_y component should also have approached zero magnitude if the satellite was actually in the neutral sheet region. Furthermore, the rapid fluctuations observed in each of the three magnetic traces are not typical of CPS field character, but rather are suggestive of a different plasma regime, namely, the PSBL.

The ISEE 1 magnetogram alone provides inadequate information to resolve the discrepancy between expected and observed signatures. Energetic particle information for this

event are available in addition to the magnetic data, and they may be studied to provide further insight into which plasma regime is being sampled by the satellite at the time of the apparent neutral sheet encounter. First, consider the energy-time spectrogram for day 75, 1979, shown in figure 5.2. At about 21:00 it appears that ISEE 1 has just left the low latitude edge of the lobe region as suggested by the very low particle densities. The satellite then encounters the high latitude edge of the PSBL indicated by the anisotropic ion fluxes, and it remains there for the duration of the hour. ISEE-1 does not appear to encounter what may clearly be called the CPS (characterized by isotropic particle distributions). Note also, the existence of very pronounced duskward flows of positive ions in the latter part of hour 21.

To refine the interpretation of the E-t spectrogram, consider the energy-phase angle spectrograms for this hour, shown in figures 5.3, 5.4, and 5.5. The LEPDEEA was in low-bit rate mode at the time of this event, and as a result, approximately eight minutes are required to acquire the data for each set of E- ϕ spectrograms. The first set of relevant frames, figure 5.3(a), begins at 21:07. The ions are anisotropic with a distinct Earthward component. The electrons, as well, are anisotropic and feature anti-Earthward beams in the 2E and 3E frames, and Earthward beams in the 5E and 6E frames. Such electron and proton distributions are characteristic of the PSBL. The second set

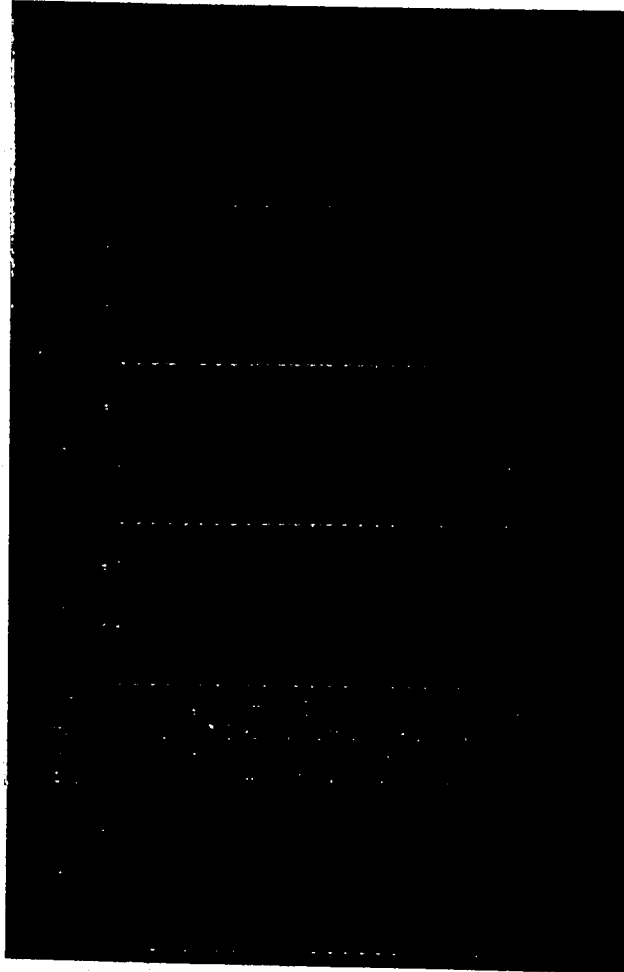
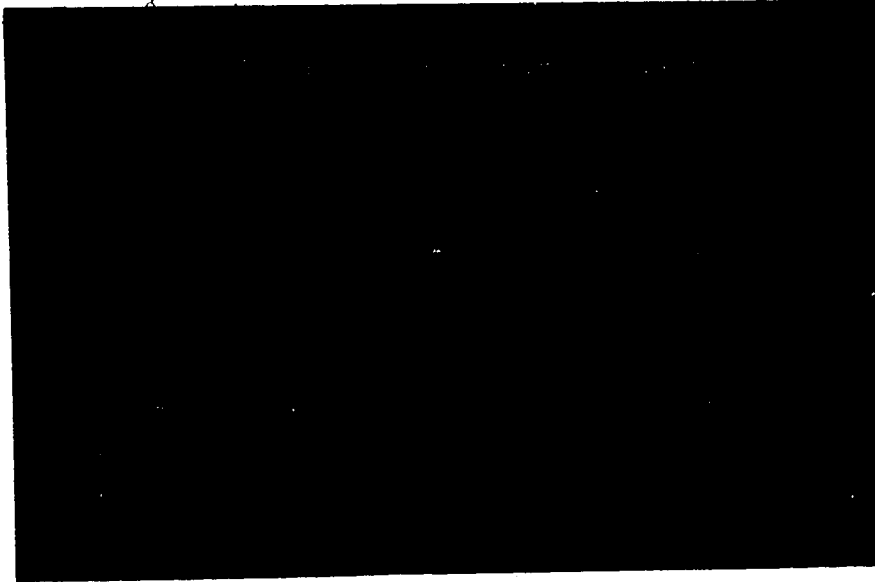


Figure 5.2 Energy-time spectrogram for day 75 (March 16), 1979.

(a)



(b)

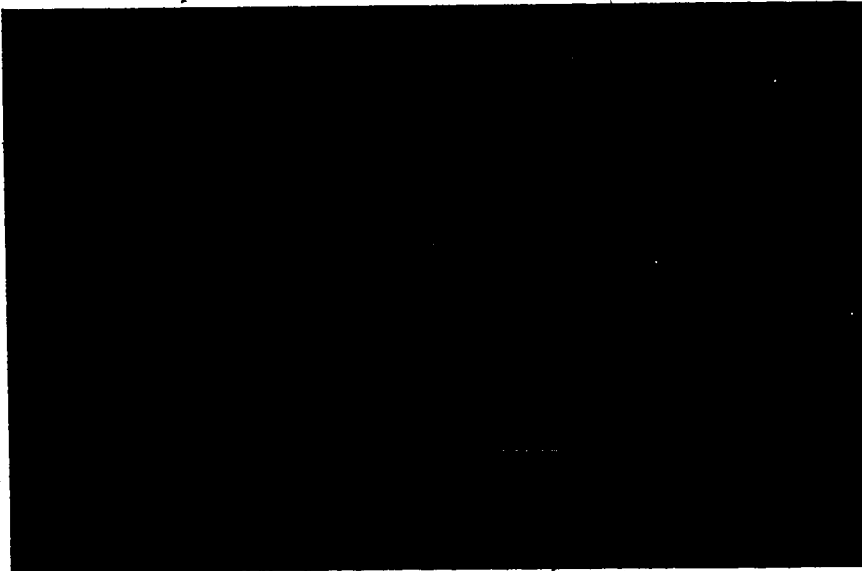
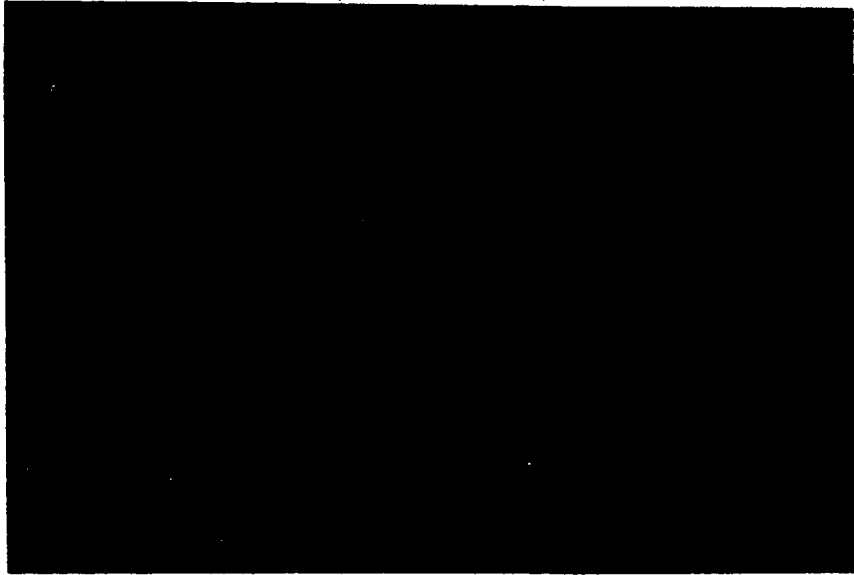


Figure 5.3 Energy-phase angle spectrograms for day 75 (March 16), 1979, with starting times of (a) 21:07 and (b) 21:15 UT.

(a)



(b)

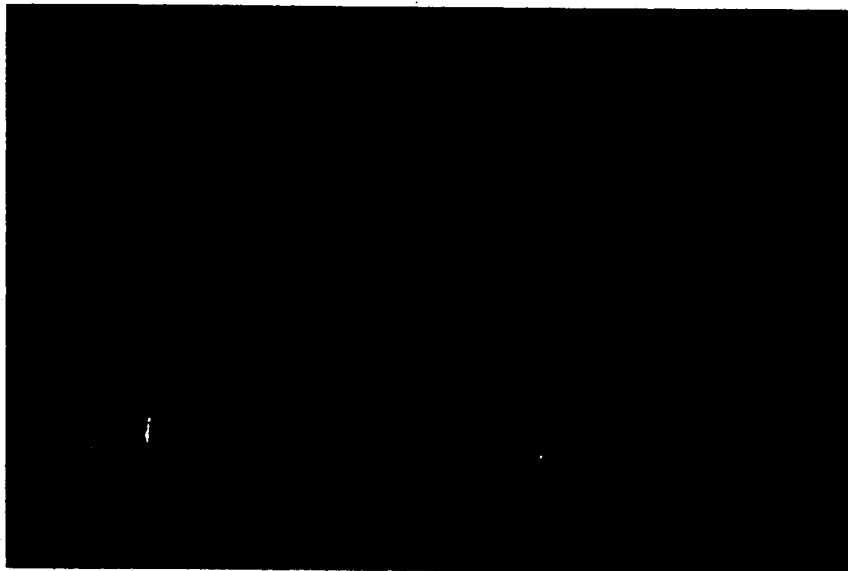
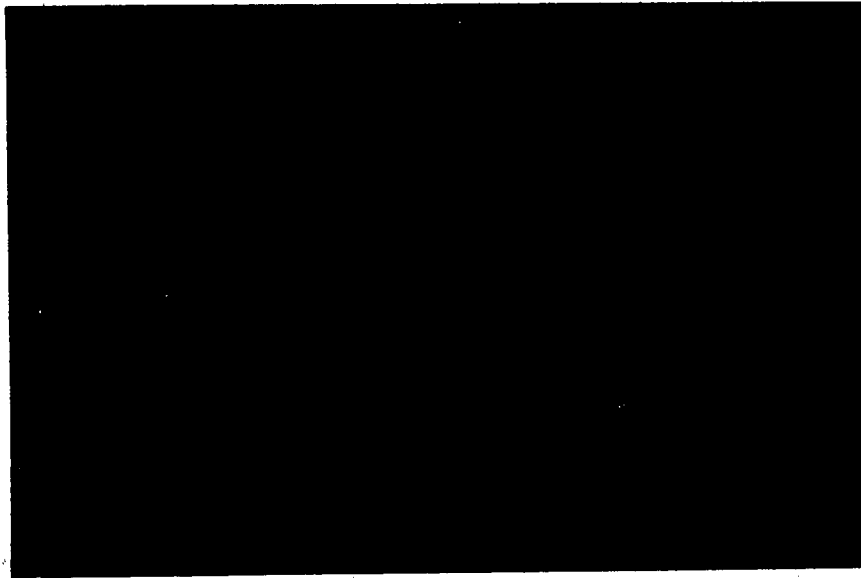


Figure 5.4 Same as figure 5.4 but for start times of (a) 21:24 and (b) 21:32 UT.

(a)



(b)

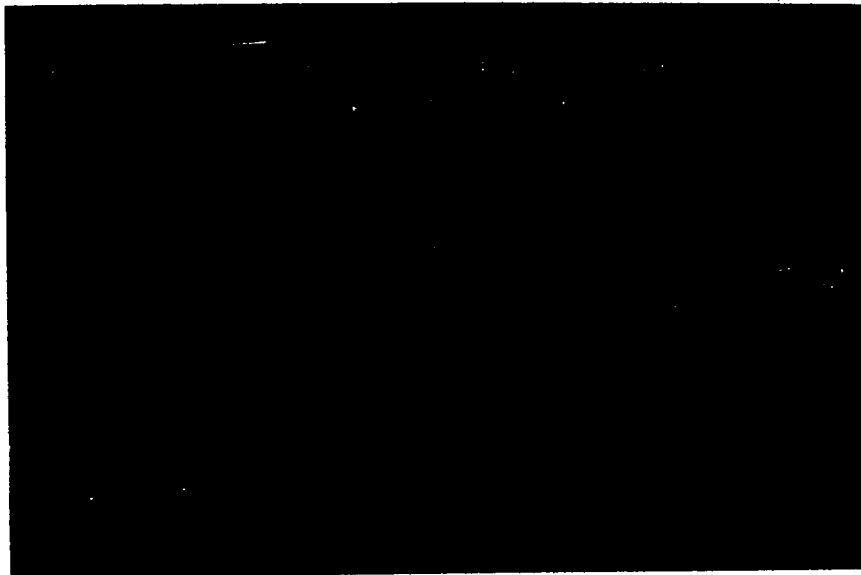


Figure 5.5 Same as figure 5.4 but for start times of (a) 21:41 and (b) 21:50 UT.

of frames (figure 5.3 (b)), begins about eight minutes later at 21:15. The particle distributions remain anisotropic in character, with the electrons exhibiting bidirectional streaming, in the Earthward and anti-Earthward directions, in frames 3E and 4E. Frames 2E, 5E and 6E remain relatively unchanged from the first set of frames.

In figure 5.4 (a), beginning at 21:24, the anisotropic nature of the particle distributions becomes increasingly pronounced. This set of frames coincides with the start of the apparent neutral sheet encounter suggested by the B_x component of on the magnetogram in figure 5.1. Ion beams are now present but note that the particle motion is in the dawn to dusk direction. Electrons exhibit bi-directional streaming, also in the Y direction. Such intense anisotropic distributions are not at all typical of CPS encounters. For the remainder of the hour (figures 5.4 (b) and 5.5, (a) and (b)) for the time interval 21:32 to 21:50 inclusive) both the ion and electron distributions retain their anisotropic character. Low energy ion beams are present, oriented approximately dawnward/Earthward, and cross-tail bidirectional streaming of the electrons persists.

So, according to the particle spectrograms, ISEE 1 appears to have travelled from the lobe through to the PSBL in the northern hemisphere, dawn sector during hour 21 on day 75, 1979. The satellite remained in or near the PSBL region throughout the hour. It is evident that ISEE-1 does not cross the neutral sheet, having never clearly

encountered the CPS regime, and the occurrence of $|B_x|=0$ nT on the magnetogram must somehow be reinterpreted. As well, the prediction of the neutral sheet position by the Russell-Brody and Fairfield models must be questioned.

It is also of interest that, according to the energy-time spectrogram for day 75, 1979 (shown in figure 5.2), ISEE 1 entered the PSBL from the CPS at approximately 19:45, after which it encountered the lobe at about 20:15. The satellite remained in the lobe until the start of hour 21, at which time the PSBL was once again traversed. Consultation with the ISEE 1 magnetogram for hour 19 (shown in figure 5.6) indicates that the satellite appears to cross the neutral sheet at approximately 19:50 (northern to southern hemisphere) since at this time $|B_x|=0$ nT. However, $|B_y|$ remains approximately constant (although of relatively small magnitude) from 19:50 onward and fails to change polarity in accordance with B_x as would be expected at a legitimate neutral sheet crossing (the magnitude of $(B_y)_{GSM}$ was calculated to be 6.5 nT at 19:50). Rapid fluctuations in all three magnetic traces are also apparent near the end of the hour. Again, the particle and magnetic data provide two different interpretations for a given event, and reconciliation of the two explanations must be obtained.

Note that this event was used by McComas and Russell (1984) in order to determine the thickness of the neutral sheet. In their analysis, the energetic particle data were not consulted and the presence of constant B_y at the

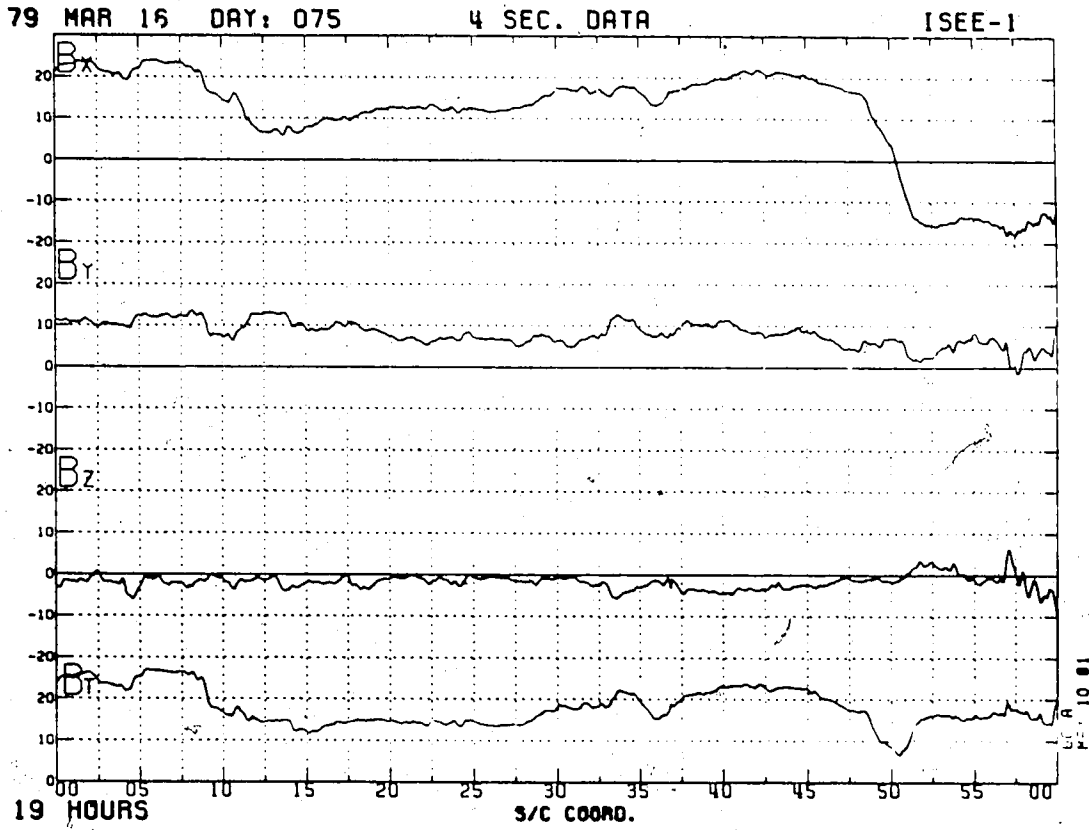


Figure 5.6 ISEE 1 magnetogram in GSE coordinates for hour 19, day 75 (March 16), 1979.

"neutral sheet" was not addressed. However, since ISEE 1 was situated at $Z_{\text{GSM}}=1.5$ Re, the predicted neutral sheet location of 0.5 Re (in GSM coordinates) from both the Russell-Brody and Fairfield models, is consistent with their interpretation.

Finally, consideration of the level of magnetospheric activity for day 75, 1979, hour 21 (figure 5.7) is not clearly representative of plasma sheet thinning due to substorm activity. The hourly averaged AE index had a value of only 55 nT, although an isolated high latitude substorm did occur at roughly 21:30. Consequently, it appears as though this sequence of events represents a typical, quiet time traversal from the lobe through the PSBL and into the CPS, and it is not likely associated with a thinning of the plasma sheet. However, although the occurrence and strength of field-aligned currents is enhanced during intervals of high magnetospheric activity (Rostoker and Eastman, 1987), according to Dandouras et al. (1986) even weak substorms may produce large perturbations in the plasma sheet.

5.2 A Second Observation of $|B_x| \approx 0$ nT in the Vicinity of the PSBL

In order to illustrate the non-uniqueness of the events discussed in the previous section, an additional example of $|B_x| \approx 0$ nT was considered when ISEE 1 was not situated at the neutral sheet but rather within the PSBL. The event takes place on day 59, 1978, hour 03. At this time ISEE 1 was

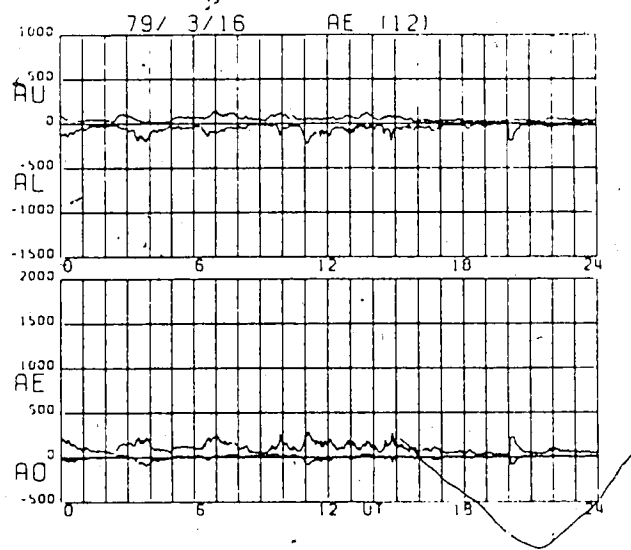


Figure 5.7 A plot of the AE index for day 75, 1979.

located at $X_{GSM} = -13 \text{ Re}$, $Y_{GSM} = -12.8 \text{ Re}$, and $Z_{GSM} = 0.5 \text{ Re}$, and the predicted Russell-Brody and Fairfield neutral sheet positions in terms of Z_{GSM} were 0.5 Re and 2.25 Re , respectively. The GSE magnetogram for this hour is shown in figure 5.8 and the corresponding E-t spectrogram is given in figure 5.9. The signatures displayed by the magnetic traces from about 03:20 until the end of the hour are very similar to those of hour 21, day 75, 1979, described above. On day 59, 1978, $|B_x|$ decreases from more than 20 nT at approximately 03:25 to between 0 and 5 nT for the remainder of the hour. The B_y component magnitude, on the other hand, increases at about 03:25 from approximately 3 nT to about 10 nT for the duration of hour 03 (in the GSM system, B_y has a magnitude of 4.7 nT at 03:45). As well, all three traces exhibit rapid fluctuations during this time interval.

Consideration of the E-t spectrogram, shown in figure 5.9, indicates a dropout in the particle responses corresponding to the time of the decrease in $|B_x|$ to ≈ 0 nT. A plot of the AE index for day 59, 1978, is shown in figure 5.10. It is evident from this plot that a peak in activity was recorded during the early part of hour 03, with a second peak of somewhat lower AE magnitude being apparent at about 03:30. The hourly averaged AE value for this time interval was 713 nT. This high level of activity is indicative of strong substorm activity.

As the plasma sheet thins during the substorm of day 59, 1978, the PSBL sweeps past ISEE 1. This takes place at

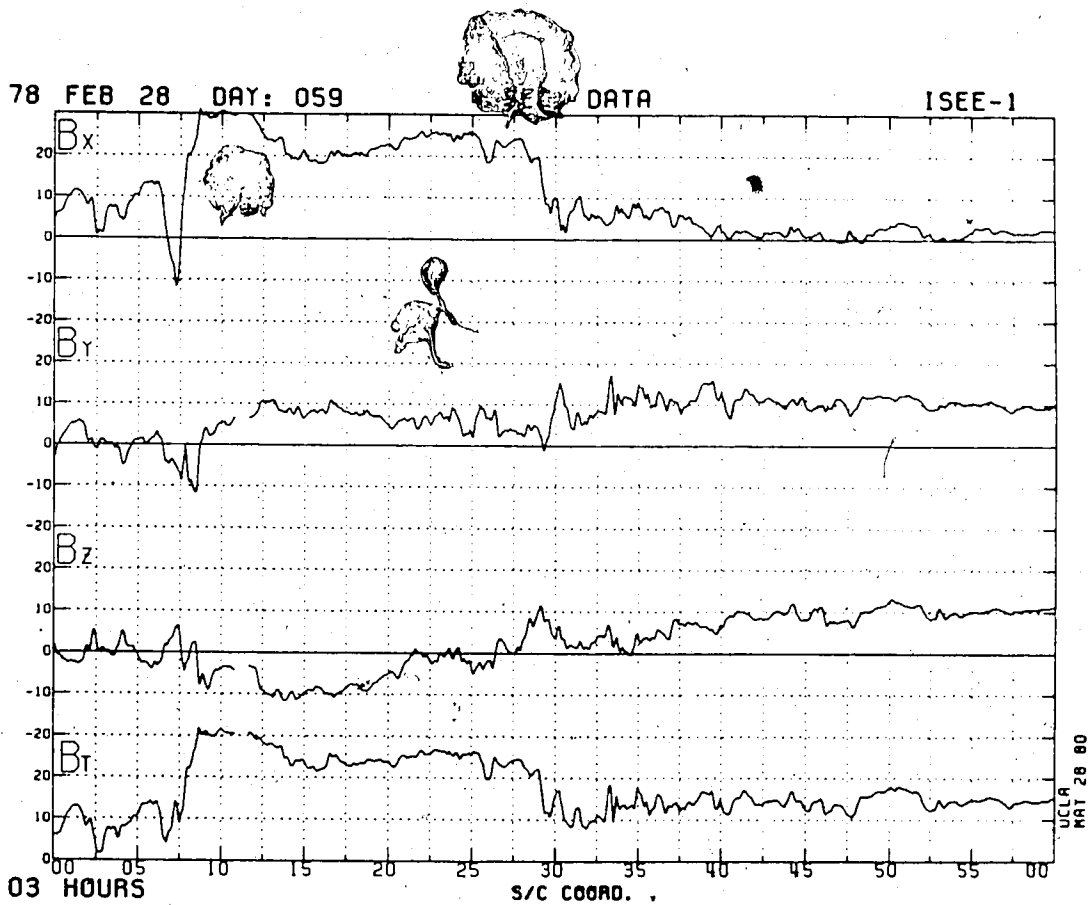


Figure 5.8 ISEE 1 magnetogram in GSE coordinates for hour 03, day 59 (February 28), 1978.



Figure 5.9 Energy-time spectrogram for day 59 (February 28), 1978.

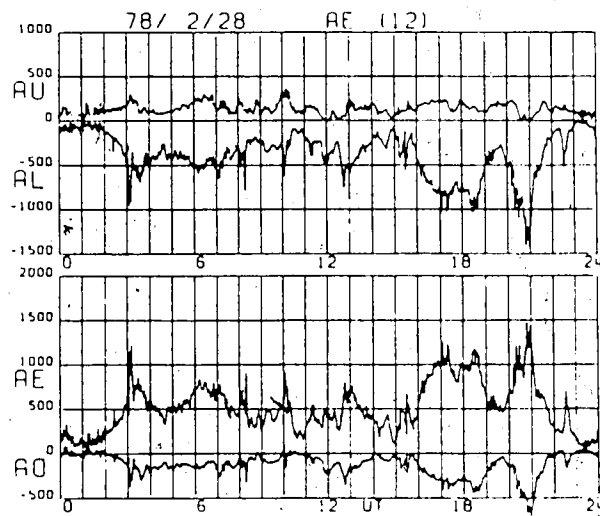


Figure 5.10 A plot of the AE index for day 59, 1978.

about 03:30, at which time the satellite observes enhanced anti-Earthward as well as duskward ion flows, as seen in figure 5.9. Therefore, the decrease in $|B_x|$ to approximately 0 nT accompanied by an increase in $|B_y|$, as observed on the corresponding magnetogram, is associated with ISEE 1 sampling the PSF regime rather than the neutral sheet region, which will be discussed further in section 5.3.

5.3 The Effect of Large-Scale Field-Aligned Currents on the Magnitude of the Cross-Tail Magnetic Field Component

In recent years, a considerable amount of evidence has been amassed suggesting that field-aligned currents flowing into and out of the high-latitude portion of the auroral oval thread the magnetotail in the region of the plasma sheet boundary layer. Estimates of these field-aligned currents range from negligible according to Fairfield (1979), who noted a lack of evidence for their presence in terms of their expected influence on the magnetotail configuration, to substantive according to Frank et al. (1981), who reported the first direct measurements of field-aligned currents in the Earth's magnetotail with plasma instrumentation. Evidence will be presented here for the generation of perturbation magnetic fields, as a result of field-aligned currents flowing in the magnetotail, which are sufficiently large that severe distortion of the normal tail magnetic field configuration may occur. One manifestation of these FAC is the production of magnetic

fields capable of cancelling the Earthward or anti-Earthward component of the background tail field in the vicinity of the PSBL. Such cases appear to be neutral sheet encounters, but in fact, they are not.

The concept of perturbations to the magnetotail magnetic field as a consequence of the presence of field-aligned current sheets (specifically, an increase in the dawn-to-dusk field component magnitude accompanied by a decrease in the X directed field component), has been invoked previously by several authors. Parks et al. (1984) studied FAC at the high latitude edge of the PSBL using ISEE 1 magnetic field measurements. They noted that B_y increased dramatically from a few nT to more than 20 nT in one of their events as a result of the presence of a FAC sheet. The increase in $|B_y|$ was accompanied by a decrease in $|B_x|$ and once ISEE 1 passed out of the vicinity of the FAC sheet, the B_x and B_y traces resumed more typical appearances, with the two components traces exhibiting similar signatures.

Elphic et al. (1985) studied filamentary FAC structures, also at the high latitude edge of the PSBL, using ISEE 1 and 2 data. They noted that $|B_y|$ is found to increase when a satellite enters the PSBL, and while within the PSBL, magnetic field fluctuations are mostly transverse to the background B_x component, that is, in the B_y direction. This behaviour they attribute to the presence of FAC. Furthermore, they state that the skew of the tail in

the B_y direction is of different polarity above and below a field-aligned current sheet and that cross-tail motion of the plasma is implied by the skew of the field since particles flow along the field lines.

Kelly et al. (1986) have studied changes in the B_y field component in order to identify field-aligned current layers from magnetic data. They have interpreted an increase in $|B_y|$ followed by a decrease as indicating the existence of two large sheet-like structures. In addition, they indicate that large-scale variations in B_x and B_y occur predominantly in the pre-midnight sector associated with the Harang discontinuity. The studies conducted by Kelly et al. involve downtail distances of 2.4 to 7 R_E , and consequently they deal primarily with near-Earth phenomena. Reference to the occurrence of B_y perturbations due to the presence of FAC has also been made by Rostoker and Eastman (1987), among others.

None of the previous works, however, have dealt with the possibility that sufficient skewing of the tail field due to the presence of FAC in the PSBL may result in the complete cancellation of the downtail magnetic field component (ie: $|B_x|$ approaches 0 nT as $|B_y|$ increases due to skewing of the field lines). In this section, a proposal will be put forward to explain some examples of the observed magnetogram signature of constant, non-zero B_y when $|B_x|=0$ in terms of magnetic perturbations resulting from the presence of field-aligned currents in the vicinity of the

PSBL. Here, the effects of large-scale currents will be addressed.

Consider a large-scale field-aligned current sheet located in the vicinity of the PSBL. Assume for simplicity that the sheet is of infinitesimal thickness and that the current flows entirely in the $-X$ direction, shown schematically figure 5.11. Magnetic perturbations due to the current sheet will be oriented perpendicular to the direction of the current flow, as indicated by the arrowheads. Above the current sheet the perturbation will be directed duskward (in a positive Y direction), whereas below the sheet the perturbation will be directed dawnward (in a negative Y direction). Adjacent field lines above and below the current sheet will become skewed in accordance with the magnetic perturbation. Allow the current sheet to thicken by the addition of an adjacent current sheet at the high latitude edge of the initial sheet. The current in this sheet will flow in the direction dictated by the magnetic perturbations induced by the initial sheet. The new sheet will also produce magnetic perturbations perpendicular to its flow direction; hence, when subsequent current layers are added they will be further rotated. As the current sheet continues to thicken eventually the magnetic field at the high latitude edge of the current layer may become oriented totally in the Y direction through the addition of a Y -directed field component and the subtraction of an X -directed field component. Note that a simple summation of

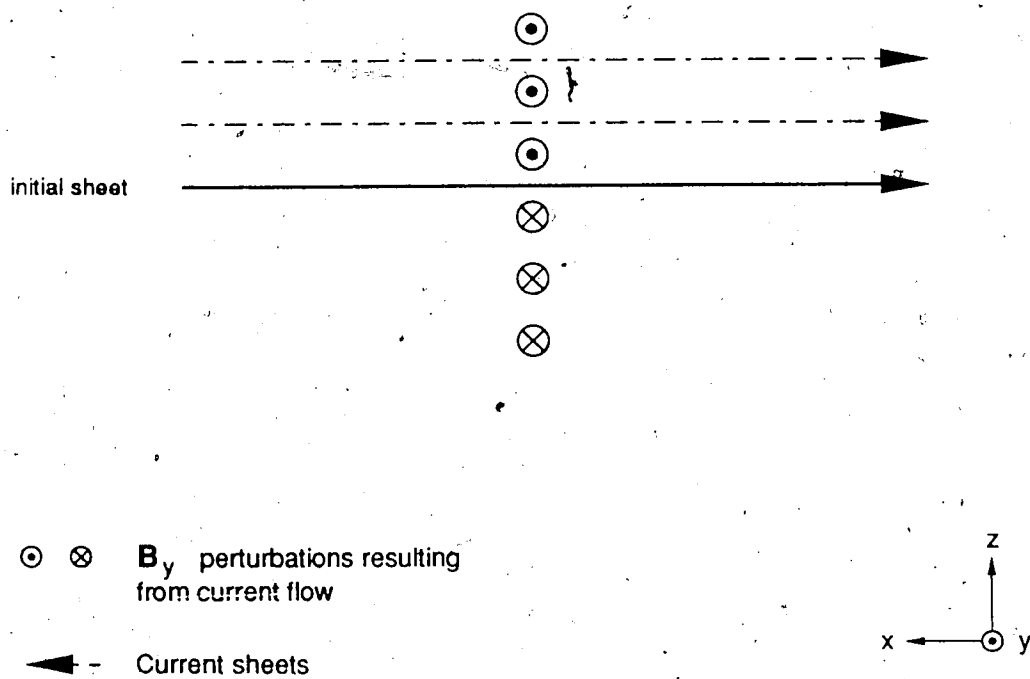


Figure 5.11 Schematic representation of the thickening of a field-aligned current layer by the addition of adjacent layers which become skewed in orientation by the magnetic perturbations which influence the new layers.

magnetic perturbations resulting from both the initial current sheet and all additional sheets, is not sufficient for the determination of the orientation of the outermost current sheet, since not only do magnetic perturbations affect field orientation above the current sheets, but as well, the field direction is altered below each current sheet. Consequently, perturbations resulting from newly added current sheets will alter the direction of current flow in the original sheet. The process of perturbations from new sheets causing skewing of the initial sheet, which subsequently influences the direction of flow in the new sheets, will eventually converge to a stable configuration. Overall, the total effect of the addition of new current sheets is an enhanced skewing of the field in the outermost current layer.

The scenario just described is precisely that which is observed in the magnetograms for day 75, 1979, hours 19 and 21, as well as for day 59, 1978, hour 03. The observed cancellation of the B_x component, coincident with an increase in the positive B_y component, is therefore explained by the influence of large-scale FAC sheets at the location of the PSBL. The bi-directional dawnward and duskward plasma flows evident in the energetic particle spectrograms for all three cases provide further confirmation that the magnetic field has become oriented in the cross-tail direction, since the particles flow along the field lines.

Quantitatively, the skewing of the background magnetic field as a result of perturbations produced by a thickening field-aligned current layer may be illustrated as follows. Consider an expansion of the initial current sheet by the addition of a second field-aligned current sheet at the high latitude edge of the initial sheet. The formalism of an infinite uniform plane current sheet to represent the field-aligned currents will be employed. A constant current intensity, I (in units of A/m), is chosen to flow in the initial sheet along the direction of pre-existing field lines. The magnetic field resulting from this current configuration is transverse and in a plane parallel to the direction of current flow. These magnetic perturbations will be of negative polarity below the current sheet but of positive polarity above the sheet. Their magnitude, which is independent of distance from the current sheet, is determined according to the following relationship (Wangness, 1979):

$$|\Delta B| = (\mu_0 I)/2 \quad (24)$$

where μ_0 is the permeability of free space, I is the current intensity and ΔB is the magnetic perturbation resulting from the current flow.

Suppose that the perturbations from the addition of one current sheet above the original sheet are sufficiently large to produce cancellation of the X-directed field component at the high latitude edge of the new sheet. Hence, the field direction above the new sheet becomes oriented completely in the Y direction. For initial field component magnitudes of $B_x=15$ nT and $B_y=6$ nT, which are values specific to the event of day 75, 1979, hour 21, it is found that the magnitude of the initial ΔB perturbation required to attain sufficient skewing of the magnetic field above the newly added current layer such that its orientation is completely in the Y direction (after convergence has been achieved) is ≈ 12 nT. The corresponding current intensity according to equation 24 is ≈ 0.02 A/m. Note that this value of I is comparable to that which Frank et al. (1981) have inferred from their observations of FAC in the PSBL. The thickness of the resulting current layer (including both sheets) may be calculated as follows (Frank et al., 1981), providing that the current density J_{\parallel} (measured in A/m²) of the layer is known:

$$\text{current layer thickness} = I/J_{\parallel} \quad (25)$$

where the thickness is measured in meters and J_{\parallel} is the current density parallel to the direction of current flow. A

current density of -3×10^{-9} A/m² was obtained for this event (at the time of 21:24) from quantitative analysis of the particle data (courtesy C.Y. Huang). Consequently, the thickness for the entire current layer is calculated to be about 6700 km, or, just over 1 Re. A value such as this is consistent with a typical thickness for FAC sheets in the PSBL (Frank et al., 1981; Speiser and Sel, 1987). However, in order for the B_y component to attain the magnitude observed for this event, it is necessary to assume that, in addition to the expansion of a FAC layer in the vicinity of the PSBL which causes B_y enhancement, the magnitude of the total field must decrease by a small amount and this is physically explainable in terms of substorm-related field magnitude reduction.

No mention has been made regarding the source region for the field-aligned current sheets nor for the mechanism by which growth of the current layer ceases. Whatever the source may be, once the FAC strengths diminish, a natural consequence is that the magnetic field skewing will also terminate, and since the perturbations to the field in the Y direction are no longer present (ie: once the FAC stop flowing) the magnetic field will return to its initial configuration, which in this case was an orientation predominantly in the X direction.

Chapter 6

Conclusions

In the foregoing research, various sources of the dawn-to-dusk magnetic field component, B_y , of the magnetotail were examined. In addition, observed discrepancies between *in situ* magnetic and particle signatures of instantaneous measurements as well as between magnetic signatures observed and those expected according to statistically derived models of the tail (ie: Tsyganenko, 1987), were investigated.

The geomagnetic field is distorted by its interaction with the solar wind, leading to the development of the overall configuration of the magnetotail. In addition, various current systems, induced by the motions of charged particles under the influence of electromagnetic fields, also modify magnetic structure. The three major sources which contribute to $|B_y|$ result from hydrodynamic tail flare and magnetic perturbations due to both the ring current and field-aligned currents. Contributions from these three sources are superimposed to provide a B_y component which is positive in sign in both the northern hemisphere dawn and southern hemisphere dusk quadrants of the tail, and negative in the southern hemisphere dawn and northern hemisphere dusk quadrants. The polarity of B_y from these sources changes both across the noon-midnight meridian plane as well as across the plane of the tail neutral sheet.

Because inconsistencies have been encountered in the present studies between observations of the tail magnetic field and predictions of statistical models, other sources of B_y must exist which are unaccounted for in these statistical models. In order to investigate such inconsistencies, studies of a statistical nature were conducted using a carefully selected data set consisting of both *in situ* magnetic field and energetic particle measurements collected by the ISEE satellites in the central plasma sheet (CPS), plasma sheet boundary layer (PSBL) and the tail lobe plasma regimes.

The determination of the plasma regime being sampled by a satellite was based on the unambiguous and diagnostic energetic particle signatures, since from preliminary consideration of the magnetic data alone it had become evident that often a unique identification of the plasma regime could not be made. Through a series of studies it was clearly demonstrated that plasma regime identification based solely on magnetic field magnitude and character is highly unreliable. For all distances downstream of the Earth between -10 and -23 Re, and in all three plasma regimes of interest, magnitudes of the B_x and B_y components in the ranges of $15 \leq B_x \leq 35$ nT and $-10 \leq B_y \leq 10$ nT, respectively, were observed (where B_x is the field component directed Earthward). This suggests that when the satellite measures a combination of B_x and B_y magnitudes within these ranges, the plasma regime being sampled cannot be uniquely identified on

the basis of the magnitudes of the magnetic field components. Therefore, the magnetic data must be used in conjunction with other available data, such as the energetic particle data, when plasma regime identification is a significant factor in the analysis of satellite data.

Regarding the crosstail component of the magnetotail, inconsistencies which became apparent between observed magnetic signatures and those predicted by the statistically derived tail models, included the frequent occurrence of a non-zero $|B_y|$ at the time of a neutral sheet encounter. Four distinct categories of tail B_y behaviour at the neutral sheet were identified in this work. These include zero-bias events (well-defined neutral sheet encounters), situations where B_y changes across the neutral sheet but which exhibit either a positive or negative bias, and finally, occurrences of constant, non-zero B_y at the neutral sheet.

A mechanism by which anomalous B_y signatures at the neutral sheet might be explained concerns both daily and seasonal variations in sun-earth geometry. The tail magnetic field measurements were initially displayed in the spacecraft coordinate system (which is essentially the same as the GSE system for the spin axis orientations of ISEE's 1 and 2). However, because of the influence of the dipole field, the GSM system of coordinates is a more appropriate system for ordering the data since it takes into account diurnal and seasonal variations resulting from precession of the geomagnetic pole around the spin axis of the Earth. In

transforming a magnetic field vector from the GSE to the GSM system, it was demonstrated that the occurrence of some of the observed positive B_y biases could be attributed to the choice of coordinate system used to order the data. However, it was also shown that not all observed B_y biases can be completely accounted for simply by coordinate transformations between the two systems. Negative B_y biases cannot be understood within this framework, and as well, some biases are in fact generated by rotation of the field into GSM coordinates in what previously appeared to be well-defined neutral sheet encounters in the GSE system. The occurrence of constant, non-zero B_y at the neutral sheet is not addressed by the above considerations.

The influence of IMF B_y on tail field geometry, as suggested by Fairfield (1979), was also studied using a statistical approach. According to Fairfield's postulate, penetration of the IMF B_y accounts for a source of tail B_y additional to those already considered in the statistical magnetotail models. The majority of the studies conducted here indicate minimal correlation between tail B_y and IMF B_y , and therefore, little in the way of convincing evidence for the penetration hypothesis was provided. Only the event subset for which B_y was constant and non-zero at the neutral sheet yielded a good correlation between tail and IMF B_y . As well, if IMF B_y penetration does actually take place, despite the poor statistical evidence for the occurrence of such a process, then the present studies

suggest that penetration would be a maximum in the tail lobe plasma regime. This is in contrast with the result of Lui (1985) which indicates that the IMF B_y penetrates the plasma sheet to a larger extent than it does the tail lobes.

Finally, it was demonstrated that certain events which appear to be neutral sheet encounters according to the criterion of $|B_x|=0$ nT but for which the simultaneous value of $|B_y|\neq 0$ nT, actually represent encounters with the PSBL. This becomes apparent once the energetic particle signatures are considered. In such cases, magnetic perturbations resulting from the presence of large-scale field-aligned currents in the vicinity of the PSBL are essentially capable of cancelling the downtail component of the magnetic field, giving the appearance of a neutral sheet encounter. As a consequence of the cancellation of the B_x component, the cross-tail magnetic field component is enhanced. This hypothesis is supported by the observation of cross-tail directed particle beams coincident with the occurrence of $|B_x|=0$ nT and $|B_y|\neq 0$ nT, and the presence of such beams indicates that the magnetic field has become oriented in the dawn-dusk direction.

Bibliography

Akasofu, S.-I., *Physics of Magnetospheric Substorms*, D. Reidel Publishing Company, Dordrecht, Holland, 1977.

Akasofu, S.-I., The magnetospheric currents: an introduction, in *Magnetospheric Currents*, edited by T.A. Potemra, p.29, American Geophysical Union, Monograph 28, 1984.

Akasofu, S.-I. and Y. Kamide, The Aurora, in *The Solar Wind and the Earth*, edited by S.-I. Akasofu and Y. Kamide, p.143, Geophysics and Physics Monographs, Terra Scientific Publishing Company, Tokyo, 1987.

Aubry, M.P., C.T. Russell, and M.G. Kivelson, Inward motion of the magnetopause before a substorm, *J. Geophys. Res.*, 75, 7018, 1970.

Axford, W.B., and C.O. Hines, A unifying theory of high-latitude geophysical phenomena and geomagnetic storms, *Can. J. Phys.*, 39, 1433, 1961.

Beard, D.B., The interaction of the terrestrial magnetic field with the solar corpuscular radiation, *J. Geophys. Res.*, 65, 3559, 1960.

Beard, D.B., The solar wind geomagnetic field boundary, *Rev. Geophys.*, 2, 335, 1964.

Behannon, K.W., Geometry of the geomagnetic tail, *J. Geophys. Res.*, 75, 734, 1970.

- Biermann, L., Kometenschweife und solare korpulscular strahlung, *Zeit. F. Astrophys.*, 29, 274, 1951.
- Biermann, L., Solar corpuscular radiation and the interplanetary gas, *Observatory*, 107, 109, 1957.
- Birkeland, K., *The Norwegian Aurora Polaris Expedition, 1902-1903*, vol.1, sec.1, Christiania, Norway, 1908.
- Birkeland, K., *The Norwegian Aurora Polaris Expedition, 1902-1903*, vol.1, sec.2, Christiania, Norway, 1913.
- Boström, R., A model of the auroral electrojets, *J. Geophys. Res.*, 69, 4983, 1964.
- Bowling, S. B., The influence of the direction of the geomagnetic dipole on the position of the neutral sheet, *J. Geophys. Res.*, 34, 5155, 1974.
- Chapman, S., The motion of a neutral ionized stream in the Earth's magnetic field, *Proc. Cambridge Phil. Soc.*, 21, 577, 1923.
- Chapman, S., and J. Bartels, *Geomagnetism*, vol. I&II, Oxford University Press, Clarendon Press, Oxford, 1940.
- Chapman, S., and V.C.A. Ferraro, A new theory of magnetic storms, *Terrestrial Magnetism and Atmospheric Electricity*, 36, 77, 1931.
- Chapman, S., and V.C.A. Ferraro, A new theory of magnetic storms, *Terrestrial Magnetism and Atmospheric Electricity*, 37, 421, 1932.
- Chen, F.F., *Introduction to Plasma Physics and Controlled Fusion*, second edition, Volume I, Plenum Press, New York, 1984.

- Coroniti, F.V., and C.F. Kennel, Changes in magnetospheric configuration during the substorm growth phase, *J. Geophys. Res.*, 77, 3361, 1972.
- Couzens, D.A., and J.H. King, *Interplanetary Medium Data Book, Supplements 3 & 3A, 1977-1985*, National Space Sciences Center (NSSDC) / World Data Center A for Rockets and Satellites (WDC-A-R&S), NASA, Goddard Space Flight Center, Greenbelt, Maryland 20771, 1986.
- Cowley, S.W.H., Magnetospheric asymmetries associated with the Y-component of the IMF, *Planet. Space Sci.*, 29, 79, 1981.
- Cowley, S.W.H., and W.J. Hughes, Observation of an IMF sector effect in the Y magnetic field component at geostationary orbit, *Planet. Space Sci.*, 31, 73, 1983.
- Dandouras, J., H. Réme, A. Saint-Marc, J.A. Sauvard, G.K. Parks, K.A. Anderson, and R.P. Lin, A statistical study of plasma sheet dynamics using ISEE 1 and 2 energetic particle flux data, *J. Geophys. Res.*, 91, 6861, 1986.
- Davis, T.N., and M. Sugiura, Auroral electrojet activity index AE and its Universal Time variations, *J. Geophys. Res.*, 71, 785, 1966.
- DeCoster R.J., and L.A. Frank, Observations pertaining to the dynamics of the plasma sheet, *J. Geophys. Res.*, 84, 5099, 1979.
- Dungey, J.W., Interplanetary magnetic field and the auroral zones, *Phys. Rev. Lett.*, 6, 47, 1961.
- Durney, A.C., and K.W. Ogilvie, Introduction to the ISEE mission, *Space Science Reviews*, 22, 679, 1978.

- Eastman, T.E., L.A. Frank, W.K. Peterson, and W. Lennartsson, The plasma sheet boundary layer, *J. Geophys. Res.*, 89, 1583, 1984.
- Eastman, T.E., L.A. Frank, and C.Y. Huang, The boundary layers as the primary transport regions of the Earth's magnetotail, *J. Geophys. Res.*, 90, 9541, 1985a.
- Eastman, T.E., B. Popielawska, and L.A. Frank, Three-dimensional plasma observations near the outer magnetospheric boundary, *J. Geophys. Res.*, 90, 9519, 1985b.
- Elphic, R.C. P.A. Mutch, and C.T. Russell, Observations of field-aligned currents at the plasma sheet boundary: an ISEE-1 and -2 survey, *Geophys. Res. Lett.*, 12, 631, 1985.
- Fairfield, D.H., On the average configuration of the geomagnetic tail, *J. Geophys. Res.*, 84, 1950, 1979.
- Fairfield, D.H., A statistical determination of the shape and position of the geomagnetic neutral sheet, *J. Geophys. Res.*, 85, 775, 1980.
- Fairfield, D.H., Structure of the geomagnetic tail, in *Magnetotail Physics*, ed. by A.T.Y. Lui, p.23, The Johns Hopkins Press, Baltimore, 1987.
- Frandsen, A.M.A., B.V. Connor, J. Van Amersfoort, and E.J. Smith, The ISEE-C vector helium magnetometer (VHM), *IEEE Transactions on Geoscience Electronics*, vol. GE-16, no. 3, 1978.
- Frank, L.A., D.M. Yeager, H.D. Owens, K.L. Ackerson, and M.R. English, -Quadr spherical LEPEDAS for ISEE's-1 and -2 plasma measurements, *IEEE Transactions on Geoscience Electronics*, vol. GE-16, no.3, 221, 1978a.

- Frank, L.A., K.L. Ackerson, R.J. DeCoster, and B.G. Burek, Three-dimensional plasma measurements within the Earth's magnetosphere, *Space Science Reviews*, 22, 739, 1978b.
- Frank, L.A., R.L. McPherron, R.J. Decoster, B.G. Burek, K.L. Ackerson, and C.T. Russell, Field-aligned currents in the magnetotail, *J. Geophys. Res.*, 86, 687, 1981.
- Gosling, J.T., D.J. McComas, M.F. Thomsen, S.J. Bame, and C.T. Russell, The warped neutral sheet in the near-Earth geomagnetic tail, *J. Geophys. Res.*, 91, 7093, 1986.
- Haerendel, G., and G. Paschmann, Interaction of the solar wind with the dayside magnetosphere, in *Magnetospheric Plasma Physics*, edited by A. Nishida, D. Reidel Publishing Company, Dordrecht, 1982.
- Hardy, D.A., H.K. Hills, and J.W. Freeman, Occurrence of the lobe plasma at lunar distances, *J. Geophys. Res.*, 84, 72, 1979.
- Hasegawa, A., and T. Sato, Generation of field-aligned current during substorm, in *Dynamics of the Magnetosphere*, edited by S.-I. Akasofu, p.529, D. Reidel Publishing Company, Dordrecht, 1980.
- Hines, C.O., The energization of plasma in the magnetosphere: hydromagnetic and particle-drift approaches, *Planet. Space Sci.*, 10, 239, 1963.
- Hones, E.W.Jr., The Earth's magnetotail, *Scientific American*, 254, 40, 1986.
- Hughes, T.J., and G. Rostoker, Current flow in the magnetosphere during periods of moderate activity, *J. Geophys. Res.*, 82, 2271, 1977.

- Hotelling, H., Analysis of a complex of statistical variables into principal components, *J. Educ. Psychol.*, 24, 417 & 498, 1933.
- Iijima, T. and T.A. Potemra, The amplitude distribution of field-aligned currents at the northern high latitudes observed by TRIAD, *J. Geophys. Res.*, 81, 2165, 1976.
- Jacobs, J.A., *The Earth's Core and Geomagnetism*, Pergamon Press Ltd., Oxford, 1963.
- Jolliffe, I.T., *Principal Component Analysis*, Springer-Verlag Inc., New York, 1986.
- Kamei T., and H. Maeda, *Auroral Electrojet Indices (AE) Data Book, No. 3*, World Data Center C2 for Geomagnetism, January-June 1978, Data Analysis Center for Geomagnetism and Spacemagnetism, Kyoto University, Kyoto, 1981.
- Kamei T., and H. Maeda, *Auroral Electrojet Indices (AE) Data Book, No. 5*, World Data Center C2 for Geomagnetism, January-June 1978, Data Analysis Center for Geomagnetism and Spacemagnetism, Kyoto University, Kyoto, 1982.
- Kavanagh, L.D.Jr., Magnetospheric structure, in *Earth's Magnetospheric Processes*, edited by B.M. McCormac, p.3, D. Reidel Publishing Company, 1972.
- Kelly, T.J., C.T. Russell, R.J. Walker, G.K. Parks and J.T. Gosling, ISEE 1 and 2 observations of Birkeland currents in the Earth's inner magnetosphere, *J. Geophys. Res.*, 91, 6945, 1986.
- Kisabeth, J.L., and G. Rostoker, Development of the polar electrojet during polar magnetic substorms, *J. Geophys. Res.*, 76, 6815, 1971.

Kisabeth, J.L., and G. Rostoker, The expansive phase of magnetospheric substorms- I. Development of the auroral electrojets and auroral arc configuration during a substorm, *J. Geophys. Res.*, 79, 972, 1974.

Lindemann, F.A., Note on the theory of magnetic storms, *Phil. Mag.*, 38, 669, 1919.

Lui, A.T.Y., Observations on the fluid aspects of magnetotail dynamics, in *Magnetotail Physics*, edited by A.T.Y. Lui, p.101, The Johns Hopkins University Press, Baltimore, 1987.

Lui, A.T.Y., Solar wind influence on magnetotail configuration and dynamics, submitted to *Proceedings of Chapman Conference on Solar Wind Magnetospheric Coupling*, August 1985.

Lui, A.T.Y., Characteristics of the cross-tail current in the Earth's magnetotail, in *Magnetospheric Currents*, Geophysical Monograph 28, edited by T.A. Potemra, p.158, American Geophysical Union, Washington, D.C., 1983.

McComas, D.J., and C.T. Russell, The near Earth current sheet: ISEE-1 and -2 case studies, *Proc. Conf. Achievements of the IMS 26-28 June 1984 Graz Austria ESA SP 217* (September 1984).

Mihalov, J.D., D.S. Colburn, R.G. Currie, and C.P. Sonett, Configuration and reconnection of the geomagnetic tail, *J. Geophys. Res.*, 73, 943, 1968.

Nicholson, D.R., *Introduction to Plasma Theory*, John Wiley and Sons, Inc., -1983.

Ogilvie, K.W., and M.D. Banks, Jr., Notes on the ISEE A+B Data Pool Tape, Goddard Space Flight Center publication, 1977a.

- Ogilvie, K.W., T. von Rosenvinge, and A.C. Durney, International sun-Earth explorer: a three-spacecraft program, *Science*, 198, 131, 1977b.
- Olson, W.P., Introduction to the topology of magnetospheric current systems, in *Magnetospheric Currents*, Geophysical Monograph 28, edited by T.A. Potemra, p.49, American Geophysical Union, Washington D.C., 1984.
- Parker, E.N., Dynamics of the interplanetary gas and magnetic fields, *Astrophys. J.*, 128, 664, 1958a.
- Parker, E.N., Interaction of the solar wind with the geomagnetic field, *Phys. Fluids*, 1, 171, 1958b.
- Parker, E.N., The hydrodynamical theory of solar corpuscular radiation and stellar winds, *Astrophys. J.*, 132, 821, 1960.
- Parks, G.K., M. McCarthy, R.J. Fitzenreiter, J. Etcheto, K.A. Anderson, R.R. Anderson, T.E. Eastman, L.A. Frank, D.A. Gurnett, C. Huang, R.P. Lin, A.T.Y. Lui, K.W. Ogilvie, A. Pedersen, H. Réme, and D.J. Williams, Particle and field characteristics of the high-latitude plasma sheet boundary layer, *J. Geophys. Res.*, 89, 8885, 1984.
- Parratt, L.G., *Probability and Experimental Errors in Science: An Elementary Survey*, John Wiley and Sons Inc., New York, 1961.
- Potemra, T.A., Birkeland currents: present understanding and some remaining questions, in *High-Latitude Space Plasma Physics*, edited by Hultqvist, B., and T. Hagfors, Plenum Publishing Corporation, 1983.
- Primdahl, F., Partial penetration of IMF B_y into the magnetosphere, *Planet. Space Sci.*, 33, 1327, 1985.

Primdahl, F. and F. Spangselev, Does IMF B_y induce the cusp field-aligned currents?, *Planet. Space Sci.*, 31, 363, 1983.

Rossi, B., and S. Olbert, *Introduction to the Physics of Space*, McGraw-Hill Book Company, New York, 1970.

Rostoker, G., and R. Boström, A mechanism for driving the gross Birkeland current configuration in the auroral oval, *J. Geophys. Res.*, 81, 235, 1976.

Rostoker, G., S.-I. Akasofu, J. Foster, R.A. Greenwald, Y. Kamide, K. Kawasaki, A.T.Y. Lui, R.L. McPherron, and C.T. Russell, Magnetospheric substorms - definition and signatures, *J. Geophys. Res.*, 85, 1663, 1980.

Rostoker, G., Triggering of the expansive phase intensification of magnetospheric substorms by northward turnings of the interplanetary magnetic field, *J. Geophys. Res.*, 88, 6981, 1983.

Rostoker, G., and T. Eastman, A boundary layer model for magnetospheric substorms, *J. Geophys. Res.*, 92, 12187, 1987.

Rostoker, G., D.N. Baker, J. Lemaire, and V. Vasyliunas, Dialog on the relative roles of reconnection and the "viscous" interaction in providing solar-wind energy to the magnetosphere, in *Magnetotail Physics*, edited by A.T.Y. Lui, p.409, The Johns Hopkins University Press, Baltimore, 1987.

Russell, C.T., Geophysical coordinate transformations, *Cosmic-Electrodynamics*, 2, 184, 1971.

Russell, C.T., and K.I. Brody, Some remarks on the position and shape of the neutral sheet, *J. Geophys. Res.*, 72, 6104, 1967.

Russell, C.T., The ISEE 1 and 2 Fluxgate Magnetometers, *IEEE Transactions on Geoscience Electronics*, vol. GE-16, no.3, 1978.

Russell, C.T., and R.C. Elphic, Initial ISEE magnetometer results: magnetopause observations, *Space Science Reviews*, 22, 681, 1978.

Russell, C.T., H.J. Singer, and R.J. Walker, ISEE Documentation: ISEE-1 and -2 Orbital Plots Generated by the UCLA Fluxgate Magnetometer Group, Goddard Space Flight Center publication, 1980.

Sato, T., Auroral Physics, in *Magnetospheric Plasma Physics*, edited by A. Nishida, p.197, D. Reidel Publishing Company, Dordrecht, 1982.

Sibeck, D.G., G.L. Siscoe, J.A. Slavin, E.J. Smith, B.T. Tsurutani, and R.P. Lepping, The distant magnetotail's response to a strong interplanetary magnetic field B_y : twisting, flattening, and field line bending, *J. Geophys. Res.*, 90, 4011, 1985.

Slavin, J.A., E.J. Smith, D.G. Sibeck, D.N. Baker, R.D. Zwickl, and S.-I. Akasofu, An ISEE 3 study of the average and substorm configurations in the distant magnetotail, *J. Geophys. Res.*, 90, 10875, 1985.

Sonnerup, B.U.Ö., and L.J. Cahill, Jr., Explorer 12 Observations of the magnetopause current layer, *Rev. Geophys. Res. and Space Physics*, 73, 1757, 1968.

Speiser, T.W., and N. Sel, Processes in the magnetotail neutral sheet, *Physica Scripta*, 1987.

Tsurutani, B.T., B.E. Goldstein, M.E. Burton, and D.E. Jones, A review of the ISEE-3 geotail magnetic field results, *Planet. Space Sci.*, 34, 931, 1986.

- Tsyganenko, N.A., Global quantitative models of the geomagnetic field in the cislunar magnetosphere for different disturbance levels, *Planet. Space Sci.*, 35, 1347, 1987.
- Van Allen, J. A., *Origins of Magnetospheric Physics*, Smithsonian Institution Press, Washington, D.C., 1983.
- Voigt, G.-H., and R.V. Hilmer, The influence of the IMF B_y component on the Earth's magneto-hydrostatic magnetotail, in *Magnetotail Physics*, edited by A.T.Y. Lui, p.91, Johns Hopkins University Press, Baltimore, p.91, 1987.
- Voigt, G.-H., A mathematical magnetospheric field model with independent physical parameters, *Planet. Space Sci.*, 29, 1, 1981.
- Voigt, G.-H., The shape and position of the plasma sheet in the Earth's magnetotail, *J. Geophys. Res.*, 89, 2169, 1984.
- Wangness, R.K., *Electromagnetic Fields*, John Wiley and Sons, Inc., New York, 1979.
- Williams, D.J., Energetic ion beams at the edge of the plasma sheet: ISEE 1 observations plus a simple explanatory model, *J. Geophys. Res.*, 86, 5507, 1981.
- Williams, D.J., Dynamics of the Earth's ring current: theory and observation, APL preprint, Johns Hopkins University, 1985.
- Zmuda, A.J., F.T. Heuring and J.H. Martin, Dayside magnetic disturbances at 1100 km in the auroral oval, *J. Geophys. Res.*, 72, 1115, 1967.

Appendix A

```
SOU GSMGSE1.FOR(2,99)
SET ECHO=OFF
CR GSMGSE1.OUT
EMPTY GSMGSE1.OUT OK
EMPTY -OBJ OK
RUN *FORTRANVS SCARDS=GSMGSE1.FOR(100,*1) SPUNCH=-OBJ
RUN -OBJ 1=GSMGSE1.OUT 7=*MSINK*
comment LIST GSMGSE1.OUT
TR GSMGSE1.OUT
C*****
C
C      CONVERSION OF MAGNETIC FIELD COMPONENTS FROM
C      THE GSM TO THE GSE COORDINATE SYSTEM
C
C      written by: Wanda Kamocki
C      Spring 1988
C
C*****
C
C      This program uses as input the magnetic field components
C      at the neutral sheet in the GSM coordinate system and
C      transforms them to the GSE coordinate system. By biases
C      are, therefore, calculated for any specified hours and
C      days throughout a chosen year.
C
C*****
C
C      Variable Definitions:
C
C      D      = the Earth's Dipole vector (GSM Z-axis)
C      D1,D2,D3 = Direction Cosines of the vector D
C      GST     = Greenwich Mean Sidereal Time (degrees/radians)
C      S      = the Sun-Earth Line (X-axis in GSE and GSM)
C      S1,S2,S3 = Direction Cosines of the vector S
C      SRASN  = Sun's Right Ascension
C      SDEC   = Sun's Declination
C
C*****
C
C      Input parameters:
C
C      Universal Time
C      IYR = 1978
C      SECS = 000.0
C
C      SPECIFY MAGNETIC FIELD AT NEUTRAL SHEET IN GSM COORD's
C      BXGSM = 0.0
C      BYGSM = 0.0
```

BZGSM = 1.0

C*****

C WRITE LEADING INFO AND TITLE LINE

```

WRITE(1,9) 'YEAR = ',IYR,
&          'BXGSM = ',BXGSM,
&          'BYGSM = ',BYGSM,
&          'BZGSM = ',BZGSM
9  FORMAT(3X,A7,I4,3X,3(A8,F3.1,3X))
WRITE(1,99)'Day', 'Seconds', 'Sun_RASN', 'Sun Decl',
&          'BXGSE', 'BYGSE', 'BZGSE'
99 FORMAT(1X,A5,3A10,3A8)

```

C SET CONSTANTS (MULTIPLY BY CONVRT TO CONVERT TO RADIANS)

CONVRT = 2.0*3.14159/360.0

```

DO 1000 IDAY=5,365,10
DO 2000 IHOUR=0,20,5
SECS = FLOAT(60*60 IHOUR)

```

C FIND DIRECTION COSINES OF GSE (GSM) X-AXIS IN GEI COORD'S
C THIS IS THE SUN-EARTH LINE (VECTOR SGEI)

CALL SUN(IYR, IDAY, SECS, GST, SLONG, SRASN, SDEC)

```

SRASN = SRASN*CONVRT
SDEC  = SDEC *CONVRT
GST   = GST  *CONVRT

```

C COMPONENTS OF X-AXIS (GSE,GSM) in GEI

```

SXGEI = COS(SRASN) * COS(SDEC)
SYGEI = SIN(SRASN) * COS(SDEC)
SZGEI = SIN(SDEC)

```

C MAGNITUDE OF EARTH DIPOLE VECTOR D (GEO COORD'S)

DGEO = 1.0

C DIRECTION COSINES OF EARTH'S DIPOLE AXIS IN GEO COORD'S

```

D1 = 0.06859
D2 = -0.18602
D3 = 0.98015

```

C COMPONENTS OF EARTH'S DIPOLE AXIS IN GEO COORD'S

```

DXGEO = D1 * DGEO
DYGEO = D2 * DGEO
DZGEO = D3 * DGEO

```

C COMPONENTS OF EARTH'S DIPOLE AXIS IN GEI COORD'S (DGEI)

```

DXGEI = DXGEO*COS(GST) - DYGEO*SIN(GST)
DYGEI = DXGEO*SIN(GST) + DYGEO*COS(GST)
DZGEI = DZGEO

```

C CROSS PRODUCT OF DGEI WITH SGEI

DSX = DYGEI*SZGEI - DZGEI*SYGEI

$$\begin{aligned} \text{DSY} &= \text{DZGEI} * \text{SXGEI} - \text{DXGEI} * \text{SZGEI} \\ \text{DSZ} &= \text{DXGEI} * \text{SYGEI} - \text{DYGEI} * \text{SXGEI} \\ \text{DSMAG} &= \text{SQRT}(\text{DSX} ** 2 + \text{DSY} ** 2 + \text{DSZ} ** 2) \end{aligned}$$

C COMPONENTS OF GSM Y-AXIS IN GEI COORD'S

$$\begin{aligned} \text{YXGEI} &= \text{DSX} / \text{DSMAG} \\ \text{YYGEI} &= \text{DSY} / \text{DSMAG} \\ \text{YZGEI} &= \text{DSZ} / \text{DSMAG} \end{aligned}$$

C COMPONENTS OF GSM Z-AXIS IN GEI COORD'S

$$\begin{aligned} \text{ZXGEI} &= \text{SYGEI} * \text{YZGEI} - \text{SZGEI} * \text{YYGEI} \\ \text{ZYGEI} &= \text{SZGEI} * \text{YXGEI} - \text{SXGEI} * \text{YZGEI} \\ \text{ZZGEI} &= \text{SXGEI} * \text{YYGEI} - \text{SYGEI} * \text{YXGEI} \end{aligned}$$

C DIRECTION COSINES OF GSM Z-AXIS IN GEI COORD'S

$$\begin{aligned} \text{VMAG1} &= \text{SQRT}(\text{ZXGEI} ** 2 + \text{ZYGEI} ** 2 + \text{ZZGEI} ** 2) \\ \text{GSMZ1} &= \text{ZXGEI} / \text{VMAG1} \\ \text{GSMZ2} &= \text{ZYGEI} / \text{VMAG1} \\ \text{GSMZ3} &= \text{ZZGEI} / \text{VMAG1} \end{aligned}$$

C DIRECTION COSINES OF GSM Y-AXIS IN GEI COORD'S

$$\begin{aligned} \text{VMAG2} &= \text{SQRT}(\text{YXGEI} ** 2 + \text{YYGEI} ** 2 + \text{YZGEI} ** 2) \\ \text{GSMY1} &= \text{YXGEI} / \text{VMAG2} \\ \text{GSMY2} &= \text{YYGEI} / \text{VMAG2} \\ \text{GSMY3} &= \text{YZGEI} / \text{VMAG2} \end{aligned}$$

C DIRECTION COSINES OF GSE (GSM) X-AXIS in GEI COORD'S

$$\begin{aligned} \text{VMAG3} &= \text{SQRT}(\text{SXGEI} ** 2 + \text{SYGEI} ** 2 + \text{SZGEI} ** 2) \\ \text{S1} &= \text{SXGEI} / \text{VMAG3} \\ \text{S2} &= \text{SYGEI} / \text{VMAG3} \\ \text{S3} &= \text{SZGEI} / \text{VMAG3} \end{aligned}$$

C DIRECTION COSINES OF GSE Y-AXIS in GEI COORDINATES

$$\begin{aligned} \text{GSEY1} &= -0.398 * \text{S3} - 0.917 * \text{S2} \\ \text{GSEY2} &= +0.917 * \text{S1} \\ \text{GSEY3} &= +0.398 * \text{S1} \end{aligned}$$

C DIRECTION COSINES OF GSE Z-AXIS in GEI COORDINATES

$$\begin{aligned} \text{GSEZ1} &= 0.0 \\ \text{GSEZ2} &= -0.398 \\ \text{GSEZ3} &= +0.917 \end{aligned}$$

C SET UP THE TRANSFORMATION MATRIX "A"

$$\begin{aligned} \text{A11} &= \text{S1} * \text{S1} & + \text{S2} * \text{S2} & + \text{S3} * \text{S3} \\ \text{A12} &= \text{S1} * \text{GSMY1} & + \text{S2} * \text{GSMY2} & + \text{S3} * \text{GSMY3} \\ \text{A13} &= \text{S1} * \text{GSMZ1} & + \text{S2} * \text{GSMZ2} & + \text{S3} * \text{GSMZ3} \\ \\ \text{A21} &= \text{GSEY1} * \text{S1} & + \text{GSEY2} * \text{S2} & + \text{GSEY3} * \text{S3} \\ \text{A22} &= \text{GSEY1} * \text{GSMY1} & + \text{GSEY2} * \text{GSMY2} & + \text{GSEY3} * \text{GSMY3} \\ \text{A23} &= \text{GSEY1} * \text{GSMZ1} & + \text{GSEY2} * \text{GSMZ2} & + \text{GSEY3} * \text{GSMZ3} \\ \\ \text{A31} &= \text{GSEZ1} * \text{S1} & + \text{GSEZ2} * \text{S2} & + \text{GSEZ3} * \text{S3} \\ \text{A32} &= \text{GSEZ1} * \text{GSMY1} & + \text{GSEZ2} * \text{GSMY2} & + \text{GSEZ3} * \text{GSMY3} \\ \text{A33} &= \text{GSEZ1} * \text{GSMZ1} & + \text{GSEZ2} * \text{GSMZ2} & + \text{GSEZ3} * \text{GSMZ3} \end{aligned}$$

```

C  B COMPONENTS IN GSE FROM THOSE IN GSM
    BXGSE = A11*BXGSM + A12*BYGSM + A13*BZGSM
    BYGSE = A21*BXGSM + A22*BYGSM + A23*BZGSM
    BZGSE = A31*BXGSM + A32*BYGSM + A33*BZGSM
CHECK  GSEMAG = SQRT(BXGSE**2 + BYGSE**2 + BZGSE**2)

C  CONVERT RADIANS BACK TO DEGREES FOR EASE OF READING
    SRASN = SRASN / CONVRT
    SDEC  = SDEC  / CONVRT

C  WRITE OUT THE RESULTS TO FILE 1 (GSMGSE1.OUT)
    WRITE(1,999) IDAY,SECS,SRASN,SDEC,
    &          BXGSE,BYGSE,BZGSE
    999  FORMAT(1X,I5,3F10.1,3F8.3)

    2000  CONTINUE
    1000  CONTINUE

C*****

STOP
END
SUBROUTINE SUN(IYR, IDAY, SECS, GST, SLONG, SRASN, SDEC)
DATA RAD /57.29578/
DOUBLE PRECISION DJ, FDAY

IF(IYR.LT.1901.OR.IYR.GT.2099) RETURN

FDAY = SECS/86400.0
DJ    = 365*(IYR-1900)+(IYR-1901)/4+IDAY+FDAY-0.5D0
T     = DJ / 36525.0
VL    = DMOD(279.696678+0.9856473354*DJ, 360.0D0)
GST   = DMOD(279.690983+0.9856473354*DJ
&      +360.*FDAY+180., 360.0D0)
G     = DMOD(358.475845+0.985600267*DJ, 360.0D0) / RAD
SLONG= VL+(1.91946-0.004789*T)*SIN(G)
&      +0.020094*SIN(2.*G)
OBLIQ= (23.45229-0.0130125*T) / RAD
SLP   = (SLONG-0.005686) / RAD
SIND  = SIN(OBLIQ)*SIN(SLP)
COSD  = SQRT(1.0-SIND**2)
SDEC  = RAD * ATAN(SIND/COSD)
SRASN= 180.0-RAD*ATAN2(COTAN(OBLIQ)*SIND/COSD,
&      -COS(SLP)/COSD)

C*****

RETURN
END

```

Appendix B

```
SOU GSEGS1.FOR(2,99)
SET ECHO=OFF
CR GSEGS1.OUT
EMPTY GSEGS1.OUT OK
EMPTY -OBJ OK
RUN *FORTRANVS SCARDS=GSEGS1.FOR(100,*1) SPUNCH=-OBJ
RUN -OBJ 1=GSEGS1.OUT 2=GSEGS1.IN 7=*MSINK*
LIST GSEGS1.OUT
TR GSEGS1.OUT
```

```
C*****
```

```
C
```

```
C      CONVERSION OF MAGNETIC FIELD COMPONENTS FROM
C      THE GSE TO THE GSM COORDINATE SYSTEM
```

```
C
```

```
C      written by: Wanda Kamocki
C      Spring 1988
```

```
C
```

```
C*****
```

```
C
```

```
C This program uses as input both the Universal Time of
C a given magnetic event as well as the magnitudes of the
C three field components specified in GSE coordinates,
C and transforms the three field components to the GSM
C coordinate system.
```

```
C
```

```
C*****
```

```
C
```

```
C Variable Definitions:
```

```
C
```

```
C D      = the Earth's Dipole vector (GSM Z-axis)
C D1,D2,D3 = Direction Cosines of the vector D
C GST     = Greenwich Mean Sidereal Time (degrees/radians)
C S      = the Sun-Earth Line (X-axis in GSE and GSM)
C S1,S2,S3 = Direction Cosines of the vector S
C SRASN  = Sun's Right Ascension
C SDEC   = Sun's Declination
```

```
C
```

```
C*****
```

```
C
```

```
C SET CONSTANTS (MULTIPLY BY CONVRT TO CONVERT TO RADIANS)
C CONVRT = 2.0*3.14159/360.0
```

```
DO 1000 I=1,2000
```

```
C*****
```

```
C
```

```
C * Input parameters:
```

```

C
C   UNIVERSAL TIME AND GSE FIELD COMPONENTS
      READ(2,*,END=2000)IYR,IDAY,IHOUR,IMIN,
      &
      &          BXGSE,BYGSE,BZGSE
      SECS = FLOAT((60*IHOUR + IMIN)*60)

C*****

C   WRITE LEADING INFO AND TITLE LINE
      WRITE(1,*) ' '
      WRITE(1,9) 'YEAR = ',IYR,
      &
      &          'BXGSE = ',BXGSE,
      &
      &          'BYGSE = ',BYGSE,
      &
      &          'BZGSE = ',BZGSE
      9  FORMAT(3X,A7,I4,3X,3(A8,F5.1,3X))
      WRITE(1,99)'Day','Seconds','Sun RASN','Sun Decl',
      &
      &          'BXGSM','BYGSM','BZGSM'
      99  FORMAT(1X,A5,3A10,3A8)

C   FIND DIRECTION COSINES OF GSE (GSM) X-AXIS IN GEI COORD's
C   THIS IS THE SUN-EARTH LINE (VECTOR SGEI)
      CALL SUN(IYR,IDAY,SECS,GST,SLONG,SRASN,SDEC)

      SRASN = SRASN*CONVRT
      SDEC  = SDEC *CONVRT
      GST   = GST  *CONVRT

C   COMPONENTS OF X-AXIS (GSE,GSM) in GEI
      SXGEI = COS(SRASN) * COS(SDEC)
      SYGEI = SIN(SRASN) * COS(SDEC)
      SZGEI = SIN(SDEC)

C   MAGNITUDE OF EARTH DIPOLE VECTOR D (GEO COORD's)
      DGEO = 1.0

C   DIRECTION COSINES OF EARTH's DIPOLE AXIS IN GEO COORD's
      D1 = 0.06859
      D2 = -0.18602
      D3 = 0.98015

C   COMPONENTS OF EARTH's DIPOLE AXIS IN GEO COORD's
      DXGEO = D1 * DGEO
      DYGEO = D2 * DGEO
      DZGEO = D3 * DGEO

C   COMPONENTS OF EARTH's DIPOLE AXIS IN GEI COORD's (DGEI)
      DXGEI = DXGEO*COS(GST) - DYGEO*SIN(GST)
      DYGEI = DXGEO*SIN(GST) + DYGEO*COS(GST)
      DZGEI = DZGEO

C   CROSS PRODUCT OF DGEI WITH SGEI
      DSX = DYGEI*SZGEI - DZGEI*SYGEI
      DSY = DZGEI*SXGEI - DXGEI*SZGEI
      DSZ = DXGEI*SYGEI - DYGEI*SXGEI

```

```

DSMAG = SQRT(DSX**2 + DSY**2 + DSZ**2)

C COMPONENTS OF GSM Y-AXIS IN GEI COORD'S
  YXGEI = DSX/DSMAG
  YYGEI = DSY/DSMAG
  YZGEI = DSZ/DSMAG

C COMPONENTS OF GSM Z-AXIS IN GEI COORD'S
  ZXGEI = SYGEI*YZGEI - SZGEI*YYGEI
  ZYGEI = SZGEI*YXGEI - SXGEI*YZGEI
  ZZGEI = SXGEI*YYGEI - SYGEI*YXGEI

C DIRECTION COSINES OF GSM Z-AXIS IN GEI COORD'S
  VMAG1 = SQRT(ZXGEI**2 + ZYGEI**2 + ZZGEI**2)
  GSMZ1 = ZXGEI/VMAG1
  GSMZ2 = ZYGEI/VMAG1
  GSMZ3 = ZZGEI/VMAG1

C DIRECTION COSINES OF GSM Y-AXIS IN GEI COORD'S
  VMAG2 = SQRT(YXGEI**2 + YYGEI**2 + YZGEI**2)
  GSMY1 = YXGEI/VMAG2
  GSMY2 = YYGEI/VMAG2
  GSMY3 = YZGEI/VMAG2

C DIRECTION COSINES OF GSE (GSM) X-AXIS in GEI COORD'S
  VMAG3 = SQRT(SXGEI**2 + SYGEI**2 + SZGEI**2)
  S1 = SXGEI/VMAG3
  S2 = SYGEI/VMAG3
  S3 = SZGEI/VMAG3

C DIRECTION COSINES OF GSE Y-AXIS in GEI COORDINATES
  GSEY1 = -0.398*S3 - 0.917*S2
  GSEY2 = +0.917*S1
  GSEY3 = +0.398*S1

C DIRECTION COSINES OF GSE Z-AXIS in GEI COORDINATES
  GSEZ1 = 0.0
  GSEZ2 = -0.398
  GSEZ3 = +0.917

C SET UP THE TRANSFORMATION MATRIX "A"
C TO GO BETWEEN GSM AND GSE IN EITHER DIRECTION
  A11 = S1*S1 + S2*S2 + S3*S3
  A12 = S1*GSMY1 + S2*GSMY2 + S3*GSMY3
  A13 = S1*GSMZ1 + S2*GSMZ2 + S3*GSMZ3

  A21 = GSEY1*S1 + GSEY2*S2 + GSEY3*S3
  A22 = GSEY1*GSMY1 + GSEY2*GSMY2 + GSEY3*GSMY3
  A23 = GSEY1*GSMZ1 + GSEY2*GSMZ2 + GSEY3*GSMZ3

  A31 = GSEZ1*S1 + GSEZ2*S2 + GSEZ3*S3
  A32 = GSEZ1*GSMY1 + GSEZ2*GSMY2 + GSEZ3*GSMY3
  A33 = GSEZ1*GSMZ1 + GSEZ2*GSMZ2 + GSEZ3*GSMZ3

```

```

C  B COMPONENTS IN GSM FROM THOSE IN GSE
    BXGSM = A11*BXGSE + A21*BYGSE + A31*BZGSE
    BYGSM = A12*BXGSE + A22*BYGSE + A32*BZGSE
    BZGSM = A13*BXGSE + A23*BYGSE + A33*BZGSE
    GSMMAG = SQRT(BXGSM**2 + BYGSM**2 + BZGSM**2)

C  CONVERT RADIANS BACK TO DEGREES FOR EASE OF READING
    SRASN = SRASN / CONVRT
    SDEC  = SDEC  / CONVRT

C  WRITE OUT THE RESULTS TO FILE 1 (GSEGSM1.OUT)
    WRITE(1,999) IDAY,SECS,SRASN,SDEC,
    &          BXGSM,BYGSM,BZGSM,GSMMAG
    999      FORMAT(1X,I5,3F10.1,4F8.3)

1000 CONTINUE
2000 CONTINUE

C*****

    STOP
    END
    SUBROUTINE SUN(IYR,IDAY,SECS,GST,SLONG,SRASN,SDEC)
    DATA RAD /57.29578/
    DOUBLE PRECISION DJ, FDAY

    IF(IYR.LT.1901.OR.IYR.GT.2099) RETURN

    FDAY = SECS/86400.0
    DJ   = 365*(IYR-1900)+(IYR-1901)/4+IDAY+FDAY-0.5D0
    T    = DJ / 36525.0
    VL   = DMOD(279.696679+0.9856473354*DJ,360.0D0)
    GST  = DMOD(279.690982+0.9856473354*DJ
    &      +360.*FDAY*80.,360.0D0)
    G    = DMOD(358.475845+0.985600267*DJ,360.0D0) / RAD
    SLONG= VL+(1.91946-0.004789*T)*SIN(G)
    &      +0.020094*SIN(2.*G)
    OBLIQ= (23.45229-0.0130125*T) / RAD
    SLP   = (SLONG-0.005686) / RAD
    SIND  = SIN(OBLIQ)*SIN(SLP)
    COSD  = SQRT(1.0-SIND**2)
    SDEC  = RAD * ATAN(SIND/COSD)
    SRASN= 180.0-RAD*ATAN2(COTAN(OBLIQ)*SIND/COSD,
    &      -COS(SLP)/COSD)

C*****

    RETURN
    END

```

TRANSFORMATION OF MAGNETIC FIELD DATA FROM GSE TO
GSM COORDINATES FOR 8 EVENTS CONSIDERED IN CHAPTER 4.

YEAR = 1979	BXGSE =	0.0	BYGSE =	1.0	BZGSE =	10.0
Day Seconds	Sun RASN	Sun Decl	BXGSM	BYGSM	BZGSM	BTOT
39 51900.0	321.7	-15.1	0.002	-0.978	9.999	10.046
YEAR = 1979	BXGSE =	0.0	BYGSE =	0.0	BZGSE =	3.5
Day Seconds	Sun RASN	Sun Decl	BXGSM	BYGSM	BZGSM	BTOT
73 52560.0	354.0	-2.6	0.000	-1.027	3.345	3.499
YEAR = 1979	BXGSE =	2.0	BYGSE =	2.5	BZGSE =	8.0
Day Seconds	Sun RASN	Sun Decl	BXGSM	BYGSM	BZGSM	BTOT
126 12960.0	42.6	16.3		385	8.370	8.613
YEAR = 1979	BXGSE =	0.0	BYGSE =	3.0	BZGSE =	6.0
Day Seconds	Sun RASN	Sun Decl	BXGSM	BYGSM	BZGSM	BTOT
42 66240.0	324.8	-14.0	0.000	0.373	6.695	6.706
YEAR = 1979	BXGSE =	5.0	BYGSE =	0.0	BZGSE =	5.0
Day Seconds	Sun RASN	Sun Decl	BXGSM	BYGSM	BZGSM	BTOT
64 38040.0	345.5	-6.2	5.000	-0.969	4.903	7.070
YEAR = 1979	BXGSE =	0.0	BYGSE =	-8.0	BZGSE =	5.0
Day Seconds	Sun RASN	Sun Decl	BXGSM	BYGSM	BZGSM	BTOT
90 41580.0	9.3	4.0	-0.00	-8.856	3.242	9.431
YEAR = 1979	BXGSE =	0.0	BYGSE =	-8.0	BZGSE =	11.0
Day Seconds	Sun RASN	Sun Decl	BXGSM	BYGSM	BZGSM	BTOT
83 5580.0	2.6	1.1	-0.00	-12.608	5.090	13.597
YEAR = 1979	BXGSE =	0.0	BYGSE =	14.0	BZGSE =	-5.0
Day Seconds	Sun RASN	Sun Decl	BXGSM	BYGSM	BZGSM	BTOT
76 1680.0	356.2	-1.7	-0.00	14.409	3.637	14.861

Appendix C

List of Symbols:

- \bar{B} = magnetic field vector (Teslas)
 \bar{E} = electric field vector (volts/m)
 \bar{F} = applied force (N)
 \bar{F}_C = centripetal force (N)
 \bar{v} = particle velocity (m/sec)
 \bar{v}_D = particle drift velocity (m/sec)
 v_{\parallel} = component of velocity along \bar{B} (m/sec)
 v_{\perp} = component of velocity perpendicular to \bar{B} (m/sec)
 v_A = Alfvén speed (m/sec)
 \bar{I} = current intensity (A/m)
 \bar{J} = current density (A/m²)
 J_{\parallel} = component of current density along \bar{B} (A/m²)
 J_{\perp} = component of current density normal to \bar{B} (A/m²)
 \bar{J}_{in} = inertial current density (A/m²)
 \bar{J}_D = diamagnetic current density (A/m²)
 P = particle pressure (N/m²)
 P_{\parallel} = particle pressure along \bar{B} (N/m²)
 P_{\perp} = particle pressure perpendicular to \bar{B} (N/m²)
 $\bar{\Omega}$ = vorticity (1/sec)
 \bar{R} = radius of curvature (m)
 \hat{r} = unit vector in the direction of \bar{R}
 μ = magnetic moment of a particle (A/m²)
 μ_0 = permeability of free space (Henry/m)
 ϵ_0 = permittivity of free space (farads/m)
 ϵ_{\parallel} = longitudinal energy of a particle (joules)
 ϵ_{\perp} = transverse energy of a particle (joules)
 ρ = mass density (kg/m³)
 σ = space charge (coulombs/m³)
 q = electric charge (coulombs)
 g = electrical conductivity (mhos/m)
 $\Delta\phi$ = magnetic flux (webers)
 ΔA = cross-sectional area (m²)
 β = ratio of particle to magnetic pressure (unitless)